Vishal Shah
Editor

Emerging Environmental Technologies



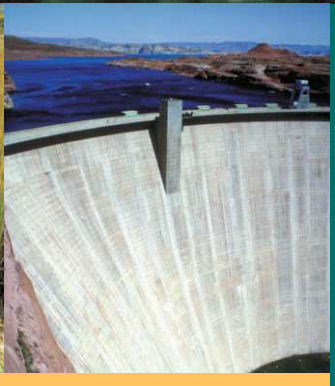

Springer

Emerging Environmental Technologies

Emerging Environmental Technologies

Edited by

Vishal Shah
Department of Biology, Dowling College, Oakdale, NY, USA

Springer

Editor
Vishal Shah
Dowling College
150 Idle Hour Blvd.
Oakdale NY 11769
USA
shahv@dowling.edu

ISBN: 978-1-4020-8785-1 e-ISBN: 978-1-4020-8786-8

Library of Congress Control Number: 2008932112

Printed on acid-free paper

9 8 7 6 5 4 3 2 1

springer.com

To my parents and Dr. Frantisek Nerud

Preface

In this day and age, it is unfortunate that the economic prosperity and development leads to disruption of the dynamic balance of the environment. The philosophy of sustainable development has been presented for a long period of time but it has not been able to bring about a substantial change in our society. The transformation of this philosophy into a practical reality seems to be far away – at least in the foreseeable future. In my opinion, the only way I see the revolution taking place is for us to incorporate 'sustainability' in our daily living and to keep pushing for a sustainable society. Meanwhile, we also need scientists to work on technologies that would lead us to that goal at a faster pace. Technologies that are 'completely' environmentally friendly are needed urgently. And if such technologies or ideas of one exists, a platform is required that showcases such ideas to the scientific and non-scientific audience. Through this book, I am happy to present the thoughts of seven different research groups whose work may lead us to the doorsteps of sustainable society.

As scientists, most of us specialize in a sub-topic that may be related to one of the three environmental components – air, land, or water. Over a period of time, we become so engrossed with the sub-discipline of our specialization that we only have glimpses of what is happening in other disciplines. I hope that this book will serve as a bridge between sub-disciplines of environmental technologies as it attempts to cover a wide array of topics across the boundaries of disciplines. The topics range from energy to catalysis to bioremediation. The book is anticipated to benefit the science and scientists as one would then be able to find common threads and problems amongst multiple disciplines. It also presents the developing technologies to non-scientific viewers who can now know about the new innovations without searching and screening within the huge reservoir of literature.

The seven articles that are presented through this book are all peer-reviewed articles and I wish to thank all the contributing authors, including the ones whose work did not make it through the peer-review process. I would also like to thank Ms. Deborah Wynne for proofreading the text.

Finally, the resounding response to the call for articles I have received over the last six months makes me believe that this book and similar ones to follow will serve as a route to assorted reading on new frontiers in environmental technologies.

New York, USA Vishal Shah

Contents

List of Contributors

R. Bhure
Center for Materials Research, Norfolk State University, 700 Park Avenue, Norfolk, VA 23504

J. Dong
Department of Chemical and Materials Engineering, University of Alberta, Edmonton, Alberta, Canada T6G 2G6

A. Mahapatro
Department of Chemistry, Center for Biotechnology and Biomedical Sciences, Center for Materials Research, Norfolk State University, 700 Park Avenue, Norfolk, VA 23504, USA

A. K. Marcus
Center for Environmental Biotechnology, Biodesign Institute
at Arizona State University, Tempe, Arizona, USA

L. C. Maxey
Oak Ridge National Laboratory, P.O. Box 2008, MS 6054, Oak Ridge, TN 37831, USA

D. N. Miao
Department of Biology, Queen's University, Kingston, ON, Canada K7L 3N6

M. S. Olson
Department of Civil Architectural and Environmental Engineering, Drexel University, 3141 Chestnut Street, Philadelphia, PA 19104, USA

G. R. Palmer
Department of Biology, Queen's University, Kingston, ON, Canada K7L 3N6

J. A. Ripmeester
Department of Biology, Queen's University, Kingston, ON, Canada K7L 3N6

B. E. Rittmann
Center for Environmental Biotechnology, Biodesign Institute at Arizona State University, Tempe, Arizona, USA

V. Shah
Department of Biology, Dowling College, Oakdale, NY 11769, USA

G. Shaver
School of Mechanical Engineering, Herrick Laboratories and Energy Center at Discovery Park, Purdue University, West Lafayette, IN 47907

R. Singh
Department of Civil Architectural and Environmental Engineering, Drexel University, 3141 Chestnut Street, Philadelphia, PA 19104, USA

C. I. Torres
Center for Environmental Biotechnology, Biodesign Institute at Arizona State University, Tempe, Arizona, USA

V. K. Walker
Department of Biology, Queen's University, Kingston, ON, Canada K7L 3N6

S. L. Wilson
Department of Biology, Queen's University, Kingston, ON, Canada K7L 3N6

Z. Wu
Department of Biology, Queen's University, Kingston, ON, Canada K7L 3N6

Z. Xu
Department of Chemical and Materials Engineering, University of Alberta, Edmonton, Alberta, Canada T6G 2G6

H. Zeng
Department of Biology, Queen's University, Kingston, ON, Canada K7L 3N6

Chapter 1
Understanding the Distinguishing Features of a Microbial Fuel Cell as a Biomass-Based Renewable Energy Technology

Bruce E. Rittmann, César I. Torres and Andrew Kato Marcus

Abstract Biomass-based renewable energy, which utilizes biomass derived from photosynthesis, could sustainably provide 67–450 EJ of energy annually. Biomass in organic wastes, for example, can annually provide 7.5 EJ of energy, and utilization of organic wastes locally as an energy source can prevent environmental pollution and reduce the energy losses associated with transportation. The technological challenge is to sustainably capture this biomass energy without creating serious environmental or social damage.

A microbial fuel cell (MFC) is a novel biomass-based technology that marries microbiological catalysis to electrochemistry. In an MFC, bacteria present at the fuel-cell anode catalyze the oxidation of diverse organic fuel sources, including domestic wastewater, animal manures, and plant residues. As an electrochemical process, an MFC converts the energy value stored in the organic fuel directly to electrical energy, avoiding combustion and combustion-associated contaminants. The main product at the anode is CO_2 that is carbon neutral. When oxygen is the oxidant at the fuel-cell cathode, an MFC produces only H_2O. An MFC is an attractive renewable energy technology, because it produces electricity at the same time it treats wastes, and it does so without producing harmful byproducts.

We introduce MFCs in the context of the general cycle for biomass-based renewable energy technology. Tracking of carbon oxidation state highlights the distinctly different approach that an MFC takes with respect to biofuels. Then, we review some of recent progress in MFC research, with an emphasis on mathematical modeling. At last, we conclude with our perspectives on biomass-based renewable energy by comparing the MFC with two more mature technologies for generating biofuels: bioethanol and anaerobic digestion to methane.

Keywords Anode · bioenergy · biofilm · biomass · microbial fuel cell

B.E. Rittmann
Center for Environmental Biotechnology, Biodesign Institute at Arizona State University, Tempe, AZ 85287-5701, USA
e-mail: Rittmann@asu.edu

V. Shah (ed.), *Emerging Environmental Technologies*,

1.1 Introduction

Renewable energy refers to energy sources that natural processes replenish in a short term. It has the potential to decrease our dependence on fossil fuels and reduce global warming. Renewable energy currently supplies approximately 14% (or 57 EJ/year) of the energy consumed by humans around the world [1], and the contribution of renewable energy in the global market is growing. Incident solar energy carries 173,000 TW of energy to Earth; that corresponds to 5.5 million EJ/year, which is more than 10,000 times greater than the current annual consumption of primary energy by human activities (418 EJ/year) [1]. Photosynthesis to produce biomass captures an average of about 140 TW, or less than 0.1% of the incident energy.

Although the average conversion percentage may seem small, photosynthesis actually produces a significant amount of biomass that embodies renewable energy. Annually, photosynthesis produces 220 billion dry tonnes of biomass in primary production, and the corresponding energy value for that biomass is 4500 EJ/year [2]. The energy value of terrestrial biomass available for human use has been estimated as 67–450 EJ [2] and, thus, corresponds to 25–110% of the current primary energy consumption.

Chynoweth et al. [3] estimated the energy potential from domestically available biomass in the United States. Energy crops can provide 22 EJ/year, and marine crops have a more significant energy potential of >100 EJ each year. On a yearly basis, 7.5 EJ of energy value is available from waste sources that include municipal solid waste, biodegradable industrial wastes, crop residues, animal wastes, sewage sludge, and sludge-grown biomass. This energy equals 7% of the U.S. energy use of 105 EJ in 2005 [4]. Among the wastes, food-processing, brewery, and agricultural wastewaters are ideal candidates for energy generation, because they contain high levels of easily degradable organic material that converts to biofuels easily using microorganism-based systems.

Wastes are produced at all human habitats, and their local consumption reduces energy losses due to transportation. In 2006, the United States generated 57.8 million tonnes of municipal organic waste, which includes food and yard trimmings [5]. Since transporting 1 tonne of municipal organic waste for 1 km by truck requires approximately 48 MJ of energy [6], transporting 57.8 tonnes for 1 km requires 2.8 PJ of energy or 459 million barrels of crude oil. Local consumption of organic wastes for energy generation can potentially save PJs of energy and provide double benefit by treating the pollutants so that they are no longer harmful to the environment.

The technological challenge is capturing this sustainable biomass energy without creating serious environmental or social damage. In the next sections, we introduce the general cycle for biomass-based renewable energy and discuss where two contemporary alternatives for capturing biomass energy – bioethanol and anaerobic digestion to methane – fit in the context. Then, we introduce the microbial fuel cell (MFC) and show where it fits in the context of the energy cycle.

1.1.1 A General Cycle for Biomass-Based Renewable Energy

Figure 1.1 shows the general cycle for biomass-based renewable energy, in which microorganisms convert biomass to fuel. The cycle has three parts: (1) production of biomass by photosynthesis, (2) generation of a convenient biofuel, and (3) generation of useful energy from the biofuel. Photosynthesis captures solar energy to reduce carbon dioxide and generate biomass in the form of plants, algae, and cyanobacteria. The biomass can be used directly as the biofuel source, or it may be used as input to the food-supply system. In the latter case, processed biomass outputs of the food-supply system, such as wastes and residues, become the biofuel source.

In most cases, the biomass used as a biofuel source is made of polymers, especially proteins, lipids, and polysaccharides. However, these complex polymers are not usually convenient for direct use in energy generation. Hence, microbiological reactions are needed to convert biomass into useful biofuels, such as methane, hydrogen, and ethanol. Biofuels can be collected and reacted with oxygen to generate useful energy. The carbon dioxide produced during microbial metabolism in parts 2 and 3 is recycled in photosynthesis and, hence, the biomass technology is carbon neutral.

Carbon changes its oxidation state during the general cycle. A carbon atom can have an oxidation state between $+4$ and -4, and the carbon in CO_2 is at its most oxidized form, $+4$. The next sections show that following the oxidation state of carbons helps understand the general cycle.

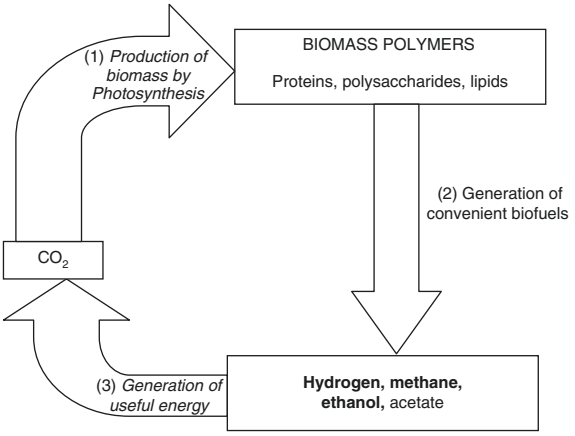

Fig. 1.1 Schematic of how microbial processes fit into the overall scheme for biomass-based renewable energy technologies. Three major biofuels (ethanol, hydrogen, and methane) appear in **bold**. Another useful biofuel is acetate. Microbial systems can participate in all three steps. (1) Photosynthesis to produce algae or cyanobacteria. (2) Fermentative conversion to produce hydrogen, methane, or ethanol, and acetate. (3) Generation of useful energy from biofuels (e.g., electricity generation from acetate via an MFC)

1.1.1.1 Production of Biomass by Photosynthesis

Photosynthesis is a biochemical reaction that converts light energy into chemical energy. Starting materials for photosynthesis are H_2O and CO_2. In typical aerobic photosynthesis, electrons from water combine with CO_2 so that the oxidation state of carbon decreases from +4 to the average oxidation state of biomass of around 0 [7]. This reduction is illustrated by the formation of carbohydrate, CH_2O, whose C has an oxidation state of 0. The O in H_2O is oxidized to form O_2:

$$\text{Half reaction for water: } 2H_2O \rightarrow O_2 + 4H^+ + 4e^-$$

$$\text{Half reaction for carbohydratesynthesis: } CO_2 + 4H^+ + 4e^- \rightarrow CH_2O + H_2O$$

$$\text{Whole reaction: } H_2O + CO_2 \rightarrow CH_2O + O_2$$

While this reaction is thermodynamically unfavorable, photosynthetic organisms capture energy from light to energize the electron removal from H_2O and drive the reduction of CO_2 (approximately $\Delta G^{0\prime} = 480$ kJ/mol CH_2O). Organisms that fix carbon for biomass synthesis using light energy are called photoautotrophs (photo = light; auto = self; troph = nourishment).

The goal of all biomass-based systems for generating useful energy is to efficiently drive the photosynthetic reaction in reverse. A glucose molecule ($C_6H_{12}O_6$) is an example of carbohydrate that can form from photosynthesis:

$$6\,H_2O + 6\,CO_2 \rightarrow C_6H_{12}O_6 + 6\,O_2$$

The glucose reaction as written requires light energy of at least 2870 kJ to form every mole of glucose. It is the absorption of solar energy that fuels the food chain on Earth and also gives the Earth's atmosphere its characteristic 21% O_2. A successful biomass-based energy technology captures this energy efficiently, usefully, and without creating serious environmental harm.

The method for energy capture depends on the type of biomass. Petroleum and dry materials like coal and wood can be combusted. Coal and petroleum are non-renewable, while the production rate of new wood is slow. Other types of biomass, such as algae and cyanobacteria, are rich in lipids that can be efficiently extracted as biodiesel and combusted. Animal manures, wastewater, and many agricultural residues are wet and cannot be combusted efficiently; they require microbiological processing (next sections) to convert the biomass to convenient biofuels. Figure 1.2 provides an overview of the steps catalyzed by microorganisms.

1.1.1.2 Hydrolysis and Fermentation

Hydrolysis is the first step in converting biomass, such as agricultural residue, animal manure, and wastewater sludge, to biofuel (Fig. 1.2). Hydrolysis converts organic solids and polymeric macromolecules to soluble molecules that

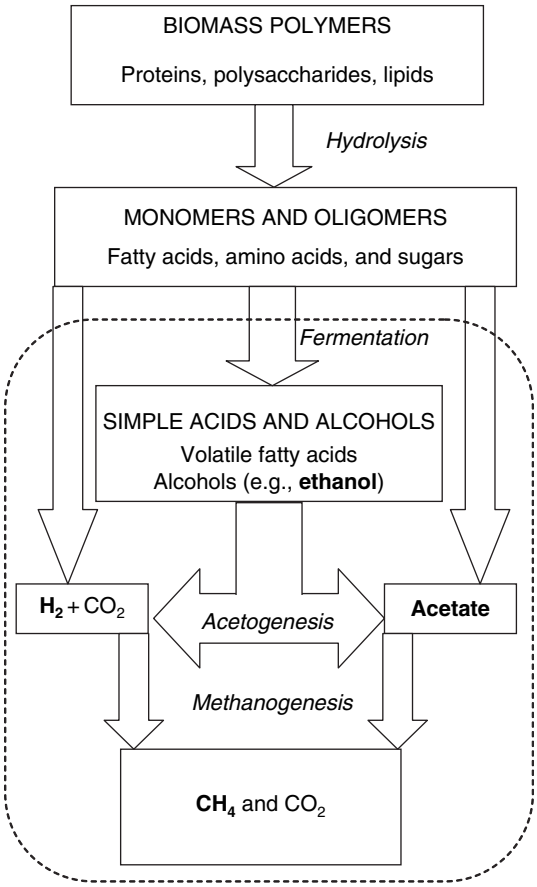

Fig. 1.2 Different stages at which biofuels such as acetate, ethanol, hydrogen, and methane are generated. Steps enclosed within dotted oval show generation of biofuels

are bioavailable for microbial metabolism. Many microorganisms produce enzymes that can hydrolyze polymers to monomers and oligomers. However, some lignocellulose materials, present in many plants, are difficult to degrade microbiologically or enzymatically. Lignocellulosic structures provide a physical barrier to enzymes or can be chemically resistant to enzymatic reaction. In these cases, mechanical, physicochemical, or chemical pretreatment can make lignocellulosic materials susceptible to enzymatic attack [8].

In biofuels production, fermentation generates biofuels from monomers by rearranging the molecular bonds within the compounds and breaking them down into smaller oxidized and reduced products. Oxidized products are typically CO_2, which carries no electrons from the original product; therefore capturing of the rest of electrons by the reduced byproduct brings the average carbon oxidation state of the fermentation products to a value more negative

than for the starting biomass. The fermentative bacteria retain a small fraction of the carbon from the original compounds to synthesize new cells, but most of the electrons and energy from the biomass are contained in the fermentation products.

Figure 1.2 shows different stages at which biofuels such as ethanol, hydrogen, and methane are generated. Ethanol is generated directly from the fermentation of sugars, such as glucose. The complete fermentation of one glucose molecule to ethanol produces two moles of ethanol and two moles of carbon dioxide:

$$C_6H_{12}O_6 \rightarrow 2\,CH_3CH_2OH + 2\,CO_2$$

This brings the average oxidation state of carbon to –2 for ethanol.

As shown in Fig. 1.2, methane is produced at the last stage of the biological processes during methanogenesis. Anaerobic (methanogenic) digestion depends on a sequence of steps that involves acidogenesis, acetogenesis, and methanogenesis. The overall goal of the anaerobic digestion technology is to convert carbons in biomass to its most reduced oxidation state, –4 in CH_4 or methane.

Microorganisms that carry out methanogenesis are termed methanogens (i.e., methane generators), and they are in the domain *Archaea*. Two major types of methanogens are hydrogenotrophic and acetoclastic methanogens. Hydrogenotrophs oxidize H_2 and reduce CO_2 to CH_4 in a form of anaerobic respiration:

$$4H_2 + CO_2 = CH_4 + 2H_2O$$

Acetoclastic methanogens ferment one molecule of acetate to produce one molecule each of CH_4 and CO_2:

$$CH_3COO^- + H_2O = CH_4 + HCO_3^-$$

As glucose and biomass have comparable average carbon oxidation states (i.e., ~0), many (e.g., Angenent et al. [9]) appropriately describe the overall reaction for methanogenesis with glucose as

$$C_6H_{12}O_6 = 3\,CO_2 + 3\,CH_4$$

in which CH_4 with the carbon oxidation state of –4 captures all the electrons from glucose. All the electrons must flow through H_2 and acetate, as shown in Fig. 1.2 and the reactions just above. Approximately 70% of the methane formed in conventional anaerobic treatment comes from acetate [9].

1.2 Microbial Fuel Cell

An MFC marries microbiological catalysis to the electrochemistry of a fuel cell. Figure 1.3 describes the flow of electrons and ions in an MFC. The fuel for an MFC is an electron donor for bacteria that live in a biofilm attached to the

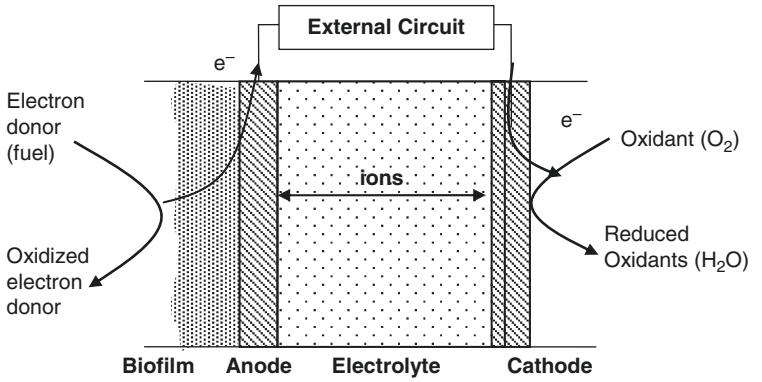

Fig. 1.3 Schematic illustration of the essential components of a MFC, particularly the separate flows of electrons (e^-) and ions from the anode to the cathode

anode and transfer electrons from the donor to the anode. For example, when acetate is the fuel, its oxidation reaction is $CH_3COO^- + 2H_2O \rightarrow CO_2 + HCO_3^- + 8H^+ + 8e^-$. In a unique form of respiratory metabolism, the anode-respiring bacteria (ARB) transfer electrons to the anode electrode, and the difference in the electrochemical potential between the anode and cathode electrodes drives the flow of electrons through an external circuit, generating electrical current and electrical energy. At the cathode, the oxidant is reduced, and the reduced oxidant carries the electrons out of the reactor. O_2 is the typical oxidant: $O_2 + 4H^+ + 4e^- \rightarrow 2H_2O$.

Since the goal of an MFC is to circuit electrons to generate electricity, completely removing electrons from organic compounds to produce CO_2 is desirable. Hence, in contrast to biofuel generation, an MFC makes the oxidation state of carbon more positive than biomass.

Dramatic advancements in MFC technology are possible today because of the recent discovery that many bacterial species are ARB [10, 11, 12]. The discovery of ARB eliminates the need for externally supplied electron shuttles, which are expensive and often toxic. Provided with suitable environmental conditions, ARB naturally establish a biofilm community on the anode [13, 14, 15]. The community structure of ARB-containing biofilm often is diverse [13, 16, 17], and the diversity is expected to be enhanced by the wide range of available fuels, which include agricultural residues, animal manures, and wastewater [14, 18, 19].

Although the novelty of an MFC is in the anode respiration by ARB, other microbial metabolic processes, such as hydrolysis and fermentation, can play significant roles in an MFC too. As shown in Fig. 1.2, hydrolysis and fermentation break down complex polymeric materials to simpler byproducts like acetate, which is a favorable electron donor for ARB. An MFC fed with fermentative substrates, such as glucose, becomes enriched with fermentative bacteria such as *Clostridia*, *Fermicutes*, and *Bacterioides* [13, 17, 20]. Fermentative products, such

as ethanol, acetate, butyrate, and propionate, have been found to accumulate in the anode [21, 22].

One study is particularly illustrative in highlighting the positive syntrophic interactions between ARB and fermenters. Ren et al. [22] demonstrated collaboration between ARB and fermenters to transfer electrons from cellulose – polysaccharide derived from beta-glucose linkage – to the anode. A pure culture of *Geobacter sulfurreducens*, a well-known ARB, was incapable of cellulose hydrolysis and anode respiration. However, in the presence of *Clostridia cellulolyticum*, which hydrolyzes and ferments cellulose to acetate, ethanol, and hydrogen, *G. sulfurreducens* used some of these fermentation byproducts to respire the anode to support the generation of electricity by an MFC. This collaboration between ARB and fermenters is analogous to the processes that occur in anaerobic digesters: McCarty describes anaerobic digestion as an assembly line in which several microbial species cooperate to break down organic materials to methane [23]. In the case of the MFC anode, several different microbial species appear to collaboratively funnel the electrons from the waste ultimately to the anode.

In the biomass-to-energy field, the important *niche* of an MFC is that it directly generates electrical energy, which relates measurable outputs from an MFC: current and voltage. Current describes the amount of charge (or electrons) passing through the circuit per unit time. Voltage describes the amount of energy that is carried by a unit charge (e.g., an electron equivalent) that passes through the circuit. Multiplied together, current and voltage define power, which is the rate at which energy is generated. Current also relates to three wastewater treatment objectives of an MFC:

- The rate and amount of the organic waste that is removed
- The generation of organic byproduct generated by fermentative bacteria
- The substrate flux and organic loading rate

When comparing MFCs to other biomass-to-energy processes, researchers consider two types of calculations to asses the energy efficiency of the process. First is the energy capture efficiency (ECE), in which an energy balance is made to determine how much energy is converted into electrical energy from the original amount of energy fed into the reactor as substrate. Second is the process energy efficiency (PEE), which is the ratio between the energy needed to run the biomass-to-energy process and the energy collected as electrical (or chemical) energy. Additionally, if the system is also used as a wastewater treatment process, then it is important to determine the treatment efficiency (TE), in which the chemical oxygen demand (COD) removal is calculated.

We use mathematical models that help us understand the interrelationships among current, voltage, ECE, and TE for an MFC process. We present the model in three parts:

1. Voltage in an MFC
2. Current density in the MFC's anode
3. Coulombic efficiency, ECE, and COD balance in an MFC

Finally, we compare MFCs to bioethanol and methanogenesis from both ECE and PEE perspectives.

1.2.1 Understanding Voltages in an MFC

1.2.1.1 Maximum Potential

The maximum potential obtained in any reaction is that of the potential difference between the half reactions of the electron donor and acceptor, occurring at the anode and cathode, respectively. Under ideal conditions, both half reactions occur at the same pH; we define $E'_{\text{rxn,max}}$ as the maximum potential for pH = 7, as most microorganisms grow at near-neutral pH:

$$E'_{-\text{rxn,max}} = E'_{-\text{acceptor}} - E'_{-\text{donor}} \tag{1.1}$$

where E'_{acceptor} and E'_{donor} are the half-reaction potentials for the respective donor and acceptor (V). The superscript $'$ denotes a pH of 7. E'_{acceptor} and E'_{donor} can be determined by the Nernst equation, shown here for a generic electron–donor reaction:

$$E'_{\text{donor}} = E^{o'}_{\text{donor}} - \frac{RT}{nF}\ln\left(\frac{[\text{red}]^{\gamma}}{[\text{ox}]^{\beta}}\right) \tag{1.2}$$

where $E^{o'}$ is the standard free energy at pH = 7 (V), R is the universal gas constant (8.314 J/mol K), T is the temperature at which the fuel cell is operated (K), n is the number of electrons transferred, F is the Faraday constant (96,485 Coulombs/mol), [ox] and [red] are the concentrations of the oxidized and reduced compounds, respectively, and γ and β are their corresponding stoichiometric coefficients. In the case of an MFC anode consuming acetate, the donor half reaction is

$$CO_2 + HCO_3^- + 8\,H^+ + 8\,e^- \rightarrow CH_3COO^- + 3\,H_2O \quad E^{o'} = -0.285\,\text{V} \tag{1.3}$$

The equilibrium anode voltage is then

$$E_{\text{donor}} = -0.285\,\text{V} - \frac{RT}{8F}\ln\left(\frac{[CH_3\,COO^-][10^{-7}]^8}{[HCO_3^-][CO_2][H^+]^8}\right) \tag{1.4}$$

Equation (1.4) shows the parameters that control E_{donor}: temperature and concentrations of reactants and products. The concentration of protons ($[H^+] = 10^{-\text{pH}}$) is a major parameter that controls E_{donor}. A change of one pH unit causes a 60 mV shift in E_{donor}. A similar case occurs with E_{acceptor}, in which

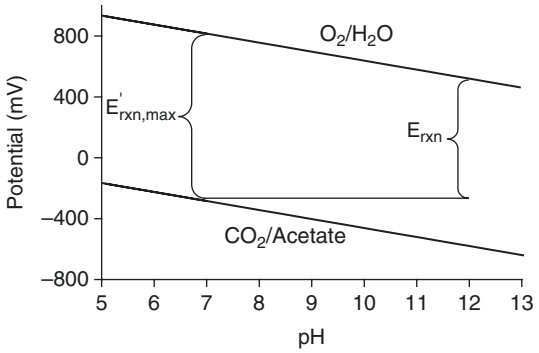

Fig. 1.4 Potential change in the half reactions of acetate oxidation and oxygen reduction as a function of pH. The slope is 59.1 mV/pH unit for both reactions. E_{rxn} is presented for the case of a $\Delta pH = 5$, where the anode is at pH = 7 and cathode is at pH = 12

the reaction for O_2 reduction is $O_2 + 4\,H^+ + 4\,e^- \rightarrow 2H_2O$. Figure 1.4 shows how the potential of each half reaction changes with pH.

The mass transport of protons from the anode to the cathode often creates a proton gradient, in which the anode surface has a lower pH, while the cathode surface has a higher pH. This is especially true for an MFC, in which the concentration of protons (and hydroxyl ions) is low due to the bacterial growth requirement of near-neutral pH. pH gradients between anode and cathode chambers have been reported to be as high as 6.4 pH units [24], which corresponds to a decrease of 378 mV from $E'_{rxn,max}$ (a 34% decrease in the available potential difference) compared to its standard value. In Fig. 1.4, we calculate an actual reaction potential, E_{rxn}, when the $\Delta pH = 5$ (anode pH = 7 and cathode pH = 12), resulting in a 27% reduction from $E'_{rxn,max}$. Maintaining a pH that is near-neutral in the anode and cathode compartments is currently one of the main challenges of MFC design and optimization [25, 26, 27].

In order to calculate the potential efficiency (PE) of an MFC process, we must take into consideration the loss due to a pH gradient between the anode and cathode compartments. We call this the pH efficiency (pHE), which is defined as

$$pHE = \frac{E_{rxn}}{E'_{rxn,max}} \tag{1.5}$$

1.2.1.2 Voltage Efficiency

Due to voltage inefficiencies, the operating voltage for any fuel cell is less than its thermodynamic value, E_{rxn}. The voltage between the anode and the cathode, V_{cell}, is the useful energy that is actually harvested. Thus, the voltage efficiency is defined as

$$\text{Voltage efficiency (VE)} = \frac{V_{\text{cell}}}{E_{\text{rxn}}} \tag{1.6}$$

The decrease of V_{cell} from E_{rxn} is caused by kinetic potential losses at the anode (η_{anode}), cathode (η_{cathode}), and in the solution between them (ohmic potential loss, η_{Ω}):

$$V_{\text{cell}} = \text{E}_{\text{rxn}} - \Sigma\eta_{\text{anode}} - \Sigma\eta_{\text{cathode}} - \eta_{\Omega} \tag{1.7}$$

Ohmic potential loss is caused by the resistance to ion flow between the anode and cathode; it is a function of current as described by Ohm's law ($\eta_{\Omega} = IR_{\Omega}$, where R_{Ω} is the ohmic resistance). Ohmic resistance is of special concern in an MFC, as water with high resistance is often present between the anode and cathode. An increase in ionic strength and a decrease in the distance between anode and cathode can decrease ohmic resistance.

In chemical fuel cells, the anode and cathode potential losses are divided into activation and concentration losses. In MFCs, the cathode reaction is usually carried out by a metal catalyst [28]; thus, these potential losses are relevant to its cathode operation. Factors such as pH, catalyst type and loading, concentrations of reactive species, and temperature are some of the important parameters for the cathode operation. Given the vast amount of information available regarding potential losses at an electrode catalyzed by a metal [29, 30], we do not discuss in detail these processes. Instead, we focus on the MFC anode losses and their relationship to current density.

1.2.2 Current Density in the MFC's Anode

In an MFC anode, bacteria in an anode biofilm serve as catalysts for e^- donor oxidation. Thus, anode processes are a combination of electrochemistry and biofilm kinetics. The correlation between the current density produced by the biofilm and the voltage losses at the anode is determined by the three processes shown in Fig. 1.5: (1) mass transport, (2) microbial processes (cell growth and respiration), and (3) the electrical potential gradient. The substrate flux is a quantity that describes the amount of e^- donor that enters the unit area of biofilm per time ($ML^{-2}T^{-1}$). The donor substrate carries electrons into the biofilm. As the donor is oxidized, the bacteria partition its electrons into cell synthesis, anode respiration, and byproduct formation. The electrical potential determines the rate of bacterial respiration, and the gradient in the electrical potential drives the conduction of electrons from the bacteria to the solid electrode [31].

Typically, biofilm kinetic models relate the flux of e^- donor into the biofilm to the rate of consumption of an electron acceptor (e.g., O_2) by respiration. A biofilm kinetic model can also provide insights into what controls the current density in an ARB biofilm. To develop those model-derived insights, we first explore the performance of an MFC biofilm anode by only considering the

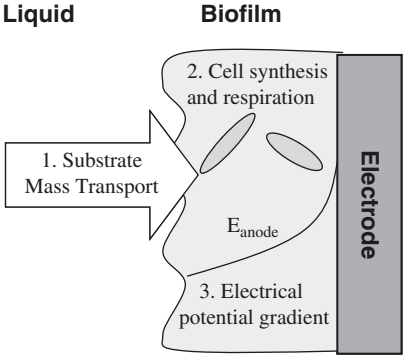

Fig. 1.5 General schematic for the three main processes that occur at the biofilm anode of an MFC and control the current density and anode potential losses: (1) mass transport brings electrons from the substrate into the biofilm, (2) cells partition electrons into different ways, and (3) electrical potential controls bacterial respiration, while the conduction of electrons from the biofilm anode into the electrode depends on the gradient of the electrical potential

limitation by electron-donor diffusion and utilization (Section 1.2.2.1). Then, we modify the biofilm kinetic model using concepts of electrochemistry so that we can explore the electrical potential limitation in the MFC anode (Section 1.2.2.2).

1.2.2.1 Limitation by Electron-Donor Diffusion and Utilization

In the following case, the anode current density is only limited by the substrate flux into the biofilm. In order to obtain the substrate flux, J_s, we must establish a mass balance within the biofilm that takes into consideration substrate diffusion and utilization. By combining Fick's law of diffusion with Monod-type kinetics of substrate consumption, Rittmann and McCarty (2001) estimate the substrate flux into the biofilm with known concentrations at both boundaries of the biofilm (i.e., S_s at the biofilm/liquid interface and S_w at the biofilm attachment wall) [32]:

$$J_s = \left[2q_{max}X_f D_f\left(S_s - S_w + K\ln\left(\frac{K+S_w}{K+S_s}\right)\right)\right]^{\frac{1}{2}} \tag{1.8}$$

in which, q_{max} is the maximum specific rate of substrate utilization ($M_{substrate}/(M_{biomass}{}^*T)$), X_f is the biomass density within the biofilm ($M_{biomass}$/Vol), D_f is the substrate molecular diffusion coefficient in the biofilm (Area/T), and K is the substrate concentration at which $r_{ut} = 0.5q_{max}X_f$ ($M_{substrate}$/Vol)

The maximum flux obtainable for a given S_s occurs when $S_w = 0$. This is referred to as a deep biofilm, for which

$$J_{s,\,deep} = \left[2q_{max}X_f D_f\left(S_s + K\ln\left(\frac{K}{K+S_s}\right)\right)\right]^{\frac{1}{2}} \tag{1.9}$$

where $J_{s,deep}$ is the substrate flux in a deep biofilm. Thus, a substrate-limited MFC must produce an electrical current that is proportional to $J_{s,\ deep}$.

In order to convert J_s into current density, j, we must take into consideration the fact that a fraction of the electrons contained in the e^- donor will be used for biomass synthesis by ARB and another fraction of electrons will end up in byproducts (such as methane, fermentation products, and soluble microbial products). The current density contains the electrons not going to those sinks, but to respiration:

$$j = \gamma_s J_s (1 - f^0_s - H) \tag{1.10}$$

where γ_s is a conversion factor from mass to coulombs for the substrate ([nF]/MW), f_s^0 is the fraction of electrons used for cell synthesis, and H is the fraction of electrons converted into byproducts [33]. In addition to the substrate flux, biomass decay contributes to the total current, but this current has been reported to be about 1% of the maximum current [15] and will not be considered in our discussion. We note that the calculation of j_{deep} depends on parameters that are specific to the microbial community and donor substrate: q_{max}, K, H, and f_s^0. Assuming our community is similar to a pure culture of *G. sulfurreducens*, a known ARB, we can estimate how j_{deep} depends on S_s and X_f. Table 1.1 shows the parameters for *G. sulfurreducens*. We assumed $H = 0$ for simplicity. These parameters are similar to those of slow-growing anaerobic cultures, such as sulfate reducers or methanogens [32].

Figure 1.6 shows the maximum current density obtained by an ARB community that is substrate-limited, utilizing the parameters in Table 1.1. At a typical X_f of 50 mg VS/cm^3, j_{deep} increases as S_s increases, with values between 0

Table 1.1 Electron-donor (ED) kinetic and stoichiometric parameters for *G. sulfurreducens*, based on the literature

Symbol	Description	Value	Units	Reference
K	Half-maximum-rate acetate concentration	1.9×10^{-3}	mg BOD/cm^3	[39][a]
q_{max}	Maximum specific rate of ED utilization	8.4	mg BOD/mg VS day	Calculated based on Bond and Lovley [40][b]
H	Fraction of e^- from electron donor utilized in byproduct formation	0	–	Assumed
f_s^0	Fraction of e^- from the e^- donor utilized for biomass synthesis	0.05	–	Based on Bond and Lovley [40]

[a] We averaged values for K_{Sd} for *G. sulfurreducens* utilizing acetate as the ED and two different electron acceptors: fumarate and iron citrate as electron acceptors [39].

[b] For *G. sulfurreducens* catalyzing acetate oxidation at an anode, the maximum rate of acetate utilization observed was 1.2 μmole μg /protein min (Bond and Lovley [40]). We made unit conversion assuming a protein content of about 55% (Whitman et al. [41]), $C_5H_7O_2N$ as the formula for cells grown with ammonium as the nitrogen source (Rittmann and McCarty [32]), and cells are 90% organic matter.

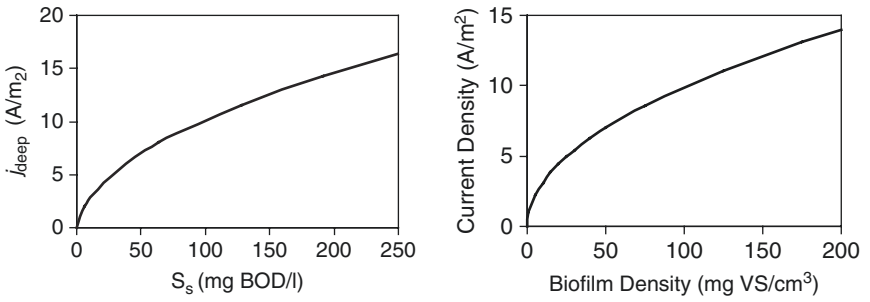

Fig. 1.6 Maximum current density for an ARB biofilm anode that is completely substrate-limited. The ARB have parameters similar to those of *G. sulfurreducens* (Table 1.1). (**a**) Maximum current density as a function of substrate concentration at the liquid–biofilm interface for a biofilm with $X_f = 50$ mg VS/cm^3. (**b**) Maximum current density as a function of biofilm density for an $S_s = 50$ mg BOD/l

and 16 A/m^2 for $S_s = 0$–250 mg BOD/l (Fig. 1.6a). At $S_s = 50$ mg BOD/l, j_{deep} increases with an increase in X_f, as shown in Fig. 1.6b, up to a maximum of 14 A/m^2 at 200 mg VS/cm^3. Given a high S_s and X_f, for example, $S_s = 500$ mg BOD/l and $X_f = 200$ mg VS/l, $j_{deep} = 47$ A/m^2. These probably are not realistic values in a wastewater treatment process that aims for low effluent BOD concentrations, but they may be realistic for energy conversion from a high-strength waste stream, such as pig manure.

The use of bacteria that have a higher q_{max} can also increase the maximum current density. However, an increase in q_{max} usually implies an increase in energy requirements for bacterial growth (leading to a lower VE), as well as a higher f_s^0 [32, 34], both of which are not desirable in an MFC process. Therefore, it would be valuable to find or engineer ARB that has a very high q_{max} and a very low f_s^0.

Table 1.2 shows the maximum current densities obtained by various MFC researchers. The maximum current densities reported (per anode surface area) are usually around 5–6 A/m^2 [35, 36], although recently current densities reported have increased up to 13 A/m^2 [26]. Reported current densities are as much as an order of magnitude less than the highest current densities shown in Fig. 1.6, but the computed values are for high substrate concentrations and the assumption of only substrate limitation. This comparison suggests that substrate limitation is not the only or main controlling factor for contemporary MFCs. Overcoming the current limitations offers the potential to increase current density significantly.

Recently, Torres et al. [25] showed that the transport of protons, produced during substrate oxidation, from inside to outside the biofilm can cause a pH inhibitory effect on ARB, thus limiting the total current produced. The current density produced by the ARB biofilm decreased linearly as the buffer

Table 1.2 Maximum current densities per anode area reported by various researchers in MFC

Reference	Reported current (A/m^2)	Main substrate	Inoculum
Fan et al. (2007) [26]	13	Acetate (1,300 mg BOD/l)	Enriched culture from wastewater
Torres et al. (2008) [25]	11.5	Acetate (1,600 mg BOD/l)	*G. sulfurreducens*-enriched mixed culture from wastewater
Fan et al. (2007) [37]	9.0	Acetate (1,300 mg BOD/l)	Enriched culture from wastewater
Liu et al. (2005) [36]	~5.5	Acetate (780 mg BOD/l)	Wastewater
Cheng et al. (2006) [35]	~5.0	Glucose (530 mg BOD/l)	Wastewater
Rozendal et al. (2007) [24]	2.4	Acetate (640 mg BOD/l)	Mixed enriched culture
Ringeisen et al. (2006) [38]	0.1	Lactate (various conc.)	*Shewanella oneidensis* DSP10
Bond and Lovley (2002) [12]	1.1	Acetate (320 mg BOD/l)	*Geobacter sulfurreducens* PCA

concentration, which serves as a proton carrier, decreased. It is possible that the maximum current density produced in many MFC studies is limited by pH inhibition and proton transport. Further studies are needed to fully integrate biofilm proton transport into a mathematical model that can estimate its effect on current density in MFCs.

1.2.2.2 Electrical Potential Limitation in the MFC Anode

In this section, we extend the model to consider the unique solid electron-acceptor respiration employed by ARB in the biofilm. The ARB biofilm carries out a novel form of respiration by transferring electrons to the anode, which is a solid conductive electrode, not a soluble molecule, such as dissolved oxygen. Although a solid, conductive electrode does not have a concentration, its electrical potential serves as an analog for calculating reaction kinetics. By combining the Monod and Nernst equations, Kato Marcus et al. [31] derived the Nernst–Monod equation to describe current density in response to the electrical potential of the anode E_{anode} (V):

$$j = j_{\max}\left(\frac{1}{1+\exp\left[-\frac{F}{RT}\left(E_{anode}-E_{KA}\right)\right]}\right) \tag{1.11}$$

where j_{max} is the maximum current density (A/m^2), E_{KA} is the anodic acceptor potential for the half-maximum-rate (V), R is the ideal gas constant (8.3145 J/mol K), F is the Faraday constant (96,485 Coulomb/mol), and T is the temperature (298.15 K). Equation (1.11) shows that $j = 0.5\ j_{\max}$ when $E_{\text{anode}} = E_{KA}$.

Figure 1.7 shows properties of the Monod and Nernst–Monod expressions in dimensionless forms that are easy to compare: the dimensionless Monod expression is $S_a^*/(1+S_a^*)$, where $S_a^* = S_a/K_{Sa}$; the dimensionless Nernst–Monod expression is $1/(1+\exp(\eta^*))$, where the dimensionless local potential is $\eta^* = F/RT(E_{anode}-E_{KA})$. The two dimensionless equations saturate to 1 as the respective variables on the horizontal axis increase. The dimensionless Monod expression has two reference points (Fig. 1.7a): at $S_a^* = 0$, the expression equals zero, because the rate of substrate utilization equals zero when there is no substrate; at $S_a^* = 1$, S_a equals K_{Sa}, and the Monod expression gives the half of the maximum rate of 0.5. In contrast, the Nernst–Monod expression has only one reference point (Fig. 1.7b): at $\eta^* = 0$, E_{anode} equals E_{KA} and the Nernst–Monod expression gives half of the maximum rate of 0.5.

We consider an example using Eq. (1.11) to understand the relationship between voltage and current in an MFC with the following parameters: a single adjustable external resistor R_{useful} (Ω), an anode surface area $A = 25$ cm^2 (0.0025 m^2), and $j_{\max} = 1$ mA/cm^2 (10 A/m^2). E_{rxn} for an O_2 MFC is often around 800 mV, and we used 250 mV to approximate inefficiencies due to non-anode processes; thus, $E_{\text{rxn}} = 800–250 = 550$ mV. We define the anode kinetic loss η_{anode} (mV) as

$$\eta_{\text{anode}} = E_{\text{anode}} - E_{\text{donor}} \tag{1.12}$$

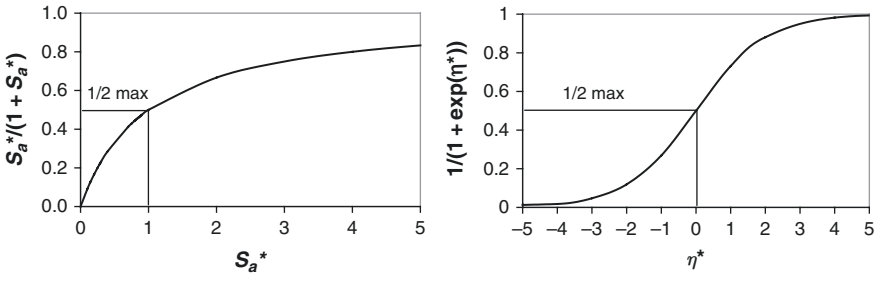

Fig. 1.7 Plots of dimensionless forms of (**a**) the Monod and (**b**) the Nernst–Monod equations

Assuming $E_{KA} = E_{donor} + 100$ mV [31], combining Eqs. (1.7), (1.11), and (1.12) yields

$$V_{cell} = jR_{useful}(25\,cm^2) = 400 - \eta_{anode} \tag{1.13}$$

$$j = j_{max}\left(\frac{1}{1+\exp[-\frac{F}{RT}(\eta_{anode} - 100\,mV)\frac{1\,V}{1000\,mV}]}\right) \tag{1.14}$$

We calculate power density as $P = jV_{cell}$ and obtain Fig. 1.8 after solving Eqs. (1.13) and (1.14) simultaneously.

An increase in j from 0 to 9 A/m^2 gradually decreases V_{cell} from 550 to about 390 mV (Fig. 1.8). Between current density values of 1 and 9 A/m^2, V_{cell} changes almost linearly with current, which is consistent with many observations [28]. Above $j = 9$ A/m^2, V_{cell} decreases rapidly due to the saturation response of the biofilm. Under electrical potential saturation, factors other than the electrical potential (e.g., electron donor and pH) limit the electrical current. Such rapid change in the voltage is observed in experimental MFCs [36, 42]. A key lesson from Fig. 1.8 is the trade-off between V_{cell} and j, and power density is one way to evaluate this trade-off. Because of an increase in current density under relatively stable V_{cell}, power density increases rapidly and reaches a maxima of 3.6 W/m^2 around 9 A/m^2 — 3.6 W/m^2 is near the currently observed maximum power density for an MFC [43]. The maxima occurs around 16 Ω, which would be the operating external resistance achieving the best power density for this particular example.

The Nernst–Monod equation describes how the potential controls the rate of generation of electrons by ARB respiration, but the electrons from respiration must be transported to the anode surface from wherever the ARB are located in the biofilm. Components in the extracellular matrix of the anode biofilm are

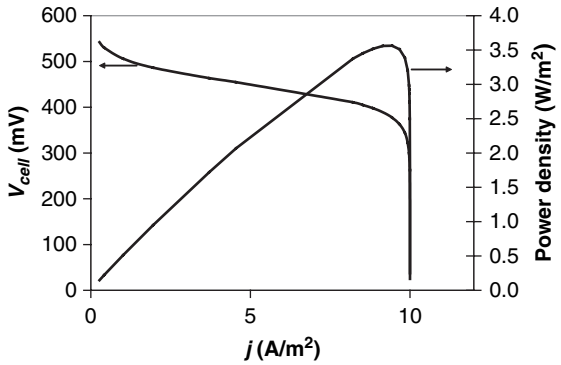

Fig. 1.8 The relationships among the current density j (A/m^2), the useful voltage that is actually harvested V_{cell} (mV), and power density (W/m^2) for an MFC example with a single variable resistor R (Ω)

implicated in the transfer of electrons from the biofilm bacteria to the anode electrode, e.g., cytochromes, conductive nanowires, and adsorbed soluble-mediators such as pyocyanine [20, 44, 45]. Based on the presence of conductive materials in the extracellular matrix of biofilm anodes, Kato Marcus et al. described the extracellular matrix as a conductor that accepts electrons from the respiration and conducts the electrons to the anode [31]. Because the biofilm matrix functions as part of the anode, the biofilm on the anode is termed a "biofilm anode."

Much like diffusion-limitation of a soluble acceptor in a biofilm, electron conduction can create an electrical potential gradient along the depth of biofilm anode, as illustrated in Fig. 1.5. Kato Marcus et al. used Ohm's law to describe the gradient in the electrical potential in the biofilm anode [31]:

$$j = \kappa_{bio} \frac{d\eta}{dz} \tag{1.15}$$

where κ_{bio} is the biofilm conductivity (mS/cm) and the local potential . Equations (1.14) and (1.15) combine to form an electron-balance that describes the generation and conduction of electrons in the biofilm anode.

In addition to the biofilm anode mechanisms, an ARB community can produce electron shuttles such as pyocyanine to facilitate the transfer of electrons through the electron-shuttle mechanism [44, 46]. Interested readers may refer to the original work that presents the model for the electron-shuttle mechanism [47].

An important take-home message from this section is that ARB require electrical potential to drive electrical current. From the perspective of an MFC operator, this implies loss of useful voltage V_{cell}. This analysis highlights the need to investigate a potential trade-off between the current and potential. In the next section, we introduce the concept of ECE, which is a useful parameter for assessing the tradeoff.

1.2.3 Coulombic Efficiency, Energy Capture Efficiency, and COD Balance in an MFC

In order to complete the efficiency analysis of an MFC, we perform COD balances to help understand the amount of current produced per substrate feed and removed in the MFC anode. COD balances can be performed at the biofilm level or at the reactor level. At the biofilm level (Fig. 1.9), a balance of substrate flux in terms of electrons helps illustrate how the electrons flow into the anode to produce an electrical current (Fig. 1.10). This is expressed mathematically by

$$J_{\text{s}} = J_{\text{e}^-} + J_{\text{H}} + J_{\text{biomas}} = j/\gamma_{\text{s}} + J_{\text{s}}^{*} H + J_{\text{s}}^{*} f_{s}^{0} \tag{1.16}$$

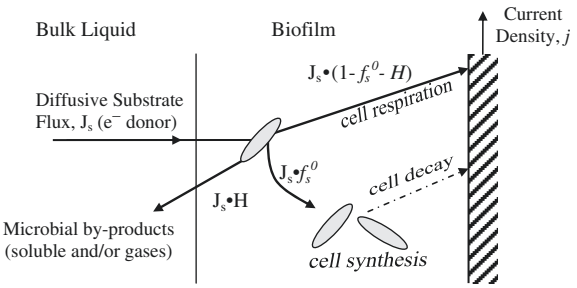

Fig. 1.9 Schematic electron flow from the e^- donor in the bulk liquid to the anode. Cell respiration and cell decay are the two contributors to current density. Cell decay is not considered in our discussion for simplicity and because it is often small

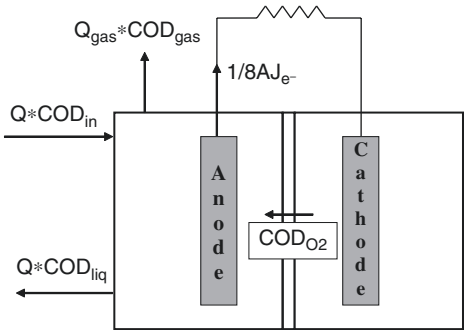

Fig. 1.10 COD balance in a continuous MFC reactor

where J_{e^-} is the fraction of substrate utilized for respiration and is equal to j/γ_s (e^- eq./L^2), J_H is the fraction of substrate used for byproduct formation and is equal to $J_s{*}H$ (e^- eq./L^2), and $J_{biomass}$ is the fraction of substrate used for biomass synthesis and is equal to $J_s{*}f_s^0$ (e^- eq./L^2). Note that Eq. (1.16) is derived from Eq. (1.10).

We can perform a similar mass balance for COD at the reactor level. In this analysis, we include the flux of O_2 (J_{O2}) across the ion-exchange membrane separating the anode compartment from the cathode. Reduction of O_2 in the anode compartment is an electron sink. Thus, the COD of the influent substrate is divided into liquid effluent COD, gas effluent COD, O_2 reduction, and current generation:

$$Q^*\mathrm{COD_{in}} = Q^*\mathrm{COD_{liq}} + Q^*_{\mathrm{gas}}\mathrm{COD_{gas}} + 1/8AJ_{e^-} + 1/8_m J_{O2} \quad (1.17)$$

where Q is the influent liquid flow rate (L/day), Q_{gas} the effluent gas flow rate (L/day), COD_{in} the influent COD concentration (g COD/L), COD_{liq} the effluent COD concentration (g COD/L), COD_{gas} the COD concentration in the gas effluent (g COD/L of gas), A the anode surface area (dm^2), A_m the ion-exchange

membrane surface area (dm^2), J_{O2} the oxygen flux across the membrane (e^- eq./L^2), and 1/8 the conversion form of 8 g COD to 1 e^- eq.

The following equations define the effluent terms for a biofilm-dominated system:

$$Q^*\mathrm{COD}_{\mathrm{liq}} = A(J_{\mathrm{biomass}+J_{\mathrm{H,liq}}})^*(1\mathrm{e}^-\mathrm{eq.}/8\,\mathrm{gCOD}) \tag{1.18}$$

$$Q_{\mathrm{gas}}{}^*\mathrm{COD}_{\mathrm{gas}} = A(J_{\mathrm{H,gas}})^*(1\mathrm{e}^-\mathrm{eq.}/8\,\mathrm{gCOD}) \tag{1.19}$$

We define coulombic efficiency in two ways. The first definition, respiration coulombic efficiency (RCE), is based on the conversion of the *removed substrate* to electrical current by ARB respiration, which can be expressed as the ratio of the current flux to the substrate flux [31]:

$$\mathrm{RCE} = \frac{\mathrm{J_{e^-}}}{\mathrm{J_s}} \tag{1.20}$$

The second coulombic efficiency, capture coulombic efficiency (CCE), is defined based on the capture of *influent COD* into electrical current. The coulombic efficiency is now the fraction of COD that was captured as current over the COD fed in the influent:

$$\mathrm{CCE} = \frac{\mathrm{COD_{e^-}A}}{\mathrm{QCOD_{in}}} = \frac{\mathrm{J_{e^-}A}}{\mathrm{QCOD_{in}}} \tag{1.21}$$

CCE is usually high (71–95%) when acetate is used [15, 21, 40, 48]. When a fermentable substrate is used, the production of fermentation byproducts, such as methane and hydrogen, can reduce the amount of recovered electrons. However, the coulombic efficiency also depends on the reactor configuration and conditions used that could lead to variances in the e^- sinks. Table 1.3 shows a wide variety of reported values of RCE and CCE.

CCE for an MFC can be low for three reasons. First, the volumetric COD loading to an MFC is disproportionately high with respect to the surface loading (which is proportional to current density). Second, a high-fraction of the COD entering the reactor is not biologically available to ARB. Third, alternate electron sinks compete with the anode electrode for COD. Two useful parameters to understand the relative impact of these processes on CCE are treatment efficiency (TE) and fraction of stabilization as current (FoSaC).

TE is a useful parameter for evaluating the COD removal (i.e., stabilization), which is a major goal of an MFC as a wastewater treatment process. TE is the percentage of COD removed from the influent by aerobic oxidation (J_{O2}) or by conversion into electrical current (J_{e^-}) and gaseous byproducts that includes hydrogen and methane ($J_{H,gas}$). The definition of the TE is

$$\mathrm{TE} = \mathrm{A}(\mathrm{J_{e^-}} + \mathrm{J_{H,gas}} + \mathrm{J_{O2}})/\mathrm{QCOD_{in}} = (\mathrm{COD_{in}} - \mathrm{COD_{liq}})/\mathrm{COD_{in}}) \tag{1.22}$$

Table 1.3 Comparison of coulombic efficiencies (CCE or RCE) obtained in various MFC studies

Reference	Value (%)	Definition	Substrate	Comments
Rabaey et al. (2005) [44]	75	CCE	Acetate	[a,b]
	59		Glucose	[b]
Freguia et al. (2007) [48]	70–100	CCE	Acetate	[a,b]
	~ 40–60		Glucose	[b]
Lee et al. (2007) [21]	71	CCE	Acetate	[a,b]
	49		Glucose	[b]
Torres et al. (2007) [21]	86	RCE	Acetate	[a,b]
	49		Ethanol	[b]
Rozendal et al. (2006) [49]	92	RCE	Acetate	[a,b]
Min and Logan (2004) [18]	65	RCE	Acetate	[a]
	28–50		Butyrate	
	14		Glucose	

[a]Acetate was the non-fermentable substrate, leading to low byproduct formation and biomass production. [b]An alternate electron acceptor was used for these studies (ferricyanide or water), eliminating the diffusion of oxygen into the reactor ($J_{O2} \approx 0$).

TE near 1 indicates an efficient removal of COD, which is a desirable attribute for a wastewater treatment process. A small TE, close to zero, indicates poor effluent quality, especially for MFCs with a high initial COD_{in}, and it may indicate a requirement for post treatment to improve the COD removal. A poor TE can result from disproportionately high influent COD and the presence of refractory organic compounds.

FoSaC evaluates the degree to which the electrical current achieved the stabilization of COD. The definition of the FoSaC is

$$\mathrm{FoSaC} = \mathrm{AJ_{e^-}/A(J_{e^-} + J_{H,gas} + J_{O2})} \tag{1.23}$$

Since a major goal of operating an MFC is to achieve stabilization through generating electrical current, a high FoSaC value is generally desirable. In contrast, stabilization through J_{O2} is undesirable, because the energy value of waste is lost. High stabilization as removal $J_{H,gas}$ has mixed benefits. Depending on the gas quality, byproducts such as hydrogen and methane can be collected to generate useful energy. However, if these gaseous byproducts are not used for energy generation, the energy value of the COD removed is lost. When gaseous byproducts are H_2S and CH_4, these gases must be captured to prevent environment pollution.

Once the coulombic efficiency and voltage efficiency are known, the final ECE can be calculated as the product of both efficiencies:

$$\mathrm{ECE} = \mathrm{VE^*CCE} = \mathrm{VE^*FoSaC^*TE} = \frac{\mathrm{E_{out}}}{\mathrm{E_{substance}}} \tag{1.24}$$

CCE is simply a product of TE and FoSaC. ECE is the fraction of the total energy contained in the original waste or substrate ($E_{substrate}$) that was

converted into electrical energy (E_{out}). These analyses indicate that understanding the flow of electrons in an MFC is important to understand the interaction of energy generation and water treatment. In this regard, careful studies that track electrons based on mass balance provide valuable information for understanding the overall process dynamics for MFCs and other energy-to-biomass processes [21, 48].

Another important concept to determine the efficiency of a biomass-to-energy process is the PEE:

$$\mathrm{PEE} = \frac{E_{out} - E_{input}}{E_{out}} \tag{1.25}$$

in which E_{input} is the amount of energy required to run the energy-to-biomass process. Therefore, PEE evaluates the net energy produced in the process, while ignoring the input energy as substrate ($E_{substrate}$). Combining PEE and ECE gives an overall efficiency (OE) from the point of view of $E_{substrate}$:

$$\mathrm{OE} = \mathrm{PEE}^{*}\mathrm{ECE} = \frac{E_{out} - E_{input}}{E_{substrate}} \tag{1.26}$$

1.3 Perspectives on Different Energy-to-Biomass Technologies

ECE and PEE are valuable tools for comparing different energy-to-biomass technologies. PEE estimates can only be obtained once the process has been tested in pilot or full scale. Therefore, it is premature to place a PEE value for MFCs, although we can predict it will be high, since MFCs do not require much energy input. ECE values for MFCs vary depending on the substrate used, experimental conditions, and acclimation of the ARB community. Under the best conditions, assuming a VE = 0.5 and CCE = 0.85 (typical of value for acetate consumption), ECE = 42.5%. For comparison, ethanol fermentation and methanogenesis are anaerobic metabolisms that synthesize biomass with a small yield. Thus, both processes produce only a small amount of microbial biomass and capture 80–90% of the electrons (CCE) as CH_4 or ethanol. How do they compare with electricity generation by an MFC?

1.3.1 Methanogenesis

Methanogenesis is a long-standing technology for stabilizing sludges and other organic wastes [9], as it has natural advantages. First, a complex community develops so that the electrons and energy in sewage, industrial, and agricultural sources can be routed to H_2, acetate, and then CH_4. Second, the anaerobic metabolism synthesizes biomass with a small yield. Thus, a methanogenesis

process produces only a small amount of microbial biomass or sludge, minimizing the cost for disposal, and captures 80–90% of the electrons from biodegradable biomass as CH_4. Third, because methane is poorly soluble in water, it naturally evolves into the gas phase and can be captured for energy generation. Although methanogenesis approximately produces equal molar ratio of CO_2 and CH_4, some CO_2 remains in solution as bicarbonate. Therefore typical effluent gas mixture from a digester is 55–75% methane. After gas cleaning, the CH_4 can be burned in a piston engine or microturbine to produce energy. CH_4 can be combusted to yield electrical energy, at $\sim$ 35% VE, and this makes its ECE $\sim$ 30%.

A major drawback for anaerobic digestion is its unit cost of methane, since it is still higher than fossil fuels [3]. The biogas produced from methanogenesis is mostly CH_4 and CO_2, but contains trace levels of H_2 and H_2S. The removal of H_2S to prevent combustion-associated byproducts is expensive and energy intensive, which results in a decrease in PEE. Furthermore, the disposal of non-degraded residual solids is costly, which means that improving the biodegradability of wastes is important for expanding the usefulness of methanogenesis. Improving biodegradability also results in more CH_4 generation, the main source of economic value. Thus, the net cost of the methane production needs to be lowered by improving the quality of biogas produced and biodegradability of the wastes.

1.3.2 Bioethanol

Most naturally occurring bacteria also produce other products, such as acetate and hydrogen, during glucose fermentation; therefore, the stoichiometric conversion of one mole of glucose molecule to two moles of ethanol is rarely observed naturally. Hence, the ethanol production industry uses mainly yeasts to selectively convert glucose to ethanol [50]. Today, ethanol production with yeast is limited to a narrow range of substrates, mainly hexose derived from plants. While metabolic engineering approaches are extending the capacity of yeasts to utilize pentoses such as xylose by introducing new genes to yeasts [51], it will be interesting to see how far these approaches will take us.

Figure 1.11 shows an energy balance for producing 1 gallon of ethanol from corn (based on Shapouri et al. [52]). An input energy of 81 MJ is required to produce corn, transport corn, convert corn to ethanol, remove the ethanol from water, and distribute the ethanol. Since the energy value of 1 gallon of ethanol is 89 MJ, the production of ethanol results in a PEE of only 9%. Co-products from ethanol production, such as corn gluten meal, can have economic value. Since producing co-products normally requires energy input, some energy balances consider the benefit of co-product production as "energy credits." Energy credits from co-products add about 18% to the energy captured, making PEE at most 22%. Given a CCE = 85% for bioethanol, if the ethanol is

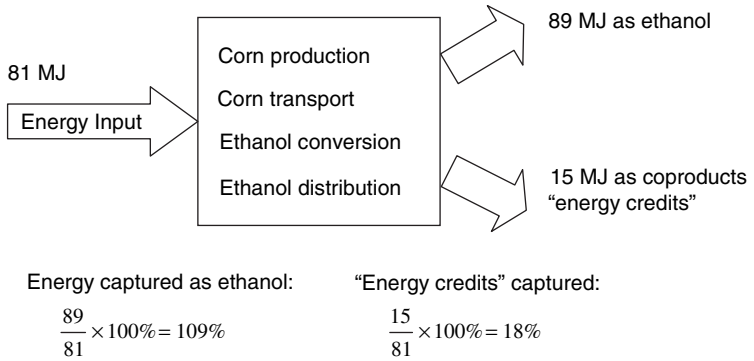

Fig. 1.11 Energy balance for producing 1 gallon of ethanol [52]

combusted to produce electricity with an efficiency of ~35% VE, its ECE is ~30%. However, its low PEE (9%) drives results in an OE of only ~3%.

Although ethanol production (at least from corn) appears to have a minimal energy gain, the impacts of intense agriculture on the environment are of concern. Modern agricultural practice is associated with negative environmental impacts, such as soil erosion, loss of biodiversity, use of pesticides, and release of non-point pollution, such as nitrogen. The release of nitrogen is a particular concern, because agricultural sources currently account for 58% of the nitrogen load to the Mississippi basin [53, 54], and approximately 31% of the agricultural nitrogen comes from fertilizers [55], which is a main input that goes into producing corn [56]. An expert committee appointed by the National Researcher Council (NRC) indicated recently that significant harm to water quality and availability can result from intense farming of corn for ethanol if new practices and techniques are not adopted [57]. Environmental concerns are not a concern exclusive to bioethanol, but for any biomass-based technologies that may result in an increased agricultural activity in the region. In that respect, anaerobic digestion and MFCs that typically target wastes, not an agricultural resource like corn, as fuel sources have an inherent advantage.

1.4 Conclusion

Biomass-based renewable energy is a carbon neutral technology that can contribute to the world's energy supply. Oxygenic photosynthesis produces biomass with a high energy value: the goal of biomass-based technology is to cleanly and efficiently harness this energy value by driving the photosynthetic reaction in reverse. Since raw biomass often is not convenient for direct use as a fuel, microbiological processes are currently being used to convert biomass to convenient biofuels. Two major microbiological processes today for biofuel generation are methanogenic anaerobic digestion and ethanol production, each

with its own pros and cons. Methanogenic digestion is socially and environmentally beneficial waste treatment process; however, the unit cost for methane production needs to be lowered. Ethanol production from corn yields marginal energy return; the environmental consequences of all crop-based ethanol require consideration.

An MFC is a developing renewable energy technology that has a unique niche with respect to other microbiological processes. Instead of generating biofuels, an MFC generates electricity directly from organic material, including wastes. An MFC exploits the unique respiratory activity of ARB that oxidize organic fuels and transfer the electrons released from oxidation to the anode. Much like in anaerobic digestion, a community of microorganisms that includes fermenters and ARB appears to cooperatively channel electrons from organic fuels to the anode. The interaction between two groups of organisms is an exciting area of research for environmental biology and microbial ecology. The current generation from an MFC is determined by the reactor pH, the presence of competing sinks for electrons, mass transport of electron donor, and electron–electron conduction in the biofilm. A mass balance on COD is a useful tool for establishing performance criteria, and we define the important and unique criteria of OE, PE, RCE, CCE, ECE, PEE and FoSaC. MFC developers can use these performance criteria to track different facets of MFC performance, thereby identifying bottlenecks and opportunities for improvement.

References

1. Goldemberg, J. and T.B. Johansson (2004). World energy assessment overview: 2004 update. United Nations Development Programme, New York.
2. Hall, D.O. and F. Rosillo-Calle (1998). In Survey of Energy Resources, 18th Edn. World Energy Council, London, 227–241.
3. Chynoweth, D.P., J.M. Owens, and R. Legrand (2001). Renewable methane from anaerobic digestion of biomass. Renew Energ 22, 1–8.
4. Energy Information Administration (2005). Annual energy outlook: with projection to 2030. U.S. Department of Energy, Washington, DC.
5. U.S. Environmental Protection Agency (2006). Municipal Solid Waste Generation, Recycling, and Disposal in the United States: Facts and Figures for 2006. U.S. Environmental Protection Agency, Washington, DC.
6. Borjesson, P. and M. Berglund (2006). Environmental systems analysis of biogas systems – Part 1: fuel-cycle emissions. Biomass Bioeng 30, 469–485.
7. Xiao, J.H. and J.M. VanBriesen (2006). Expanded thermodynamic model for microbial true yield prediction. Biotechnol Bioeng 93, 110–121.
8. Wyman, C.E., B.E. Dale, R.T. Elander, M. Holtzapple, M.R. Ladisch, and Y.Y. Lee (2005). Coordinated development of leading biomass pretreatment technologies. Biores Technol 96, 1959–1966.
9. Angenent, L.T., K. Karim, M.H. Al-Dahhan, and R. Domiguez-Espinosa (2004). Production of bioenergy and biochemicals from industrial and agricultural wastewater. Trends Biotechnol 22, 477–485.

10. Kim, B.H., H.J. Kim, M.S. Hyun, and D.H. Park (1999). Direct electrode reaction of Fe(III)-reducing bacterium, Shewanella putrefaciens. J Microbiol Biotechnol 9, 127–131.
11. Kim, H.J., H.S. Park, M.S. Hyun, I.S. Chang, M. Kim, and B.H. Kim (2002). A mediator-less microbial fuel cell using a metal reducing bacterium, Shewanella putrefaciense. Enzyme Microb Technol 30, 145–152.
12. Bond, D.R., D.E. Holmes, L.M. Tender, and D.R. Lovley (2002). Electrode-reducing microorganisms that harvest energy from marine sediments. Science 295, 483–485.
13. Rabaey, K., N. Boon, S.D. Siciliano, M. Verhaege, and W. Verstraete (2004). Biofuel cells select for microbial consortia that self-mediate electron transfer. Appl Environ Microbiol 70, 5373–5382.
14. Liu, H., R. Ramnarayanan, and B.E. Logan (2004). Production of electricity during wastewater treatment using a single chamber microbial fuel cell. Environ Sci Technol 38, 2281–2285.
15. Torres, C.I., A. Kato Marcus, and B.E. Rittmann (2007). Kinetics of consumption of fermentation products by anode-respiring bacteria. Appl Microb Biotechnol 77, 689–697.
16. Kim, B.H., H.S. Park, H.J. Kim, G.T. Kim, I.S. Chang, J. Lee, and N.T. Phung (2004). Enrichment of microbial community generating electricity using a fuel-cell-type electrochemical cell. Appl Microbiol Biotechnol 63, 672–681.
17. Kim, G.T., G. Webster, J.W.T. Wimpenny, B.H. Kim, H.J. Kim, and A.J. Weightman (2006). Bacterial community structure, compartmentalization and activity in a microbial fuel cell. J Appl Microbiol 101, 698–710.
18. Min, B., J.R. Kim, S.E. Oh, J.M. Regan, and B.E. Logan (2005). Electricity generation from swine wastewater using microbial fuel cells. Water Res 39, 4961–4968.
19. Zuo, Y., P.C. Maness, and B.E. Logan (2006). Electricity production from steam-exploded corn stover biomass. Energ Fuel 20, 1716–1721.
20. Gorby, Y.A., S. Yanina, J.S. McLean, K.M. Rosso, D. Moyles, A. Dohnalkova, T.J. Beveridge, I.S. Chang, B.H. Kim, K.S. Kim, D.E. Culley, S.B. Reed, M.F. Romine, D.A. Saffarini, E.A. Hill, L. Shi, D.A. Elias, D.W. Kennedy, G. Pinchuk, K. Watanabe, S. Ishii, B. Logan, K.H. Nealson, and J.K. Fredrickson (2006). Electrically conductive bacterial nanowires produced by Shewanella oneidensis strain MR-1 and other microorganisms. P Natl Acad Sci USA 103, 11358–11363.
21. Lee, H.S., P. Parameswaran, A. Kato Marcus, C.I. Torres, and B.E. Rittmann (2007). Evaluation of energy-conversion efficiencies in microbial fuel cells (MFCs) utilizing fermentable and non-fermentable substrates. Water Research 42, 1501–1510.
22. Ren, Z.Y., T.E. Ward, and J.M. Regan (2007). Electricity production from cellulose in a microbial fuel cell using a defined binary culture. Environ Sci Technol 41, 4781–4786.
23. McCarty, P.L. (1964). Anaerobic waste treatment fundamentals: Part I – Chemistry and microbiology. Public Works 95, 91–94.
24. Rozendal, R.A., H.V.M. Hamelers, R.J. Molenkmp, and J.N. Buisman (2007). Performance of single chamber biocatalyzed electrolysis with different types of ion exchange membranes. Water Res 41, 1984–1994.
25. Torres, C.I., A. Kato Marcus, and B.E. Rittmann (2008). Proton transport inside the biofilm limits electrical current generation by anode-respiring bacteria. Biotechnol Bioengr 100, 872–881.
26. Fan, Y.Z., H.Q. Hu, and H. Liu (2007). Sustainable power generation in microbial fuel cells using bicarbonate buffer and proton transfer mechanisms. Environ Sci Technol 41, 8154–8158.
27. Rozendal, R.A., H.V.M. Hamelers, and C.J.N. Buisman (2006). Effects of membrane cation transport on pH and microbial fuel cell performance. Environ Sci Technol 40, 5206–5211.
28. Logan, B.E., B. Hamelers, R. Rozendal, U. Schrorder, J. Keller, S. Freguia, P. Aelterman, W. Verstraete, and K. Rabaey (2006). Microbial fuel cells: methodology and technology. Environ Sci Technol 40, 5181–5192.

29. Bard, A.J. and L.R. Faulkner (2001). Electrochemical Methods: Fundamentals and Applications. 2nd ed. John Wiley, New York, xxi, 833.
30. Larminie, J., A. Dicks, and Knovel (2003). (Firm), Fuel Cell Systems Explained. 2nd ed. John Wiley, Chichester, West Sussex, xxii, 406.
31. Kato Marcus, A., C.I. Torres, and B.E. Rittmann (2007). Conduction based modeling of the biofilm anode of a microbial fuel cell. Biotechnol Bioeng 98, 1171–1182.
32. Rittmann, B.E. and P.L. McCarty (2001). Environmental biotechnology: principles and applications. McGraw-Hill Book Co., Boston, 754 pp.
33. VanBriesen, J.M. and B.E. Rittmann (2000). Mathematical description of microbiological reactions involving intermediates (vol 67, pg 35, 1999). Biotechnol Bioeng 68, 705–705.
34. VanBriesen, J.M. (2002). Evaluation of methods to predict bacterial yield using thermodynamics. Biodegradation 13, 171–190.
35. Cheng, S., H. Liu, and B.E. Logan (2006). Increased power generation in a continuous flow MFC with advective flow through the porous anode and reduced electrode spacing. Environ Sci Technol 40, 2426–2432.
36. Liu, H., S.A. Cheng, and B.E. Logan (2005). Production of electricity from acetate or butyrate using a single-chamber microbial fuel cell. Environ Sci Technol 39, 658–662.
37. Fan, Y., H. Hu, and H. Liu (2007). Enhanced coulombic efficiency and power density of air-cathode microbial fuel cells with an improved cell configuration. J Power Sources 171, 348–354.
38. Ringeisen, B.R., E. Henderson, P.K. Wu, J. Pietron, R. Ray, B. Little, J.C. Biffinger, and J.M. Jones-Meehan (2006). High power density from a miniature microbial fuel cell using Shewanella oneidensis DSP10. Environ Sci Technol 40, 2629–2634.
39. Esteve-Nunez, A., M. Rothermich, M. Sharma, and D. Lovley (2005). Growth of Geobacter sulfurreducens under nutrient-limiting conditions in continuous culture. Environ Microbiol 7, 641–648.
40. Bond, D.R. and D.R. Lovley (2003). Electricity production by Geobacter sulfurreducens attached to electrodes. Appl Environ Microbiol 69, 1548–1555.
41. Whitman, W.B., D.C. Coleman, and W.J. Wiebe (1998). Prokaryotes: the unseen majority. P Natl Acad Sci USA 95, 6578–6583.
42. Liu, H. and B.E. Logan (2004). Electricity generation using an air-cathode single chamber microbial fuel cell in the presence and absence of a proton exchange membrane. Environ Sci Technol 38, 4040–4046.
43. Rabaey, K. and W. Verstraete (2005). Microbial fuel cells: novel biotechnology for energy generation. Trends Biotechnol 23, 291–298.
44. Rabaey, K., N. Boon, M. Hofte, and W. Verstraete (2005). Microbial phenazine production enhances electron transfer in biofuel cells. Environ Sci Technol 39, 3401–3408.
45. Reguera, G., K.P. Nevin, J.S. Nicoll, S.F. Covalla, T.L. Woodard, and D.R. Lovley (2006). Biofilm and nanowire production leads to increased current in Geobacter sulfurreducens fuel cells. Appl Environ Microbiol 72, 7345–7348.
46. Pham, T.H., N. Boon, P. Aelterman, P. Clauwaert, L. De Schamphelaire, L. Vanhaecke, K. De Maeyer, M. Hofte, W. Verstraete, and K. Rabaey (2008). Metabolites produced by Pseudomonas sp enable a Gram-positive bacterium to achieve extracellular electron transfer. Appl Microbiol Biotechnol 77, 1119–1129.
47. Picioreanu, C., I.M. Head, K.P. Katuri, M.C.M. van Loosdrecht, and K. Scott (2007). A computational model for biofilm-based microbial fuel cells. Water Res 41, 2921–2940.
48. Freguia, S., K. Rabaey, Z.G. Yuan, and J. Keller (2007). Electron and carbon balances in microbial fuel cells reveal temporary bacterial storage behavior during electricity generation. Environ Sci Technol 41, 2915–2921.
49. Rozendal, R.A., H.V.M. Hamelers, G.J.W. Euverink, S.J. Metz, and C.J.N. Buisman (2006). Principle and perspectives of hydrogen production through biocatalyzed electrolysis. Int J Hydrogen Energ 31, 1632–1640.

50. Lin, Y. and S. Tanaka (2006). Ethanol fermentation from biomass resources: current state and prospects. Appl Microbiol Biotechnol 69, 627–642.
51. Kuyper, M., M.M.P. Hartog, M.J. Toirkens, M.J.H. Almering, A.A. Winkler, J.P. van Dijken, and J.T. Pronk (2005). Metabolic engineering of a xylose-isomerase-expressing Saccharomyces cerevisiae strain for rapid anaerobic xylose fermentation. Fems Yeast Res 5, 399–409.
52. Shapouri, H., J.A. Duffield, and M. Wang (2001). The energy balance of corn ethanol: an update. U.S. Department of Agriculture, Washington, DC.
53. Goolsby, D.A., W.A. Battaglin, B.T. Aulenbach, and R.P. Hooper (2001). Nitrogen input to the Gulf of Mexico. J Environ Qual 30, 329–336.
54. Hey, D.L. (2002). Nitrogen farming: harvesting a different crop. Restor Ecol 10, 1–10.
55. Goolsby, D.A., W.A. Battaglin, G.B. Lawrence, R.S. Artz, B.T. Aulenbach, R.P. Hooper, D.R. Keeney, and G.J. Strensland (1999). Flux and sources of nutrients in the Mississippi-Atchafalya river basins. National Oceanic and Atmospheric Administration, Washington, DC.
56. Graboski, M.S. (2002). Fossil energy use in the manufacture of corn ethanol. National Corn Growers Association, Chesterfield, Missouri, USA.
57. Committee on Water Implications of Biofuels Production in the United States (2007). Water Implications of Biofuels Production in the United States. National Research Council, Washington, DC.

Chapter 2
Screening Microbes for Ice-Associating Proteins with Potential Application as 'Green Inhibitors' for Gas Hydrates

V.K. Walker, S.L. Wilson, Z. Wu, D.N. Miao, H. Zeng, J.A. Ripmeester and G.R. Palmer

Abstract The survival of microbes at low temperatures is important for our understanding of overwintering and the mechanisms of stress adaptation. However, such organisms also deserve attention for the potential they hold as sources of products to address practical problems and for providing environmentally responsible options. One such threat to the ecosystem is the danger posed by the unexpected and catastrophic formation of gas hydrates in pipelines during drilling operations, transport and throughout fractionation. The most popular chemical gas hydrate inhibitors are themselves toxic, making the discovery of new 'green' hydrate inhibitors a high priority. Recently, we have shown that antifreeze proteins, which inhibit ice growth, can also inhibit gas hydrate formation. Although current sources of these proteins are not sufficient for these applications, we believe that microbial products can be a part of the solution to this challenge that poses a special threat to both marine and northern ecosystems. Here, we outline strategies and methods for the isolation of microbes with these properties.

Keywords Gas hydrates · gas exploration · antifreeze proteins · ice nucleators · freeze–thaw · ice affinity · overwintering

2.1 The Gas Hydrate Problem

Gas hydrates are made of crystalline ice-like cages of water that house small gases such as methane or propane, and form when temperature and pressure conditions are favorable. They are found naturally in the permafrost regions as well as near the continental shelves under the sea. In all, world wide deposits of gas hydrates are estimated at ~200 million trillion cubic feet. Gas hydrates will undoubtedly be used to offset the world's energy thirst within the next couple of decades since they represent a vast reservoir of potential energy and wealth,

V.K. Walker
Department of Biology, Queen's University, Kingston, ON, Canada K7L 3N6
e-mail: walkervk@queensu.ca

V. Shah (ed.), *Emerging Environmental Technologies*,

more than twice that of all known coal, oil and gas deposits [1]. However, although hydrates offer opportunities for economic prosperity, these 'fire ices' can also spontaneously form whenever moisture, small gases such as methane or propane and appropriate pressures meet in drilling and transportation pipes. Gas hydrate crystallization and subsequent blockages present a public and environmental safety problem. When hydrate growth cannot be controlled, there can be accidents, which can cause loss of life as well as local environmental deterioration. One such example is afforded by the explosion of the Piper Alpha oil platform in the North Sea in 1988. Many such incidents are avoided, thanks to chemical inhibitors, which can melt hydrates. Currently, the most popular chemical hydrate inhibitors are methanol and ethylene glycol. However, in some sectors, particularly in marine and northern areas, these chemical hydrate inhibitors themselves constitute an environmental risk since they are flammable and poisonous, and thus there are a growing number of restrictions on their use [2]. To address this challenge, we urgently require environmentally friendly, 'green' gas hydrate inhibitors.

The following paper outlines our approach to the problem. Based on the hypothesis that the icy cages of hydrates might act as an alternative substrate to ice-associating molecules, we tested the ability of antifreeze proteins (AFPs) to bind to model gas hydrates. Remarkably, just as these proteins can inhibit the growth of ice, we have observed that they also inhibit hydrate growth [3, 4]. Unfortunately, the proteins with the most promising activity toward hydrates are difficult to produce in quantities necessary to have practical utility for the gas and oil industry. Thus, we have turned our attention to the isolation of ice-associating molecules from microorganisms. For this we must first discover microbes with these properties. We believe that this represents our best hope to address this particular environmental problem.

2.2 Ice-Associating Molecules from Extremophiles

Microbes show an extraordinary variety of adaptations to extreme conditions. Thermophiles, organisms that survive at temperatures near boiling in places such as thermal vents, have provided a variety of gene products, such as thermophilic enzymes, which in turn, have allowed the development of new solutions for practical problems. For example, the discovery of a DNA polymerase from *Thermus aquaticus* (Taq polymerase) has facilitated the current revolution in genome analysis [5]. Other extremophiles are resistant to pH extremes (acidophiles and alkalophiles), salts (halophiles), desiccation (xerophiles), pressure (barophiles) and other stresses [6]. Psychrophiles or psychrotolerant bacteria, which are hardy at low temperatures, have more recently commanded attention. This can be partially attributed to the interest in prospecting for ice-associating proteins from psychrophiles that may find uses in the preservation of frozen products or for enzymes that are active at low temperatures. As a result, microbes with these

characteristics have been sought at high altitudes, in Arctic regions, glacial cores, ice accretions and in Antarctic lakes. Indeed, Antarctic expeditions have been organized with the purpose to identify bacteria with AFPs, which bind to ice crystals and arrest their growth [7].

To survive subzero temperatures, certain microbes protect themselves against growing ice crystals which could damage membranes, critically increase their cell volume and oppose the osmotic gradient produced by the increasing extracellular solute concentration [8]. They survive these stresses by the production of cryoprotectants [7] that can lower ice nucleation temperatures and stabilize membranes and cell fluids. Shorter acyl chains [8] and unsaturated fatty acids [9] may become more abundant in the membrane. Low temperatures also influence the production of chaperones, cold stress proteins and carotenoids that may confer protection from UV irradiation, oxidative stress and the maintenance of membrane fluidity [10]. Among these, low temperature adaptive proteins are the AFPs and ice nucleation proteins.

AFPs and antifreeze glycoproteins were first characterized and cloned from cold-water fish, and later from other metazoans that overwinter in temperate latitudes [11]. Ironically, it was years after their first discovery that they were first noted and subsequently cloned in a bacterial species [12]. AFPs inhibit freezing in a non-colligative manner by binding to ice and making the addition of water molecules unfavorable, which results in a change in the equilibrium freezing point [13, 14]. Since melting is affected in a colligative manner, the interaction between AFPs and the ice surface results in a separation of the freezing point and the melting point, a phenomenon termed thermal hysteresis [15]. Ice crystal growth can be perturbed even by small quantities of AFP since local ice curvature results from the adsorption of the proteins to the surface of the ice crystal (the adsorption-inhibition hypothesis [15, 16, 17]). Adsorption to certain ice faces by AFPs seems to be by a surface-to-surface complementarity of fit, made possible by regularly spaced residues on the regularly spaced crystal lattice. Once adsorbed to ice, AFPs sit 'snugly', assisted by van der Waals and hydrophobic interactions [18].

AFPs also impede water mobility at the ice crystal surfaces thereby decreasing the probability of recrystallization. It is assumed that some freeze-tolerant organisms, such as certain insects and plants, produce AFPs to prevent the growth of large, damaging ice crystals that form at temperatures close to melting [19, 20, 21], a property known as ice recrystallization (IR). IR inhibition activities, and putative AFPs have been reported in a few bacteria including *Moraxella* sp. [22], *Pseudomonas putida* [12, 23, 24], *Micrococcus cryophilus* and *Rhodococcus erythropolis* [25] as well as cyanobacterial mats [26], *Chryseobacterium* sp. C14 [27] and in several Antarctic *Proteobacteria*, including *Marinomonas protea* [7, 28].

In contrast to AFPs, ice nucleating proteins (INPs) prevent extensive supercooling and allow ice to form at temperatures close to freezing. These proteins are presently known and cloned from only three genera of bacteria, including *Pseudomonas*, *Xanthomonas* and *Erwinia*/*Pantoea* [12, 22, 23, 24, 29, 30]. INPs

are highly repetitive proteins that are located on the outer membrane [23, 31, 32] and aggregates of INPs likely provide templates for ice nucleation [29, 33]. Because the INP sequences are very similar [34], yet the bacteria are evolutionarily divergent, it has been suggested that the genes have been horizontally transferred to several members of the plant-associated microbial community [35]. Since many of these microbes are considered plant pathogens, it has been speculated that INPs may serve to deliberately cause frost injury to plants, thereby increasing the fitness of the host bacteria [36]. A few of these proteins have been recombinantly expressed and one strain of *Pseudomonas syringae* is used commercially for 'snow making' (Snomax, York Snow Inc., Centennial CO, USA). In another application, a genetically manipulated, INP-minus version of these bacteria can be successfully used when warranted by a short growing season [36]. The introduced microbes inhibit the formation of ice on crops, reducing extensive frost damage at temperatures just below freezing.

The search for novel products from ice-associating microorganisms that survive in extreme locations can be expensive and bureaucratically cumbersome. In contrast, our investigations are based on the assumption that ice-associating products can be found in microbes that also inhabit more easily sampled environments, including our own backyards. Techniques for identification and isolation are described and discussed in the following sections.

2.3 Proposed Technology for Microbe Selection

Although microbes with low temperature adaptations may not be abundant if conditions are warm, presumably all that is required for their discovery is a powerful method of selection in order to recover the rarer cells with these properties. New selection regimes have been developed for this purpose.

2.3.1 Cryocycler Selection

We designed an instrument for automatically subjecting microbial cultures to programmed freeze–thaw treatments and dubbed it a 'cryocycler' (Fig. 2.1). This instrument switches between two fixed temperature baths containing ethylene glycol by using solenoid-activated valves. In this way it can achieve maximum heating and cooling rates. Only a relatively few freeze-resistant microbes have been shown to survive such strong selection, even after starting with tens of thousands of cells from a mixed consortium [27]. Routinely, soil samples are obtained from easily accessible temperate locations and cultured in dilute medium. Full strength, rich medium can also be used. However, our observations suggest that when using rich medium there is less culturable diversity in soils from regions, such as boreal outcrops, surmised to be more nutrient limited. Vials containing the cultured consortium are then placed in a

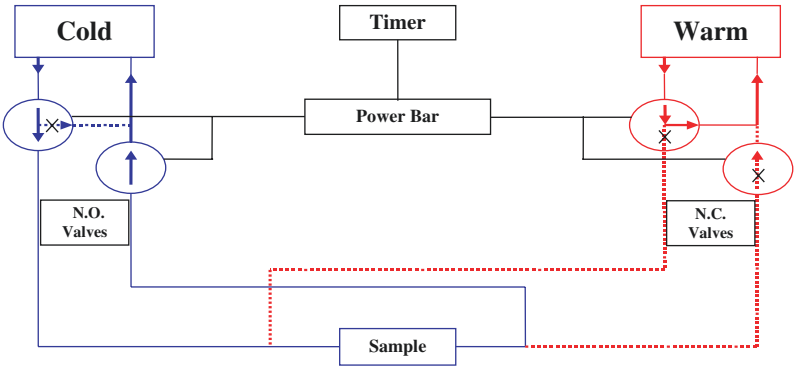

Fig. 2.1 Diagram of the cryocycler designed to automatically subject microbial cultures to freeze–thaw cycles. Solid lines show the flow pattern in the 'power-off' state with the valves in position to circulate cold ethylene glycol (e.g. –18°C) through the jacketed sample chamber. Dotted lines show the flow pattern during the warm (e.g. 5°C) 'power-on' state (adapted from [27])

jacketed glass chamber that is filled with ethylene glycol. Typically, triplicate samples are subjected to a freeze–thaw regime consisting of a 2 h cycle at temperatures below the freezing point and just above the melting point (e.g., –18 and 5°C with average warming rates of 0.5°C/min and cooling rates of 1.0°C/min, although other protocols have also been used). Aliquots that are removed periodically during the cycling are then monitored for surviving cells. It is important to note that occasionally, cultures that originated as single isolates and used as controls can supercool rather than freeze at temperatures close to 0°C. Thus to ensure that all samples freeze at the same temperature, a few sterilized AgI crystals should be added to the cultures at the start of the experiments.

Experiments using the cryocycler show that the viability of the various soil consortia is dramatically reduced by multiple freeze–thaw cycles, with cell numbers typically decreasing by five orders of magnitude after 48 cycles (Fig. 2.2). The decrease in viability does not simply result from a reduction in numbers since the phenotype of the colonies suggests that there is a shift in the complexity of the populations. Early experiments on the cryocycler demonstrated that there was a differential susceptibility to freeze–thaw treatments depending upon the species and the origin of the communities. For example, when $\sim 10^8$ cells of *Escherichia coli* or *Pseudomonas chlororaphis* were subjected to freeze–thaw cycling, none remained viable after 24 and 48 cycles, respectively. Survivors of this stringent regime, in several experiments using different starting populations, included species of *Chryseobacterium*, *Pseudomonas*, and *Buttiauxella*. Recovered viable species often had interesting properties (see the following sections).

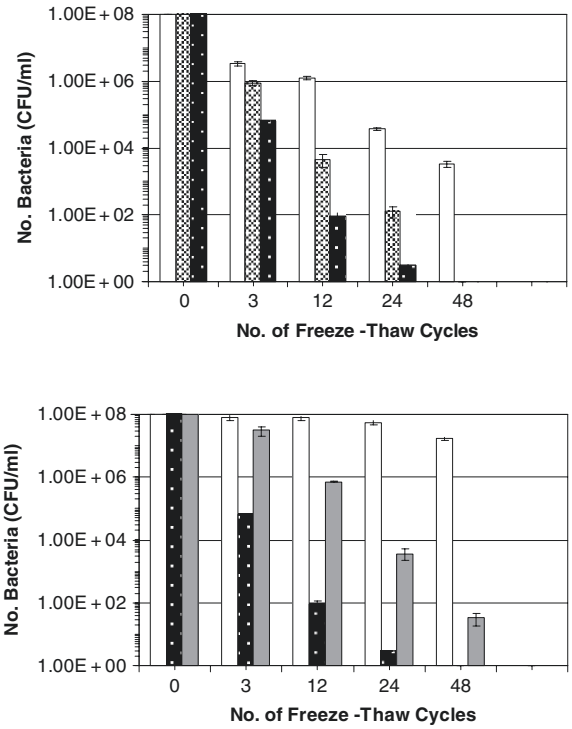

Fig. 2.2 Viability of microbial cultures as a function of the number of freeze–thaw cycles in the cryocycler. *Upper histograms*: viable cells (colony forming units or CFU/ml) in mixed cultures derived from one of the soils tested (*first white bar* in each cycle set) were compared to pure cultures of *P. chlororaphis* (hatched, *second bar* in each cycle set) or *E. coli* (*black, third bar* in the cycle sets) in 48 freeze–thaw cycles. *Lower histograms*: viability of single colony isolates after serial freeze–thaw cycles. Microbes that survived two consecutive 48 freeze–thaw cycles were used to initiate cultures from single colonies of *Chryseobacterium* sp. C14 (*first white bar* in each set) and *Enterococcus* sp. (*grey, third bar* in each cycle set), and these were subjected to further freeze–thaw treatments. *E. coli* (*black, second bar* in each cycle set) was again used as a control. *Error bars* represent standard deviations (modified from [50])

Unexpectedly some microbes, such as *Enterococcus* sp., survived freeze–thaw cycles as part of a consortium, but were less freeze–thaw resistant in isolation (Fig. 2.2 and not shown). Further investigation revealed that their survival was influenced by the presence of another bacterium, *Chryseobacterium* sp. C14. When *Enterococcus* sp. and this *Chryseobacterium* strain were cultured together, both showed freeze–thaw resistance [27]. Furthermore, when pelleted *Enterococcus* sp. cells were resuspended in the cell-free, spent medium obtained from *Chryseobacterium* sp. cultures, their survival increased 1000-fold. Thus, these selection experiments also appear to reveal something about the dependence and interaction of certain microbes in their communities.

2.3.2 Ice-Affinity Selection

Another new method of microbe selection takes advantage of the principle that when ice grows slowly it excludes solutes. Charles Knight devised methodology some years ago to examine the adsorption of proteins on the faces of ice [37] and this was subsequently tailored to allow ice-affinity purification of AFPs [38]. A modification of this procedure has now been adopted for the selection of microbes that are included into a growing elongated hemisphere of polycrystalline ice. The apparatus consists of an 'ice finger' or brass cylinder in which temperature-controlled ethylene glycol solution is circulated (Fig. 2.3). The sample beaker contains dilute cultures initiated from sites of interest. The sample is maintained just at the freezing point and frost is allowed to accumulate on the cold finger by water condensed from the air. After lowering the cold finger into the sample solution, an ice ball or 'Popsicle' is formed. It is important to grow the ice slowly (about 0.01 ml/min) over a 24–48 h period. After approximately 50% of the culture is frozen, the ice is rinsed and then melted to obtain the microorganisms that partition into the ice phase. Individual colonies can be obtained after limited dilution or by culturing on nutrient plates.

In experiments where cultures were initiated with single isolates, *E. coli* numbers were reduced four orders of magnitude in the melted ice fraction compared to the original sample [39]. In contrast, when a *Chryseobacterium* isolate, originally discovered after cryocycler selection, was subjected to ice affinity, the recovery from the ice represented a reduction of only two orders of magnitude in cell number. Although this strain of *Chryseobacterium* is 5–6 fold more freeze-tolerant than *E. coli* after a single freeze period, the observed differential recovery encouraged us to use ice affinity to fractionate cultured communities in order to reduce both the complexity of the original population

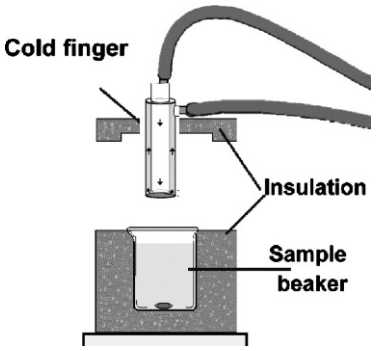

Fig. 2.3 Diagram of the ice finger apparatus fabricated to select microbial cells with an affinity for ice. Small arrows show the flow pattern of chilled ethylene glycol through the ice finger. The sample in the beaker is stirred with a magnetic stir bar while ice forms on the finger (modified from [38])

as well as cell numbers. Isolates recovered from these experiments in initial experiments included two species of *Chryseobacterium*, three of *Pseudomonas*, three of *Acinetobacter*, two of *Bacillus* and a *Paenibacillus* species [39]. Again, a number of the recovered strains had interesting properties.

2.3.3 Screens for Ice Nucleation, Ice Recrystallization, Inhibition and AFP Activity

Although not selective techniques, these methods have been developed as tools to screen isolates for these properties. Ice nucleation screens are set up essentially as previously described ice nucleation assays [31, 40, 41]. Briefly, small samples are loaded onto a polarizing filter, placed in the cryocycler chamber, and illuminated from below with a fiber-optic source. As the chamber temperature is lowered from –1 to –15°C (at 0.1–0.2°C/min), software-controlled digital photographs are captured every 60 sec through a crossed polarizing filter. After freezing the samples become visible due to the rotation of the plane of polarization by the ice crystals, and these images are automatically analyzed and transferred to a spread sheet. The temperature at which 90% of the samples freeze is taken as the ice nucleation temperature of the most active fraction of the sample. Groups of cultures containing ice nucleators normally freeze at temperatures above –8°C, with control, samples freezing at about –12°C. This method was used to identify *P. borealis* isolates with ice nucleation activities [39] and to optimize the growth conditions for the production of INPs in *P. syringae, P. borealis* and recombinant cultures (S. Wu, D.N. Miao and V.K. Walker, unpublished).

The average ice nucleation temperature of any isolate or lysate can be determined using a thermal analyzer. This apparatus records temperatures from thermistors placed in 2–3 ml samples that are chilled from approximately 5 to –15°C at 1°C/min. The heat of fusion of first-order freezing and thawing phase transitions causes temperature changes in the sample which are used to record freezing and thawing [42]. Because of the larger volumes, samples containing ice nucleators normally freeze above –8°C, with controls freezing at this point or lower. A typical profile from the thermal analyzer shows that *P. borealis*, identified using ice-affinity, has ice nucleation activity (Fig. 2.4).

Another technique that has not been used by our group, but which has been successfully employed to screen bacteria obtained from Antarctic lakes [7] detects isolates that inhibit IR. Crude lysates from individual isolates are placed into 96-well microtiter plates, brought to 30% sucrose (vol/vol) and quickly frozen at –70°C. After incubation at –6°C for many hours (typically overnight), frozen isolates with IR inhibition activity can be recognized since they appear more opaque than the transparent lysates with no activity. IR inhibition is correlated with AFP activity since at temperatures close to melting. AFPs prevent the formation of large crystals, which have a relatively clear appearance. In our experience, we have found crossed polarizing filters to be helpful

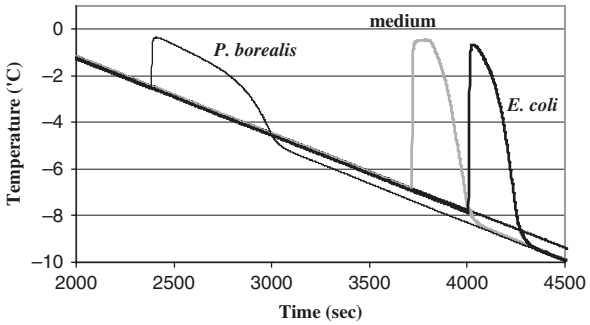

Fig. 2.4 Representative thermal profiles showing the heat of fusion in 2 ml samples. A reference thermistor recording (*straight, thin black line*) shows the temperature of a control sample containing ethylene glycol. *P. borealis* cultures (approximately $\sim 1 \times 10^{-8}$ CFU/ml) show freezing beginning at –2.5°C. Culture medium and *E. coli* cultures (at $\sim 1 \times 10^{-8}$ CFU/ml) show freezing at –7 and –8°C, respectively, ([50] reproduced by permission of The Royal Society of Chemistry)

in distinguishing differences between lysates. This protocol has been used to successfully identify more than a dozen bacteria with putative AFPs, including those from the genera *Idiomarina, Rhodococcus* (an *Actinobacteria*), *Pseudomonas, Bacillus* and *Marimonas* [7]. One of the latter isolates has now been extensively studied and the Ca^{++}-dependent AFP has been purified and described [28].

This screening technique is also useful when used as an assay for the characterization of microbes isolated by selective regimes; we have used it to examine *Chryseobacterium* isolates identified after cryocycler selection as well as ice-affinity selection. IR inhibition activity is apparent in these (Fig. 2.5), but after treatment with protease, activity was destroyed [27]. This suggests that these particular microbes may have AFP activity.

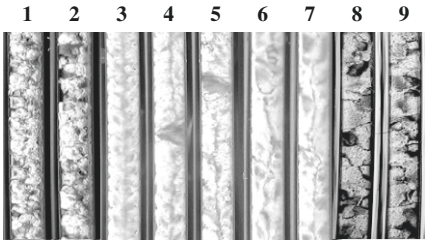

Fig. 2.5 Inhibition of ice recrystallization. Screens are usually conducted in microtiter plates, but samples in microcapillaries held at –6°C and examined between crossed polarizing filters more easily demonstrate this principle. From *left* to *right* samples include sample buffer controls (1, 2), serial dilutions of 0.2, 0.02 and 0.002 mg/ml AFP solutions (3–5), *Chryseobacterium* sp. C14 cultures (6, 7), and *E. coli* cultures (8, 9). Note that only the AFP controls and the *Chryseobacterium* cultures have crystals too small to be observed at this magnification and the overlying 'feathery' pattern, seen in rapidly frozen samples, is apparent. Bacterial cultures were at $\sim 2 \times 10^{-8}$ CFU/ml (adapted from [27])

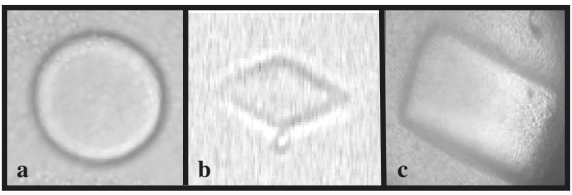

Fig. 2.6 Crystal shape assay. Ice crystals grown in the presence of (**a**) control solutions such as buffer (shown), *E. coli* or medium, (**b**) Type I fish AFP and (**c**) *P. borealis* cultures were examined under a microscope (40x) ([50] reproduced by permission of The Royal Society of Chemistry)

Microscopic analysis of ice crystal morphology is another method for examining lysates and cultured samples, but it has not yet been adapted for the screening of large sample sets. Typically it is done by freezing a microscopic volume of solution in an oil droplet placed in a nanoliter osmometer. After freezing, the temperature is slowly increased until a single crystal remains. Only then is the temperature lowered slightly, and subsequently held constant, so that the morphology of the ice crystal shape can be noted [43]. For example, when ice crystals formed in the presence of the *Chryseobacterium* isolate, obtained after selection in the cryocycler, the morphology was not disc-like as is seen in the presence of *E. coli*, but rather more oblong [39]. Crystals formed in the presence of the ice-affinity selected *P. borealis* were not bipyramidal as seen with many fish AFPs, but more hexagonal or rectangular (Fig. 2.6). These different crystal shapes likely reflect the preferential adsorption of these proteins to different ice faces.

2.4 Prospects for Applications to the Energy Sector and Elsewhere

The development of these new selective methods has allowed us to imitate the rigors of high latitude environments in the laboratory and has resulted in the selection of a group of microorganisms with a high proportion of ice-associating properties. Although the analysis of the selected cultures is still in progress, a total of 70% (9/13) of the recovered, identified genera have some type of ice-associating activity. Four of 13 genera were recovered using both the cryocycler and ice affinity methods (Wilson and Walker, unpublished). In addition, of the 13, almost all have been previously described as associating with ice and have been recovered by others from samples obtained from glacial cores, Antarctic lakes or sea ice [7, 44]. As mentioned previously, ice-associating activities do not appear to be very common properties amongst bacteria. To date, AFPs have been described in half a dozen genera, but the corresponding sequences, which appear to be dissimilar from one another, have been characterized or cloned and expressed from only a few of these [12, 22, 28, 45]. In contrast, INPs, which have been described in a few plant-associating bacteria, appear to be homologous proteins [35]. Thus methods to select and recover ice-active microorganisms from a variety of habitats, including

late summer-collected soil samples, are notable. This success demonstrates that sampling in extreme or highly remote areas may not be required for the isolation of strains with these properties. With the aid of these selective techniques, it may even transpire that these properties are not quite as rare as we had once assumed.

Why is it important to identify microbes with psychrophilic adaptations? For the basic scientist, knowledge about survival under extreme conditions and insights into the evolution of these resistant traits will suffice. However, there are also other reasons to identify these organisms. Such microbes offer the prospect that proteins with interesting properties such as antifreeze and ice nucleating activities can be more readily identified. In addition, these isolates are likely to produce enzymes that are sufficiently active at low temperatures to be useful for applications under extreme conditions. Examples could include the bioremediation of spills and polluted sites in the far north and on the sea bed. Nucleation of freezing at consistent temperatures close to 0°C could save energy costs for various industrial chilling processes including frozen food production, freeze-concentration and food preservation and transportation [46]. Strains of *P. borealis* are classified as plant beneficial bacteria since certain soil-borne plant pathogens are suppressed [47], and our ice-affinity recovered *P. borealis* showed impressive nucleation activity (S. Wu and V.K. Walker, unpublished). Indeed, the ice nucleation activities are so high that our isolate approaches that of commercial snow making preparations derived from *P. syringae*, a plant pathogen [36]. Thus, there may be applications, including cloud seeding over agricultural areas, where the use of *P. borealis*-derived nucleators could be preferable.

However, amongst the most urgently needed products are environmentally friendly gas hydrate inhibitors. This need is likely to become acute within the next two decades as the search for energy drives the industry to deeper waters and under the permafrost. Thus it is our hope that products isolated from psychrophiles will prove useful for the inhibition of gas hydrates. As previously indicated, AFPs inhibit the formation of gas hydrates [3, 4] and should represent ideal 'green inhibitors'. However, they currently cannot be produced in the volumes required for their practical application in the field. AFPs can be isolated from fish and insect serum, but these sources do not represent a reasonable option. Recombinant DNA technology has allowed the production of many foreign products in simple cells, but in this case, neither *E. coli* nor yeast cells can efficiently and accurately fold the same AFPs [48, 49] that are the most active against hydrates.

The ability to screen psychrophiles for ice-associating properties should permit the identification of products that can also act as hydrate-associating molecules in order to change the kinetics of gas hydrate formation. Preliminary experiments in our labs (E. Huva, J.A. Ripmeester and V.K. Walker, unpublished) suggest that microbes with antifreeze as well as ice nucleating activities can influence hydrate formation. This is a significant finding since it represents a glimmer of hope that an affordable, environmentally benign method to control and inhibit hydrate formation may be found in microbes isolated by the selection techniques described in this chapter. Indeed, challenging and

expensive expeditions to polar regions, glaciers and high altitudes may not be required to prospect for microbes with 'ice resistance'. It may be only necessary to continue to develop and use these strong selective techniques to recover those organisms with useful properties. It is hoped that microbial gene products can be more easily folded in bacterial vectors and that high levels of cost-effective production would be possible. Thus these microbes may reward us with reagents that can contribute to environmental safety and help secure a safe and effective methodology for the energy sector.

2.5 Conclusion

Gas hydrate deposits will be important sources of energy in the future, as traditional sources of energy become more costly to exploit, and will undoubtedly be used for gas storage and transportation. However, since the offshore industry is going to deeper waters, with consequent increased pressures and decreased temperatures, unpredicted hydrate formation is a major economic concern for industry. More significantly, the formation of these 'fire ices' are of environmental concern because of their blow out potential and the possible pollution linked to the use of chemical hydrate inhibitors. The need for green inhibitors is urgent and ice-associating proteins and glycoproteins offer the promise of environmentally safe alternatives. The described innovations for the selection of microbes with these properties now offer the real prospect of an emerging technological solution to a very real environmental risk.

Acknowledgments The majority of our described research was funded by Discovery and Equipment grants from the Natural Sciences and Engineering Research Council (Canada) and a Queen's University Research Chair to V.K. Walker. Drs. Mike Kuiper and Peter Davies are acknowledged for their encouragement and two anonymous referees are thanked for their advice on the manuscript.

References

1. Kevenvolden, K.A. (1999) *Proc. Nat. Acad. Sci. USA*, 96, 3420.
2. Oellrich, L.R. (2004) *in*: XVII National Heat and Mass Transfer Conference IGCAR pp 70.
3. Zeng, H., Wilson, L.D., Walker, V.K., Ripmeester, J.A. (2006) *J. Amer. Chem. Soc.*, 128, 2844.
4. Zeng, H., Moudrakovski, I.L., Ripmeester, J.A., Walker, V.K. (2006) *AIChE J.*, 52, 3304.
5. Saiki, R.K., Gelfand, D.H., Stoffel, S., Scharf, S.J., Higuchi, R., Horn, G.T., Mullis, K.B., Erlich, H.A. (1988) *Science*, 239, 487.
6. Reysenbach, A., Shock, E. (2002) *Science*, 296, 1077.
7. Gilbert, J.A., Hill, P.J., Dodd, C.E., Laybourn-Parry, J. (2004) *Microbiol.*, 150, 171.
8. Mindock, C.A., Petrova, M.A., Hollingsworth, R.I. (2001) *Biophys. Chem.*, 89, 13.
9. Broadbent, J.R., Lin, C. (1999) *Cryobiology*, 39, 88.
10. Chattopadhyay, M., Jagannadham, M. (2001) *Polar Biol.*, 24, 386.
11. DeVries, A.L., Wohlschlag, D.E. (1969) *Science*, 163, 1073.

12. Muryoi, N., Sato, M., Kaneko, S., Kawahara, H., Obata, H., Yaish, M.W.F., Griffith, M., Glick, B.R. (2004) *J. Bacteriol.*, 186, 5661.
13. DeVries, A. (1971) *Science*, 172, 1153.
14. Yeh, Y., Feeney, R.E. (1996) *Chem. Rev.*, 96, 601.
15. Raymond, J.A., DeVries, A.L. (1977) *Proc. Natl. Acad. Sci. USA*, 74, 2581.
16. Harrison, K., Hallett, J., Burcham, T.S., Feeney, R.E., Kerr, W.L., Yeh, Y. (1987) *Nature*, 328, 241.
17. DeOliveira, D.B., Laursen, R.A. (1997) *J. Am. Chem. Soc.*, 119, 10627.
18. Davies, P.L., Baardsnes, J., Kuiper, M.J., Walker, V.K. (2002) *Philos. Trans. R. Soc. Lond. B. Biol. Sci.*, 357, 927.
19. Mazur, P. (1984) *Am. J. Physiol. (Cell Physiol.)*, 247, C125.
20. Knight, C.A., Duman, J.G. (1986) *Cryobiology*, 23, 256.
21. Barrett, J. (2001) *Intl. J. Biochem. Cell Biol.*, 33, 105.
22. Yamashita, Y., Nakamura, N., Omiya, K., Nishikawa, J., Kawahara, H., Obata, H. (2002) *Biosci. Biotechnol. Biochem.*, 66, 239.
23. Xu, H., Griffith, M., Patten, C.L., Glick, B.R. (1998) *Can. J. Microbiol.*, 44, 64.
24. Kawahara, D., Li, J., Griffith, M., Glick, B.R. (2001) *Curr. Microbiol.*, 43, 375.
25. Duman, J.G., Olsen, T.M. (1993) *Cryobiology*, 30, 322.
26. Raymond J.A., Fritsen, C.H. (2001) *Cryobiology*, 43, 63.
27. Walker, V.K., Palmer, G.R., Voordouw, G. (2006) *Appl. Environ. Microbiol.*, 72, 1784.
28. Gilbert, J.A., Davies, P.L., Laybourn-Parry, J. (2005) *FEMS Microbiol. Lett.*, 245, 67.
29. Yankofsky, S.A., Nadler, T., Kaplan, H. (1997) *Curr. Microbiol.*, 34, 318.
30. Muryoi, N., Matsukawa, K., Yamade, K., Kawahara, H., Obata, H. (2003) *J. Biosci. Bioeng.*, 95, 157.
31. Kozloff, L.M., Schofield, M.A., Lute, M. (1983) *J. Bacteriol.*, 153, 222.
32. Kozloff, L.M., Lute, M., Westaway, D. (1984) *Science*, 226, 845.
33. Ruggles, J.A., Nemeckek-Marshall, M., Fall, R. (1993) *J. Bacteriol.*, 175, 7216.
34. Deininger, C.A., Mueller, G.M., Wober, P.K. (1988) *J. Bacteriol.*, 170, 669.
35. Wolber, P.K., Warren, G.J. (1991) *in:*Microbial Ecology of Leaves, eds., Andrews, J.H., Hirano, S.S., Springer-Verlag, New York, pp. 315.
36. Hirano, S.S., Upper, C.D. (2000) *Microb. and Molec. Biol. Rev.*, 64, 624.
37. Knight, C.A., Cheng, C.C., DeVries, A.L. (1991) *Biophys. J.*, 59, 409.
38. Kuiper, M., Lankin, C., Gauthier, S.Y., Walker, V.K., Davies, P.L. (2003) *Biochem. Biophys. Res. Commun.*, 300, 645.
39. Wilson, S.L., Kelley, D.L., Walker, V.K. (2006) *Environ. Microbiol.*, 8, 1816.
40. Vali, G., (1971) *J. Atmos. Sci.*, 28, 402.
41. Maki, L.R., Galyan, E.L., Chang-Chien, M.M., Caldwell, D.R. (1974) *Appl. Environ. Microbiol.*, 28, 456.
42. Borchardt, H.J., Daniels, F. (1957) *J. Amer. Chem. Soc.*, 79, 41.
43. Chakrabartty, A., Hew, C.L. (1991) *Eur. J. Biochem.*, 202, 1057.
44. Christner, B.C., Mosley-Thompson, E., Thompson, L.G., Reeve, J.N. (2005) *in:* Life in Ancient Ice, eds., S.O. Rogers and J. Castello, Princeton University Press, Princeton, pp. 209.
45. D'Amico, S., Collins, T., Marx, J.-C., Feller G., Gerday, C. (2006) *EMBO Rep.*, 7, 385.
46. Davison, J. (1988) *Nature Biotech.*, 6, 282.
47. Raaijmakers, J.M., Vlami, M., de Souza, J.T. (2002) *Antonie van Leeuwenhoek* 81, 1572.
48. Walker, V.K., Kuiper, M.J., Tyshenko, M.G., Doucet, D., Graether, S.P., Liou, Y.-C., Sykes, B.D., Jia, Z., Davies, P.L., Graham, L.A. (2001) *in*: Insect Timing: Circadian Rhythmicity to Seasonality, eds., Denlinger, D.L., Giebultowicz, J.M., Saunders, D.S., Elsevier, Amsterdam, pp. 199–211.
49. Tyshenko, M.G., d'Anjou, M., Davies, P.L., Daugulis, A.J., Walker, V.K. (2006) *Protein Expr. Purif.*, 47, 152.
50. Walker, V.K., Wilson, S.L., Wu, Z., Huva, E., Palmer, G.R., Voordouw, G., Zeng, H., Ripmeester, J.A. (2007) *in:* Physics and Chemistry of Ice, ed., Kuhs, W.F., Royal Society of Chemistry Publishing, Dorchester, pp. 86.

Chapter 3
Surface Reactions: Bio-catalysis an Emerging Alternative

Anil Mahapatro and Rahul Bhure

Abstract Interfacial phenomena and reactions will dominate the performance of current micro and nano devices, which are increasingly being used in a large number of applications in the areas of biotechnology, clinical diagnosis, food safety testing, and environmental testing. Due to the extremely high area to volume ratio, interfacial interactions become the dominant factor in determining the device performance in which they are being used. Self-assembled monolayers (SAMs) provide excellent platforms to study these interfacial reactions. Chemical modifications of these SAMs are carried out using existing organic methodologies. Apart from limitations due to the steric bulk of the interface these organic techniques also have severe limitation in that they use toxic metal catalyst and solvents and also may use high temperature and pressure in certain reactions. This review focuses on the various organic reactions carried out on these SAMs. Challenges and limitations of current organic reactions at surfaces are discussed. Emerging 'green chemistry' biocatalytic techniques as an alternative for performing surface modifications of these SAMs are reviewed. These biocatalytic reactions offer the potential for milder reactions conditions, avoiding toxic metal catalysts and also the potential to carry these surface reactions in solvent-less conditions. Although limited research exists in this emerging field the potential environmental benefits warrants further work in this growing area.

Keywords Bio-catalysis · surface reactions · self-assembled monolayers · enzyme catalysis

A. Mahapatro
Department of Chemistry, Center for Biotechnology and Biomedical Sciences, Center for Materials Research, Norfolk State University, 700 Park Avenue, Norfolk, VA 23504, USA
e-mail: amahapatro@nsu.edu

V. Shah (ed.), *Emerging Environmental Technologies*,

3.1 Description of the Environmental Problem

'Green chemistry' is essentially a way of thinking rather than a new branch of chemistry and is about utilizing a set of principles that seek to reduce the environmental impact of chemical processes and products. It involves pulling together tools, techniques and technologies that can help chemists and chemical engineers in research, development and production to develop more eco-friendly and efficient products and processes, which may also have significant financial benefits. Green chemistry aims to improve the way that chemicals are both produced and used in chemical processes in order to reduce any impact on man and the environment. The promotion of green chemistry is one of the most important ways in which chemistry and chemists can contribute to sustainable development.

Society has many concerns about 'chemicals' and their uses. For example, safety issues such as fire and explosion, health effects such as carcinogenicity and endocrine disruption, and environmental impacts such as global warming and impacts on wildlife. Society's growing concern for the environment and pressures for greater control of chemicals in the environment has now coalesced in the arena of 'Sustainable Development'. Green chemistry is a major component in the way that chemistry as well as the chemical and related industries, have led and responded to sustainable development.

The term 'green chemistry' was first coined by the US Environmental Protection Agency. Their early definition of the subject is still widely quoted: *'"Green Chemistry" is the utilization of a set of principles that reduces or eliminates the use or generation of hazardous substances in the design, manufacture and application of chemical products'*. However, in practice green chemistry is nowadays taken to cover a much broader range of issues than the definition suggests. Using and producing better chemicals with less waste, green chemistry also involves reducing other associated environmental impacts, in particular reducing the amount of energy used in chemical processes.

In practice, green chemistry embraces concepts such as (a) atom efficiency – designing processes to maximize the amount of raw material that is converted into the product; (b) energy conservation – designing more energy efficient processes; (c) waste minimization – recognizing that the best form of waste disposal is not to create waste in the first place; (d) substitution – using safer, more environmentally benign raw materials and solvents or solvent free processes.

Although the importance of green chemistry and its environmental impact has been widely acknowledged, little work has been pursued to apply these principles in the growing area of nanotechnology. Nanotechnology is a new field of science broadly defined as research and technology development intended to create, understand and use nano scale (0.1–100 nm) structures or devices. Nanotechnology applies the principles of engineering, electronics, physical and materials science and manufacturing to molecular and submicron

level. The basis of the field is that bulk properties of materials made from nano sized structures differ significantly from that of the original material. By altering the sizes of those building blocks, controlling their internal and surface chemistries and controlling their assembly, new materials with new set of properties can be designed. The different nanostructures currently being extensively reviewed include nano particles (biodegradable, ceramic, magnetic, etc.), nano wires and nano tubes, nano porous structures and self-assembled monolayer (SAMs).

Development and fabrication of nano devices for tailored end application necessitates the surface modification of these nano structured functional devices. These modification are carried out using traditional organic methodologies which are inherently non-environmentally friendly due to the use of toxic catalysts, excessive solvents, multiple protection deprotection steps, harsh reaction conditions and limited catalyst recyclability [1]. As the applications of nanotechnology increases, there would be a growing need to develop environmentally friendlier or green chemistry methodologies for functionalization and modification of these nanostructures to create value added products. This review aims to look into some of the surface modification reactions on SAMs, the current technology available for such reactions and the limitation of the available methodologies. This review also looks at emerging biocatalytic methodologies and its potential as an alternative for carrying out these surface modification reactions.

3.2 Review of Existing Literature and Technology

3.2.1 Introduction

Interfacial reactions are becoming an increasingly important subject for studies with wide spread applications such as catalysis [2], electronics [3], chemical sensing [4, 5], and many other applications [6, 7]. Interfacial phenomena dominate the performance of micro and nano devices which are currently being extensively studied. Furthermore, because of the extremely high area to volume ratio, interfacial interactions become the dominant factor for determining device performance. The interface layer can be as simple as a plain polymer or complex as a multiple layer of chemicals and biological components. Understanding the rules that govern these surface reactions provides important information for fundamental studies in chemistry and biochemistry [8, 9]. Also the availability of numerous analytical techniques capable of detecting chemical changes in films that are few nanometers thick [10], have made studies of interfacial and surface reactions a viable and important area of modern science.

Self-assembly provides a simple route to organize suitable organic molecules on noble metal and selected nano cluster surfaces by using monolayers of long

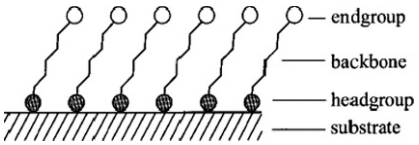

Fig. 3.1 Idealized view and structural model of SAM on metal substrate

chain organic molecules with various functionalities like –SH, –COOH, $–NH_2$, silanes, etc. These surfaces can be effectively used to build-up interesting nano level architectures. Flexibility with respect to the terminal functionalities of the organic molecules allows the control of the hydrophobicity or hydrophilicity of the metal surface, while the selection of length scale can be used to tune the distant-dependent electron transfer behavior. Organo-inorganic materials tailored in this fashion are extremely important in nanotechnology to construct nano electronic devices, sensor arrays, super capacitors, catalysts, rechargeable power sources, etc. [11].

SAMs are perhaps the best model for studying these interfacial reactions. Figure 3.1 shows an idealized view and structural model of a SAM on a metal substrate. SAMs are defined as monomolecular films of a surfactant formed spontaneously on a substrate upon exposure to a surfactant solution. Virtually any functional group can be introduced in these monolayers as a tail group, and this ability to precisely control surface composition makes them an invaluable tool for studying interfacial reactions. Co-adsorption of two different types of SAMs leads to formation of a mixed monolayer, thus enhancing control over surface composition. SAMs can also be prepared on highly curved surfaces, such as colloids, which makes it possible to use conventional analytical techniques for characterization [12].

Because of the wide use of SAMs in surface science and technologies, this review focuses predominately on interfacial reactions based on SAMs.

3.2.2 Self-Assembled Monolayers

SAMs have aroused wide spread interest as they provide an opportunity to define the chemical functionality of surfaces with molecular precision. SAM modified surfaces are highly useful for investigating several fundamental phenomena such as distance-dependent electron transfer [13], mechanism of single electron transfer, observation of molecular event such as coulomb staircase [14], etc., on artificially designed nanostructures. Due to the highly ordered nature and tight packing, these monolayers on metallic surfaces are also important for several practical applications such as chemical sensing [15], control of surface properties like wettability and friction [16], corrosion protection, patterning, semiconductor passivation, and optical second harmonic generation [17]. Formation of SAM also provides unique applications such as stabilization of nano

particles by isolating them from their environment, where particle growth and agglomeration by different mechanisms can be prevented.

With the proper terminal functional groups, SAMs can be used to both physically and chemically attached protein molecules. Physical attachment is achieved by the hydrophobic or electrostatic interactions between protein molecules and surfaces. The SAMs can also be tailored to form hydrophobic or charged layers, and therefore adsorb protein molecules via the hydrophobic interaction or electrostatic forces [18]. Silin et al. [19] investigated the non-specific binding of human immunoglobulin G (hIgG) and bovine serum albumin (BSA) on gold surfaces modified by alkyl thiol molecules with different terminal groups: CH_3, C_6H_4OH, COOH, NH_2, OH, and oligoethylene oxide (OEO) [19]. They concluded that the capacity to bind protein depends on both surface chemical group and protein molecules.

Two families of SAMs have received the most attention, SAMs of alkanethiols on gold and alkylsilanes on silicon.

3.2.2.1 Alkanethiols on Gold

Alkanethiols are the most popular reagents used to form SAMs on gold surfaces. The chemisorption of these alkanethiol molecules on the gold surface is based onto the interaction of thiolate molecules with the gold lattice. Due to the advantages of easy preparation, high stability, and reproducible closely packed structures, the coupling of organo-sulfur compounds to gold surfaces has been widely explored and well established. Since thiols on gold have been particularly well studied it has been used as a model system for a variety of applications including biomaterial and biosensor surfaces [20]. The preparation of SAMs on gold is simple. The clean substrate is immersed in a 1–10 mM solution of the desired alkanethiol at room temperature and after approximately 1 h, the surface is covered with a near perfect monolayer. It is generally believed that the thiol group binds to the gold as a thiolate [16], resulting in an extremely densely packed, crystalline monolayer. Detailed information regarding the formation of thiol monolayers on gold are discussed elsewhere [21]. The choice of the head group thus determines the surface topography, as the underlying substrate becomes completely inaccessible to the molecules in solution. For example, clean gold is naturally hydrophilic, but the formation of SAMs makes it possible to control the contact angle of water on the surface to any value between 0° (–OH and $–CO_2H$ groups) and 118° ($–CF_3$ groups) depending on the functional group on the surface [22]. The surface energy of a given SAM can also be altered by making a 'mixed' SAM with two (or more) components. The problem of bulky head groups is avoided by mixing with less bulky thiols in the feed solution. When the alkanethiols are of equal chain length, the ratio of thiols in the SAM will resemble the ratio in solution [23].

3.2.2.2 Alkylsilanes on Silicon

The formation of SAMs of alkylsilanes on silicon or glass is more complex. These monolayers are covalently bound to surface hydroxy groups through Si–O bonds. The molecules used in the formation of such monolayers are either chlorodimethyl long chain alkylsilanes, alkyltrichlorosilanes, or trialkoxy(alkyl)silanes [24]. The alkylchlorosilane derivatives react spontaneously with clean Si/SiO_2 or glass, whereas the alkoxysilanes need to be heated, in order to convert the alcohols into leaving groups. The more commonly used alkylchlorosilanes are either deposited from the vapor phase or from solution. These molecules partially hydrolyze in solution, forming oligomers before settling down on the surface into a polymeric network. The hydrolysis of trichlorosilane derivatives can, however, also result in polymer networks 'dangling off' the surface [25]. Experimental evidence, however, do suggests that long alkylsilanes form very tightly packed monolayers that are only slightly less dense than alkanethiols on gold [21].

3.2.3 Mixed Self-Assembled Monolayers

Monolayers comprising a well-defined mixture of molecular structures are called 'mixed' SAMs [26, 27, 28, 29, 30, 31]. There are three easy methods for synthesizing mixed SAMs: (1) co-adsorption from solutions containing mixtures of thiols (RSH + R'SH), (2) adsorption of asymmetric disulfides (RSSR'), and (3) adsorption of asymmetric dialkylsulfides (RSR'). Mixed SAMs provide a useful methodology for incorporating into a SAM a molecular species whose own physical dimensions would preclude a direct, well-organized assembly. Mixed SAMs are also useful for defining gradients of interfacial composition that, in turn, are useful for studying the properties and biology of cells.

The adsorption of mixture of thiols allows the formation of SAMs with widely varying compositions [22, 32]. The formation of mixed SAMS of methoxytri(ethylene glycol)-undecenyldimethylchlorosilane and dodecyldimethylchlorosilane (DDMS) were prepared by self-assembly from organic solution in the presence of an organic base [31]. The composition of the mixed SAMs was found to depend directly and linearly on the composition of the silanization solution. This mixed SAM system prohibited the non-specific adsorption of a variety of proteins. Mixed SAMs allow the surface properties to be fine-tuned within the range of the properties of the SAMs formed from the pure compounds.

3.2.4 Surface Characterization

The products of organic synthesis in solution can easily be purified and subsequently analyzed with rapid, sensitive techniques such as NMR spectroscopy,

mass spectrometry, elemental analysis and X-ray spectroscopy. Solid-phase synthesis greatly facilitates the purification of products and has become the backbone of modern combinatorial chemistry, but the characterization of products bound to the solid supports is more difficult. Solid-state NMR spectroscopy is one possible way to monitor a reaction, but in general, the products can only be fully analyzed after cleavage from the support. When working with reactions on monolayers, the problems of monitoring the reaction, determining the products and estimating the yield become quite significant. The extremely small quantities involved render most analytical tools useless, and very often, a combination of techniques is necessary to prove the structure on the surface. Monolayers on gold nano particles/colloids (20 nm size range) have been used as models for 2D SAMs [33] and their reactivity studied by NMR spectroscopy in solution. However, as these small particles are highly curved, it is not always straightforward to extrapolate yields from nano particles to planar surfaces.

One of the advantages of SAMs on smooth, reflective surfaces, is that reactions on these monolayers can be studied by a wide range of techniques including infrared spectroscopy [34], infrared spectroscopic ellipsometry (IRSE) [35], scanning electron microscopy [18], contact angle measurements [36], atomic force microscopy (AFM) [37], surface plasmon resonance [38], ellipsometry [39], low-angle X-ray reflectometry [40], surface acoustic wave and acoustic plate mode devices [41], X-ray photoelectron spectroscopy [39], sum frequency spectroscopy [42], quartz crystal microbalance [43], electrochemical methods [44], confocal and optical microscopes [45], secondary ion mass spectrometry (SIMS) [46] and near-edge X-ray absorption fine structure (NEXAFS) [47]. Details of these techniques are discussed elsewhere [21].

In practice, IR spectroscopy, ellipsometry and XPS are the techniques most widely used to study chemical transformations, whereas AFM is particularly useful to image-patterned surfaces. The introduction of fluorescent tags and their detection using (confocal scanning) fluorescence microscopy is widely used to study the attachment of labeled biomolecules to a substrate. The quantitative analysis can be quite difficult, however, instead of determining the yield while the molecules are in the monolayer, it is also possible to cleave the products from the solid support and analyze the molecules 'off-line'. Using very sensitive analytical tools, even the tiny amounts of material cleaved from substrates can be characterized. Butler et al. [48] measured the efficiency of phosphoramidite-based oligonucleotide synthesis on surface tension arrays using capillary electrophoresis of cleaved products.

3.2.5 Surface Modification of SAMs

The modification of surface properties through the selection of the appropriate terminal functional group in the monolayer has led to the development of an emerging research field 'surface organic chemistry', where the aim is to control

the physicochemical properties of man made surfaces by the functionalization of these surfaces, yielding formation of 'tailor-made' surfaces. Chemical transformations on SAMs have been studied in detail and provide new mechanistic insights as well as routes to tailored surface properties [49, 50, 51]. Methodologies of surface modification of SAMs focus on two strategies: (a) chemical modification and attachment of organic molecules after formation of SAMs and (b) attachment prior to assembly, i.e., the desired attachment on alkanethiols are carried separately in solution and the synthesized molecules are then assembled on gold surfaces. This review focuses on chemical modification of SAMs after assembly to a substrate.

Variation of the head group of the monolayer makes it possible to control wettability, etc., and also allows the introduction of different chemical moieties with specific properties such as non-specific binding of proteins to surfaces. For example, the introduction of oligoethylene glycol functionality to the end of the alkyl chain results in protein-resistant properties [52]. Thus instead of synthesizing different thiols/silanes with different head groups, it is more convenient to use a number of 'standard' SAMs and subsequently perform reactions on SAMs to modify the surface chemistry. Performing reactions on SAMs allows us to tune the properties of surfaces at the molecular level, but due to the nature of SAMs (tightly packed, movements of molecules within monolayers restricted) the choice of reaction is important. One must consider that steric effects are likely to be exacerbated for certain surface reactions, leading to an energy barrier higher than would be expected in solution chemistry. To successfully functionalize a SAM, reaction conditions must not cause destruction of the monolayer or damage the underlying substrate.

Over the last decade, a considerable number of reactions have been studied [49, 50]: (i) olefins: oxidation [53, 54], hydroboration, and halogenation [55]; (ii) amines: silylation [56, 57], amidation [58], and imine formation [59]; (iii) hydroxyl groups: reaction with anhydrides [60], isocyanates [61], epichlorohydrin and chlorosilanes [62]; (iv) carboxylic acids: formation of acid chlorides [63], mixed anhydrides [64] and activated esters [65]; (v) carboxylic esters: reduction and hydrolysis [66]; (vi) aldehydes: imine formation [67]; (vii) epoxides: reactions with amines [68], glycols [69] and carboxyl-terminated polymers [70]. A list of all the major classes of reactions on SAMs plus relevant examples are discussed comprehensively elsewhere [50]. Section 3.2.6 will provide a more detailed look at reactions with some of the common functional SAMs, i.e., hydroxyl- and carboxyl-terminated SAMs.

The surface modification of polymers with self-assembled molecular structures has also been studied. Ratner and co-workers [71] have described a simple, one-step procedure for generating ordered, crystalline methylene chains on polymeric surfaces via urethane linkages. The reaction of dodecyl isocyanate with surface hydroxyl functional groups, catalyzed by dibutyltin dilaurate, formed a predominantly all-*trans*, crystalline structure on a crosslinked poly (2-hydroxyethyl methacrylate) (pHEMA) substrate was demonstrated. X-ray photoelectron spectroscopy and time-of-flight SIMS showed that the surface

reaction reached saturation after 30 min at 60°C. These findings are significant in that the possibilities for using structures similar to self-assembled monolayers (SAMs) are expanded beyond the rigid gold and silicon surfaces used throughout most of the available literature. Thus, SAMs, biomimetics for ordered lipid cell wall structures, can be applied to real-world biomedical polymers to modify biological interactions. The terminal groups of the SAM-like structure can be further functionalized with biomolecules or antibodies to develop surface-based diagnostics, biosensors, or biomaterials [71].

3.2.6 Organic Reactions on SAMs

3.2.6.1 Reactions of Hydroxy-Terminated SAMs

The reaction between substrate-bound alcohols and fluoroacetic anhydrides (Fig. 3.2) has been studied and the reaction was estimated to give a 80–90% yield. The reaction was thought not to go to completion because the larger fluorine atoms lead to a sterically hindered environment [72]. The reaction was studied in more detail by Leggett and co-workers [60]. XPS experiments showed that trifluoroacetic anhydride completely reacted with the hydroxy monolayer, but longer chain anhydrides were found to give only an 80% conversion. Hydroxy-terminated SAMs on gold react with alkyltrichlorosilanes in an analogous manner to the chemisorption of trichlorosilane on hydroxysilicon substrates. This reaction represents the first example of the preparation of double layers using both the trichlorosilane and thiol methods of monolayer formation [62]. The reaction between phenyl isocyanate and hydroxyl bearing SAMs has been described by Himmel et al. [73] The resulting urethane linkage was obtained in an 87% yield in the condensed phase reaction. This urethane linkage was found to be thermally unstable at temperatures above room temperature, as shown by the strong decrease of the nitrogen signal in XPS. The resulting monolayer bound phenyl groups were found to be ordered with respect to the original monolayer.

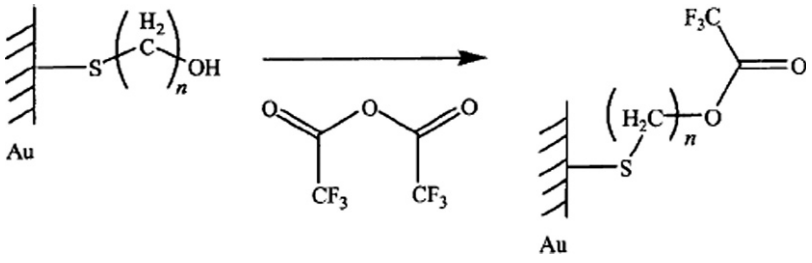

Fig. 3.2 Reaction of hydroxyl-terminated SAM

3.2.6.2 Reactions of Carboxylic Acid-Terminated Monolayers

Carboxylic acid-terminated monolayers self-assembled onto Au substrates have been studied by Leggett and co-workers [60]. The reaction between a carboxylic acid functionalized SAM and trifluoroethanol in the presence of di-*tert*-butylcarbodiimide, an activator added to make the carboxylic acid monolayer more susceptible towards nucleophilic attack, [65] was found to proceed slowly with only a 60% rate of conversion after several days. These sluggish reaction rates are in agreement with comparably slow reactions on poly(methacrylic acid) where steric interactions are believed to be responsible for the long reaction times [74]. The authors concluded that the slow reaction on the monolayer was due to a combination of (a) bulky *tert*-butyl groups on the diimide combined with the lack of space within the carboxylic acid SAM preventing attack, (b) the sterically hindered nature of backside attack from the approaching alcohol directed towards the carbonyl group, and (c) the adsorption of alcohol contaminants due to hydrogen bonding between the carboxylic acid and the ethanol used in preparation of the monolayer.

Terminal carboxyl groups in monolayers can also be activated by treatment with carbodiimides such as dicyclohexylcarbodiimide (DCC) or 1-ethyl-3-(3-dimethylaminopropyl)carbodiimide (EDC) [15]. Alternatively, conversion to a mixed anhydride can be effected by reaction of a carboxyl-terminated film with ethyl chloroformate [64]. Exposure of the surface to gaseous $SOCl_2$ has been reported to produce carboxyl chloride groups [63, 75]. These activated acid derivatives then react smoothly with alcohols or amines to form esters or amides (Fig. 3.3).

Coster et al. have investigated immobilization of dendrimers on Si–C linked carboxylic acid-terminated monolayers on silicon(111) [76]. Poly(amidoamine) dendrimers were attached to activated undecanoic acid monolayers, covalently linked to smooth silicon surfaces via Si–C bonds. XPS results suggest amide bond formation between the dendrimer and the surface carboxylic acid groups.

3.2.6.3 Other Organic Reactions on SAMs

Studies have been carried out to investigate the similarities and differences between chemical reactions in solution (three-dimensional reactions) and

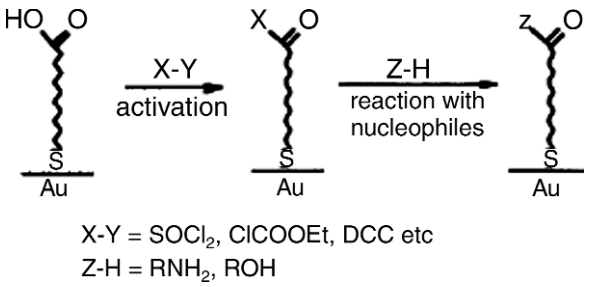

Fig. 3.3 Reaction of carboxyl-terminated SAM

interfacial surface chemical reactions (two-dimensional reactions). A variety of terminal functional groups and their chemical transformations on SAMs after their assembly have been examined [59, 60, 62, 63, 64, 65, 66, 67, 73, 77, 78, 79, 80, 81, 82, 83, 84, 85]. These studies have shown that many organic reactions that work well in solution are difficult to apply at surfaces because of steric hindrance. In such a hindered environment, backside reactions (e.g., S_N2 reaction) and reactions with large transition state (e.g., esterification, saponification, Diels–Alder reaction and others) often proceed slowly [17]. All these methodologies also use organic solvents and involve tedious multi-step protection deprotection chemistries [63, 86, 87, 88, 89].

Cooks and co-workers [90] have carried out studies on silylation of OH-terminated self-assembled monolayer surface through low-energy collisions of ions. Using a multi-sector ion–surface scattering mass spectrometer, reagent ions of the general form, SiR_3+ were made to collide with a hydroxy-terminated self-assembled monolayer (HO-SAM) surface at energies of nearly 15 eV. These ion–surface interactions resulted in covalent transformation of the terminal hydroxy groups at the surface into the corresponding silyl ethers due to Si–O bond formation. This result demonstrates that multi-step reactions can be performed at a surface through low-energy ionic collisions. Other gas phase methods have been reported for surface modification of SAMs, however, they do not provide the versatility and control over surface chemistry that chemical reaction provide, possibly due to vapor pressure requirements and the absence of catalysts [91, 92].

These studies show that the rules that govern chemical reactions in solution would be different from that at the interfaces. The intimate study of reactions and interactions within such films and with external reagents is sure to widen our understanding of the molecular behavior of such surfaces – an area that has not received sufficient attention for organic chemists.

3.3 Proposed Technology for Surface Reactions on SAMs

3.3.1 Biocatalysis on Surfaces

Relatively, very few reports exist on use of biocatalytic methodologies for carrying out surface modification of SAMs. Use of enzymes in organic synthesis [93] and polymer science [1] is well established and has been discussed elsewhere within comprehensive reviews. The rapidly increasing interest in in vitro enzyme-catalyzed organic and polymeric reactions has been due to the fact that several families of enzyme utilize and transform not only their natural substrates but also a wide range of unnatural compounds to yield a variety of useful products. Recent advances in non-aqueous enzymology have significantly expanded the potential conditions under which these reactions can be

performed. Use of enzyme for surface modification of SAMs on metal surfaces could offer distinct advantages such as (1) development of methodologies of attachment of organic moieties on SAMs after their assembly on metal surfaces, which due to steric hindrance are difficult to achieve via chemical means; (2) avoid multiple protection deprotection steps due to their high selectivity for a given organic transformation; (3) possibly, avoid the use of organic solvents by carrying out these reactions in bulk (solvent less), or aqueous medium; (4) use of mild reaction conditions (room temperature to 70°C) thus, ensuring structural integrity of the SAMs formed; and (5) reported selectivity of enzyme reactions may provide spatial and topographical ordering of the surface.

There are numerous reports of hydrolysis of lipid monolayers using different lipases [94, 95]. Relatively few reports demonstrate lipase catalyzed esterification synthesis on air/water monolayers [96, 97]. Specifically, Singh et al. have reported use of lipase lipozyme for the synthesis of glycerol and fatty acid on steric acid monolayers [96]. Singh et al. have also reported lipase-catalyzed synthesis esterification of oleic acid with glycerol in monolayers [97]. Turner et al. [98] have reported the hydrolysis of a phospholipid film which was covalently attached via chemical methods to a silica surface. However, the rigid structural ordering of the SAMs on the metal surface offers significant bulk steric hindrance which may not be the case in the flexible lipid and air/water monolayers as reported above. Breitinger's group have reported the phosporolytic synthesis of silica modified maltoheptaoside-alkoxysilane anchor molecules [99].

Enzymatic, surface-initiated polymerizations of aliphatic polyesters was reported for wider clinical use of aliphatic polyesters [100]. The hydroxyl-terminated SAM acted as an initiation site for lipase B catalyzed ROP of aliphatic polyesters, such as poly(ε-caprolactone) and poly(*p*-dioxanone) (Fig. 3.4). Another example of enzymatic SIP is the polymerization of poly(3-hydroxybutyrate) (PHB), where PHB synthase, fused with a His-tag at the N-terminus, was immobilized onto solid substrates through transition-metal complexes, Ni (II)-NTA, and the immobilized PHB synthase catalyzed the polymerization of 3-®-hydroxybutyryl-coenzyme A (3HB-CoA) to PHB [101]. Loos et al. have reported the surface-initiated polymerization of glucose-1-phosphate with potato phosphorylase as a catalyst on modified silica particles [102].

Recently, Mahapatro et al. demonstrated the surface modification of functional self-assembled monolayers on 316L stainless steel via lipase (Novozyme-435) catalysis (Fig. 3.5) [103]. SAMs of 16-mercaptohexadecanoic acid (–COOH SAM) and 11-mercapto-1-undecanol (–OHSAM) were formed on 316L SS, and lipase catalysis was used to attach therapeutic drugs – perphenazine and ibuprofen, respectively, on these SAMs. The reaction was carried out in toluene at 60°C for 5 h using Novozyme-435 as the biocatalyst. The FTIR, XPS and contact angle measurements collectively concluded biocatalytic surface modification of SAMs.

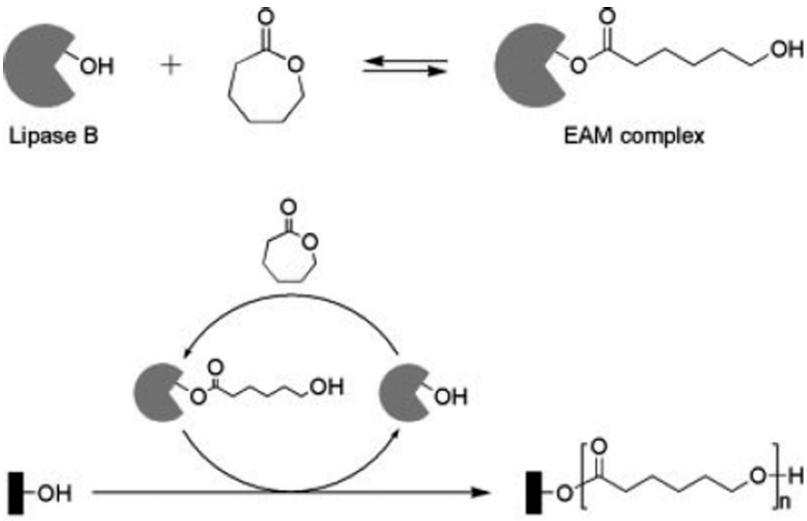

Fig. 3.4 Enzymatic surface-initiated polymerizations

Biocatalysis could thus provide a viable alternate methodology for surface modification of SAMs with inherent advantages of enzyme catalysis and it also provides the possibility to overcome some of the limitations of organic methodologies mentioned in previous sections. Much work needs to be carried out to evaluate the viability of biocatalytic techniques for use in interfacial reactions such as surface modification of SAMs.

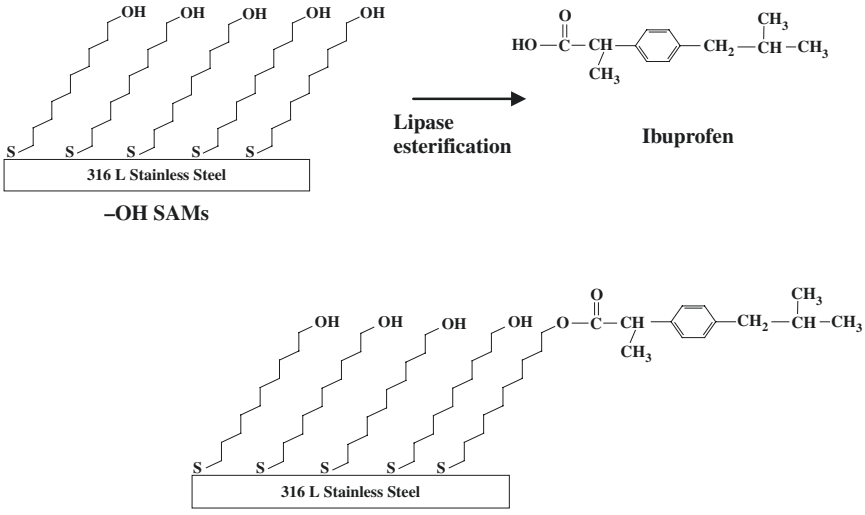

Fig. 3.5 Enzymatic modification of hydroxyl-terminated SAMs

3.4 Summary, Conclusion and Future Outlook

We reviewed some recent findings in the field of biosurface organic chemistry, by focusing on interfacial chemical reactions on self-assembled monolayers (SAMs). Although most type of organic reactions can be performed on SAMs, steric hindrance and diffusion barriers can hamper the yield or rate of reactions at the surface. Very limited reports exist on biocatalytic methodologies for surface modification reactions on SAMs. However, advantages of mild reaction conditions and other inherent advantages of biocatalytic techniques offer promise in this growing field of biosurface organic chemistry. The enforced positioning of functional groups in SAMs also has great potential for selective rate enhancement and inhibition, which may provide links to better understanding of enzymatic reactions.

Acknowledgments The authors would like to acknowledge the Center of Materials Research and the NIH Center of Biotechnology and Biomedical Science at Norfolk State University for its financial support.

References

1. Gross, R. A., Kumar, A., Kalra, B. Polymer synthesis by in vitro enzyme catalysis. Chemical Reviews. 2001, *101*(7), 2097–2124.
2. Clark, J. J., Macquarrie, D. J. Environmentally friendly catalytic methods. Chemical Society Reviews. 1996, *25*(5), 303–310.
3. Mirkin, C. A., Ratner, M. A. Molecular electronics. Annual Review of Physical Chemistry. 1992, *43*, 719–754.
4. Ricco, A. J., Crooks, R. M. Special issue on chemical sensors. Accounts of Chemical Research. 1998, *31*(5), 200.
5. Crooks, R. M., Ricco, A. J. New organic materials suitable for use in chemical sensor arrays. Accounts of Chemical Research. 1998, *31*(5), 219–227.
6. Ulman, A. Formation and structure of self-assembled monolayers. Chemical Reviews. 1996, *96*(4), 1533–1554.
7. Allara, D. L. Critical issues in applications of self-assembled monolayers. Biosensors & Bioelectronics. 1995, *10*(9/10), 771–783.
8. Mrksich, M. Using self-assembled monolayers to understand the biomaterials interface. Current Opinion in Colloid & Interface Science. 1997, *2*(1), 83–88.
9. Mrksich, M., Whitesides, G. M. Using self-assembled monolayers to understand the interactions of man-made surfaces with proteins and cells. Annual Review of Biophysics and Biomolecular Structure. 1996, *25*, 55–78.
10. Ulman, A., Editor, *Self-Assembled Monolayers of Thiols. In: Thin Films, Academic Press, San Diego*. 1998, *24*.
11. Love, J. C., Estroff, L. A., Kriebel, J. K., Nuzzo, R. G., Whitesides, G. M. Self-assembled monolayers of thiolates on metals as a form of nanotechnology. Chemical Reviews. 2005, *105*(4), 1103–1169.
12. Hostetler, M. J., Murray, R. W. Colloids and self-assembled monolayers. Current Opinion in Colloid & Interface Science. 1997, *2*(1), 42–50.

13. Becka, A. M., Miller, C. J. Electrochemistry at omega-hydroxy thiol coated electrodes. IV: Comparison of the double layer at omega-hydroxy thiol and alkanethiol monolayer coated Au electrodes. Journal of Physical Chemistry. 1993, *97*, 6233–6239.
14. Dorogi, M., Gomez, J., Osifchin, R., Andres, R. P., Reifenberger, R. Room-temperature Coulomb blockade from a self-assembled molecular nanostructure. Physical Review B.1995, *52*(12), 9071.
15. Duan, C., Meyerhoff, M. E. Immobilization of proteins on gold coated porous membranes via an activated self-assembled monolayer of thioctic acid. Mikrochimica Acta. 1995, *117*(3–4), 195–206.
16. Bain, C. D., Troughton, E. B., Tao, Y. T., Evall, J., Whitesides, G. M., Nuzzo, R. G. Formation of monolayer films by the spontaneous assembly of organic thiols from solution onto gold. Journal of the American Chemical Society. 1989, *111*(1), 321–335.
17. Yan, L., Huck, W. T. S., Whitesides, G. M. Self-assembled monolayers (SAMS) and synthesis of planar micro- and nanostructures. Journal of Macromolecular Science-Polymer Reviews. 2004, *C44*(2), 175–206.
18. Lopez, G. P., Biebuyck, H. A., Whitesides, G. M. Scanning electron microscopy can form images of patterns in self-assembled monolayers. Langmuir. 1993, *9*(6), 1513–1516.
19. Silin, V., Weetall, H., Vanderah, D. J. SPR studies of the nonspecific adsorption kinetics of human IgG and BSA on gold surfaces modified by Self-Assembled Monolayers (SAMs). Journal of Colloid and Interface Science. 1997, *185*(1), 94–103.
20. Tosatti, S., Michel, R., Textor, M., Spencer, N. D. Self-assembled monolayers of dodecyl and hydroxy-dodecyl phosphates on both smooth and rough titanium and titanium oxide surfaces. Langmuir. 2002, *18*(9), 3537–3548.
21. Ulman, A. *An Introduction to Ultra Thin Organic Films: from Langmuir-Blodgett to Self-Assembly*, Academic Press, London, 1991.
22. Bain, C. D., Evall, J., Whitesides, G. M. Formation of monolayers by the coadsorption of thiols on gold: variation in the head group, tail group, and solvent. Journal of the American Chemical Society. 1989, *111*(18), 7155–7164.
23. Tsao, M. W., Hoffmann, C. L., Rabolt, J. F., Johnson, H. E., Castner, D. G., Erdelen, C., Ringsdorf, H. Studies of molecular orientation and order in self-assembled semifluorinated n-alkanethiols: single and dual component mixtures. Langmuir. 1997, *13*(16), 4317–4322.
24. Chen, W., Fadeev, A. Y., Hsieh, M. C., Oener, D., Youngblood, J., McCarthy, T. J. Ultrahydrophobic and ultralyophobic surfaces: some comments and examples. Langmuir. 1999, *15*(10), 3395–3399.
25. Fadeev, A. Y., McCarthy, T. J. Self-assembly is not the only reaction possible between alkyltrichlorosilanes and surfaces: monomolecular and oligomeric covalently attached layers of dichloro- and trichloroalkylsilanes on silicon. Langmuir. 2000, *16*(18), 7268–7274.
26. Boozer, C., Chen, S., Jiang, S. Controlling DNA orientation on mixed ssDNA/OEG SAMs. Langmuir. 2006, *22*, 4694–4698.
27. Li, S., Cao, P., Colorado, R., Yan, X., Wenzl, I., Shmakova, O. E., Graupe, M., Lee, T. R., Perry, S. S. Local packing environment strongly influences the frictional properties of mixed CH_3- and CF_3-terminated alkanethiol SAMs on Au(111). Langmuir. 2005, *21*, 933–936.
28. Twardowski, M., Nuzzo, R. G. phase dependent electrochemical properties of polar self-assembled monolayers (SAMs) modified via the fusion of mixed phospholipid vesicles. Langmuir. 2004, *20*, 175–180.
29. Ma, F., Lennox, R. B. Potential-assisted deposition of alkanethiols on Au: controlled preparation of single- and mixed-component SAMs. Langmuir. 2000, *16*, 6188–6190.
30. Lahiri, J., Isaacs, L., Grzybowski, B., Carbeck, J. D., Whitesides, G. M. Biospecific binding of carbonic anhydrase to mixed SAMs presenting benzenesulfonamide ligands: a model system for studying lateral steric effects. Langmuir. 1999, *15*, 7186–7198.

31. Hoffmann, C., Tovar, G. E. M. Mixed self-assembled monolayers (SAMs) consisting of methoxy-tri(ethylene glycol)-terminated and alkyl-terminated dimethylchlorosilanes control the non-specific adsorption of proteins at oxidic surfaces. Journal of Colloid and Interface Science. 2006, *295*(2), 427–435.
32. Laibinis, P. E., Fox, M. A., Folkers, J. P., Whitesides, G. M. Comparisons of self-assembled monolayers on silver and gold: mixed monolayers derived from HS(CH2)21X and HS(CH2)10Y (X, Y = CH3, CH2OH) have similar properties. Langmuir. 1991, *7*, 3167–3173.
33. Ingram, R. S., Hostetler, M. J., Murray, R. W., Schaaff, T. G., Khoury, J., Whetten, R. L., Bigioni, T. P., Guthrie, D. K., First, P. N. 28 kDa alkanethiolate-protected Au clusters give analogous solution electrochemistry and STM Coulomb staircases. Journal of the American Chemical Society. 1997, *119*(39), 9279–9280.
34. Liley, M., Keller, T. A., Duschl, C., Vogel, H. Direct observation of self-assembled monolayers, ion complexation, and protein conformation at the gold/water interface: an FTIR spectroscopic approach. Langmuir. 1997, *13*(16), 4190–4192.
35. Meuse, C. W. Infrared spectroscopic ellipsometry of self-assembled monolayers. Langmuir. 2000, *16*(24), 9483–9487.
36. Sigal, G. B., Mrksich, M., Whitesides, G. M. Effect of surface wettability on the adsorption of proteins and detergents. Journal of the American Chemical Society. 1998, *120*(14), 3464–3473.
37. O'Brien, J. C., Stickney, J. T., Porter, M. D. Preparation and characterization of self-assembled double-stranded DNA (dsDNA) microarrays for protein: dsDNA screening using atomic force microscopy. Langmuir. 2000, *16*(24), 9559–9567.
38. Mrksich, M., Sigal, G. B., Whitesides, G. M. Surface plasmon resonance permits in situ measurement of protein adsorption on self-assembled monolayers of alkanethiolates on gold. Langmuir. 1995, *11*(11), 4383–4385.
39. Ruan, C. M., Bayer, T., Meth, S., Sukenik, C. N. Creation and characterization of n-alkylthiol and n-alkylamine self-assembled monolayers on 316L stainless steel. Thin Solid Films. 2002, *419*(1–2), 95–104.
40. Wasserman, S. R., Whitesides, G. M., Tidswell, I. M., Ocko, B. M., Pershan, P. S., Axe, J. D. The structure of self-assembled monolayers of alkylsiloxanes on silicon: a comparison of results from ellipsometry and low-angle x-ray reflectivity. Journal of the American Chemical Society. 1989, *111*(15), 5852–5861.
41. Dahint, R., Grunze, M., Josse, F., Renken, J. Acoustic plate mode sensor for immunochemical reactions. Analytical Chemistry. 1994, *66*(18), 2888–2892.
42. Petralli-Mallow, T. P., Plant, A. L., Lewis, M. L., Hicks, J. M. Cytochrome c at model membrane surfaces: exploration via second harmonic generation-circular dichroism and surface-enhanced resonance raman spectroscopy. Langmuir. 2000, *16*(14), 5960–5966.
43. Hook, F., Rodahl, M., Kasemo, B., Brzezinski, P. Structural changes in hemoglobin during adsorption to solid surfaces: effects of pH, ionic strength, and ligand binding. Proceedings of the National Academy of Sciences of the United States of America. 1998, *95*(21), 12271–12276.
44. Ostuni, E., Yan, L., Whitesides, G. M. The interaction of proteins and cells with self-assembled monolayers of alkanethiolates on gold and silver. Colloids and Surfaces, B: Biointerfaces. 1999, *15*(1), 3–30.
45. Chen, C. S., Mrksich, M., Huang, S., Whitesides, G. M., Ingber, D. E. Geometric control of cell life and death. Science (Washington, DC.). 1997, *276*(5317), 1425–1428.
46. Makohliso, S. A., Leonard, D., Giovangrandi, L., Mathieu, H. J., Ilegems, M., Aebischer, P. Surface characterization of a biochip prototype for cell-based biosensor applications. Langmuir. 1999, *15*(8), 2940–2946.
47. Genzer, J., Sivaniah, E., Kramer, E. J., Wang, J., Koerner, H., Char, K., Ober, C. K., DeKoven, B. M., Bubeck, R. A., Fischer, D. A., Sambasivan, S. Temperature

dependence of molecular orientation on the surfaces of semifluorinated polymer thin films. Langmuir. 2000, *16*(4), 1993–1997.
48. Butler, J. H., Cronin, M., Anderson, K. M., Biddison, G. M., Chatelain, F., Cummer, M., Davi, D. J., Fisher, L., Frauendorf, A. W., Frueh, F. W., Gjerstad, C., Harper, T. F., Kernahan, S. D., Long, D. Q., Pho, M., Walker, J. A., II, Brennan, T. M. In situ synthesis of oligonucleotide arrays by using surface tension. Journal of the American Chemical Society. 2001, *123*(37), 8887–8894.
49. Chechik, V., Crooks, R. M., Stirling, C. J. M. Reactions and reactivity in self-assembled monolayers. Advanced Materials. 2000, *12*, 1161–1171.
50. Sullivan, T. P., Huck, W. T. S. Reactions on Monolayers: Organic Synthesis in Two Dimensions. European Journal of Organic Chemistry. 2003, 17–29.
51. Chi, Y. S., Lee, J. K., Lee, K.-B., Kim, D. J., Choi, I. S. Biosurface organic chemistry: interfacial chemical reactions for applications to nanobiotechnology and biomedical sciences. Bulletin of the Korean Chemical Society. 2005, *26*(3), 361–370.
52. Chapman, R. G., Ostuni, E., Yan, L., Whitesides, G. M. Preparation of mixed self-assembled monolayers (SAMs) that resist adsorption of proteins using the reaction of amines with a SAM that presents interchain carboxylic anhydride groups. Langmuir. 2000, *16*(17), 6927–6936.
53. Maoz, R., Sagiv, J. Penetration-controlled reactions in organized monolayer assemblies. II: Aqueous permanganate interaction with self-assembling monolayers of long-chain surfactants. Langmuir. 1987, *3*(6), 1045–1051.
54. Maoz, R., Sagiv, J. Penetration-controlled reactions in organized monolayer assemblies. I: Aqueous permanganate interaction with monolayer and multilayer films of long-chain surfactants. Langmuir. 1987, *3*(6), 1034–1044.
55. Haller, I. Covalently attached organic monolayers on semiconductor surfaces. Journal of the American Chemical Society. 1978, *100*(26), 8050–8055.
56. Kurth, D. G., Bein, T. Monomolecular layers and thin films of silane coupling agents by vapor-phase adsorption on oxidized aluminum. Journal of Physical Chemistry. 1992, *96*(16), 6707–6712.
57. Kurth, D. G., Bein, T. Quantification of the reactivity of (3-aminopropyl)triethoxysilane monolayers with the quartz microbalance. Angewandte Chemie. 1992, *104*(3), 323–325 (See also Angew Chem, Int Ed Engl, 1992, 1931(1993), 1336–1998).
58. Kurth, D. G., Bein, T. Surface reactions on thin layers of silane coupling agents. Langmuir. 1993, *9*(11), 2965–2973.
59. Moon, J. H., Shin, J. W., Kim, S. Y., Park, J. W. Formation of uniform aminosilane thin layers: an imine formation to measure relative surface density of the amine group. Langmuir. 1996, *12*(20), 4621–4624.
60. Hutt, D. A., Leggett, G. J. Functionalization of hydroxyl and carboxylic acid terminated self-assembled monolayers. Langmuir. 1997, *13*(10), 2740–2748.
61. Persson, H. H. J., Caseri, W. R., Suter, U. W. Versatile method for chemical reactions with self-assembled monolayers of alkanethiols on gold. Langmuir. 2001, *17*(12), 3643–3650.
62. Ulman, A., Tillman, N. Self-assembling double-layers on gold surfaces – the merging of 2 chemistries. Langmuir. 1989, *5*(6), 1418–1420.
63. Duevel, R. V., Corn, R. M. Amide and ester surface attachment reactions for alkanethiol monolayers at gold surfaces as studied by polarization modulation fourier-transform infrared-spectroscopy. Analytical Chemistry. 1992, *64*(4), 337–342.
64. Wells, M., Crooks, R. M. Interactions between organized, surface-confined monolayers and vapor-phase probe molecules. X: Preparation and properties of chemically sensitive dendrimer surfaces. Journal of the American Chemical Society. 1996, *118*(16), 3988–3989.

65. Leggett, G. J., Roberts, C. J., Williams, P. M., Davies, M. C., Jackson, D. E., Tendler, S. J. B. Approaches to the immobilization of proteins at surfaces for analysis by scanning-tunneling-microscopy. Langmuir. 1993, *9*(9), 2356–2362.
66. Wang, J. H., Kenseth, J. R., Jones, V. W., Green, J. B. D., McDermott, M. T., Porter, M. D. SFM tip-assisted hydrolysis of a dithiobis(succinimidoundecanoate) monolayer chemisorbed on a Au(111) surface. Journal of the American Chemical Society. 1997, *119*(52), 12796–12799.
67. Horton, R. C., Herne, T. M., Myles, D. C. Aldehyde-terminated self-assembled monolayers on gold: immobilization of amines onto gold surfaces. Journal of the American Chemical Society. 1997, *119*(52), 12980–12981.
68. Pirrung, M. C., Davis, J. D., Odenbaugh, A. L. Novel reagents and procedures for immobilization of DNA on glass microchips for primer extension. Langmuir. 2000, *16*(5), 2185–2191.
69. Maskos, U., Southern, E. M. Oligonucleotide hybridizations on glass supports: a novel linker for oligonucleotide synthesis and hybridization properties of oligonucleotides synthesized in situ. Nucleic Acids Research. 1992, *20*(7), 1679–1684.
70. Luzinov, I., Julthongpiput, D., Liebmann-Vinson, A., Cregger, T., Foster, M. D., Tsukruk, V. V. Epoxy-terminated self-assembled monolayers: molecular glues for polymer layers. Langmuir. 2000, *16*(2), 504–516.
71. Kwok, C. S., Mourad, P. D., Crum, L. A., Ratner, B. D. Surface modification of polymers with self-assembled molecular structures: multitechnique surface characterization. Biomacromolecules. 2000, *1*(1), 139–148.
72. Bertilsson, L., Liedberg, B. Infrared study of thiol monolayer assemblies on gold: preparation, characterization, and functionalization of mixed monolayers. Langmuir. 1993, *9*(1), 141–149.
73. Himmel, H. J., Weiss, K., Jager, B., Dannenberger, O., Grunze, M., Woll, C. Ultrahigh vacuum study on the reactivity of organic surfaces terminated by OH and COOH groups prepared by self-assembly of functionalized alkanethiols on Au substrates. Langmuir. 1997, *13*(19), 4943–4947.
74. Alexander, M. R., Wright, P. V., Ratner, B. D. Trifluoroethanol derivatization of carboxylic acid-containing polymers for quantitative XPS analysis. Surface and Interface Analysis. 1996, *24*(3), 217–220.
75. Baker, M. V., Landau, J. Self-assembled alkanethiolate monolayers as thin insulating films. Australian Journal of Chemistry. 1995, *48*(6), 1201–1211.
76. Bocking, T., Wong, E. L. S., James, M., Watson, J. A., Brown, C. L., Chilcott, T. C., Barrow, K. D., Coster, H. G. L. Immobilization of dendrimers on Si-C linked carboxylic acid-terminated monolayers on silicon(111). Thin Solid Films. 2006, *515*(4), 1857–1863.
77. Sagiv, J. Organized monolayers by adsorption. 1. Formation and structure of oleophobic mixed monolayers on solid-surfaces. Journal of the American Chemical Society. 1980, *102*(1), 92–98.
78. Maoz, R., Sagiv, J. Penetration-controlled reactions in organized monolayer assemblies. 1. Aqueous permanganate interaction with monolayer and multilayer films of long-chain surfactants. Langmuir. 1987, *3*(6), 1034–1044.
79. Maoz, R., Sagiv, J. Penetration-controlled reactions in organized monolayer assemblies. 2. Aqueous permanganate interaction with self-assembling monolayers of long-chain surfactants. Langmuir. 1987, *3*(6), 1045–1051.
80. Kurth, D. G., Bein, T. Quantification of the reactivity of 3-aminopropyl-triethoxysilane monolayers with the quartz-crystal microbalance. Angewandte Chemie-International Edition in English. 1992, *31*(3), 336–338.
81. Kurth, D. G., Bein, T. Surface-reactions on thin-layers of silane coupling agents. Langmuir. 1993, *9*(11), 2965–2973.

82. Lofas, S., Johnsson, B. A novel hydrogel matrix on gold surfaces in surface-plasmon resonance sensors for fast and efficient covalent immobilization of ligands. Journal of the Chemical Society-Chemical Communications. 1990(21), 1526–1528.
83. Lee, Y. W., Reedmundell, J., Sukenik, C. N., Zull, J. E. Electrophilic siloxane-based self-assembled monolayers for thiol-mediated anchoring of peptides and proteins. Langmuir.1993, *9*(11), 3009–3014.
84. Kohli, P., Taylor, K. K., Harris, J. J., Blanchard, G. J. Assembly of covalently-coupled disulfide multilayers on gold. Journal of the American Chemical Society. 1998, *120*(46), 11962–11968.
85. Tillman, N., Ulman, A., Elman, J. F. Oxidation of a sulfide group in a self-assembled monolayer. Langmuir. 1989, *5*(4), 1020–1026.
86. Yan, L., Marzolin, C., Terfort, A., Whitesides, G. M. Formation and reaction of interchain carboxylic anhydride groups on self-assembled monolayers on gold. Langmuir.1997, *13*(25), 6704–6712.
87. Smith, E. A., Wanat, M. J., Cheng, Y. F., Barreira, S. V. P., Frutos, A. G., Corn, R. M. Formation, spectroscopic characterization, and application of sulfhydryl-terminated alkanethiol monolayers for the chemical attachment of DNA onto gold surfaces. Langmuir. 2001, *17*(8), 2502–2507.
88. Frutos, A. G., Brockman, J. M., Corn, R. M. Reversible protection and reactive patterning of amine- and hydroxyl-terminated self-assembled monolayers on gold surfaces for the fabrication of biopolymer arrays. Langmuir. 2000, *16*(5), 2192–2197.
89. Brockman, J. M., Frutos, A. G., Corn, R. M. A multistep chemical modification procedure to create DNA arrays on gold surfaces for the study of protein-DNA interactions with surface plasmon resonance imaging. Journal of the American Chemical Society. 1999, *121*(35), 8044–8051.
90. Wade, N., Evans, C., Jo, S., Cooks, R. G. Silylation of an OH-terminated self-assembled monolayer surface through low-energy collisions of ions: a novel route to synthesis and patterning of surfaces. Journal of Mass Spectrometry. 2002, *37*, 591–602.
91. Hu, J., Liu, Y. B., Khemtong, C., El Khoury, J. M., McAfoos, T. J., Taschner, I. S. Photochemical patterning of a self-assembled monolayer of 7-diazomethylcarbonyl-2,4,9-trithiaadmantane on gold films via wolff rearrangement. Langmuir. 2004, *20*, 4933–4938.
92. Wade, N., Gologan, B., Vincze, A., Cooks, R. G., Sullivan, D. M., Bruening, M. L. Esterification and ether formation at a hydroxyl-terminated self-assembled monolayer surface using low-energy collisions of polyatomic cations. Langmuir. 2002, *18*(12), 4799–4808.
93. Roberts, S. M. Preparative biotransformations. Journal of the Chemical Society-Perkin Transactions 1. 2001, *13*(13), 1475–1499.
94. Tanaka, K., Yu, H. Lipase activity on lipid/polymer binary monolayers: lateral diffusion-controlled enzyme kinetics. Langmuir. 2002, *18*(3), 797–804.
95. Laboda, H. M., Glick, J. M., Phillips, M. C. Influence of the structure of the lipid water interface on the activity of hepatic lipase. Biochemistry. 1988, *27*(7), 2313–2319.
96. Singh, C. P., Shah, D. O. Lipase-catalyzed esterification in monolayers and microemulsions. Colloids and Surfaces a-Physicochemical and Engineering Aspects. 1993, *77*(3), 219–224.
97. Singh, C. P., Skagerlind, P., Holmberg, K., Shah, D. O. A comparison between lipase-catalyzed esterification of oleic-acid with glycerol in monolayer and microemulsion systems. Journal of the American Oil Chemists Society. 1994, *71*(12), 1405–1409.
98. Turner, D. C., Peek, B. M., Wertz, T. E., Archibald, D. D., Geer, R. E., Gaber, B. P. Enzymatic modification of a chemisorbed lipid monolayer. Langmuir. 1996, *12*(18), 4411–4416.

99. Breitinger, H.-G. Synthesis of silica-bound amylose by phosphorolytic elongation of immobilised maltoheptaosyl hydrazides. Tetrahedron Letters. 2002, *43*(35), 6127–6131.
100. Yoon, K. R., Lee, K. B., Chi, Y. S., Yun, W. S., Joo, S. W., Choi, I. S. Surface-Initiated, enzymatic polymerization of biodegradable polyesters. Advanced Materials. 2003, *15*(24), 2063–2066.
101. Kim, Y.-R., Paik, H.-J., Ober Christopher, K., Coates Geoffrey, W., Batt Carl, A. Enzymatic surface-initiated polymerization: a novel approach for the in situ solid-phase synthesis of biocompatible polymer poly(3-hydroxybutyrate). Biomacromolecules. 2004, *5*(3), 889–894.
102. Loos, K., Braunmühl, V. V., Stadler, R., Landfester, R., Spiess, H. W. Saccharide modified silica particles by enzymatic grafting. Macromolecular Rapid Communications. 1997, *18*(10), 927–938.
103. Mahapatro, A., Johnson, D. M., Patel, D. N., Feldman, M. D., Ayon, A. A., Agrawal, C. M. Surface modification of functional self assembled monolayers (SAMs) on 316L Stainless Steel via lipase catalysis. Langmuir. 2006, *22*, 901–905.

Chapter 4
Enabling Simultaneous Reductions in Fuel Consumption, NO_x, and CO_2 via Modeling and Control of Residual-Affected Low Temperature Combustion

Greg Shaver

Abstract There are currently 200 million vehicles on the road in the United States alone, resulting in the consumption of 600 billion liters of fuel each year. With annual growth rates of vehicle sales and miles driven at 0.8 and 0.5%, respectively, our domestic challenges are no less than two-fold: increasing dependence on foreign sources of transportation fuel [1] and the release of significant amounts of greenhouse and smog-generating chemicals, including CO_2 and NO_x [2]. There is a solution – by integrating advanced internal combustion engines (ICEs) on hybrid powertrains there is a wonderful opportunity to realize a 50% reduction in fuel consumption by 2020 (Heywood et al. 2003). A significant step to meeting this goal will be the implementation and coordinated control of a number of exciting, evolving engine technologies: direct, multi-point fuel injection; flexible intake and exhaust valve actuation (i.e., variable valve actuation (VVA)); real-time, production-viable in-cylinder sensing/estimation; cooled exhaust gas recirculation (EGR), and dual-stage variable geometry turbocharging. Exploring the most capable and cost-effective mix of these technologies is a key challenge in the ongoing effort to deliver the most effective engines to end-users (both individuals and industry). One particularly promising approach leveraging these advances, residual-affected low temperature combustion (LTC), exhibits a substantial increase in efficiency by 10–15% compared to spark-ignition (SI), and has NO_x and soot levels that are dramatically lower than either diesel or SI. However, to date LTC has been difficult to practically implement because it has no specific initiator of combustion and is subject to cyclic coupling through the temperature of reinducted or trapped combustion gases. This chapter details the merits and history of residual-affected LTC, and the approaches being pursued in academia and industry to meet the aforementioned hurdles to practical on-road implementation.

G. Shaver
School of Mechanical Engineering, Herrick Laboratories and Energy Center at Discovery Park, Purdue University, West Lafayette, IN 47907, USA
e-mail: gshaver@purdue.edu

V. Shah (ed.), *Emerging Environmental Technologies*,

Keywords Clean combustion · HCCI · model-based control · efficiency · IC engines

4.1 Motivation and Context

4.1.1 Societal Impact of Advanced Internal Combustion Engine Methodologies

According to the 2006 Department of Energy (DOE) Annual Energy Outlook [1] a ~50% increase in transportation demand is expected by the year 2030 (Fig. 4.1). Because the vast majority of transportation fuels are hydrocarbons (or have processing which require hydrocarbon combustion), the demand increase corresponds to a ~50% increase in the transportation-related release of CO_2, a global warming gas, into our atmosphere. Of added concern is the United States' growing dependence on foreign sources of transportation fuels. By 2030, the U.S. demand for transportation fuel is expected to exceed 26 million barrels per day, a 25% increase over the current demand (Fig. 4.2). With domestic sources already flatlined at 10 million barrels per day, 60% of our transportation fuel will come from foreign sources by 2030. There is a solution. Through the incorporation of advanced internal combustion engines (ICEs) on hybrid powertrains, aggressive reductions in fuel consumption and emissions can be realized in a cost-effective approach. As an example of this point, Heywood et al. [2] argue that aggressively pursued hybrid drivetrain technologies will allow fuel consumption reduction to about 56% of what is expected in 2020 as a result of normal evolution of vehicle technology. Heywood et al. also argue that

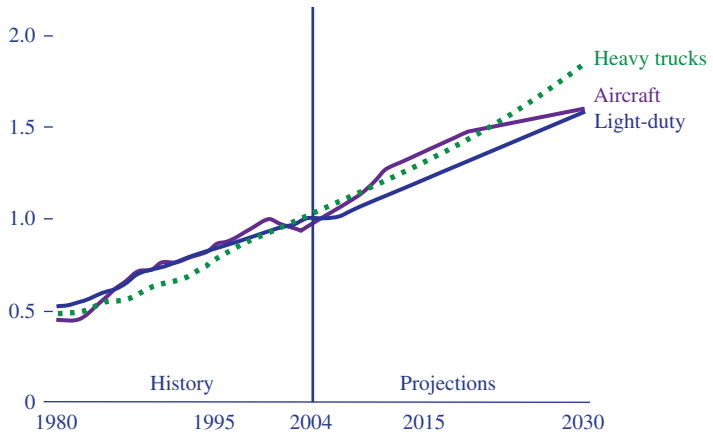

Fig. 4.1 Transportation travel demand by mode. index, 2004 = 1
Source: DOE 2006 annual energy outlook [1]

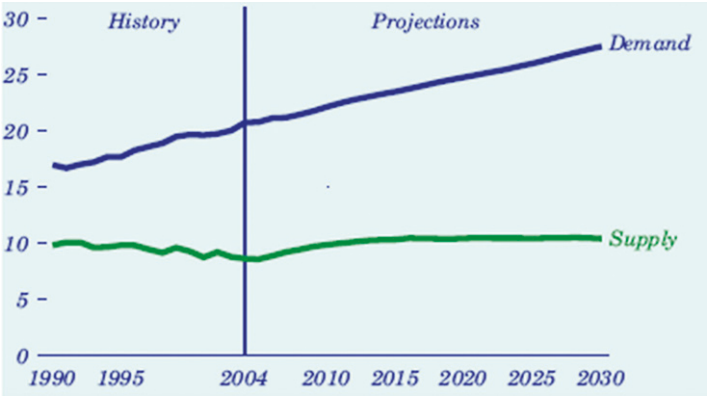

Fig. 4.2 U.S. petroleum product demand and supply (millions of barrels per day) Source: DOE 2006 annual energy outlook [1]

> Considering the uncertainties of long-range predictions and judging solely by lowest life-cycle energy use and greenhouse (GHG) releases, there is no current basis for preferring either fuel cell (FC) or ICE hybrid power plants for mid-size automobiles over the next 20 years or so using fuels derived from petroleum or natural gas. That conclusion applies even with optimistic assumptions about the pace of future FC development. Hybrid vehicles are superior to their nonhybrid counterparts and their advantages are greater for ICE than for FC designs.

In other words, advanced hybrid powertrains incorporating ICEs are expected to be competitive with FC vehicles in 2020, and beyond, even with optimal advancements assumed for FC and hydrogen processing technologies. In all cases, these predictions assume aggressive technological advances in electric drivetrain components, the ICE and the coordinated design, control and manufacture of the drivetrain. Substantial improvements in ICEs are also required and are possible [3]:

> . . . historical trends showing the ratio of gasoline engine power to displaced volume determined by Chon and Heywood [4] show a nearly linear improvement of about 0.5% per year. Future technological improvements such as increasing use of variable valve timing, gasoline direct-injection, improved turbocharger performance for diesels, and reduced engine friction, are expected to continue this trend. Hence for 2020, the wide-open-throttle (WOT) torque for these engines is increased by 10% overall.

In other words, novel combustion strategies, including low temperature combustion (LTC), yield promise for cleaner and more efficient powertrains.

4.1.2 Opportunities for Leveraging Novel ICE Technologies

Residual-affected LTC and other novel combustion strategies represent significant advances for ICEs. As noted in Section 4.1.1, hybrid powertrains

incorporating these advanced combustion approaches represent the greatest promise for simultaneously reducing fuel consumption and environmentally harmful exhaust emissions. These novel combustion strategies are enabled by advanced actuation, sensing and control, specifically

- direct, multi-point fuel injection
- flexible intake and exhaust valve actuation (i.e., variable valve actuation (VVA))
- real-time, in-cylinder sensing/estimation
- real-time feedback control

Here the goal is the in-cylinder reduction of greenhouse gases with simultaneous increases in efficiency. In order to develop these strategies the physics of these new combustion strategies and their dynamic coupling with other components on the drivetrain must be well understood. This requires the development and implementation of strategies for the modeling and control of novel combustion strategies, including one particularly promising strategy, residual-affected LTC, an approach for increasing efficiency and reducing NO_x emissions in ICEs.

4.1.3 Low Temperature Combustion (LTC)

4.1.3.1 Process and Benefits

LTC exhibits improvements in efficiency of up to 15–20% compared to a conventional spark ignited (SI) engines, making LTC efficiencies comparable to diesel engines. LTC strategies essentially reduce the in-cylinder, post combustion temperature by 'homogenizing' the combustion event, leading to 'flameless' combustion. This can be achieved by the compression-induced combustion of a well-mixed reactant (i.e., fuel and air) and residual (i.e., combustion products) mixture. This LTC approach (combustion homogenization via compression-induced autoignition of a well-mixed reactant/residual "charge") is often referred to as "premixed charge compression ignition" (PCCI) or "homogenous charge compression ignition" (HCCI). The resulting reduction in the peak combustion temperature leads to dramatically lower NO_x levels (in fact, to levels which typically require advanced aftertreatment solutions) compared to conventional SI and diesel strategies. Unlike diesel combustion, the lack of fuel rich regions in LTC results in little or no particulate emissions, a common issue with diesel strategies. One effective strategy for achieving LTC is through the reinduction or trapping of residual exhaust gas via VVA. This methodology of using residual gas is called residual-affected LTC. The key processes in residual-affected LTC are depicted in Fig. 4.3.

Residual-affected LTC (referred to as just LTC in the rest of the chapter) via exhaust reinduction is achieved by using flexible VVA to hold the intake and

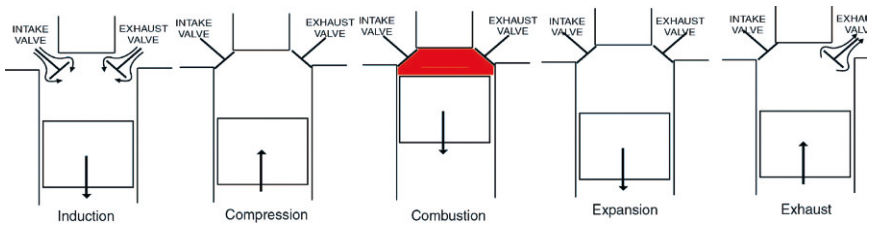

Fig. 4.3 Key processes in residual-affected LTC

exhaust valves open during a portion of the intake stroke. This leads to the induction of both air and residual (previously exhausted combustion product) gases from the intake and exhaust manifolds, respectively. Fuel is either introduced into the intake manifold area prior to induction or via early in-cylinder injection to assure that it is well mixed with the air and residual prior to combustion. Residual-affected LTC can also be achieved by retaining some exhaust gas in the cylinder by closing the exhaust valve early during the exhaust stroke. Again, this is made possible with a flexible valve system. The specific amounts of air and residual, as well as the amount of compression (via final valve closure), are varied through modulation of the intake and exhaust valves. Following the induction process, the compression of the reactant/residual mixture results in increase of both the in-cylinder mixture concentrations and temperature. If the reactant concentration and temperature reach sufficient levels, a uniform autoignition process occurs. A key characteristic of the autoignition process is that there is no direct trigger for its initiation. In the conventional SI and diesel strategies, the onset of the combustion event is triggered with the application of a spark or fuel injection, respectively. However, in LTC the combustion process has no direct combustion initiator. If autoignition occurs, the conversion of reactants to combustion products during the combustion event elevates the in-cylinder gas pressure and temperature. During the expansion stroke this elevated pressure is used to effectively push the piston, resulting in the extraction of useful work. The exhaust stroke then expels the hot combustion products into the exhaust manifold. Unlike conventional strategies, a portion of the exhausted gas is then reinducted or trapped for use during the subsequent engine cycle. It is this reinduction/trapping process that couples engine cycles through the exhaust gas temperature.

Despite its efficiency and emissions benefits, LTC exhibits some fundamental challenges which must be addressed prior to the production-viable implementation of the process.

4.1.3.2 LTC Challenges

No Direct Initiator of Combustion

As noted previously, residual-affected LTC has no specific initiator of combustion. Ensuring that combustion occurs with acceptable timing, or at all, is more

complicated than in the case of either SI or diesel combustion. Combustion timing in LTC is dominated by chemical kinetics, which depends on the in-cylinder concentrations of reactants and products, their temperature and the amount of compression.

Cycle-to-Cycle Coupling

Subsequent engine cycles are coupled through the residual temperature. Because the inducted reactant gas is heated by the residual, the residual temperature from an engine cycle directly affects the chemical kinetic-dominated combustion event on the subsequent cycle. The cyclic coupling plays a fundamental role in steady-state operation, operating point changes and mode transitions. If care is not taken combustion timing becomes unstable, leading to misfire, an unacceptable condition.

Dilution Limit

During LTC, the reactants (fuel and air) are diluted with either residual gas or air. This dilution decreases the amount of work that can be extracted for a given engine geometry. For these reasons, practical LTC will be accompanied with either conventional SI or diesel strategies in a multi-mode engine. At high load conditions the engine will run in the conventional mode. At low to moderate load conditions the engine will run in LTC mode. A key issue is the transition from the conventional mode to LTC. For residual-affected strategies, cyclic coupling exists during transitions into the LTC mode. In fact, due to the higher exhaust temperatures associated with the conventional modes, the dynamics of a mode transition into LTC are even more dramatic than intra-LTC operating point changes.

Cylinder-to-Cylinder Coupling

Coupling between engine cylinders also exists through the residual temperature, as combustion gas exhausted from one cylinder may be reinducted by a neighboring cylinder. Additionally, the presence of neighboring cylinder heat transfer will become important. A strategy for controlling multi-cylinder LTC engines will have to include these cylinder-coupling effects.

Achieving High Levels of Fuel–Air–Residual Mixing – Fuel Premixing or Early Injection?

In order to achieve a well-mixed fuel–air–residual mixture, the fuel must be either premixed with the air prior to induction through the intake valve or be injected into the cylinder early. Both approaches present challenges. Premixing in the intake can be achieved successfully with an atomizer [5]. Unfortunately, this can add expense and complexity. Early injection using injectors designed for conventional injection (i.e., when the piston is near top dead center) often leads to wall wetting, which increases consumption and soot emissions.

Vigor of Combustion Process

Due to the vigor of the autoignition event, LTC is notably noisier than either of the conventional IC methodologies. While the uniform nature of the combustion event reduces the peak in-cylinder temperature, and therefore NO_x, the rapid rise in in-cylinder pressure elevates the combustion-induced noise. This necessitates closed-loop control of the combustion timing and evolution to achieve reductions in the rate of pressure rise.

Solution: Control of the LTC Process

To practically implement residual-affected LTC, closed-loop control must be used to address the aforementioned challenges.

4.2 Modeling and Control of LTC

4.2.1 History of LTC

The application of LTC to ICEs has been studied since 1979 when it was concurrently applied to two-stroke engines by Onishi et al. [6] and Noguchi et al. [7] through use of hot residual gas retained in the cylinder. Since then a large number of studies of LTC from an experimental and modeling point of view have been completed. More recently, control of the process has become another focus of the research community.

In the very earliest experimental work of Onishi et al., several key characteristics of residual-affected LTC were identified, including the importance of achieving necessary levels of hot residual to achieve autoignition, uniform mixing between residual and reactant, and repeatable presence of residual gases on a cycle-to-cycle basis. In both Onishi et al. and Noguchi et al., the improvements in efficiency and emissions reduction were identified. The work of Najt and Foster 1983 [8] outlines the first use of LTC in a 4-stroke engine and outlines a physical explanation of the process utilizing a simple single-zone model of the process. Building on the work of Najt and Foster, Thring [9] examined the use of a gasoline fuel in an LTC engine. In these early works, it was observed that LTC exhibits some fundamental challenges, including a part-load limitation and lack of a direct combustion initiator.

4.2.2 Approaches to Modeling LTC

To understand LTC, the dependence of the combustion process on gas exchange through the intake and exhaust valves, composition of inducted

gases, level of mixedness and heat transfer must be well understood. The development and validation of models facilitates this understanding. A wide variety of modeling approaches have been considered, including from least to most complex:

1. zero-dimensional thermo-kinetic
2. quasi-dimensional thermo-kinetic
3. segregated, sequential fluid mechanics – thermo-kinetic multi-zone approaches
4. multi-dimensional fluid mechanics with coupled kinetics

Each approach presents its own set of advantages and disadvantages. The implementation of one approach over another depends on the aim of the user.

4.2.2.1 Zero-Dimensional Thermo-Kinetic Models

Models of this type utilize a single-zone approach to modeling the in-cylinder gases. There are a large number of efforts in this area [10, 11, 12, 13, 14, 15, 16, 17, 18, 19, 20, 21]. The first law of thermodynamics is applied to a homogeneous mixture of in-cylinder gases. The effects of the fluid mechanics are not directly considered except, in some cases, when deriving relevant heat transfer coefficients. The composition of the gases are either determined with standard valve flow relations or through approximation from steady-state experiment. In this approach, the largest computational cost is associated with the chemical kinetics model, which can vary from a very simple temperature threshold to detailed kinetics utilizing thousands of rate equations. The benefits of the zero-dimensional approach follow from the homogeneity assumption of the in-cylinder gases, resulting in a dramatic reduction in complexity and computational costs relative to more complex modeling approaches. Zero-dimensional thermo-kinetic models can capture LTC engine outputs, including work output, combustion timing and peak in-cylinder pressures. However, due to the homogeneity assumption, near wall/piston quenching effects are difficult to capture, leading to inaccuracies predicting emissions and completeness of combustion. Additionally, these approaches cannot capture the mixing process during induction.

4.2.2.2 Quasi-Dimensional Thermo-Kinetic Models

This modeling approach [22, 23, 24, 25] builds on the zero-dimensional modeling approach by considering multiple zones in the cylinder. By using this methodology the effects of temperature stratification and near wall/crevice quenching can be considered. This leads to improvements in emissions prediction compared to the zero-dimensional approaches, albeit at the expense of added modeling complexity and computation.

4.2.2.3 Segregated, Sequential Fluid Mechanical – Thermo-Kinetic Multi-Zone Approaches

These approaches [26, 27] attempt to more tightly couple the mixing process prior to combustion and the chemical kinetics of the autoignition process. The distribution of reactant and diluting gas is modeled with a fluid mechanics solver. Prior to the combustion event the gases are sequestered into a number of zones. The combustion process is then carried out by using a multi-zone combustion approach like that used in the quasi-dimensional models. This approach allows the mixing process during induction to be modeled, so that the effects of inhomogeneity on the autoignition process can be explicitly captured.

4.2.2.4 Multi-Dimensional Fluid Mechanics with Coupled Kinetics

In this approach [28, 29, 30, 31, 32, 33], by far the most complex and computationally intensive, an attempt is made to completely couple the fluid mechanics and chemical kinetics in three dimensions. In this case, the fluid mechanics and chemical kinetics solvers are run in parallel so that the effect of the combustion process on the fluid motion, and vice versa, can be explicitly captured. This approach allows more accurate representation of composition and temperature inhomogeneities, in some cases leading to more accurate predictions of NO_x and soot formation.

As outlined previously, the last 10 years has seen substantial progress in LTC modeling. With a variety of approaches a large number of important engine characteristics have been captured, including combustion timing, peak in-cylinder pressure, work output, maximum rate of pressure rise, exhaust gas temperature, emissions and extent of combustion. The dynamic cycle-to-cycle coupling via exhaust gas temperature that exists with residual-affected LTC strategies has also been recently captured for the first time in a modeling strategy [34, 35]. For residual-affected LTC this coupling plays a fundamental role in steady-state operation, during operating point changes, and across SI-to-LTC (or diesel-to-LTC) mode transitions. The dynamic nature of the cycle-to-cycle coupling also has critical implications for controlling the process, because the control inputs depend not only on the desired engine behavior for the current engine cycle, but also on what occurred during the previous cycle.

4.2.3 Approaches to Control of LTC

4.2.3.1 Control Strategies Derived from "Black-Box" or "Data-Driven" Models

In a number of experimentally validated studies, closed-loop control has been utilized to fix combustion timing. Several approaches have been demonstrated [36, 37, 38, 39]. Agrell et al. [36] used valve timings to effectively alter the

compression ratio and control combustion timing. Olsson et al. [38] modulated the fuel amount to vary the work output while altering the mixture ratio of two fuels to control combustion timing –a timing control strategy also adopted by Bengtsson et al. [39]. Haraldsson et al. [37] took a similar approach but used compression ratio instead of fuel mixture to shift combustion timing. These studies indicate the usefulness of effective compression ratio and inducted gas composition as control inputs for LTC.

4.2.3.2 Control Strategies Derived from Physics-Based Models

Each of these authors either used tuned controllers or synthesized a strategy from a black-box model. Recent contributions [40, 41, 42, 43, 44] have also demonstrated that LTC controllers can also be synthesized using physics-based approaches. A physics-based control approach allows for a fundamental understanding of how control inputs affect the dynamics of the LTC process. Furthermore, the approach is easily generalizable to other LTC engines because model parameters are directly based on physical quantities, such as the cylinder geometry, fuel used, cylinder/manifold orientation, etc. What follows is an example of how "simulation models" and control design-amenable "control models" can be developed, validated and utilized for generalizable physics-based LTC control.

4.3 Examples of Physics-Based LTC Control

4.3.1 Status and Merits of Physics-Based LTC Modeling and Control

While LTC is a complex physical process, the aspects most relevant for control – in-cylinder pressure evolution, combustion timing, work output, cycle-to-cycle dynamics, and cylinder-to-cylinder coupling – can be captured with accurate, intuitive, physics-based simulation and control models [34, 45, 46]. From physics-based control models, a variety of novel control strategies are possible. For example, Shaver et al. [41, 42] developed a controller that has been implemented on a single-cylinder engine testbed to successfully track desired work output, in-cylinder peak pressure and combustion timing during constant engine speed operation via modulation of two control inputs, inducted gas composition and effective compression ratio. These efforts will be outlined below. The focus of future work must address the relaxation of the single-cylinder, constant speed conditions, such that the physics-based approach applies more generally to the following additional conditions and configurations:

- multi-cylinder configuration
- variable engine speed operation

- utilization of cylinder-independent, cycle-to-cycle modulation of reactant gas equivalence ratio (i.e., the amount of fuel), a key next step in the practical implementation of LTC.

4.3.2 Leveraging LTC "Simulation Models" for Control Design

In [34, 35, 47, 48], the author and colleagues formulated a single-cylinder 10-state simulation model which predicts the effects of the VVA system on the LTC combustion process during constant engine speed. A single-zone model of the in-cylinder gases captures the compression, combustion initiation, energy release and expansion processes. An integrated Arrhenius rate describes the dependence of combustion timing on reactant concentration, temperature, and amount of compression. The in-cylinder dynamics are coupled with a single-zone model of the exhaust manifold gases to predict the cycle-to-cycle coupling through the exhaust gas temperature resulting in the first model of LTC capable of capturing the cyclic coupling. The resulting model agrees with experimental values of inlet reactant flow rate, combustion timing, in-cylinder pressure evolution, work output and exhaust gas temperature during steady-state operation. The dynamics of operating point change and mode-transition dynamics are also captured – another first in LTC research. The simulation model provides valuable insights for the formulation of control strategies – inducted gas composition can be varied via modulation of the valves, residual-affected LTC exhibits a self-stabilizing behavior due to the competing influences of mixture temperature and reactant concentration, and cyclic coupling is inherent to the process and must be included. Furthermore, given its physically oriented formulation it should be extendable to other conditions, including dynamic wall temperature conditions [49] and multi-cylinder, variable engine speed operation. Additionally, the simulation model has provided an excellent virtual testbed for analyzing feedback control strategies.

4.3.3 Physics-Based "Control Models" for LTC

Using insights gained from the simulation modeling effort, the author and colleagues developed a reduced-order nonlinear control-oriented model [40, 41, 42, 50] with inducted gas composition and effective compression ratio as inputs and peak pressure and combustion timing as outputs. This was achieved by discretizing, as shown in Fig. 4.4, the LTC process into six distinct stages: induction, compression, combustion, expansion, exhaust, and residence in the exhaust manifold. Pictorially, the inputs and outputs of the control model are shown in Fig. 4.5.

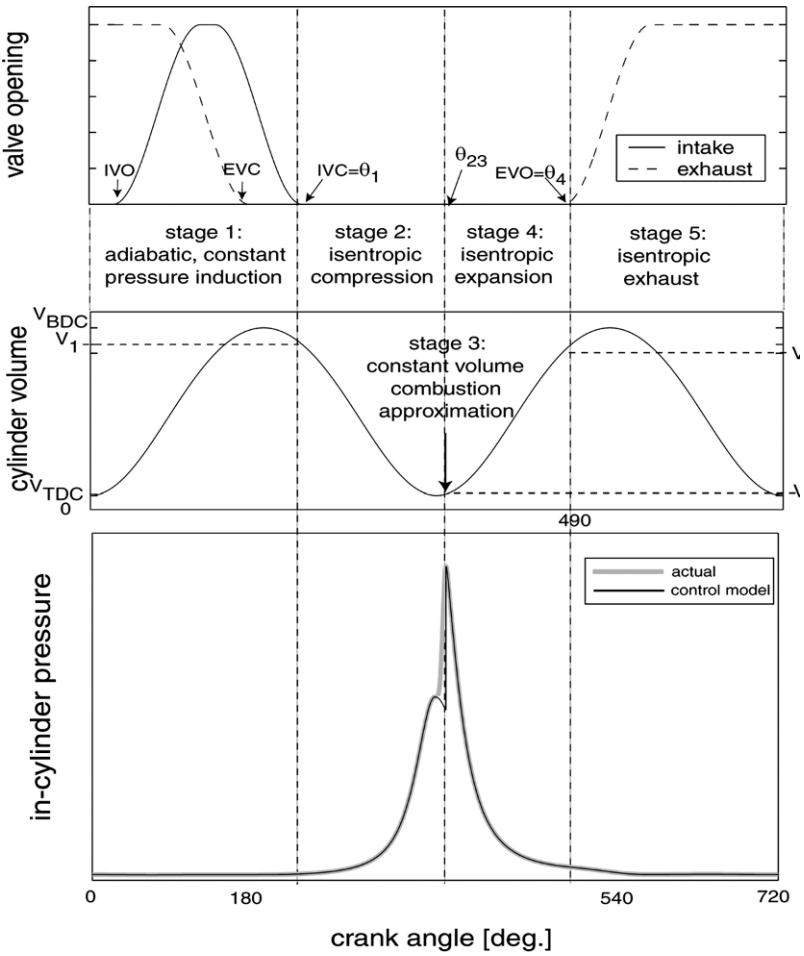

Fig. 4.4 Discretization of in-cylinder LTC processes

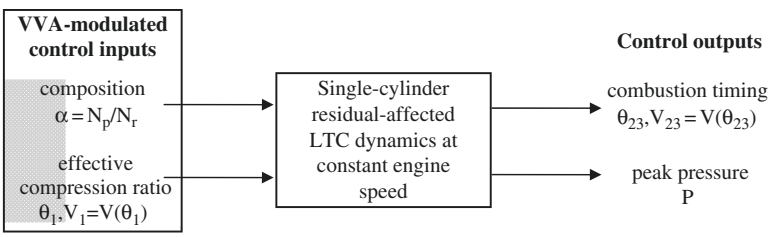

Fig. 4.5 Previously developed control model structure

The first model input is the inducted gas composition, which is formulated as the ratio of moles of reinducted product (i.e., previously exhausted combustion gas) to moles of inducted reactant charge (i.e., fuel and air), denoted α. The second model input is the final valve closure, which dictates the volume, $V_1 = V(\theta_1)$, at the start of compression and therefore the effective compression ratio. Model outputs are the peak pressure, P, and the volume at the onset of combustion, $V_{23} = V(\theta_{23})$, which acts as a proxy for combustion timing. By linking the thermodynamic states of the system together, a dynamic model of peak pressure, P, and phasing, θ_{23}, for residual-affected LTC is formulated. Here the modeling techniques are applied to propane-fueled LTC. The model will also apply to other fuels by making appropriate changes to the fuel-specific model constants (in particular the lower heating value). The LTC control model dynamics for single-cylinder, constant engine speed operation have the following mathematical form:

$$
\begin{aligned}
P_\kappa &= \frac{\left((1-\varepsilon)LHV_{C_3H_8} + c_v \frac{V_{1,\kappa}^{\gamma-1}}{V_{23,\kappa}^{\gamma-1}} T_{in}\right)(1+\alpha_{\kappa-1})\left(P_{\kappa-1} - \frac{V_{1,\kappa-1}^{\gamma}}{V_{23,\kappa-1}^{\gamma}}\right)\frac{V_{1,\kappa}}{V_{23,\kappa}} + \chi\alpha_\kappa(1-\varepsilon)LHV_{C_3H_8}\frac{V_{1,\kappa}^{\gamma}}{V_{23,\kappa}^{\gamma}}P_{\kappa-1}^{1/\gamma}}{c_v T_{in}(1+\alpha_{\kappa-1})\left(xP_{\kappa-1} - \frac{V_{1,\kappa-1}^{\gamma}}{V_{23,\kappa-1}^{\gamma}}\right) + \chi\alpha_\kappa(1-\varepsilon)LHV_{C_3H_8}P_{\kappa-1}^{1/\gamma}} \\
&= f_1(states; inputes) \\
&= f_1(P_{\kappa-1}, \theta_{23,\kappa}, \theta_{23,\kappa-1}; \alpha_\kappa, \alpha_{\kappa-1}, \theta_{1,\kappa}, \theta_{1,\kappa-1})
\end{aligned}
\tag{4.1}
$$

Here the subscript k and k–1 denote the variable value at the current and previous engine cycles, respectively. Other parameters include

- c_v – average constant volume specific heat for the reactant and residual gases
- T_{in} – temperature of the incoming reactant gas, assumed constant
- LHV_{C3H8} – lower heating value of propane for a given number of moles of reactant (a measure of the amount of energy released during combustion), constant assuming a fixed equivalence ratio ϕ
- ε, χ – constants related to in-cylinder and exhaust manifold heat transfer
- γ – specific heat ratio

The presence of cycle-to-cycle dynamics is evident by inspection of Eq. 4.1, as the current peak pressure P_k depends on the previous cycle peak pressure P_{k-1} and combustion timing $\theta_{23,k-1}$. This is a very powerful expression as it relates a desired model output, the peak pressure, to the model inputs, the molar ratio of the reinducted products and reactants, α, and the final valve closure timing $\theta_{1,k}$ (via $V_{k,1}$). Additionally, note the dependence on the combustion timing (represented by the combustion volume, V_{23}). What is now required is a physics-based expression for the combustion timing.

By using a simplified version of the integrated Arrhenius rate used in the simulation model, a nonlinear dynamic model of the following form can be derived for the combustion timing:

$$\theta_{23,\kappa} = \frac{C_1 \left(\frac{c_v T_i (1+\alpha_{\kappa-1}) P_{\kappa-1} - \frac{V_{1,\kappa-1}}{V_{23,\kappa-1}}^{\gamma} + \chi \alpha_\kappa P_{\kappa-1}^{1/\gamma} c3}{c_v V_{1,\kappa} P_{\kappa-1} - \frac{V_{1,\kappa-1}}{V_{23,\kappa-1}}^{\gamma} (1+\alpha_{\kappa-1})} \right)^{a+b}}{exp\left[\frac{-E_a}{R} \frac{c_v P_{\kappa-1} - \frac{V_{1,\kappa-1}}{V_{23,\kappa-1}}^{\gamma} (1+\alpha_{\kappa-1})(1+\alpha_\kappa)}{c_v T_i (1+\alpha_{\kappa-1}) P_{\kappa-1} - \frac{V_{1,\kappa-1}}{V_{23,\kappa-1}}^{\gamma} + \chi \alpha_\kappa P_{\kappa-1}^{1/\gamma} c3} \left(\frac{V_{TDC}}{V_{1,\kappa}} \right)^{\gamma-1} \right]} + \Delta\theta + \theta_{TDC} \qquad (4.2)$$

such that

$$\begin{aligned} \theta_{23,\kappa} &= f_2(\text{system states; system inputs}) \\ &= f_2(P_{\kappa-1}, \theta_{23,\kappa-1}; \alpha_\kappa, V_{1,\kappa}, \alpha_{\kappa-1}, V_{1,\kappa-1}) \end{aligned}$$

The constant C_1 is a linear function of the engine speed and inversely dependent on the equivalence ratio ϕ (again, a metric for the amount of fuel per unit amount of air). Together, the dynamic equations (Eqs. 4.1 and 4.2) for peak pressure and combustion timing complete the physics-based control model of residual-affected LTC under single-cylinder constant engine speed conditions. Like the simulation model, the control model's physically oriented formulation is extendable to other conditions, including residual trapping [51] and multi-cylinder, variable engine speed operation.

Once formulated, the control model was validated against both experimental data and the more complex simulation model during both steady-state and transient operating conditions. The control model was then used as a launching point for the development of the several physics-based control strategies, resulting in the first generalizable, validated, and experimentally implemented control approach for residual-affected LTC engines.

4.3.4 Synthesis and Implementation of Controllers from Control Models

By using the control model described in Section 4.3.3, the author and colleagues developed the very first physics-based, experimentally validated control strategy for LTC [40]. This approach relies on the ability to vary the inducted gas composition with the VVA system and the existence of an operating manifold with nearly constant combustion timing. Specifically, the control model was used to synthesize a strategy capable of cycle-to-cycle control of peak pressure through modulation of the inducted gas composition. Here a linear control law was synthesized from a linearized version of the nonlinear peak pressure dynamics. The self-stabilizing nature of the process is used to maintain nearly constant combustion timing without direct control of the timing. The stability of this linear controller, in closed-loop with the full nonlinear peak pressure dynamics, was formulated in [52]. In this work, a Lyapunov-based analysis utilizing sum of squares decomposition and a theorem from real algebraic

geometry, the Positivstellensatz, is used to estimate the domain of attraction for the nonlinear system with the linear control law. The resulting region of attraction proves stability of the system over the desired portion of the state space. Physically, this means that the linear control stabilizes the nonlinear system over the desired operating range of LTC.

In [41, 43], the author and colleagues examined a natural next step, the simultaneous control of peak pressure and combustion timing. The approach outlined here approximately decouples the cycle-to-cycle dynamics of combustion timing and peak in-cylinder pressure by controlling them on separate time scales with different control inputs (inducted composition and effective compression ratio, respectively). A physics-based $H2$ framework is used to determine a linear control law. Timing controller gains are selected via pole placement to achieve a response time that is slightly slower than the pressure controller.

An even more capable physics-based LTC control strategy [42, 50] outlines a strategy for the simultaneous, coordinated control of combustion timing and peak pressure on the same time scale through modulation of inducted gas composition and effective compression ratio. The controller used is directly synthesized from a linearized version of the complete control model outlined in Section 4.3.3. Tracking responses for combustion timing and peak pressure occur within 4–5 engine cycles. Additionally, a reduction in control effort is realized due to the coordinated modulation of the control inputs.

4.3.5 Future Work Required for This LTC Control Approach

While the work completed to date is promising, it is important to note that these results have been applied under the following limiting conditions and assumptions:

- single-cylinder configuration: cylinder-to-cylinder dynamics have been ignored at this point
- constant engine speed: engine speed will vary during practical implementation of LTC, must be considered
- molar ratio of reactants/products and effective compression ratio (both modulated via intake and exhaust valve timing) have been the only control inputs considered: the cylinder-independent cycle-to-cycle injection of fuel represents another capable control input which should be studied using a physics-based approach

In order to practically implement LTC, the dynamics associated with cylinder-to-cylinder coupling and variable engine speed must be considered. Furthermore, the availability of direct in-cylinder fuel injection provides the opportunity to vary the amount of fuel delivered on a cycle-to-cycle and cylinder-to-cylinder basis, a capability that has yet to be exploited in previous

physics-based LTC control results. A benefit of a physics-based approach to modeling and control of LTC is that previous work may be extendable to additional operating conditions (e.g., variable engine speed), configurations (e.g., multiple cylinders), and control inputs (e.g., cylinder-independent, cycle-to-cycle modulation of fuel).

Consider the control model equations (Eqs. 4.1 and 4.2)

- under the formulation only the two "system outputs" (peak pressure P and combustion timing θ_{23}) and the two "system inputs" (inducted gas composition, α and effective compression ratio) are assumed to vary on a cycle-to-cycle basis
- while the control model depends on the equivalence ratio ϕ and engine speed, these parameters are assumed constant, with no change on a cycle-to-cycle basis
- the temperature of the reinducted residual gas is only related to the gas exhausted by the same cylinder on the previous engine cycle, with no dependence on the temperature of exhaust from neighboring cylinders.

To accommodate practical multi-cylinder, variable speed operation the control model, and the controller synthesized from it, must reflect variation of the engine speed and dependence of residual temperature on the exhaust from neighboring cylinders. Furthermore, a cycle-to-cycle variation of the equivalence ratio could be used to reflect the modulation of injected fuel as another control input. The reformulation and validation of the control models with cycle-to-cycle modulation in equivalence ratio and engine speed variation should be key tasks in future efforts.

As done in previous work, the discretization and simplification of the induction, compression, combustion, expansion, and exhaust processes, as shown in Fig. 4.4 might be useful and valid assumptions in future efforts. Furthermore, integrating a physics-based description of the cylinder-coupling process in a control model framework will be necessary to develop generalizable control strategies for multi-cylinder residual-affected LTC.

4.4 Conclusion

A wonderful opportunity exists to capitalize on recent improvements in on-engine technologies in the pursuit of cleaner and more efficient automobiles. While a considerable amount of attention has been given to hybrid and FC approaches, significant improvements can be made, and are required, in the area of advanced combustion strategies. One such strategy, LTC combines benefits of both diesel and SI methodologies to produce a strategy that has NO_x and soot emissions significantly lower than either approach. Residual-affected LTC uses VVA to reinduct or trap hot combustion gases, enabling dilute, stable autoignition. As a result, residual-affected LTC has an efficiency

exceeding SI and matching diesel. While these characteristics of LTC can address increasing environmental regulatory demands, there are some fundamental challenges. To practically implement residual-affected LTC, closed-loop control must be used for several reasons: there is no direct combustion trigger; cycle-to-cycle and cylinder-to-cylinder dynamics exist through the residual gas temperature; multiple combustion modes are required; and early fuel delivery is required and difficult. Although LTC is a complex physical process, this chapter has reviewed modeling efforts which show that the aspects most relevant for control – in-cylinder pressure evolution, combustion timing, work output and cycle-to-cycle dynamics – can be captured in relatively simple and intuitive physics-based simulation and control models. In a specific case, it is shown that from physics-based "control models" a variety of generalizable strategies can be developed to control LTC. Work must continue in this area to develop production-viable engines utilizing LTC.

References

1. DOE. Department of Energy (DOE) Annual Energy Outlook 2006: With Projections to 2030. Energy Information Administration, Office of Integrated Analysis and Forecasting, U.S. Department of Energy, Washington, DC 20585, 2006.
2. J.B. Heywood et al. The Performance of Future ICE and Fuel Cell Powered Vehicles and Their Potential Fleet Impact. John B. Heywood, Malcolm A. Weiss, Andreas Schafer, Stephane A. Bassene, and Vinod Natarjan. Energy Laboratory Report # MIT EL 04P-254, December 2003.
3. M.A. Weiss et al. On the Road in 2020: A life-cycle analysis of new automobile technologies. Malcolm A. Weiss, John B. Heywood, Elisabeth M. Drake, Andreas Schafer, and Felix F. AuYeung. Energy Laboratory Report # MIT EL 00-003 Energy Laboratory, October 2000.
4. D.M. Chon and J.B. Heywood, "Performance Scaling of Spark-Ignition Engines: Correlation and Historical Analysis of Production Engine Data," SAE paper no. 2000-01-0565, presented at 2000 SAE World Congress & Exposition, Cobo Center, Detroit, MI, March 6–9, 2000.
5. S. Midlam-Mohler, Y. Guezennec, G. Rizzoni, S. Haas, H. Berner, and M. Bargende, "Mixed-mode HCCI/DI with external mixture preparation," FISITA 2004 World Automotive Congress, 2004.
6. S. Onishi, S.H. Jo, K. Shoda, P.D. Jo, and S. Kato. Active thermo-atmosphere combustion (ATAC) – a new combustion process for internal combustion engines. SAE 790501, 1979.
7. M. Noguchi. A study on gasoline engine combustion by observation of intermediate reactive products during combustion. SAE 790840, 1979.
8. P.M. Najt and D.E. Foster. Compression-ignited homogeneous charge combustion. SAE 830264, 1983.
9. R.H. Thring. Homogeneous-charge compression ignition (HCCI) engines. SAE 892068, 1989.
10. J.R. Smith, S.M. Aceves, C.K. Westbrook, and W.J. Pitz. Modeling of homogeneous charge compression ignition (HCCI) of methane. Proceedings of the 1997 ASME Internal Combustion Engine Fall Technical Conference, 1997-ICE-68, 29:85–90, 1997.
11. M. Christensen, B. Johansson, P. Amneus, and F Mauss. Supercharged homogeneous charge compression ignition. SAE 980787, 1998.

12. S.M. Aceves, J.R. Smith, C.K. Westbrook, and W.J. Pitz. Compression ratio effect on methane HCCI combustion. Journal of Engineering for Gas Turbine and Power, 121:569–574, 1999.
13. J. Kusaka, et al. Predicting homogeneous charge compression ignition characteristics of various hydrocarbons. Proceedings of the 15th Internal Combustion Engine Symposium (International), Seoul, Korea, 1999.
14. Y. Yamasaki and N. Iida. Numerical simulation of auto-ignition and combustion of n-butane and air mixtures in a 4-stroke HCCI engine by using elementary reactions. SAE 2000-01-1834, 2000.
15. Y.K. Wong and G.A. Karim. A kinetic examination of the effects of recycled exhaust gases on the auto-ignition of homogeneous n-heptane-air mixtures in engines. SAE 2000-01-2037, 2000.
16. T. Lovas, F. Mauss, C. Hasse, and N. Peters. Modelling of HCCI combustion using adaptive chemical kinetics. SAE 2002-01-0426, 2002.
17. J.E. Dec. A computational study of the effects of low fuel loading and EGR on heat release rates and combustion limits in HCCI engines. SAE 2002-01-1309, 2002.
18. S.S. Goldsborough and P. Van Blarigan. A numerical study of a free piston IC engine operating on homogeneous charge compression ignition combustion. SAE 1999-01-0619, 1999.
19. S.B. Fiveland and D.N. Assanis. A four stroke homogeneous charge compression ignition engine simulation for combustion and performance studies. SAE 2000-01-0332, 2000.
20. J. Hiltner, R. Agama, F. Mauss, B. Johansson, and M. Christensen. HCCI operation with natural gas: Fuel composition implications. Proceedings of the 2000 ASME Internal Combustion Engine Fall Technical Conference, 2000-ICE-317, 35:11–19, 2000.
21. R. Ogink and V. Golovitchev. Gasoline HCCI modeling: Computer program combining detailed chemistry and gas exchange processes. SAE 2001-01-3614, 2002.
22. T. Noda and D.E. Foster. A numerical study to control combustion duration of hydrogen-fueled HCCI by using multi-zone chemical kinetics simulation. SAE 2001-01-0250, 2001.
23. W.L. Easley, A. Agarwal, and G. A. Lavoie. Modeling of HCCI combustion and emissions using detailed chemistry. SAE 2001-01-1029, 2001.
24. S.B. Fiveland and D.N. Assanis. Development and validation of a quasi-dimensional model for HCCI engine performance and emissions studies under turbocharged conditions. SAE 2002-01-1757, 2002.
25. M. Kraft, P. Maigaard, F. Mauss, M. Christensen, and B. Johansson. Investigation of combustion emission in a HCCI engine. Proceedings of the Combustion Institute, 28:1195–1201, 2000.
26. S.M. Aceves, et al. Cylinder-geometry effect on HCCI combustion by multi-zone analysis. SAE 2002-01-2869, 2002.
27. A. Babajimopoulos, D.N. Assanis, and S.B. Fiveland. Modeling the effects of gas exchange processes on HCCI combustion and an evaluation of potential control through variable valve actuation. SAE 2002-01-2829, 2002.
28. T. Miyamoto, et al. A computational investigation of premixed lean diesel combustion – characteristics of fuel-air mixture formation. SAE 1999-01-0229, 1999.
29. J. Kusaka, K. Tsuzuki, Y. Daisho, and T. Saito. A numerical study on combustion and exhaust gas emissions characteristics of a dual-fuel natural gas engine using a multi-dimensional model combined with detailed kinetics. SAE 2002-01-1750, 2002.
30. A. Agarwal and D.N. Assanis. Multi-dimensional modeling of ignition, combustion and nitric oxide formation in direct injection natural gas engines. SAE 2000-01-1839, 2000.
31. S.C. Kong, C.D. Marriot, C.J. Rutland, and R.D. Reitz. Experiments and CFD modelling of direct injection gasoline HCCI engine combustion. SAE 2002-01-1925, 2002.

32. S. Hong, M. Wooldridge, and D.N. Assanis. Modeling of chemical and mixing effects on methane auto-ignition under direct injection stratified charge conditions. Proceedings of the 29th International Symposium on Combustion, 2002.
33. P.N. Kannan and A. John. Dependence of fuel-air mixing characteristics on injection timing in an early-injection diesel engine. SAE 2002-01-0944, 2002.
34. G.M. Shaver, M. Roelle, J.C. Gerdes, P.A. Caton, and C.F. Edwards. Dynamic modeling of HCCI engines utilizing variable valve actuation. ASME Journal of Dynamic Systems, Measurement and Control, 127(3):374–381, 2005.
35. G.M. Shaver, M. Roelle, and J.C. Gerdes. modeling cycle-to-cycle coupling in hcci engines utilizing variable valve actuation. Proceedings of the 1st IFAC Symposium on Advances in Automotive Control, Salerno, Italy, pp. 244–249, 2004.
36. F. Agrell, H.-E. Angstrom, B. Eriksson, J. Wikander, and J. Linderyd. Transient control of HCCI through combined intake and exhaust valve actuation. SAE 2003-01-3172, 2003.
37. G. Haraldsson, P. Tunestal, B. Johansson, and J. Hyvonen. HCCI combustion phasing with closed-loop combustion control using variable compression ratio in a multi cylinder engine. JSAE 20030126, 2003.
38. J.-O. Olsson, P. Tunestal, and B. Johansson. Closed-loop control of an HCCI engine. SAE paper 2001-01-1031, 2001.
39. J. Bengtsson, P. Strandh, R. Johansson, P. Tunestal, and B. Johansson. Cycle-to-cycle control of a dual-fuel HCCI engine. SAE 2004-01-0941, 2004.
40. G.M. Shaver and J.C. Gerdes. Cycle-To-Cycle Control Of HCCI engines. Proceeding of the 2003 ASME International Mechanical Engineering Congress and Exposition, IMECE2003-41966, Washington, DC, 2003.
41. G.M. Shaver, M. Roelle, J.C. Gerdes, J.-P. Hathout, J. Ahmed, A. Kojic, P.A. Caton, and C.F. Edwards. A physically based approach to control of HCCI Engines with variable valve actuation. International Journal of Engine Research, 6(4):361–375(15), July 2005.
42. G.M. Shaver, M.J. Roelle, and J.C. Gerdes. Physics-based modeling and control of residual-affected HCCI engines. ASME Journal of Dynamic Systems, Measurement and Control, 2008 (in press).
43. G.M. Shaver, M.J. Roelle, and J.C. Gerdes. Decoupled control of combustion timing and peak pressure on an HCCI engine. Proceedings of the American Control Conference, Portland, Oregon, pp. 3871–3876, 2005.
44. G.M. Shaver, J.C. Gerdes, and M. Roelle. Physics-based closed-loop control of phasing, peak pressure and work output in HCCI engines utilizing variable valve actuation. Proceeding of the American Control Conference, Denver, Co., pp. 150–155, 2004.
45. D.J. Rausen, A.G. Stefanopoulou, J.-M. Kang, J.A. Eng, and T.-W. Kuo. A mean-value model for control of homogeneous charge compression ignition (HCCI) engines. Jounal of Dynamic Systems, Measurement and Control, 127:355, 2005.
46. M. Canova, L. Garzarella, M. Ghisolfi, S. Midlam-Mohler, Y. Guezenned, and G. Rizzoni. A control-oriented mean-value model of HCCI diesel engines with external mixture formation. ASME IMECE, Nov. 5–11, 2005.
47. G.M. Shaver, M.J. Roelle, and J.C. Gerdes. Modeling cycle-to-cycle coupling and mode transition in HCCI engines with variable valve actuation. IFAC Journal on Control Engineering Practice (CEP), 14(3):213–222, 2006.
48. M. Roelle, G.M. Shaver, and J.C. Gerdes. Tackling the transition: A multi-mode combustion model of SI and HCCI for mode transition control. Proceedings of the 2004 ASME International Mechanical Engineering Congress and Exposition, Anaheim, California, 2004.
49. M. Roelle, A.F. Jungkunz, N. Ravi, and J.C. Gerdes. A dynamic model of recompression HCCI combustion including cylinder wall temperature. Proceedings of the 2006 ASME International Mechanical Engineering Congress and Exposition, Anaheim, California, 2006.

50. G.M. Shaver, M.J. Roelle, J.C. Gerdes. A 2-input, 2-state model of residual-affected HCCI engines. American Control Conference, Minneapolis, Minnesota, 2006.
51. N. Ravi, M. Roelle, A.F. Jungkunz, and J.C. Gerdes. A physically based two-state model for controlling exhaust recompression HCCI in gasoline engines. Proceedings of the 2006 ASME International Mechanical Engineering Congress and Exposition, Anaheim, California, 2006.
52. G.M. Shaver, A. Kojic, J.C. Gerdes, J.-P. Hathout, and J. Ahmed. Contraction and Sum of Squares Analysis of HCCI Engines, In the Proceedings of the 2004 IFAC Symposium on Nonlinear Control Systems, Stuttgart, Germany, 2004.

Chapter 5
Flexible Sunlight—The History and Progress of Hybrid Solar Lighting

L. Curt Maxey

Abstract Over the past 150 years lighting has evolved significantly, enabling great spatial, temporal, and intellectual extension of the human domain. With the ability to safely generate light on demand, complex living and working spaces have evolved. The length of a useful day is no longer limited to sunlit hours. Intellectual pursuits continue around the clock, allowing the productivity that was once associated with "burning the midnight oil" to occur in well-lighted homes, businesses, and universities. With this progress has come an enormous energy burden. Lighting now accounts for one-third of the non-residential electricity usage and is the largest single use of electricity in non-residential buildings. The majority of the activity in non-residential buildings still occurs during hours when the sun is shining, making it possible to offset at least part of the electrical lighting load through daylighting. Introducing daylighting into existing buildings requires cultural and technical development. As a culture we must comprehend the value of daylighting, in terms of societal and environmental benefits. However, to introduce daylighting into existing buildings, the technology must be available in a form that is compatible with existing infrastructure. The technology must also be presented in a way that enables it to be embraced by the architects and lighting designers that will be responsible for implementing it. Hybrid solar lighting is a daylighting solution that is specifically designed to be flexibly integrated into modern building systems.

Keywords Solar energy · lighting · daylighting · sunlight direct · skylight · renewable resources · energy efficiency · fiber optic · remote source lighting

L.C. Maxey
Oak Ridge National Laboratory, MS 6054, Oak Ridge, TN 37831, USA
e-mail: sol2008qst@comcast.net

V. Shah (ed.), *Emerging Environmental Technologies*,

5.1 Introduction

The controlled lighting of interior space has changed the world to a far greater degree than any other human achievement. Mastery over the ability to see is, fundamentally, the most "enabling" technology ever introduced. Yet, the lighting of interior spaces has been so successful and so ubiquitous, for so long, that few citizens of industrialized societies would immediately identify the invention of the electric light bulb as one of the most significant achievements of human civilization. It was, however, the invention that made it possible to provide abundant light to interior spaces safely, conveniently, and reliably at all times of the day or night. The timeline in Fig.5.1 shows the progression of lighting technology from oil lamps through the emergence of solid-state lighting [1].

Throughout the 1900s, the use of the sun as a light source for illuminating building interiors evolved considerably. As we entered the century, the sun was our primary source of interior light during the day, and the electric light bulb was only slowly gaining practicality. Until the 1940s, sunlight remained the primary means for lighting buildings, with electric lights as a supplement. Eventually, however, the cost and performance of electric lamps improved, and the sun was displaced as our primary method of lighting building interiors. During the heightened energy awareness of the 1970s, a renewed interest in day lighting emerged, yet that interest was outweighed by the convenience and cost of electric light sources that could be placed virtually anywhere within buildings. Moreover, it became clear that the effective architectural integration of daylight into modern buildings required skill and finesse to avoid potential

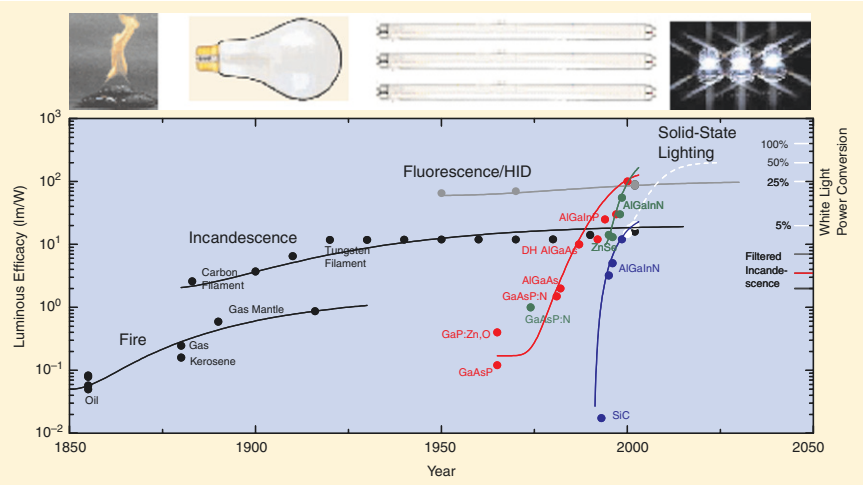

Fig. 5.1 Evolution of various interior lighting technologies. (Reprinted with permission from Tsao, J. Y. (2004) Solid-State Lighting: Lamps, Chips and Materials for Tomorrow, *IEEE Circuits & Devices*, 20(3), 28–37 (May/June) (© 2004 IEEE))

pitfalls (glare, variability, difficulty of control, requisite architectural modifications, and excessive illumination) [2].

As the interest in daylighting for interior spaces has continued, many conceptual and technical improvements have made its applications easier and more reliable. The development of architectural daylighting designs that minimize glare and over-illumination have matured as a result of continued interest. The combination of energy-efficient dimmable lighting ballasts and reliable "daylight harvesting sensors" has enabled daylighting to be combined with artificial lighting in a harmonious manner that achieves consistent illumination.

Architecturally effective daylighting strategies add to the aesthetic and environmental value of modern buildings, and yet the size of our buildings often makes daylighting options very limited. Skylights provide light in spaces that are far from exterior walls, but traditional skylight designs have often been associated with poor thermal characteristics and excessive maintenance issues (leakage). Skylight designs have traditionally been large optical openings that contribute substantially to a building's heating and air-conditioning loads, create non-uniform lighting conditions, and are difficult to integrate into existing structures. Modern skylight designs are much more aesthetically diverse and include a variety of passive optical features to improve the lighting performance and versatility of the designs.

5.2 Environmental Problems Addressed by Hybrid Solar Lighting

The use of electricity for lighting is, like many other things, a blessing when applied judiciously and a curse when expended recklessly. Within the United States, lighting accounts for more than one-third of all the electricity consumed for non-residential use. Conservation with respect to how we use electric lighting can significantly reduce that usage. Daylighting is one means for achieving that conservation without abandoning the convenience of lighted interior space.

To balance the demands of growing electricity needs with limited production and distribution capability, conservation must play an immediate and sustained role. There is neither sufficient generating capacity nor grid distribution infrastructure to sustain our present rate of growth. Adding power plants or grid capacity is a lengthy and complicated process. Moreover, if the power plants are fossil-fueled, the problems of environmental pollution and greenhouse gas emissions are only exacerbated by the new facilities.

There are incentives in the United States for private individuals and businesses to add renewable resources to their energy supply. An even more promising indicator is the Energy Policy Act of 2005, which mandates that federal facilities "Reduce facility energy use per square foot by 2 percent per year through the end of 2015 or by 20 percent by the end of FY 2015, relative to 2003 baseline."

In the short term, there will continue to be blackouts and other inconveniences associated with the limited supply and distribution structure. In the long term, by embracing conservation and responsible environmental stewardship as a culture, we can manage our energy usage in a way that enables manageable growth, with renewable resources generating a substantial portion of our energy budget.

Fortunately, amidst an array of challenging environmental and energy options, daylighting is a relatively easy concept to promote. It is significant in terms of the energy it can displace and it offers ancillary benefits in terms of aesthetics and comfort.

Architectural design of daylighting systems that are both energy efficient and aesthetically appealing is an active area of research and development that is producing elegant and efficient designs for new buildings. Throughout the world, systems are being designed to introduce daylight into existing buildings. Skylight designs have evolved significantly and now offer many options for introducing sunlight into existing buildings in a way that enhances the aesthetics of the roof and ceiling. Daylighting systems with exterior reflectors (both fixed and tracking) to direct light into buildings are being designed to meet a variety of economic and cultural needs.

Introducing daylighting into existing buildings is one of the more difficult challenges that daylighting system designers face. A large portion of modern non-residential ceiling space is constructed using suspended ceiling components and standardized luminaires. While it is applicable to a variety of environments, hybrid solar lighting (HSL) was specifically designed to address the needs of those types of environments. The initial HSL systems were all designed with "hybrid" luminaires that combined the sunlight and electric light together in a single standardized luminaire. The HSL designs have evolved to include other luminaire options but the hybrid luminaire is still the mainstay of the systems. HSL has provided the ability to seamlessly integrate daylighting into non-residential ceilings in a way that is unique from other commercially available daylighting systems.

5.3 Origins of Fiber Optic Daylighting Systems

Early after the introduction of fiber optic technology, the concept of using fiber optics for transmitting concentrated sunlight was discussed. There were several immediately perceived advantages to this approach. By concentrating the sunlight, very small roof penetrations could allow a few optical fibers, heavily laden with sunlight, to illuminate large areas. This would reduce the impact on insulation efficacy and potential roof leaks. Unlike skylights, these fibers would allow the light to be bent at will, so that the light could easily be routed around structures and into areas where it was needed. When lighting needs changed, the fibers could then be re-routed. The concept of "flexible sunlight"

Fig. 5.2 One implementation of the Himawari daylighting system

had been born. One of the first attempts to commercialize fiber-coupled daylighting was the Himawari system, shown in Fig. 5.2.

In addition to the obvious advantages of concentration and flexibility, the use of optical fibers and concentrating optics provided the option of filtering the light to remove ultraviolet (UV) and IR wavelengths. The removal of the IR wavelengths could eliminate virtually all heating from the daylight that entered the room, and the removal of the UV could reduce the potential for the light to produce fading (technically known as photo bleaching) of fabrics and structures in the lighted area. By comparison with conventional skylights, fiber optic daylighting could significantly reduce heating and cooling loads imposed by the daylighting systems.

With the creative application of optical filtering, fiber optic daylighting systems offered additional degrees of freedom. As early as 1983, a fiber optic daylighting system that also included photovoltaic (PV) conversion was proposed [3]. In this system, a dichroic mirror filter would be inserted into the light from a focusing lens to reflect the visible portion of the light into fibers for illumination. The IR light would pass through the dichroic mirror to strike a PV cell and be converted into electricity for other applications.

Presently, at least three commercial fiber optic daylighting systems are being marketed around the world, Himawari (Japan), Parans (Sweden), and Sunlight Direct (United States) [4]. Of these, the only one for which the author has reliable cost and performance information is the Sunlight Direct "Hybrid Solar Lighting" (HSL) system. The Himawari system (Fig. 5.2) is believed to be the first commercial fiber optic daylighting system and dates back to at least the early 1970s. That system, which uses a tracking concentrator with multiple Fresnel lenses, transmits the light through quartz fibers, which have very low loss but are very expensive compared to plastic optical fibers. Anecdotal information from a source familiar with a Himawari system sold in the United States several years ago, suggests that the Himawari system cost was (at that time) between $1/lumen and $5/lumen depending on the system type. By contrast, the HSL system being marketed by Sunlight Direct (capable of producing around 40,000 lumens) had an installed cost of approximately $0.50/lumen in 2007 but is being projected at $0.35/lumen for 2008. Of the three known fiber optic daylighting systems, the Sunlight Direct HSL system is believed to be the only one that combines natural and artificial light in a hybrid luminaire and is specifically designed for compatibility with existing ceilings and lighting. The HSL system has been installed in a significant number of beta test sites, including research institutions, universities, and retail outlets [5]. The evolution of the HSL system will be discussed in more detail, but first we should consider some of the motivations behind the development of any daylighting system.

5.4 Biological and Cultural Benefits of Daylighting

Much has been written about the potential benefits of natural lighting versus artificial lighting. There is enough anecdotal information to suggest that the solar spectrum (which is dramatically different than the spectra emitted by electric light sources) may be a better option, in terms of overall physical and mental health, than electric light. By extension, the reasoning suggests that improved mental and physical health results in positive behavioral changes. There have been some controlled experiments to validate various claims, but many of the claims are still rather speculative. Before discussing the claimed benefits of daylighting, it is worth considering some heuristic discussions regarding biological mechanisms that could play a role in producing them.

It is widely accepted that the spectral response of the human eye, under normal levels of illumination (the so called "photopic" response), is very similar to the spectrum of visible sunlight, which is shown in Fig. 5.3. Currently, there is no single undisputed photopic spectral diagram, but one from the International Commission on Illumination (CIE) that is frequently used is shown in Fig. 5.4 [6]. For the purpose of this discussion it is not important to quibble over just how precisely the two spectra are matched. The point to be appreciated is that, from a systems standpoint, when the spectral response of a receiver (the eye) is

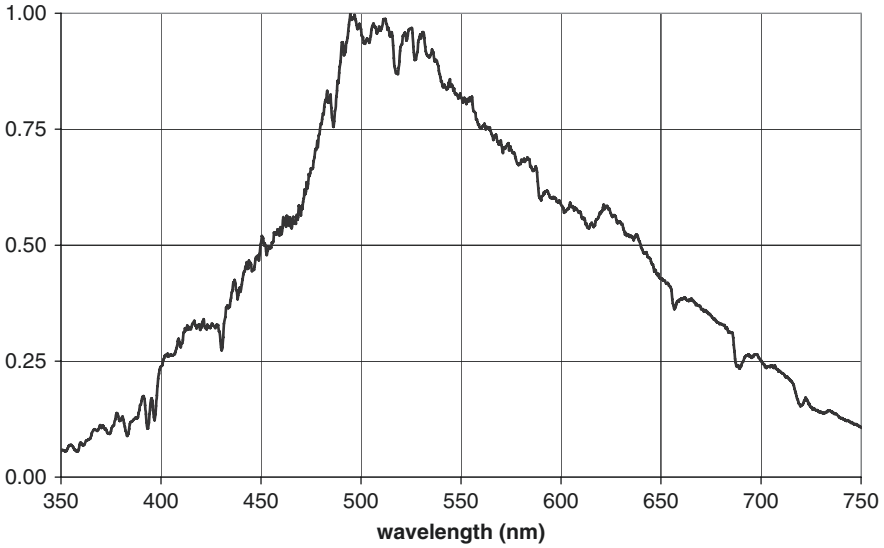

Fig. 5.3 Normalized visible spectrum of direct sunlight

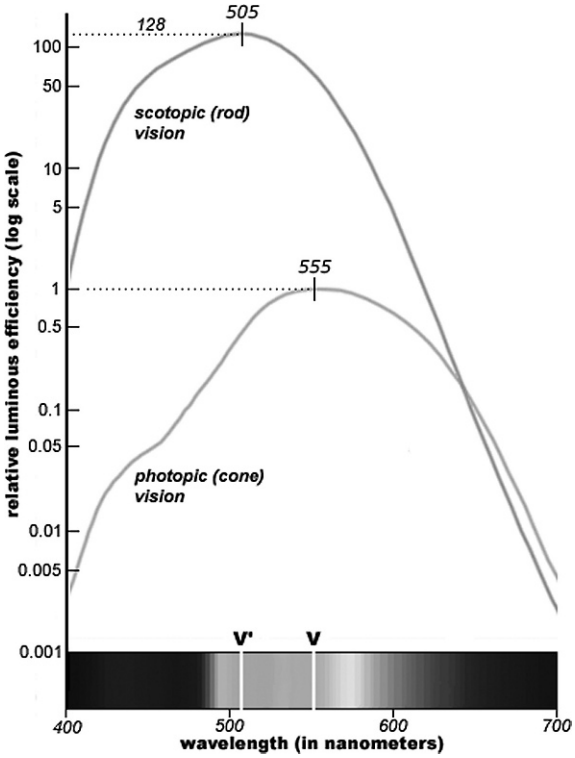

Fig. 5.4 Scotopic and photopic eye response curves

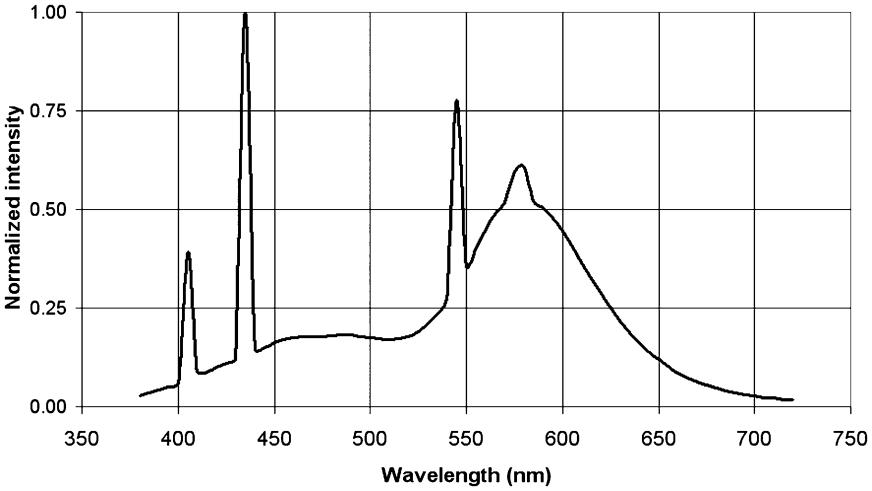

Fig. 5.5 Normalized spectrum of typical (4,000 K) fluorescent lamp

very closely matched to the spectral characteristics of a source (e.g., the sun), the performance of the resulting system would reasonably be expected to exceed that of a system in which the two were mismatched. The significance of this reasoning becomes important when we consider the spectrum of an average (4,000 K, T8) fluorescent bulb, shown in Fig. 5.5.

Clearly the fluorescent spectrum that is shown differs significantly from the visible portion of the solar spectrum. Thus the wavelength distribution is not optimized for human vision. From a systems point of view, one could reasonably speculate that visual acuity for tasks such as reading would be poorer under the fluorescent spectrum in Fig. 5.5, compared to the visual acuity one would experience when performing the same tasks under the same quantity of light with the solar spectrum shown in Fig. 5.3. Reduced visual acuity is a source of discomfort and diminished visual performance that also leads to decreased feelings of well-being. Anyone who has experienced a decline in visual acuity due to age or other factors can attest to the malaise it creates. By extension, we can reason that if visual acuity is increased under natural lighting, improvements in one's feeling of well-being and improvements in one's performance on tasks requiring visual acuity (reading, writing, and detailed physical work) might also be increased.

Beyond visual acuity issues, it is generally appreciated that organisms respond differently, at an organic level, to optical stimulation from different portions of the spectrum. Certainly the UV spectrum has its organic benefits (vitamin D production and prevention of rickets) and hazards (sunburn and carcinoma). In addition, the use of fiber optic blankets that emit blue-green light have become common in the treatment of infants with elevated bilirubin levels. These are limited examples of organic spectral affects that are generally

accepted as being valid. It is reasonable to expect that there may be others, perhaps subtle, perhaps not, that are yet to be accepted.

While the organic mechanisms are not fully understood, it is well known that light plays a significant role in psychological health. One very familiar example is the psychological phenomenon that occurs with reduced winter lighting conditions. It is widely appreciated that, during winter months, inhabitants of northern latitudes are often affected by a condition known as "seasonal affect disorder" or SAD, which can manifest as a severe depression in extreme cases. Whether the quality of light is important in this regard, or merely the quantity of light received, the ability of light to play a profound role in one's general sense of well-being is appreciated.

These and other potential mechanisms by which lighting can affect health, happiness, and performance can be explored in depth elsewhere but the sum of these discussions lays the groundwork for some credible mechanisms that may explain some of the positive attributes that have been attributed to natural lighting. Among these benefits, there are claims that workers feel better, have fewer health complaints, and higher productivity when exposed to natural lighting. Similarly, there is evidence that students remain healthier and perform better academically in environments where natural lighting is prevalent. In both work and school environments, the absenteeism rates (which are easily quantified) have been shown to decrease with natural lighting [7].

From a cultural standpoint there are obvious financial and social advantages to having workers and students that are productive, present, healthy, and happy. Factors that have even a small influence over these characteristics can, over time, have dramatic economic and societal impact. From the standpoint of pure economics, some retailers have discovered benefits that daylight can have on the retail environment. Retailers are starting to use daylighting in their stores specifically to enhance their store environment, increase sales, create a more pleasant shopping environment, attract customers, and improve color rendering. Using daylighting also has aesthetic benefits that encourage customers to enter the store [7].

If even a portion of the claimed biological and cultural benefits associated with the natural solar spectrum are true, the positive societal influence of increased use of daylighting could vastly outweigh the benefits in energy savings. In the near term, however, the economic justification for the use of daylighting to offset energy usage will predominantly determine the extent to which daylighting is implemented.

5.5 Energy and Environmental Benefits of Daylighting

In industrialized nations, the majority of the inhabitants leave their homes at some point during the daytime to spend time in non-residential buildings. Non-residential buildings remain lighted (mostly by electric lighting) throughout the

hours when the sun is shining, with a significant portion of them turning out their lights sometime after the sun goes down. By contrast, residential lighting needs often go dormant during the day, because the inhabitants are engaged in jobs or education that keeps them inside non-residential buildings. Thus, if we want to consider the practical impact of daylighting on energy usage, it makes sense to focus primarily on non-residential buildings. Non-residential buildings are major consumers of electricity for lighting, and the peak demand for that lighting occurs during daylight hours.

Within the United States, lighting accounts for more than one-third of all the electricity consumed for non-residential use. Within non-residential buildings, lighting is the single largest use of electricity. In addition to the direct energy load associated with electric lighting, less than 25% of the electricity consumed for lighting actually produces light; the rest generates heat, which increases the need for air-conditioning [8].

The chart in Fig. 5.6 shows the electricity usage in non-residential buildings and in these (2004) numbers, electricity used for lighting accounted for 1.12 quadrillion British thermal units per year [9]. Electricity used for space cooling represented almost half as much electricity usage as lighting. The electrical demand for both lighting and cooling could be significantly reduced through the use of daylighting that did not add to the heat load in a building.

When we consider the economics of using renewable resources (such as sunlight) to offset electricity usage, the relatively low cost of electricity presently makes it difficult to justify the investment on the basis of economics alone. The average cost of US commercial electricity in 2006 was just under $0.09 per kilowatt hour (kWh). However, with declining fossil fuel reserves and increasing concern about greenhouse gas emissions, we can anticipate rising electricity costs as well as increased economic incentives for implementing renewable resources.

When considering the various fuel sources for electricity generation in the United States (Fig. 5.7) [10], one might argue that the impact of oil and gas reserves on electricity costs will be mitigated by the fact that almost one-half of US electricity is generated by burning coal. However, as liquid fuel reserves

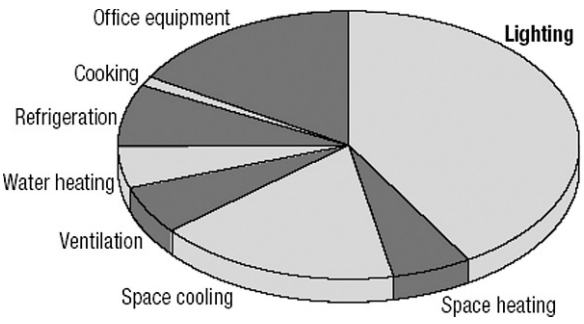

Fig. 5.6 Electricity usage in non-residential buildings

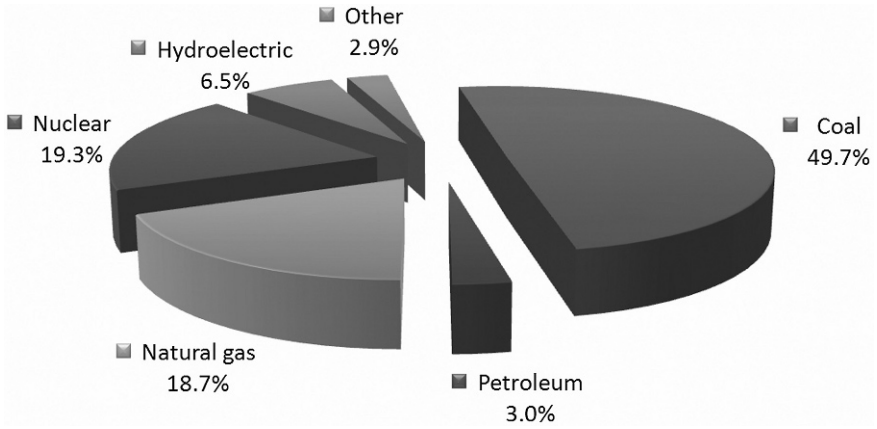

Fig. 5.7 Sources of electricity in the United States (2005)

become less plentiful, the conversion of coal into liquid fuels will increase to meet the increase in demand. In addition to these raw economic factors, the use of government regulation and incentive programs are likely to have a significant impact on the economics of daylighting.

Concern over greenhouse gas emissions is expected to continue to fuel contempt over the burning of fossil fuels (for transportation as well as electricity). As a result, it is likely that we will see carbon dioxide emissions regulated in a way that raises the cost of electricity generated by burning fossil fuels. Taxation of greenhouse emissions combined with tax incentives for using renewable resources, such as solar energy, will make it easier to justify the investment in daylighting systems that offset energy usage in non-residential buildings.

If we accept that the economic factors for incorporating renewable resources will continue to improve, it raises the question of how the use of daylighting can be increased in non-residential buildings. The most obvious method requires constructing new buildings with daylighting incorporated into their architecture. However, to achieve an impact on the electrical lighting load presented by existing non-residential space, there must be some means by which daylighting can be incorporated into those structures. This was the driving concept behind the development of the HSL fiber-coupled daylighting system.

5.6 Development of the HSL System

The HSL system was conceived at the Oak Ridge National Laboratory (ORNL) in the mid-1990s. This system was more than a daylighting system, it was a hybrid system that included electric light. The concept of a fiber-coupled

daylighting system was not new. However, no previous system concepts had focused on integrating electric lighting as a fundamental part of the system. There were perceived to be major advantages with this approach. First, to have a daylighting system achieve rapid acceptance in the architectural and lighting design communities, there was a definite advantage to having the lighting components look like and fit with other commonly used lighting components. A fluorescent troffer design was the first implementation of a hybrid lighting luminaire. Second, by integrating the daylight source and the electric light source into the same fixture, it simplified the challenge of harmoniously blending the two sources. With the use of a daylight harvesting sensor and dimmable fluorescent ballasts, the fluorescent troffer design enabled the spatial and temporal uniformity of the light from the luminaires to remain constant as sky conditions varied. Although the design existed only on paper, the integrated nature of the HSL system was emphasized in every promotional presentation to potential sponsors, lighting designers, and architects (Fig. 5.8). The integration of the natural and electric light into a lighting system that could be seamlessly introduced into existing buildings greatly facilitated the early acceptance of the HSL concept.

Initial prototype development—When funding for an initial prototype system was finally acquired, many system elements had to come together in a very short period of time. The fundamental components for a system; collection optics, a tracking system, optical fiber, and a luminaire all had to be selected and or developed in a period of a few months. For the HSL concept to continue to receive acceptance by the lighting community, the first prototype system had to be developed using components that would achieve impressive performance but could ultimately be manufactured as reasonably priced commodity items.

The selection of an off-the-shelf collection optic was one of the most critical elements. To ensure maximum optical throughput, a high-quality glass

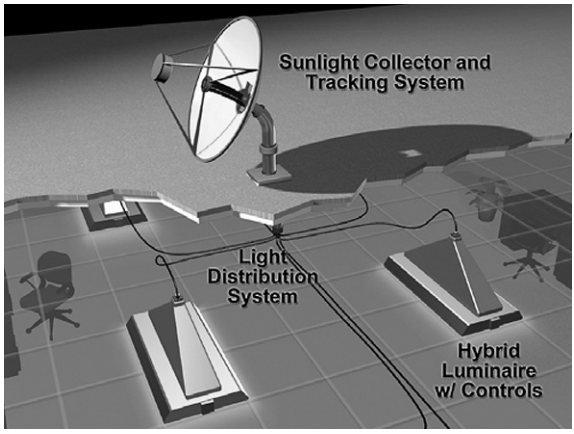

Fig. 5.8 Conceptual diagram of HSL system

parabolic first-surface mirror was selected, despite its high initial cost and sole-source limitation. The rationale was that molded plastic parabolic mirrors could eventually be produced in quantity. To keep the mirror pointed at the sun, a tracking system had to be identified or developed. Early experiments with sun-pointing sensors had suggested that they might not be adequate for maintaining the required pointing accuracy. Ultimately, a dual-axis open-loop tracking system was selected from a third-party source. This system, when accurately programmed with the latitude, longitude, date and time was capable of maintaining 0.1 pointing accuracy without any position sensor feedback. The drawback to the open-loop tracking system was that it required careful calibration to account for any alignment errors in the system. A specialized camera-based sun pointer was developed for use in the calibration procedure [11].

The choice of an appropriate optical fiber was another essential element. Glass and plastic bundles, large core plastic waveguides, and even a liquid core specialized waveguide were all considered. Ultimately, large core (12-mm) waveguides constructed from fully cured polymethacrylate (PMA) were selected. These waveguides eliminated the optical losses due to the packing factor in fiber bundles, by having only one core. In addition, the material had higher optical transmission and was significantly softer than polymethylmethacrylate (PMMA). The combination of optical and mechanical properties made the PMA waveguides attractive for this application. Although the basic PMA product was offered by several vendors, the optical properties varied significantly [12]. Eventually a product was selected that had good transmission and negligible color shift.

Directing the light from the primary mirror required a secondary mirror assembly. A segmented secondary mirror assembly was designed that divided the concentrated light from the primary into eight individual foci. The secondary mirror segments were designed with a dichroic coating that reflected only the visible wavelengths, allowing the IR to pass through the mirrors. The optical waveguide mounting assemblies were designed with alignment features that allowed each of eight waveguides to be aligned to one of the segmented foci. A specialized alignment system and procedure was developed to ensure that each of the fibers was aligned to the optical axis of the parabolic primary mirror [13]. Due to the fact that there were no alignment features on the primary mirror that could reliably be used to identify the optical axis, a portion of the initial assembly procedure required measuring the parabolic mirror with a portable coordinate measurement instrument, as shown in Fig. 5.9. Using these measurements, the optical axis of the mirror was identified, and the mirror was cemented into a specially designed mounting cradle. The fully assembled prototype concentrator–tracker assembly with transmission fibers is shown in Fig. 5.10. The sun pointer used for the calibration of the system is mounted on the segmented secondary mirror assembly.

Fig. 5.9 Measurement of the primary mirror to identify the optical axis

The first luminaires that were developed for the HSL system used side-emitting PMMA rods that were etched with a pattern of precision light-scattering grooves. The patterned grooves, shown in Fig. 5.11, were designed to provide uniform illumination along the entire length of the rods. The 1-m

Fig. 5.10 Fully assembled prototype HSL concentrator and tracker

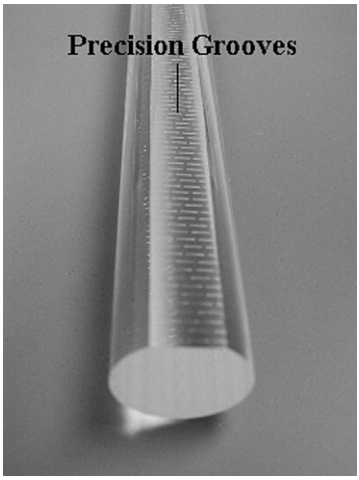

Fig. 5.11 Closeup of side-emitting rod showing light-scattering grooves

rods, which were commercially available from the fiber vendor, fit easily within a conventional fluorescent troffer. Two of the side-emitting rods were mounted in between T8 fluorescent tubes, as shown in Fig. 5.12. Significant testing was performed to evaluate the uniformity of the light emission pattern from the natural light emitted by the side-emitting rods, as compared to the pattern of light emitted by the fluorescent tubes. This information was used to adjust the design to minimize any variation in the light emitted by the two sources [14].

The first field installation of an HSL system was in 2002, for use with a photo-bio-reactor at Ohio University, rather than for conventional lighting. As such, the system contained all of the prototype HSL system components except for the luminaires. The installation of the first field system is shown in Fig. 5.13.

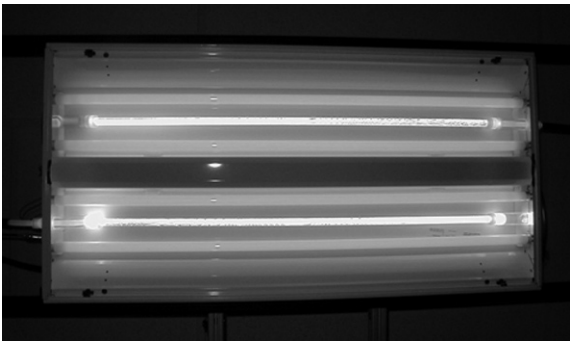

Fig. 5.12 Fully assembled prototype HSL luminaire, with diffusing lens removed

Fig. 5.13 First field installation of HSL system (2002)

5.7 Evolution and Commercialization of HSL

With the development of the first demonstration systems, it became possible for people to directly experience the impact of the HSL technology. The results were dramatic for the visitors to the ORNL HSL development laboratory. The popularity of the concept gained momentum, and the design continued to evolve. The drive to reduce component costs and system complexity led to changes in the design itself. The 12-mm optical waveguides that were used in the original prototypes were awkward to work with, and their continued supply from the preferred vendor was not guaranteed. Smaller PMMA fibers were in prolific supply, and despite their limitations, they offered greater flexibility and more design options. The glass primary mirror offered excellent optical quality,

but the cost and weight were unacceptable. No suitable plastic primary mirrors were available, and producing one required advancing the state of the art in plastic mirror manufacturing. The segmented secondary mirror imposed a significant optical alignment challenge during the assembly of the systems and required the machining of an expensive faceted mounting structure. The limitations associated with tracking system flexibility mandated that ORNL develop a dedicated tracker controller that could work with varying system geometries.

By 2004, the optical system had been redesigned and the segmented secondary mirror replaced with a single elliptical mirror, the large core PMA waveguides had been replaced with a single bundle of 127 PMMA 3-mm fibers, a molded plastic primary mirror had been developed, custom tracker control electronics and software were installed, and the services of an outside mechanical engineering firm had been employed to refine the overall packaging. The new design, shown in Fig. 5.14, was beginning to look more like a product than a prototype.

During the development of the second-generation HSL system, one of the original inventors, Duncan Earl, began laying the groundwork for a spin-off company, Sunlight Direct. That company licensed the technology from ORNL and eventually produced further refinements to the system. One of the most significant changes in the optical design was a novel means for reducing the packing fraction losses in the fiber bundle. Sunlight Direct developed a proprietary method for producing a hexagonal bundle with minimal packing losses

Fig. 5.14 Second-generation HSL system (2004)

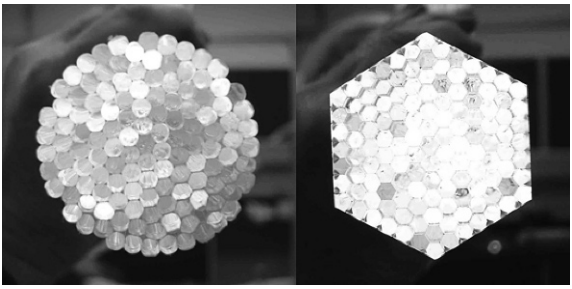

Fig. 5.15 Comparison of fiber bundles in second- and third-generation HSL units

(Fig. 5.15). In addition to the changes to the optical collector, Sunlight Direct expanded the luminaire options available for the HSL system.

In early 2006, Sunlight Direct introduced its first commercial version of the HSL system, incorporating all of the changes it had introduced into the system (Fig. 5.16). In addition to the hexagonal fiber bundle, it had developed a

Fig. 5.16 First commercial HSL system introduced by Sunlight Direct (2006)

custom mixing rod to adapt the light to the hexagonal shape. Sunlight Direct had also continued to work on the molding technology for the primary mirror, and the mirror quality was approaching that of the glass mirror that had been used in the initial prototypes.

With the design of the system reaching maturity, detailed spectral characterization of the optical system was conducted to evaluate the efficacy of the different components and their impact on the overall performance of the system [15]. The spectral characterization of the system showed that the natural light from the HSL luminaires (measured with the electric lights extinguished) differed only slightly from the solar spectrum, with a small loss in the red portion of the spectrum (Fig. 5.17).

At the time of this writing, more than 20 HSL systems are installed at various locations throughout the United States with ten of those organizations participating in the detailed beta test program [5]. Figure 5.18 shows an installation in progress at ORNL with four units on a newly constructed building, and Fig. 5.19 shows various views of an installation at the Walmart in McKinney, TX.

The energy performance at the beta test sites is monitored to accumulate energy savings data. The plot in Fig. 5.20 shows the impact of the HSL system on the energy used for lighting in a typical office environment. These data, from San Diego State University, represent the energy used to provide lighting in an office area at the university. The data show the onset of energy usage, when the lights are turned on early in the morning. The full electrical load of

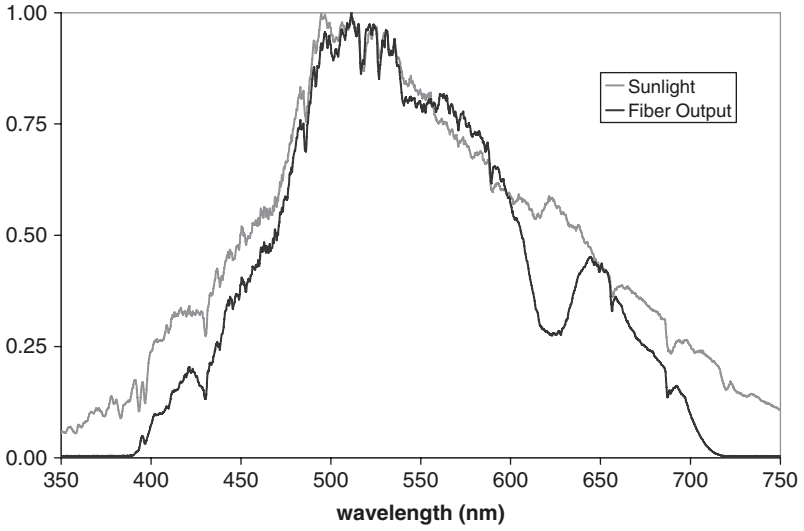

Fig. 5.17 Normalized comparison of direct sunlight and light from HSL fibers

Fig. 5.18 Four HSL units being installed on newly constructed ORNL building

Fig. 5.19 HSL installation at Walmart in McKinney, TX

the lights is present at that time, because there is not yet enough sunlight available to provide any useful lighting from the HSL system. As the sun climbs higher during the day, the quantity of natural light available increases, and in response, the electric lights dim to maintain a uniform level of illumination throughout the day. In the afternoon, as the solar energy weakens, the electrical lighting again increases to maintain the illumination level. Finally, as the office inhabitants depart in the afternoon, the electrical load is turned off.

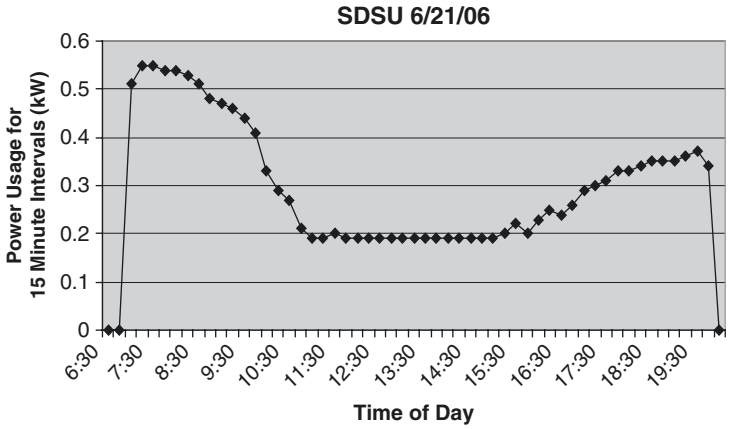

Fig. 5.20 Typical plot showing electrical energy displacement by HSL

5.8 Discussion and Conclusion

HSL is providing a novel means for introducing daylighting into existing non-residential buildings in a way that seamlessly integrates with the existing infrastructure. By its nature, HSL is a technically complex product that has all of the maintenance concerns of any system with moving parts and, like other solar technologies, must be cleaned occasionally to ensure optimum performance. Because of the precision pointing requirements the system must be monitored from time to time and will never have the simplicity offered by a passive skylight. In addition, HSL requires direct, unobstructed sunlight and cannot effectively use diffuse light in overcast conditions, whereas skylights can. Unlike other daylighting alternatives, however, HSL provides the ability to integrate sunlight into existing buildings in a way that blends seamlessly with other lighting systems and can be routed through complex paths if needed. Despite its limitations, early adopters are embracing the HSL technology for its lighting quality, its ease of integration, and its novelty. The concept of making the technology compatible with existing lighting and architectural environments has played a major role in its early acceptance. The HSL technology has decreased significantly in cost as the product has evolved, but the cost is still keeping the technology limited to the early adopter market. Cost reductions due to design changes and economy of scale are expected to further decrease the installed cost of the systems by as much as 50% by 2010.

Acknowledgments Research at Oak Ridge National Laboratory was sponsored by the US Department of Energy's Office of Energy Efficiency and Renewable Energy and the Tennessee Valley Authority.

References

1. Tsao, J. Y. (2004) Solid-State Lighting: Lamps, Chips and Materials for Tomorrow, *IEEE Circuits & Devices*, 20(3), 28–37 (May/June).
2. Muhs, J. D. (2000) Design and Analysis of Hybrid Solar Lighting and Full-Spectrum Solar Energy Systems, *Proceedings of ASES 2000 Conference*, Madison, Wisconsin, June 16–21.
3. Fraas, L. M., Pyle, W. R., and Ryason, P. R. (1983) Concentrated and Piped Sunlight for Indoor Illumination, *Applied Optics*, 22, 578–582.
4. Proefrock, P. (2007) Fiber Optic Solar Lighting Roundup, Ecogeek, September 2006 http://www.ecogeek.org/content/view/246/ (acc. October 2007).
5. Lapsa, M. V., et al. (2007) Direct Use of Solar Energy for Lighting—Results of the Hybrid Solar Lighting Field Trial Program. *Proceedings American Solar Energy Society, Solar 2007 Conference*, Cleveland, Ohio, July 8–12.
6. Human Color Vision (1996) Kaiser and Boynton, Optical Society of America, May.
7. Edwards, L., and Torcellini, P. (2002) A Literature Review of the Effects of Natural Light on Building Occupants, National Renewable Energy Laboratory Report NREL/TP-550-30769, July. Available at http://www.osti.gov/bridge/
8. http://www.eere.energy.gov/solar/cfm/faqs/third_level.cfm/name=Solar%20Lighting/cat=The%20Basics (acc. October 2007).
9. Solar FAQs—Hybrid Solar Lighting (2004) U.S. Department of Energy, DOE/GO-102004-xxxx June 2004; http://www.ornl.gov/sci/solar/pdfs/SolarFAQsHybridLight.pdf (acc. July 2008).
10. http://en.wikipedia.org/wiki/Image:Sources_of_electricity_in_the_USA_2006.png (acc. July 2008).
11. Beshears, D. L., et al. (2003) Tracking Systems Evaluation for the "Hybrid Lighting System," *Proceedings—International Solar Energy Conference*, Kohala Coast, Hawaii, March 16–18.
12. Cates, M. R., et al. (2003) Characterization of Transmission Properties of 3 M LF120C Plastic Optical Light Guide. *Proceedings—International Solar Energy Conference*, Kohala Coast, Hawaii, March 16–18.
13. Maxey, L. C., et al. (2003) A Deterministic Method for Aligning Multiple Optical Waveguides to a Paraboloidal Collector. *Proceedings—International Solar Energy Conference*, Kohala Coast, Hawaii, March 16–18.
14. Earl, D. D., et al. (2003) Performance of a New Hybrid Solar Lighting Luminaire Design. *Proceedings—International Solar Energy Conference*, Kohala Coast, Hawaii, March 16–18.
15. Maxey, L. C., et al. (2007) Spectral Transmission of a Solar Collector and Fiber Optic Distribution Hybrid Lighting System. *Proceedings of American Society for Mechanical Engineers (ASME) Energy Sustainability 2007*, Long Beach, California, June 27–30.

Chapter 6
Synthesis, Characterization, and Application of Magnetic Nanocomposites for the Removal of Heavy Metals from Industrial Effluents

Zhenghe Xu and Jie Dong

Abstract Magnetic nanocomposites with tailored surface functionalities have found a wide range of applications, including biological cell separation, waste remediation, gas purification, and raw material recovery from complex multiphase systems. The challenge to magnetic nanocomposite particles for these applications is to synthesize the particles of strong magnetic properties with high density of reactive functional groups, diversity of functionalities, and durability of surface films. In this chapter, the research and development of magnetic nanocomposite particles for applications to industrial effluent treatment are reviewed. Molecular self-assembly (SA), direct silanation, and mesoporous silica coating on magnetic particles were developed for the preparation of magnetic nanocomposites.

In SA, 16-mercaptohexadecanoic acid was anchored onto the γ-Fe_2O_3 surface through chemical bonding between the carboxylic head group of the surfactant and iron on γ-Fe_2O_3 surface, leaving the thiol or disulfide groups reactive. In the direct silanation, 3-aminopropyl triethoxy silane (APTES) films were silanized on bare magnetic particles from toluene and water. To improve the stability of silanized films, two-step silica-coating method was developed using sol–gel reaction, followed by dense-liquid silica coating. APTES films prepared by the silanation on the two-step silica-coated magnetic particles were found to be more robust than the ones silanized on bare magnetic particles. Furthermore, an innovative procedure of synthesizing mesoporous silica coatings on magnetic particles was developed to increase specific surface area of controlled pore sizes. This approach was based on the molecular templating, followed by sol–gel and templates removal. The resultant products showed a significant increase in specific surface area and were amenable for functionalization by silanation reaction.

The functionalized magnetic nanocomposites were effective for removal or recovery of heavy metal ions such as Cu^{2+}, Zn^{2+}, Ni^{2+}, Ag^{+}, and Hg^{2+} from

Z. Xu
Department of Chemical and Materials Engineering, University of Alberta, Edmonton, Alberta, Canada T6G 2G6
e-mail: Zhenghe.Xu@ualberta.ca

V. Shah (ed.), *Emerging Environmental Technologies*,

aqueous solutions. Loaded metal ions could be stripped off by acid washing. Selective separation of different metal ions was achieved by controlling the solution pH. Magnetic nanocomposites particles with reactive functional groups have great potential applications in industrial, biological, and pharmacological processes.

Keywords Magnetic nanocomposite particles · industrial effluent treatment · heavy metal removal · molecular self-assembly · direct silanization · two-step silica coating · mesoporous silica coating · molecular templating · sol–gel reaction · templates removal · surface functionalization

6.1 Introduction

The problem of disposing industrial wastes is as old as industry itself. Industrial wastes often cause serious water, air, and soil pollution. Heavy metals are frequently found from chemical manufacturing, petroleum, fossil fuel combustion, painting and coating, mining, extractive metallurgy, nuclear, and many other industries [1, 2]. The heavy metals most often implicated in accidental human poisoning are lead, mercury, arsenic, and cadmium. Some heavy metals, such as zinc, copper, chromium, iron, and manganese, are required by the body in trace amounts, but these same elements can be toxic at higher concentrations in human body. In addition to impair fetuses development, poisoning of heavy metals generally can cause the damage of kidneys, brain, blood, livers, central nervous, digestive, and skin system. These toxicities have been well established in scientific literature. Heavy metals can enter ground water aquifer by direct industrial and consumer waste disposal or released from soils, other industry solid wastes as a result of acid rain leaching.

The regulated levels of various heavy metal ions in drinking water are extremely low. For example, the World Health Organization has set a maximum guideline concentration of 0.01 mg/L for As in drinking water [3] and the US Environmental Protection Agency (EPA) has set a maximum limit of 0.005 mg/L for Pb and 0.65 mg/mL for Cu in drinking water [4]. It is a big challenge to remove these metal ions to such a low level from large volume, low concentration effluents in a cost effective manner. Discharge of metals to the environment not only causes serious health concerns but also is a waste of dwindling and valuable resources. Moreover, financial benefit could be gained by recovering these metals while detoxifying the water for recycling or soft disposal. Recovery of metals from effluent streams is thus in line with the principles of sustainable development.

Growing concerns about the environmental pollution, economic impact, and the potential threat that these heavy metals pose to human being stimulated increasingly stringent control on the discharge of industrial wastes. Considerable efforts have been devoted to developing fundamental understandings and viable technologies to reduce environmental consequences of industrial wastes,

aiming at cost effective and sustainable removal or selective recovery of heavy metals from industrial effluents [5, 6, 7, 8].

6.2 Existing Technologies for Heavy Metal Removal

A number of approaches have been developed or suggested for the treatment of industrial effluents in order to meet mandatory discharge standards. The most commonly used techniques are precipitation, adsorption, ion exchange, reverse osmosis, and ion flotation. A brief overview of these existing technologies is given here.

6.2.1 Precipitation

Precipitation is a well-known process capable of removing heavy metals from aqueous solution [9]. For example, by the addition of sodium hydroxide or lime, the solution pH is raised to a regime exceeding the solubility of metal hydroxides, causing the precipitation of metal hydroxides and lowering the concentration of metal ions in solution. This method is effective for the removal of large quantities of metals from contaminated water and is extensively used in industry because of its simplicity. The problems associated with precipitation process are slow solid–liquid separation, low density of solids, and the ultimate disposal of the voluminous sludge which often contains a high content of water. The inappropriate disposal of unstable precipitates may cause secondary contamination of water because metal ions can be leached out from the sludge, returning to the aqueous environment. In addition, a polishing step is required for most precipitation processes in order to achieve low residual levels of metal ions in the processed water. Furthermore, precipitation is a costly method without the offset of producing secondary resources. There are only a few metals that can precipitate to form a valuable solid product, such as gypsum for the construction industry.

6.2.2 Adsorption

Adsorption process is based on the adsorption of soluble contaminants in solution onto a solid adsorbent. The widely used material of adsorption is activated carbon though sandstone, fly ash, clay, and other surface reactive adsorbents are often used in wastewater treatment. This method is capable of removing most toxic species, including Cu^{2+}, Cr^{4+}, Pb^{2+}, Hg^{2+}, and Zn^{2+}. Since most adsorption processes are preformed in a column packed with adsorbents, a prefiltration step is needed for most industrial applications in order to remove finely divided solids which may, otherwise, clog the channels

available for transporting liquid. Regeneration of the adsorbent and the cost for carbon replacement are issues to be concerned with. In addition, the surface functionalization by solvent deposition and covalent attachment on ceramic supports as commonly used failed to demonstrate high ligand coverage and stability of the attached functional groups. These drawbacks can be overcome by applying the sol–gel processing method to form a silica network with functional ligands [10].

6.2.3 Ion Exchange

The ion-exchange process relies on the exchange of certain undesirable cations or anions in wastewater with sodium, hydrogen, chloride, etc., in porous polymer resins of either a styrene or an acrylic matrix. The ion-exchange process continues until the solution being treated exhausts the resin exchange capacity. The exhausted resin must be regenerated by other chemicals which replace the ions captured in the ion-exchange operation, thus converting the resin back to its original composition for reuse in the next cycle. Many chelating resins have been reported but they do not show physical rigidity due to swelling of the polymeric skeleton, poor wettability, small surface area, poor selectivity, slow adsorption rate, and challenge in regeneration [11, 12]. Clogging and regeneration of resins, similar to that encountered in the adsorption process by activated carbon, may also be experienced in this approach. In practice, wastewater to be treated by ion exchange is generally pre-filtered to remove suspended solids which could mechanically clog the resin bed.

6.2.4 Reverse Osmosis

In industry, reverse osmosis removes minerals from boiler water at power plants. The water is boiled and condensed over and over again and must be as pure as possible to avoid fouling or corrosion of boilers. It is also used to clean effluent and brackish groundwater. The apparent limitations of this approach are concerns with membrane lifetime, loss in flux rate, relatively small amount of effluent that can be treated and limited types of materials that can be removed. Some solutions (strong oxidizing agents, solvents, and other organic compounds) can cause dissolution of the membrane materials. Fouling of membranes by suspended solids in wastewater is another concern. Pretreatment of effluents is thus necessary for reverse osmosis system.

6.2.5 Ion Flotation

Ion flotation involves the removal of surface-inactive ions from aqueous solutions by the addition of surfactants capable of forming ion–surfactant pairs,

and the subsequent passage of gas bubbles through the solutions. Due to the surface active nature of the surfactant, the ion–surfactant pairs are concentrated at the air/water interface of bubbles which float to the surface of the solution where they are removed as foams. In general, an ionic surfactant (known as collector in mineral processing) of opposite charge to the surface-inactive contaminants is used to induce an electrostatic force between them, thus forming ion–collector pairs. However, it is possible to use a non-ionic surfactant capable of forming coordination bonds with contaminants as a collector [13]. Ion flotation has been widely applied in base metal recovery, wastewater treatment, removal of radioactive elements from water, and the recovery of precious metals [14, 15]. The major advantage of ion flotation over activated carbon adsorption is that air bubbles are relatively inexpensive to produce and no desorption step is required. However, a stoichiometric ratio of surfactant molecules to ions to be removed is needed in ion flotation. Therefore, the process can be quite expensive and may only be used to float ions in solutions of low concentration.

In summary, each technique reviewed has its own limitations in industrial applications although they have been practiced to a varying degree. Low selectivity, complex to operate, high capital and energy costs, and slow separation kinetics are the commonly inherent shortcomings. In addition, it is also inefficient in treating waste streams that contain low concentrations of contaminants and may fail when handling wastes of complex chemistry. Because the active materials are difficult to regenerate, these processes generate significant amounts of secondary waste.

6.3 Magnetic Composite Sorbents (MCS)

MCS refers to the tailoring of physical, chemical, and surface properties of magnetic composites to enable selective or non-selective attachment to the composites of ions, molecules, macromolecules, cells, colloidal particles, or liquid phases from complex fluid systems [16]. In essence MCS is an interdisciplinary subject since it requires an integrated approach involving the manufacture and surface hybridization of appropriate composites with careful attention to the constraints imposed by end users. The properties of the composite particles are of critical importance to the successful application of the technology. The composite particles must fulfill a number of criteria relating to their shape, size, porosity, mechanical strength, chemical inertness, density, magnetic properties, wettability, surface charge, surface concentration of reactive groups, cost, ease of manufacture, sterilizability, aggregation properties, and regeneration [16].

Some application examples of this technology are the use of magnetite particles to accelerate the coagulation of sewages [17], removal of radio nuclides from milk by functionalized polymers such as resin with embedded

magnetite [18], the adsorption of organic dyes by poly(oxy-2,6-dimethyl-1, 4-phenylene) [19], removal of an azo-dye, acid red B (ARB) from water by $MnO–Fe_2O_3$ composites as adsorbent–catalyst materials [20], oil spill remediation by polymer-coated magnetic particles [21], and removal of heavy toxic metals and purification of the hazardous waste waters by magnetic filtration/sorption technology [22, 23, 24]. In addition, magnetic nanoparticles with appropriate surface coatings have found various biomedical applications, as contrast agents in MRI (magnetic resonance imaging), colloidal mediators for cancer magnetic hyperthermia, and active constituents of drug-delivery platforms, as well as for tissue repair, cell and tissue targeting, and transfection [25, 26, 27, 28].

For selective recovery or removal of heavy metals from voluminous industrial effluents with suspended solids, the use of MCS is of particular importance, as the technique combines the advantages of technical feasibility and flexibility with economic value and environmental acceptability. A schematic illustration of MCS is shown in Fig. 6.1 [29]. In this figure, magnetic composite particles are added to a hydrometallurgical processing suspension that contains precious metal ions and many other waste solid particulates. The precious metal ions selectively adsorb on the added magnetic composite particles through molecular recognition by surface functional groups. Along with the magnetic particles, the adsorbed metal ions are separated from the suspension by an external magnetic field. The metal ions loaded on the isolated magnetic particles can be stripped off by, for example, acid washing, and the particles can then be reused. Precious metals can, on the other hand, be produced from the concentrated ion solution by precipitation, crystallization, and/or electrowinning.

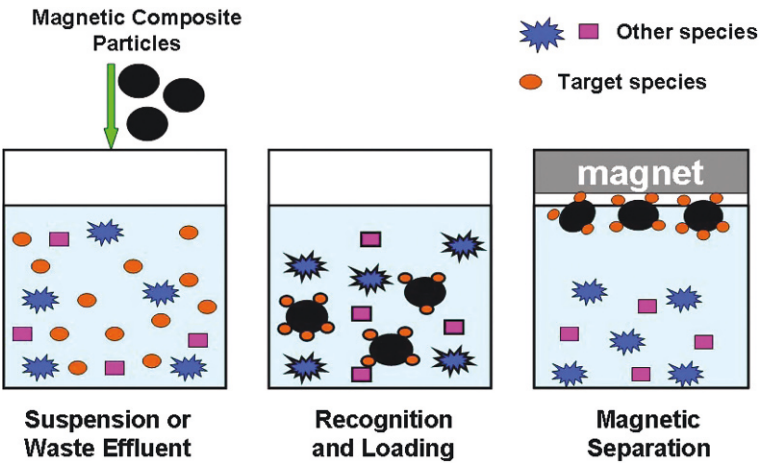

Fig. 6.1 Illustration of magnetic separation technology in metal recovery from an industrial effluent

The methods used to prepare the magnetic particles can be divided into two general types [30]. The first method involves the coating of an existing magnetic material. Representative examples of this type are adsorption of proteins onto nickel microspheres [31], coupling of functionalized polymeric silane on magnetite [32, 33], adsorption of serum albumin onto aggregates of magnetite or other magnetic metal oxides during or immediately after ultrasonic disruption of the aggregates [34, 35], polymerization of monomers in the presence of magnetite [36, 37], encapsulation of iron oxide by emulsion polymerization [38, 39], and adsorption of Protein A to magnetite [40]. The second method involves the generation of the magnetic material in the presence of the coating material. Representative examples are precipitation of magnetite in the presence of dextran [41], serum albumin [42], and arabinogalactan [43]. A related method is the precipitation of magnetite in the pores or on the surface of an existing particle as magnetic tags [44].

In magnetic composite synthesis, magnetite is the most commonly used magnetic material since particles prepared from freshly precipitated magnetite are claimed to be superparamagnetic [45], a property which facilitates re-suspension of the particles after magnetic separation. Other magnetic materials, such as γ-Fe_2O_3, metallic iron, cobalt, and nickel, are also used. In a recent review [46], Li et al. elaborated the synthesis, properties, and environmental applications of nanoscale iron-based materials. Different physical and chemical methods used for synthesizing nanoiron-based particles with desired size, structure, and surface properties were reported. The applications of this kind of particles include degradation of chlorinated organic compounds (such as trichloroethane (TCA), trichloroethene (TCE), tetrachloroethene, or carbon tetrachloride), removal of metallic ions (such as arsenic (As), lead (Pb), mercury (Hg), and chromium (Cr)) and inorganic contaminants (such as selenium (Se), denitrification and reduction of carbon monoxide (CO)). A key mechanism of these applications is oxidative nature of iron.

Lu et al. [47], on the other hand, provided a detailed report on the special features, synthesis, protection/stabilization, functionalization, and application of magnetic nanoparticles. Substantial progress in the size and shape control of magnetic nanoparticles has been made by developing methods such as co-precipitation, thermal decomposition and/or reduction, and molecular template or hydrothermal synthesis. Protection of magnetic particles against corrosion remains a major challenge. Therefore suitable protection strategies, for example, surfactant/polymer coating, silica coating, and carbon coating of magnetic nanoparticles or embedment of nano magnetic particles in a matrix/support have been emphasized. Properly protected magnetic nanoparticles can be used as building blocks for the fabrication of various functional systems and applied to catalysis and biotechnology.

It is evident that the application of magnetic nanocomposite particles to separation science and technology offers great flexibility. A key-and-lock relationship shown in Fig. 6.2 [48] can be developed to describe various applications of magnetic nanocomposites. The lock varies from metals or toxic species as in

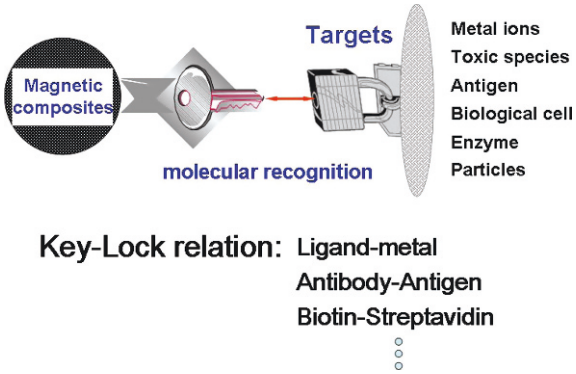

Fig. 6.2 Key-lock relation in potential applications of magnetic composites particles

environmental applications, to antigen or streptavidin as in biological applications, while the key could be a specific ligand, antibody, or biotin. In this communication, we focus on the research progress over the last ten years on the development of magnetic nanocomposites particles as sorbent for industry effluent management. The approaches such as molecular self-assembly (SA), direct silanation, two-step silica coating, and mesoporous silica coating for preparation of magnetic nanocomposites particles and their target applications will be reviewed.

6.4 Methods for the Preparation of Magnetic Nanocomposites

6.4.1 Molecular Self-Assembly (SA)

SA is a process of spontaneous formation of a functionalized organic molecular (surfactant) layer on an inorganic substrate in an organic or aqueous solvent [49]. The preparation and characterization of self-assembled (SA) monolayer coatings of various organic surfactants on flat metal or metal oxide surfaces have been reported in a number of publications. These include alkysilane surfactant on hydroxylated surfaces, such as silica and aluminum oxide; alkanethiolates on gold, silver, and copper; alcohol and amines on platinum; and carboxylic and hydroxamic acids on aluminum oxide and silver oxide [50, 51, 52, 53, 54, 55, 56, 57, 58, 59]. In more recent publications, bolaamphiphiles with two different reactive head groups at both ends of the molecule are used to manipulate the architecture of organic films on flat metal or metal oxide surfaces such as gold, silica, and aluminum oxide [60, 61, 62, 63, 64]. By controlling the relative reactivity of the two functional groups with the surface, one functional group can anchor chemically onto the surface and the other remains reactive to target species. However, most of the fabrications of SA monolayers are limited to flat substrates and few publications have described

the preparation and characterization of SA coatings using bolaamphiphiles on metal or metal oxide powders, particularly of magnetic iron oxides which have potential applications in drug-delivery, magnetic carrier technology, raw material recovery, biological cell separation, magnetic fluids, magnetic ink, and magnetic memory media [65, 66, 67, 68, 69, 70].

In our laboratory [71], 16-mercaptohexadecanoic acid (MHA) ($HS(CH_2)_{15}COOH$) was assembled onto nanosized magnetic particles (γ-Fe_2O_3) from chloroform. To elucidate the reactivity of polar groups with γ-Fe_2O_3, stearic acid [$CH_3(CH_2)_{16}COOH$], are also self-assembled into monolayer coatings on magnetic particles and characterized by X-ray photon spectroscopy (XPS), diffuse-reflectance infrared Fourier transform spectroscopy (DRIFTS), and film flotation. It is expected that the carboxylic head group (−COOH) of MHA preferentially anchors to the surface of the magnetic particles so that the thiol (−SH) on the other end remains available for different reactions.

The most significant spectral change in the XPS spectra of γ-Fe_2O_3 with and without self-assembled layers is the appearance of two C_{1s} bands at 288.3 (COO−) and 284.6 eV (C–C) [72], when the γ-Fe_2O_3 powders were treated by stearic acid and MHA. The ratio of area under the C_{1s} band of higher binding energy to that of lower binding energy was calculated to be ca. 1:17 and 1:15 for γ-Fe_2O_3 self-assembled with stearic acid and MHA, respectively. These values are in excellent agreement with those derived from the molecular structure. For the MHA treated sample, a sulfur band of S_{2p} at 163.3 eV was observed. This band is characteristic of –SH or –S–S– groups without oxidization to sulfate. These spectral changes indicate the presence of self-assembled stearic acid and MHA layer on γ-Fe_2O_3.

To determine the orientation of surfactant molecules in the SA monolayers, a surface-sensitive, DRIFTS was used, and the spectra are shown in Fig. 6.3. Over the high wavenumber region, the CH_2 stretching vibration bands at 2,924 and 2,851 cm^{-1} are observed, suggesting the presence of a hydrocarbon chain as anticipated. The CH_2 bands appeared at the same band positions for bulk MHA and for MHA coated on γ-Fe_2O_3. However, the bands are sharper for the MHA on γ-Fe_2O_3 than for bulk MHA, indicating a more ordered polymethylene chain and confirming the assembly of a densely packed surfactant monolayer. However, over the low wavenumber region, the MHA on γ-Fe_2O_3 resulted in a different spectral feature than bulk MHA. The absence of the carbonyl band at 1,703 cm^{-1} and the presence of a carboxylate band at 1,433 cm^{-1} for the MHA on γ-Fe_2O_3 suggest not only the anchoring of carbonyl groups on γ-Fe_2O_3, transferring a carbonyl to the carboxylate functionality, but also the absence of the second MHA layer, i.e., only a monolayer coverage. Should the second layer be present, a mixed functionality of carboxylate from the first layer (band at 1,433 cm^{-1}) and carbonyl from the second layer (band at 1,703 cm^{-1}) would be observed.

From film flotation test, the differences of critical surface tensions of MHA-coated γ-Fe_2O_3, stearic acid-coated particles, and DTDPA (3,3′-dithiodipropionic acid)-coated particles further confirmed that the terminal group of the MHA

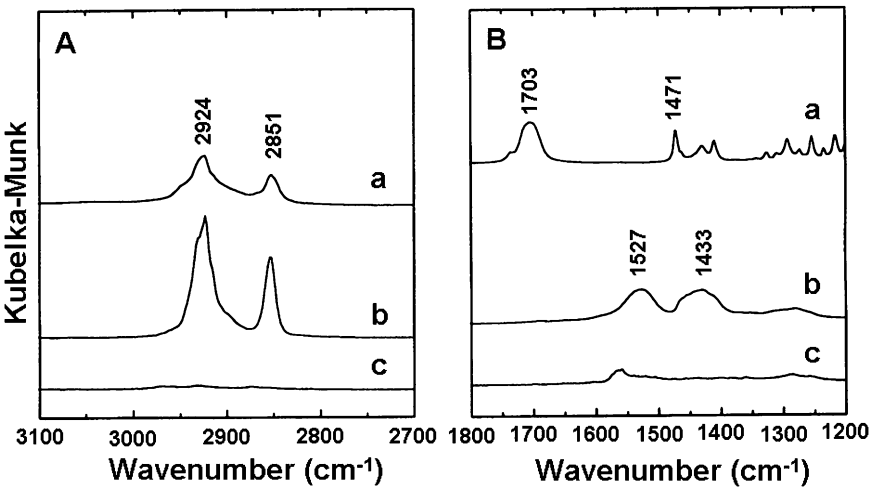

Fig. 6.3 Infrared spectra in the high (**A**) and low-frequency (**B**) regions for (a) MHA in KBr, (b) MHA on γ-Fe_2O_3, and (c) γ-Fe_2O_3

coated on γ-Fe_2O_3 is thiol or bisulfide, rather than a carbonyl, sulfate, or sulfonate functionality. It also indicated that long chain hydrocarbon association of amphiphiles is necessary for a densely packed monolayer, such as MHA on γ-Fe_2O_3.

To examine the nature of the packing of various surfactants on the γ-Fe_2O_3 particle surface and to investigate the stability of self-assembled layers to harsh environments, leaching experiments were conducted by placing the treated particles in acidic (pH 3) and alkaline (pH 10) media. These experiments showed that the surface coatings with stearic acid and MHA are stable in aqueous solutions over a pH range from 3 to 10 for a few days. No ferric ions were leached into the solution, indicating that the surface coatings are tightly packed. After the leachate was removed and the powder dried, the same values of critical surface tension were obtained, suggesting that the surfactant layer prepared with stearic acid and MHA remained stable under the test conditions. In contrast, ferric ions were detected (by sodium thiocyanide titration) in leachate of DTDPA-coated γ-Fe_2O_3 exposed to distilled water. These observations confirm the packing information inferred from DRIFTS and film flotation.

It is important to note that a monolayer coating of MHA on γ-Fe_2O_3 only reduced the saturation magnetization (M_s) of magnetic particles marginally (2 emu/g) from 52.7 emu/g of bare γ-Fe_2O_3. The particles remained super-paramagnetic after coating.

The magnetic particles fabricated with thio or disulfide groups have potential applications in various areas. It is well known that thio and disulfide groups have strong affinity with precious metals, such as gold, silver, and copper [73, 74]. The fabricated magnetic particles of large surface area could, therefore, be used to

capture gold and silver ions from their leachates. The metal-loaded magnetic particles can then be readily separated from leaching solutions using magnetic separation. In addition, the approach can be readily extended to the fabrication of magnetic particles with other customized functional groups by controlling the reactivity of functional groups of a bolaamphiphile with magnetic particles. The functionalized magnetic particles can be used to recover secondary resources or to remove toxic species from industrial effluents by controlling the reactivity of functional groups with targeted species in the effluents. In addition, the special affinity of thio with antibodies makes fabrication of thio-containing magnetic nanoparticles of special interest in the biological applications.

6.4.2 Direct Silanation

Although self-assembled bolaamphiphile monolayer on magnetic particles is densely packed and stable in acidic and basic environments, the control of the reactivity between the two functional groups and the substrate is crucial in determining the quality of the coatings. The ideal case is that one functional group anchors chemically to the surface while the other is unreactive to the surface. This requirement limits the type of functional groups that can be directly introduced onto the magnetic particles.

A more general approach to fabricating magnetic nanocomposites is direct silanation. Silanation is to use silane-coupling agents to tailor surface properties of metal oxides [75]. A typical silane-coupling agent has the structure of $Y–(CH_2)_n–Si–X_3$, where X represents the alkoxy or halide groups and Y, the organic functional groups, including amine, thiol, carboxylic, phosphate, vinyl, cyanide, and methacrylate. The $Si–X_3$ group hydrolyzes readily in the presence of water and catalyst to form silanol groups which couples with surface metal hydroxyl groups, forming Si–O–M bonds upon dehydration. As a result, the organic functional groups (Y) remain reactive on the surface. This unique feature of silane-coupling agents has made silanation a widely used method in modifying surface properties. A large volume of literature is available in this area [76, 77, 78, 79, 80, 81].

In the patent of Whitehead et al. [82], they described the procedures of direct silanation of functional groups, including aminophenyl, amino, hydroxyl, sulphydryl, aliphatic, and mixed functional groups, on paramagnetic particles and pointed out the potential applications of the resultant magnetic particles. However, no fundamental characterizations of the silanized films are available, in particular the stability of the coatings and possible leaching of iron from the substrate.

It should be noted that coating of silane-coupling agents by silanation is a multistep process. A triangular relationship among substrate, silane, and solvent, along with the parameters that need to be considered, is shown in Fig. 6.4 [6]. Evidently, hydrolysis is necessary but must be controlled to avoid intramolecular condensation of silane-coupling molecules. It is also important

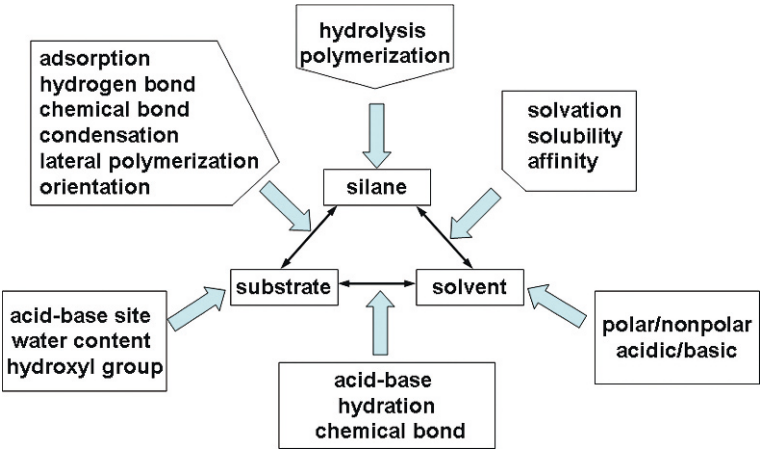

Fig. 6.4 Interactions involved in silanation. [6]

to hydrolyze surface metal species to obtain the maximum density of bindings between coupling agent and surface. The interactions and competition between the solvent–solute, solvent–substrate, and solute–substrate dictate both coverage and quality of the resultant film. The last (but not the least) parameter (not included in Fig. 6.4) that needs to be considered is the post-curing during which thermal dehydration enhances chemical binding between substrate and coupling molecules and lateral polymerization among the coupling molecules, resulting in a robust film.

In our laboratory, we synthesized and studied the silanation of superparamagnetic (γ-Fe_2O_3) particles with focus on characterization of the coated organic films, such as organo-amine functional groups (3-aminopropyl triethoxy silane (APTES)). The characteristics investigated included the state of the amine groups, the binding of silane on magnetic particles, and the stability of the film [6].

APTES were silanized on γ-Fe_2O_3 from both water and toluene solutions. The presence of N_{1s} and Si_{2p} bands on XPS spectra of synthesized particles suggests that APTES has deposited on γ-Fe_2O_3 from both solutions. The two bands of nitrogen centered at 399.4 and 401.3 eV are attributed to the protonated and non-protonated amines, respectively. The fraction of amines protonated is larger in the films silanized from water (26%) than that from toluene (17%), indicating the stronger interaction of amine groups with γ-Fe_2O_3 in water than in toluene. Band-fit analysis revealed that the proportion of oxygen in Si–O environment is higher for the film silanized in water (24%) than in toluene (14%), suggesting a higher degree of hydrolysis of APTES on γ-Fe_2O_3 from water. The XPS analysis also suggests the deposition of APTES as monolayers, and the moderate increase in the number of APTES molecules on γ-Fe_2O_3 from aqueous solutions is attributed to the increased APTES

packing density rather than the formation of a three-dimensional gelation which involves three-dimensional links among APTES molecules.

To determine the degree of hydrolyzation of ethoxy groups and subsequent cross-linking, which have significant impact on the density and stability of the film, DRIFT spectra were therefore collected. In contrast to silanization in water, DRIFTS spectra of the APTES film deposited from toluene solutions showed vibrational bands of methyl group at 2,974 and 2,887 cm^{-1}, indicating the presence of small fraction of unhydrolyzed ethoxy groups in the film. The unhydrolyzed ethoxy groups on the surface are anticipated to inhibit the lateral polymerization of APTES, thus resulting in a poorer packing density and lower surface coverage films of lower stability than those of the film silanized from water where the hydrolysis is more effective. This observation is consistent with the findings from XPS.

To further confirm the orientation of APTES on γ-Fe_2O_3, the electrokinetics (zeta potentials) of the coated particles were measured. The isoelectric point (IEP), the point where zeta potential is zero, of the particles silanized with APTES from water and toluene was found at about pH 8.5 and 9.2, respectively, in contrast to pH 4.5 for uncoated γ-Fe_2O_3. The similar electrokinetics confirms the condensation of APTES on γ-Fe_2O_3 from both water and toluene with amine groups facing the environment and remaining reactive. The difference in the measured zeta potentials using the particles silanized in water and toluene reflects mainly the variation of APTES orientation on the particles. A slightly lower IEP value observed for the particles silanized in water suggests that more amine groups were hidden inside the film compared to the silanation in toluene. As a result, the contribution from amine groups to the number of positive surface sites decreases while that from silanol groups to the number of negative sites increases. These two effects result in a lower IEP of γ-Fe_2O_3 particles silanized in water than in toluene as experimentally observed. This finding is consistent with XPS analysis, which showed a higher degree of protonation of amine groups considered to bind with the surface.

The stability of the silanized APTES films on γ-Fe_2O_3 was investigated by leaching the particles in pH 2 HCl solutions for 20 h. It was found that the amount of iron leached out reduced from 60 mg/g for unsilanized γ-Fe_2O_3 to 34 mg/g for silanized γ-Fe_2O_3 in water and toluene. Compared to the particles coated with MHA using the SA method, the amount of iron leached out is significant, suggesting that the original particles were not fully protected by APTES, compounded with some degree of detachment of APTES from the surface in acid solutions, for direct silanation from water and toluene.

Detachment of silanized APTES was confirmed by zeta-potential measurements as shown in Fig. 6.5. After leaching, the zeta potentials shifted back towards the zeta-potential values of unsilanized particles. Figure 6.5 also shows a much greater shift in IEP by base attack, suggesting that the APTES coating is less stable in basic than in acidic environments. Similar trends in electrokinetics were observed for particles silanized from toluene. In the base environment, an IEP shift from pH 9 to 4.3 was observed. However, in acidic solution, the films

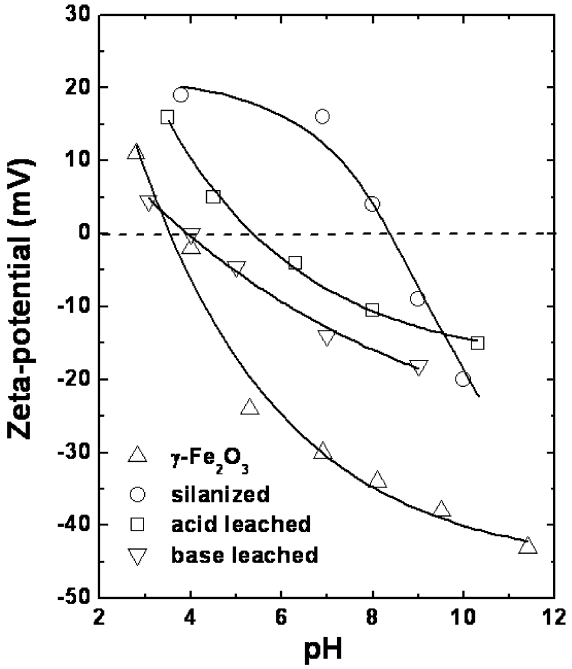

Fig. 6.5 Zeta-potentials of APTES-silanized magnetic particles from water before and after acid and base leaching

formed in toluene were more stable with an IEP shift from pH 9.0 to 8.5 as compared to that from pH 8.5 to 5.5 for the particles silanized in water. This may be related to the lower degree of protonation of amine groups in the films formed from toluene. The protonated amine, attached to the surface through electrostatic attraction, may be detached in acid solution as amine molecules are more soluble at low pH.

Clearly, the direct silanation of APTES from water and toluene solutions on γ-Fe_2O_3 is not suitable for engineering magnetic composite particles for environmental and biological applications. Since silica is more stable in acidic solutions than iron oxide, an alternative approach is to coat the magnetic particles with a thin silica film first, followed by conventional silanation on silica, to improve the film stability and density of surface functionality.

6.4.3 A Novel Two-Step Silica Coating

The challenge for the applications of magnetic nanocomposites is to improve the stability of magnetic particles against coagulation and leaching in an acidic environment, with maximized magnetization in an external magnetic field. Ultrathin silica films coated on nanosize magnetic particles are of special interest due to

their high stability against aggregation and acid leaching with minimal reduction of magnetization. The silica surfaces are amenable for further functionalization by silanation, using silane-coupling agents to produce functional magnetic nanocomposites. This approach remains, therefore, a principal method in engineering magnetic nanocomposites. Two conventional methods suitable for silica coatings on finely dispersed particles are sol–gel and dense-liquid processes.

6.4.3.1 Sol–Gel Process

The sol–gel process is a commonly used method for coating fine particles. The coating is performed in an organic solvent and the process is based on hydrolysis of precursors, such as tetraethoxy silane (TEOS), in the presence of water and a catalyst, followed by condensation of hydrolyzed TEOS on surface containing metal hydroxyls. With controlled hydrolysis of TEOS, an M–O–Si chemical linkage is established between surface metallic atoms (M) and TEOS, followed by lateral polymerization and finally formation of a three-dimensional network via siloxane bond formation (Si–O–Si) with increasing TEOS concentration and degree of hydrolysis. However, it is well-known that silica coatings by the sol–gel process are porous, as schematically shown in Fig. 6.6a. To protect the substrate particles from dissolving in acidic solutions, a thick layer of coatings is required, which reduces the magnetizability significantly and hinders the technological applications of magnetic nanocomposites.

6.4.3.2 Dense-Liquid Process

This method was first introduced by Iler in 1959 to coat titania with a silica layer from supersaturated silica solutions [83]. Nowadays, the dense-liquid process is widely used to form silica films on surfaces of carbon, steel, alumina, and polymer resins to promote adhesion, to minimize photodegradation, and/or to prevent materials oxidation/corrosion [84, 85, 86]. By controlling the supersaturation level of monosilicic acid (constant reactant addition), silica layers can be formed on surfaces through heterogeneous followed by homogeneous coatings. It has been recognized that surface coating using the dense-liquid process is a complex physicochemical process. At least three competitive processes are present simultaneously: (i) heterogeneous coatings (on a substrate of

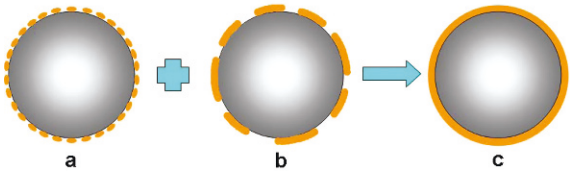

Fig. 6.6 Schematics of silica-coated magnetic nanocomposites by (**a**) sol-gel, (**b**) dense-liquid, and (**c**) two-step, i.e. (**a**) followed by (**b**), processes

different chemical compositions; e.g., SiO_2 on γ-Fe_2O_3); (ii) homogeneous coatings (on a substrate of the same chemical compositions; e.g., SiO_2 on SiO_2); and (iii) homogeneous nucleation (e.g., formation of SiO_2 nuclei) followed by homogeneous coatings. In general, the lowest supersaturation level is required for homogeneous coatings, followed by heterogeneous coatings, and finally homogeneous nucleation, which requires an excess energy, as predicted by the Kelvin equation, to account for extremely high curvatures of nuclei [87, 88]. Although in general, homogeneous nucleation can be avoided by careful control of (silica) supersaturation level just above the critical concentration of heterogeneous coatings (on maghemite), the homogeneous surface coating often presents a challenge to uniform surface coatings. It is evident that, as soon as the substrate is coated with silica even at the submonolayer level, the growth of the coated area (a process similar to homogeneous coating) prevails because it requires a lower supersaturation level. As a result, a non-uniform and patchwise (island) coating, as schematically shown in Fig. 6.6b, is often obtained. With the dense-liquid-coating process, it is therefore inevitable to expose substrate cores to the environment and poison the system by the released species, unless a thick coating layer is applied.

6.4.3.3 Two-Step Coating

It is clear that neither the sol–gel nor the dense-liquid process could meet the requirement of making magnetic nanocomposites of certain technological applications. To coat magnetic particles with a thin protective silica layer and minimize reduction of saturation magnetization, a novel two-step coating process (the sol–gel followed by the dense-liquid coating) has been developed in our laboratory [89]. This approach is based on the idea that the sol–gel process can coat a surface uniformly, although the film is often porous, as shown in Fig. 6.6a. In the second step, using the dense-liquid process, the residual ethoxy groups in nano or microsize pores of the silica film prepared using the sol–gel process are further hydrolyzed, and the pores are anticipated to be closed by and filled with silica under low supersaturation conditions. It is clear that the two-step silica-coating process integrates the advantages of uniform coatings by the sol–gel process and a low supersaturation level required for homogeneous coating by the dense-liquid process. As a result, a uniform thin silica layer, as shown in Fig. 6.6c, can be coated on maghemite or any other magnetic nanoparticles to protect the particles with minimal reduction in saturation magnetization (a key feature of magnetic nanocomposite sorbent) and to provide a surface for further functionalization. It is important to note that the objective of the two-step coating is not to coat more silica on the particles but rather to protect the substrate particles with the thinnest silica coatings possible to maximize the magnetic property of the coated particles.

For comparison, the silica was coated on γ-Fe_2O_3 at the 11 wt% silica level using these three methods. The presence of a silicon band at 103.4 eV and an additional oxygen band at 532.8 eV on the XPS spectra of coated particles

confirms the coating of silica on γ-Fe_2O_3. By the analysis of XPS narrow-scan spectra, semi-quantitative analysis showed an area ratio of silica to iron band (Si/Fe) of 0.7, 4.1, and 4.1 for particles coated using the dense-liquid, sol–gel, and two-step processes, respectively. A higher Si/Fe ratio indicates a high degree of silica coating. It is evident that the silica-coating efficiency is comparable for the sol–gel and two-step processes, higher than that of the dense-liquid process.

The formation of silaxone bonds was confirmed for all the coatings by DRIFTS [48]. In contrast to the dense-liquid or two-step-coating process, unhydrolyzed ethoxy was detected for particles coated using only the sol–gel process. The presence of Si–OEt terminal groups is partially responsible for the porous nature of the coated films by the sol–gel process.

To further study the surface properties of the magnetic nanocomposite particles, the electrokinetics of the particles was measured, and the obtained IEP for maghemite particles coated with different methods are summarized in Table 6.1. As shown, the IEP of pH 3 for maghemite coated using the dense-liquid process is significantly lower than that for uncoated maghemite particles (pH_{IEP} 4.5). However, this value is higher than the IEP of fused silica (pH_{IEP} 2.1), suggesting that silica was coated on maghemite, but only partially (probably in the form of islands) by the dense-liquid process, as illustrated schematically in Fig. 6.6b. When the sol–gel process was used, an IEP of pH 2.4 was obtained, showing an improved coating compared with the dense-liquid process. This value, however, remains slightly higher than the IEP of fused silica, indicating that the surface coating is either incomplete or porous, as confirmed later by leaching tests (Table 6.1). When the two-step process was used, an identical electrokinetic behavior between the coated particles and fused silica was observed over the pH range studied, indicating the same surface properties between the two and confirming a full coverage of particles with silica. It is important to note that silica-like electrokinetics of silica-coated maghemite with the two-step process ensures its dispersion, as required in many of its technological applications.

Leaching tests were conducted to further examine the state of silica film on γ-Fe_2O_3. The results also are summarized in Table 6.1 along with the saturation magnetization of coated particles. It is evident that the amount of iron leached out was below the detection limits for the particles coated with the two-step process in contrast to the single-step, either sol–gel or dense-liquid process where 1.1 or 2.8 mg of Fe per gram of particles was detected, respectively.

Table 6.1 Characteristics and stability of silica-coated γ-Fe_2O_3 by dense liquid, sol–gel, and two-step coating processes

Sample and methods	IEP (pH)	Fe leached in 0.01 M HCl (mg/g)	M_s (emu/g)
γ-Fe_2O_3	4.5	60.3	52.0
DL coating	3.0	2.8	48.5
Sol–gel	2.4	1.1	43.2
Two-step	2.2	–	42.5

Moreover, the saturation magnetization is comparable for particles coated with silica using the sol–gel and two-step processes, suggesting that the amount of silica on the surface is virtually the same and confirming the important role of the film structure in protecting the matrix component of magnetic sorbents for biological and environmental applications. It is evident that the two-step silica-coating process is successful in making base materials that can be further functionalized by the conventional silanation process to produce magnetic sorbents of a desired functionality.

6.4.4 Mesoporous Silica Coating

Despite the advantage of easy separation from complex multiphase systems by using MCS, the limited specific surface area of existing magnetic sorbents presents a major challenge to these applications of many technological importances. Even for very fine maghemite (γ-Fe_2O_3) particles ($\sim$30 nm), for instance, a specific surface area of only ca. 40 m^2/g is reported [48]. A further decrease in particle size to increase specific surface area is not desirable, because the magnetic forces exerted on these tiny magnetic particles are extremely weak for any substantial migration of the particles to a desired location for separation. Since the specific surface area for a given surface functionality determines separation capacity, there is an urgent need for an innovative approach to increase the surface area of magnetic sorbents.

Surfactant-templated mesostructure materials have played a prominent role in materials chemistry during the last decade. The excitement began with the discovery of hexagonally ordered mesoporous silicate structure by Mobil Corp. (M41S materials) [90, 91, 92] and by Kuroda, Inagaki, and co-worker (FSM-16 materials) [93, 94]. Having extremely high surface areas, these materials are easily accessible and of uniform nanopore structures and specific pore volume. Most importantly, the pore sizes exceeded those attainable in zeolites and they could be tuned in the nanometer scale by choosing an appropriate surfactant templating system, sometimes with a co-solvent or swelling agent [95, 96, 97, 98, 99, 100]. As a result, the applications of mesoporous materials in a wide range such as adsorption, separation, catalysis, biological sensing, medical diagnosis and treatment, molecular engineering, and nanotechnology were envisioned [101, 102, 103, 104, 105, 106, 107, 108].

However, the use of bulk mesoporous siliceous materials in many science and technological applications has inherent limitations, especially for adsorption and separation of targets or contaminants from multiphase industrial effluents of complex nature. One noticeable challenge is to separate the loaded fine particles from industrial effluents for safe disposal or recovery of the adsorbed valuables and recycle of the sorbents.

The above application limitations inherent in mesoporous materials and magnetic sorbents led us to develop a mesoporous material-based MCS. It is

anticipated that incorporating mesoporous coatings on a magnetic core could increase the specific surface area of the resultant magnetic particles drastically without sacrificing magnetization characteristics. Mesoporous magnetic nanocomposite particles of sufficiently high specific surface area formed in this way could be easily separated from a multiphase complex system by magnetic separation and effectively recycled or reused.

6.4.4.1 The Synthesis Process of Mesoporous Silica-Coated Magnetic Particles

The concept of template-based synthesis of mesoporous magnetic nanocomposite particles is illustrated in Fig. 6.7. In this synthesis, a thin silica layer is deposited on the surface of magnetite particles of desired sized (I). The purpose of silica layer is to protect the magnetic core from being leached into the mother system under severe industrial conditions. The resultant silica surface also facilitates the assembly of structured surfactant templates. With a negatively charged silica surface, cationic surfactant micelles self-assemble on the negatively charged silica layer (II), forming the desired structure. This step is highly dependent on micelle solution concentration and solvent quality [109]. The mesoporous silica network on the magnetic core (III) is formed by filling the spaces among the assembled micelle templates using the conventional sol–gel process [90, 110]. During sol–gel reaction, the positive nature of molecular templates promotes the formation of silica precipitates within the voids among the templates, resulting in a three-dimensional continuous silica network. After calcinations at desired temperatures to remove the surfactant templates from the formed silica network, pores are left on the surface (IV). The silica surface of the so-formed mesoporous magnetic nanocomposite particles allows a variety of surface functionalities to be obtained by versatile silanation chemistry (V), which enables "molecular recognition" in numerous applications [6, 111, 112].

The prepared mesoporous magnetic nanocomposite particles have the following important attributes: strong magnetization for efficient magnetic separation; large specific surface area for high loading capacity; well-sealed silica coatings to prevent the substrate materials from leaching into the mother

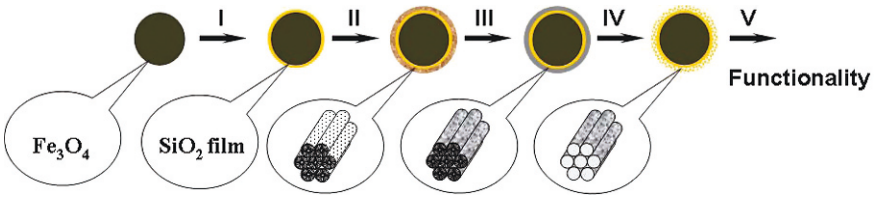

Fig. 6.7 Illustration of the proposed synthesis process for the preparation of mesoporous magnetic nanocomposite particles: dense-liquid-silica coating (**I**), molecular templating (**II**), sol-gel process (**III**), calcination (**IV**), and functionalization (**V**). [122]

system, as these could otherwise potentially contaminate or interfere with the normal functions of the system; and robust and specific functional groups on the surface to recognize and capture desire targets effectively.

6.4.4.2 Characterization of the Synthesis Process

Templating Study by AFM

Since the formation of mesoporous silica is built on the templates of surfactant molecular suprastructure, studies on the interactions of micelles with silica wafer which is used to represent the silica-coated surface on magnetic particles, were performed first.

Figure 6.8 (solid squares) shows the interaction forces between a cantilever tip and bare silica wafer in pure ethanol. There is a measurable attraction between the two at the separation distance below 10 nm. This attractive force is attributed to van der Waals forces. After replacing the ethanol by 5 mmol/L CTAC (cetyl-trimethyl-ammonium chloride) in ethanol solution and incubation for 1 h, a repulsive force between the tip and the sample starting at 20 nm during approaching is evident, as shown in Fig. 6.8 by open squares. This long-range repulsion is attributed to overlap of electric double layers around two positively charged surfaces. It appears that the cationic CTAC surfactant adsorbs on both AFM tip and silica surfaces, rending them both positively charged. At a separation distance around 9 nm, a maximum repulsive force barrier is observed and the tip jumps inward by a distance of 5.7 nm. After this jump-in, a continuous increase in repulsive force is observed as the sample pushed upward against the AFM tip by about 4 nm. This type of force profiles over such a short separation distance suggests a surface of compressible nature,

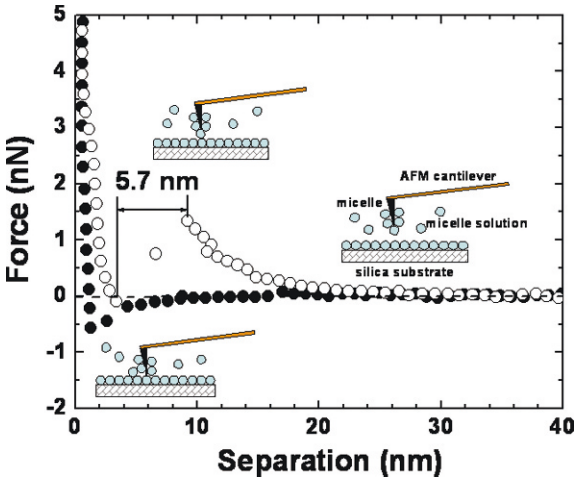

Fig. 6.8 Interaction forces between a bare silica wafer and AFM tip in ethanol (*solid squares*) and CTAC ethanol solutions (*open squares*)

in great contrast to the case measured in pure ethanol, indicating a soft silica surface in CTAC ethanol solutions. Considering all the details in this force profile, we can interpret the observed jump-in being the removal of a single layer of micelles from the gap between the tip and sample under the applied force of AFM tip. It is therefore reasonable to conclude that the silica surface is covered by CTAC micelles, and the size (diameter) of micelles or thickness of single layer micelles on silica is around 5.7 nm.

The AFM images of silica in ethanol and 5 mmol/L CTAC ethanol solution are shown in Fig. 6.9a,b, respectively. The silica wafer in ethanol exhibits a smooth, featureless topography (Fig. 6.9a). The image of silica wafer obtained in CTAC ethanol solution (Fig. 6.9b), on the contrary, shows well-defined features. It is interesting to note that the size of high spots is of 6 nm range, a value very close to the jump-in distance observed on the force profile. It appears that CTAC at 5 mmol/L concentration in ethanol forms pseudo-spherical micelles. These micelles are assembled on silica surface with well-defined voids of 10-nm diameter. For better view, a higher magnification image of the marked area is shown on the left corner with circles to highlight the voids. By filling in these voids with desired materials and removing the micelles, one can obtain mesoporous surfaces of desired materials. Clearly these assembled micelles can serve as templates for synthesis of mesoporous silica coatings on silica-coated magnetic particles.

Structural properties of surfactants and micellar solutions are crucial when preparing mesoporous structures. Surfactants in solution assemble into structures whose geometry can be described by the surfactant packing parameter [113, 114]. This packing parameter is defined as $g = v/al$, where ν is the volume of the surfactant tail, a is the effective head group area, and l is the length of the extended surfactant tail. An increase in the packing parameter represents a

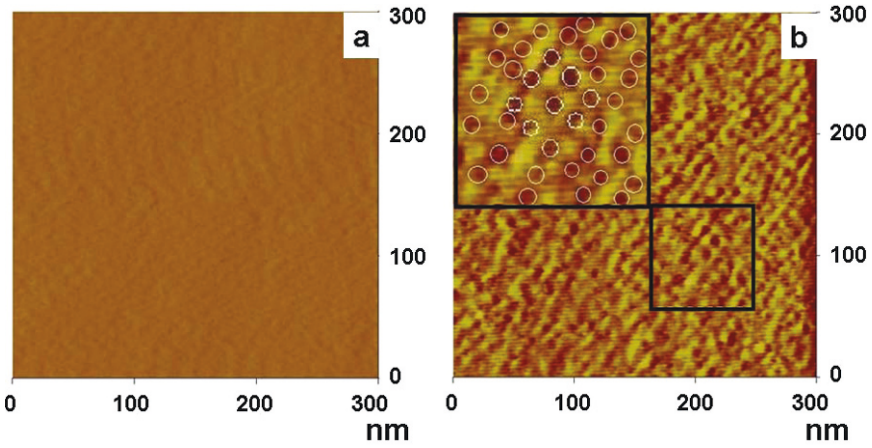

Fig. 6.9 Silica wafer in ethanol (**a**) and CTAC solutions (**b**) (*circles* represent voids to be filled by silica using sol-gel method)

reduction in curvature of surfactant aggregates. Such change may be achieved by altering the surfactant chain length, introducing twin chains, adding electrolytes, or by addition of polar and non-polar organic additives. Addition of short-chain alcohols as co-surfactants can also be used to alter the packing parameter, resulting in elongated micelles. Furthermore, addition of short-chain amine co-surfactants can decrease the pore size of the inorganic structures. By controlling the packing parameter of different surfactants, mesoporous materials of different structures have been synthesized [115, 116, 117, 118, 119]. Detailed descriptions of reaction variables are available in many monographs [109, 110, 120, 121].

Synthesis Process Monitored by Zeta-Potential Measurement

To confirm the role of each step in the proposed synthesis process, the zeta-potential distributions of bare magnetite (Fe_3O_4) (step I in Fig. 6.7 previous), dense-liquid silica (DLS) coated magnetite (step II in Fig. 6.7 previous), templated DLS magnetite (step III), sol–gel coated particles with templates (step IV), and the particles after calcination (step V) were measured over a wide pH range and the results are shown in Fig. 6.10.

The IEP of the bare magnetite is at pH 6.8, which is close to the value of mineral magnetite. After DLS coating, the IEP of the coated particles was found at pH 2.0, which is same as the IEP for mineral or fused silica. This silica

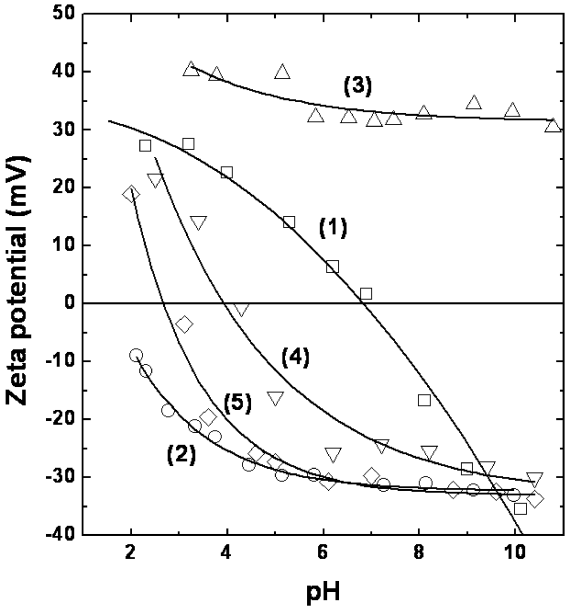

Fig. 6.10 Zeta potentials of different particles: (1) bare magnetite particles; (2) DLS coated magnetite particles; (3) templated DLS magnetite (4) sol-gel coated particles with templates; and (5) particles after calcination

coating acts as a protective layer to avoid direct contact of the magnetite core with the liquid to be treated. The negative charge of the silica-coated surface, on the other hand, facilitates the assembly of cation surfactant micelles arisen from electrostatic attraction. After molecular templating, the zeta potentials of the resultant particles were positive over a wide pH range. This resembles the zeta-potential variation of an oil droplet or air bubble with pH in CTAC aqueous solutions. After sol–gel reaction to fill the voids observed in the AFM images (Fig. 6.9b), the particles become negatively charged again. The measured IEP of the collected particles is at pH 4.0, which is different from that for a silica surface. This observation suggests that the trapped CTAC template partially balances the negative charge of silica in the templates voids. After calcination, the surfactant was removed, leaving behind the silica network on the magnetite surface, which has the IEP at pH 2.6, identical to the IEP value for silica. This finding confirms a full coverage of magnetite by silica, making the coated surface silica-like. To further confirm the protection of magnetite particles by the two-step silica coatings, the coated particles were immersed in a 1 M acid solution. The results showed a negligible amount of iron being leached out after a 12 h immersion, indicating good protection of magnetite by silica coatings.

To further verify the necessity and success of each step described in Fig. 6.7, the samples collected at various stages of the synthesis are characterized by DRIFT and XPS. The results can be found in our related publications [122].

The morphology of Fe_3O_4 and mesoporous silica-coated Fe_3O_4 is observed by TEM. Figure 6.11 shows that bare Fe_3O_4 has a well-defined crystalline feature with sharp edges and corners. In contrast, the TEM image of mesoporous silica-coated Fe_3O_4 shows diffuse edges. Combined with the evidence from

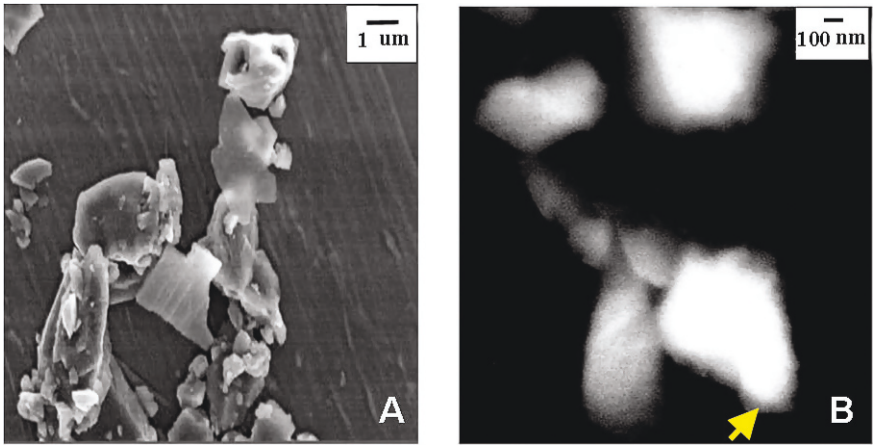

Fig. 6.11 TEM images of untreated Fe_3O_4 particles (**A**) and Fe_3O_4 particles with template-assisted silica coatings (**B**). Micrograph (**B**) is a dark-field image, obtained with tilt illumination

XPS analysis, these edges can be confidently considered as a homogeneous silica shell around the Fe_3O_4 cores. Figure 6.11b also shows that no more than one spherical core is included in each composite particle, suggesting that the aggregation of primary particles during synthesis is minimal.

Other Properties

To determine the porous nature of template-assisted silica coatings on the magnetite particles, standard nitrogen adsorption–desorption tests were performed. A large hysteresis existing between the adsorption and desorption branches, which is characteristic of highly porous materials, confirms the formation of mesopores on the magnetite particles. The detailed analysis of the results using the Brunauer–Emmett–Teller (BET) adsorption equation resulted in an increase in specific surface area from 0.07 to 52.3 m^2/g of total material by the deposition of a mesoporous silica film on magnetite cores [122].

To obtain a uniform and well-covered mesoporous silica layer on magnetic particles of high specific surface areas, the control of sol–gel conditions is extremely important. Many synthesis conditions, such as reaction time, reaction temperature, reactant concentration, type and amount of catalyst, and the quality of solvent, could affect the properties of the resultant silica coatings. Thus, optimizing sol–gel conditions by factorial design to minimize the numbers of synthesis while analyzing synergetic effects among different factors were studied [123]. The specific surface area of produced mesoporous silica-coated Fe_3O_4 was improved from 52.3 to 150 m^2/g, which provides three times more chances of the prevalence of functional groups, so the efficiency of the synthesized magnetic sorbent will be increased.

The magnetization characteristics of synthesized particles is a major concern for potential industrial applications. A strong magnetization is required for the collection by magnet from a complex, multiphase system. As shown in Fig. 6.12 the room temperature saturation magnetization of bare magnetite is 85.5 emu/g, which reflects the properties of Fe_3O_4 without any oxidation. For the final mesoporous magnetic nanocomposite particles, the saturation magnetization remains strong at 73.0 emu/g. The observed decrease of 15% in saturation magnetization is attributed to the coating of diamagnetic silica. Such a reduction does not hinder the subsequent magnetic separation after the resultant mesoporous magnetic particles are loaded with heavy metal ions. More importantly, magnetite particles coated with mesoporous silica remain fairly paramagnetic as shown by minimal coercivity and hysteresis on the magnetization curves (Fig. 6.12). This magnetization characteristic ensures that the magnetite particles do not become permanently magnetized after exposure to an external magnetic field, which in turn permits the particles to be re-dispersed without significant aggregation when the external magnetic field is removed.

Our study above clearly shows that with the concept outlined in Fig. 6.7, mesoporous magnetic nanocomposite particles can be successfully synthesized. The synthesized particles possess the necessary attributes of strong

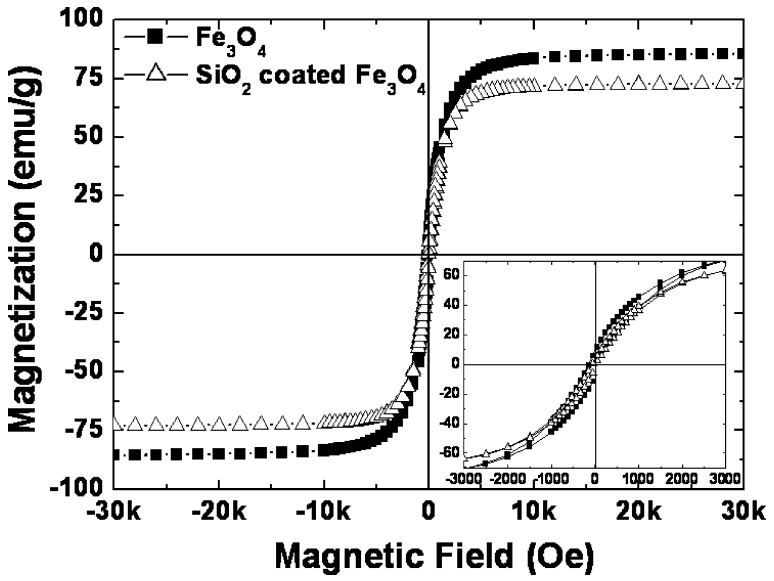

Fig. 6.12 Room temperature magnetization of bare magnetite and mesoporous magnetic nanocomposite particles

magnetization and high specific surface area for their applications as magnetic sorbents. The dense-liquid method followed by the template-assisted sol–gel process resulted in the formation of a uniform, mesoporous thin silica coating on magnetite particles. The resultant particles are well protected for iron leaching from cores, while providing surface amenable for functionalization via well-defined silane-coupling reactions. The functionalized particles have potential applications in a variety of science and engineering disciplines.

6.4.5 Silanation on Mesoporous Silica-Coated Magnetic Particles

As mentioned earlier, the synthesized mesoporous magnetic particles exhibited the necessary attributes of strong magnetization, high specific surface area and good protection of magnetic cores for applications as magnetic sorbents. Based on previous success of functionalizing silica surfaces using APTES to obtain reactive amino groups of high affinity for metals [6, 112], APTES was the common choice as silane-coupling agent. Furthermore, use of this short-chain alkane amine minimized blockage of pore channels.

The self-assembly of silane-coupling agents by silanation is a multistep process. In addition to complex interactions among the substrate, silane, and solvent, many other parameters need to be considered. According to Feng et al. [112], the number of surface silanol groups and the amount of adsorbed water

molecules on mesoporous materials are two key parameters in determining the density and quality of the functionalized monolayers. As can be seen from the silane-coupling reaction schematically illustrated in Fig. 6.4, surface silanols are essential because they are the active centers for silane condensation and anchoring on the particle surfaces through siloxane chemical bonds. Adsorbed surface water is necessary for the hydrolysis of APTES in toluene, which initializes the condensation reaction process. However, the presence of excess free water is deleterious to the formation of a clean monolayer, as APTES is known to polymerize into white solid precipitates in the presence of water. The precipitates can potentially block the pores and hence reduce the effective surface area of the functionalized sorbents. For these reasons, a proper amount of water for the hydrolysis of APTES needs to be employed to obtain a monolayer of silanized APTES on the pore surfaces only.

Calcination at 540°C to remove surfactant templates and obtain mesoporous particles (Section 6.4.4) dehydrates the mesoporous silica-coated magnetite surface and depletes most of the silanol groups. Such a dehydrated surface would result in a poor surface coverage of functional groups if silanized directly. In this study, to optimize the reaction conditions for depositing alkoxysilane monolayers on mesoporous silica-coated Fe_3O_4 surfaces, the particles were rehydrated carefully by steaming the samples. The amount of surface-adsorbed water was controlled by drying. High-purity toluene was used through out the synthesis since toluene was reported in literature to be excellent for removing excess water and forming organic monolayers.

As shown in DRIFTS spectrum b of Fig. 6.13B, obtained with the steamed and dried samples, the presence of a sharp H–O vibrational band at 3,750 cm^{-1} confirms the successful hydrolysis of siloxane bonds by steaming. DRIFTS spectrum c of the silanized mesoporous-Fe_3O_4 in Fig. 6.13B exhibits the characteristic bands of APTES. A pair of weak broad bands at 3,400–3,250 cm^{-1} is evident in the spectrum. These two bands are assigned to free amino asymmetric and symmetric stretching vibrations. A strong band at 1,568 cm^{-1} is assigned to the deformation bending vibrations of free amine groups on the surface. In addition, two bands at 2,932 and 2,860 cm^{-1} assigned to asymmetric and symmetric stretching vibrations of CH_2 in alkyl chains, along with a band at 1,483 cm^{-1} assigned to CH_2 bending vibrations, are evident. These spectral features confirm the silanation of APTES on the particle surfaces. It is interesting to note that the characteristic bands of Si–O–C at 1,167, 1,105, 1,083, and 959 cm^{-1} almost disappeared after silanation. This finding suggests that most of the ethoxy groups in APTES were hydrolyzed. Two strong bands at 1,126 and 1,041 cm^{-1} (characteristic of siloxane Si–O–Si stretching vibrations) remained after silanation, indicating that the surface binding of APTES was not by silanols but rather by siloxane bonds. The presence of siloxane binding was further supported by the disappearance of IR bands at 3,745 cm^{-1}, assigned to the stretching vibrations of surface silanols in the spectra of silica-coated magnetic particles before calcination and steamed particles (spectrum b in Fig. 6.13B).

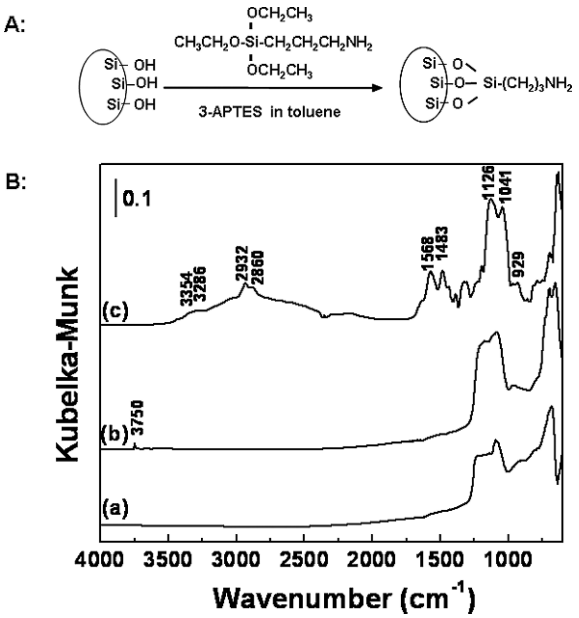

Fig. 6.13 (**A**) Schematic diagram for the synthesis of mesoporous-Fe_3O_4 silanized by 3-APTES. (**B**) DRIFTS spectra of mesoporous-Fe_3O_4 magnetic particles; after (a) calcination, (b) rehydroxylation, and (c) silanation by 3-APTES from toluene

6.5 Practical Applications of MCS

Utilizing the magnetic composite particles to selectively remove heavy metals from industrial effluents or contaminated municipal water or to be used in biological cell separation and biological sensing, the most important thing is to functionlize the surface with specific ligands having specific interaction with targets (heavy metals or bio-molecules), endowing the surface a strong and specific affinity for targeted metal ions. There are two ways to reach this goal, one is direct molecular self-assembling and the other one is by silanation of specific function groups, which allows more versatile groups to be used. The silanation is a promising avenue for introducing specific surface functional groups on mesoporous silica surfaces [112, 124, 125, 126, 127, 128, 129].

6.5.1 SA Monolayer

6.5.1.1 Cu^{2+} and Ag^{+} Removal

The MHA-coated γ-Fe_2O_3 particles (Section 6.4.1) prepared by the SA method contain reactive thiol and/or disulfide groups that are known to have strong

affinity to various metal ions such as gold, silver, and copper. This application is illustrated in our loading tests of Cu^{2+} and Ag^{+} on MHA-coated γ-Fe_2O_3 particles from 10 mmol/L $CuSO_4$ or $AgNO_3$ solutions. The narrow-scan XPS spectra of the loaded particles separated from the liquid/suspension with a hand magnet are shown in Fig. 6.14. The load of Cu^{2+} and Ag^{+} on the MHA-coated particles is evident from the presence of Cu_{2p} (934 and 954 eV) and Ag_{3d} (368 and 374 eV) XPS bands on spectra, respectively. The area ratio of the copper satellite band to its $2p_{3/2}$ band is lower than expected, suggesting that some of the copper ions are in the cuprous state. It appears that some of cupric ions were reduced to cuprous ions, accompanied by the oxidation of thiol to disulfide, which accounts for the presence of an additional sulfur band of higher binding energy but lower intensity. The surface metal-to-sulfur atomic ratio was found to be 0.6 and 0.8 for copper and silver, respectively. These results suggest a 1:2 (metal-to-sulfur) binding for divalent copper and 1:1 binding for monovalent silver. It is clear that the metal loading efficiency is sufficient for the MHA-coated magnetic sorbents to be used in the removal or recovery of Ag^{+} and Cu^{2+} from industrial effluents.

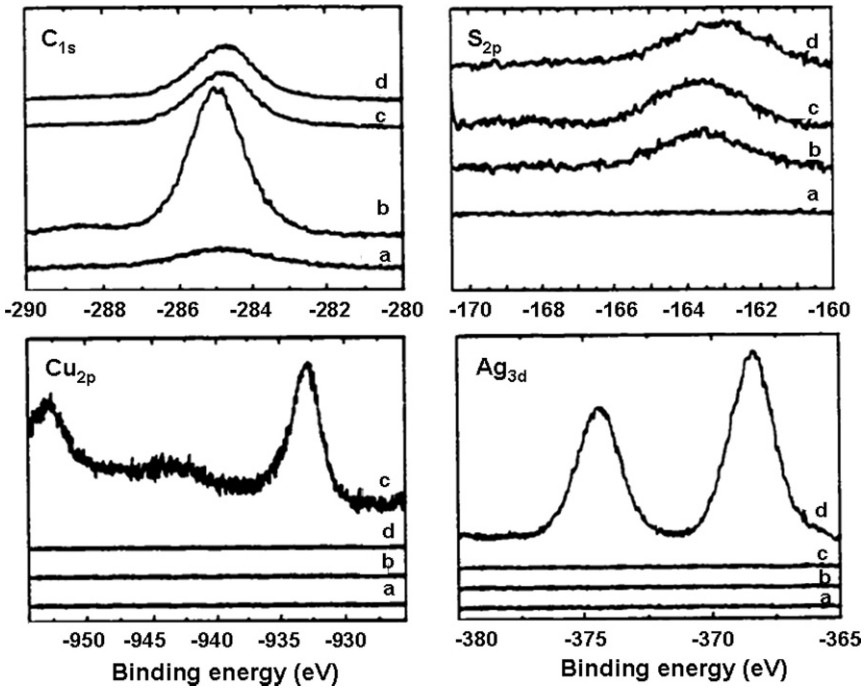

Fig. 6.14 XPS spectra of narrow scans for the interested elements (a) γ-Fe_2O_3; (b) thiol-type magnetic sorbents; (c) after copper loading; and (d) after silver loading

6.5.2 Silanized Monolayers on Two-Step Silica-Coated γ-Fe_2O_3

6.5.2.1 Cu^{2+} and Zn^{2+} Removal

The silanized magnetic particles with reactive amine groups are found to confer specific adsorption for heavy metal ions, including divalent mercury, lead, copper, zinc, manganese, and monovalent silver in contaminated aqueous and non-aqueous solutions [130].

It was shown (Section 6.4.2) that APTES films directly silanized onto γ-Fe_2O_3 were unstable in alkaline solutions, although the films silanized from toluene were relatively stable in acidic solutions. An idea to coat γ-Fe_2O_3 with a thin silica layer before silanation was proposed in order to obtain a stable silanized film. In Section 6.4.3, it was shown that dense thin silica films were successfully coated onto γ-Fe_2O_3 using the sol–gel process followed by DLS coating. The purpose of silica coating is to make the surface more amenable for silanation. It has been well-documented that silanized films on silica are relatively stable compared to those directly silanized on other metal oxides [131]. The silanation of silica-coated magnetic particles using APTES in toluene is performed. Toluene is used as a solvent simply due to the fact that the films formed on the magnetic particles are relatively stable compared to those formed from water as shown in Section 6.4.2. The silanized films on silica-coated magnetic particles were characterized by XPS, DRIFTS, zeta-potential measurements, leaching test, and thermal gravimetric analysis (TGA) as well-documented in literature [48]. It is found that the silanized films on silica-coated magnetic particles were more stable in acid solution than on bare magnetic particles, but both unstable in alkaline solutions.

Copper loading on the silanized silica-coated magnetic particles of reactive amine groups is shown in Fig. 6.15. For comparison, copper loading on silica-coated magnetic particles is also shown in this figure. It is evident that at a given pH 5.3, copper can be removed effectively from low concentration solutions (e.g., 100% removal from a 12 ppm solution). With increasing initial copper ion concentrations, the copper removal efficiency decreases as copper loading approaches the capacity limit of about 0.18 mmol of Cu per gram of particles. In contrast, the copper loading on the silica-coated magnetic particles is significantly lower than that on the silanized particles, suggesting the important role of reactive amine groups in this application. It should be noted that the metal ion loading is pH-dependent. The protonation of amino groups and detachment of silane-coupling agents are both influenced by pH, thus they will affect metal ion adsorption. In addition, various metal ions such as copper and zinc showed different loading performance, leading to selective adsorption and removal/recovery of various metals. This is demonstrated in our previous publication [48].

6.5.2.2 Stripping of Metal Ions and Recycling of Magnetic Sorbents

Stripping of metal ions from loaded magnetic particles is a major step for the subsequent recovery of metals by electrowinning, while the recycling of magnetic particles is a necessary step to offset the high price of magnetic sorbents by lowering

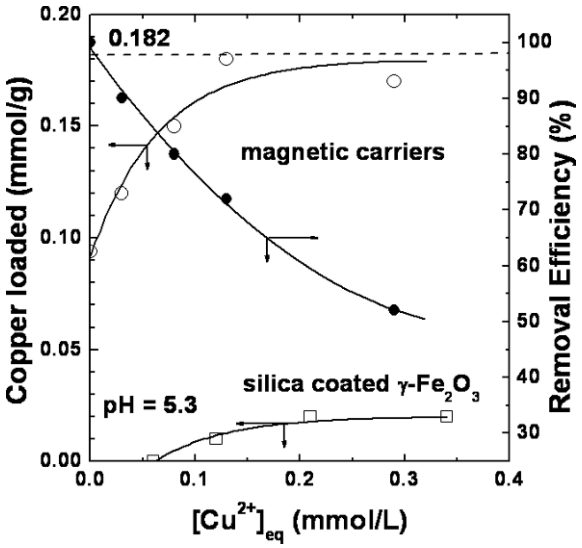

Fig. 6.15 Copper loading on and removal from APTES silanized on silica-coated γ-Fe_2O_3 particles, in comparison to silica-coated γ-Fe_2O_3 particles at loading pH 5.3

the cost in industrial applications. Many methods such as acid washing, EDTA (ethylenediamine tetraacetate) extraction, and electrowinning can be used to strip-off metal ions from loaded magnetic sorbents. An ideal method would detach metal ions effectively while maintaining maximum reactivity of magnetic sorbents.

The results of the stripping tests using nitric acid (0.01 M) are shown in Fig. 6.16. The amount of copper detached vs the amount of copper loaded

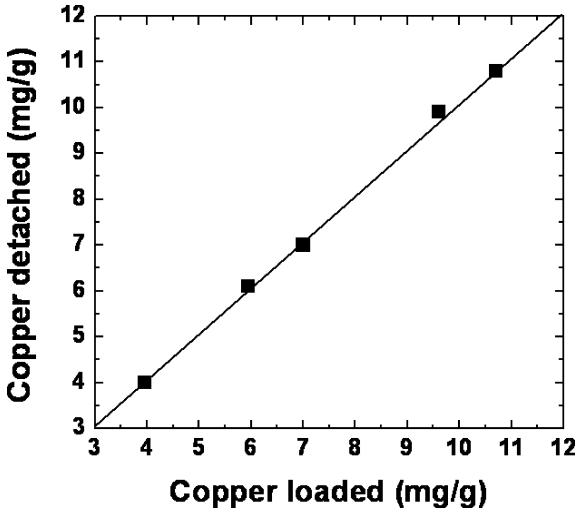

Fig. 6.16 The amount of copper detached vs the amount of copper loaded

exhibits a linear relation with the line passing through the origin of the coordinate and a slope of 1, indicating the complete detaching of loaded copper ions. The mechanism of copper detachment by acid washing seems similar to that in the regeneration of exhausted ion-exchange resins often used in wastewater management. The detachment is most likely accomplished by ion exchange due to the high chemical potential of hydrogen ions in acidic solutions, which compete with copper ions for amino groups on magnetic sorbents.

After stripping off metal ions, the recycled magnetic carriers were characterized by XPS, DRIFTS, zeta-potential measurements, and the copper loading test to determine the density and reactivity of silanized films remained on magnetic sorbents. The results from the analysis all indicate a partial detachment of immobilized silanes from the surface after acid stripping. Moreover, in DRIFTS the band at 1,580 cm^{-1} for amino groups on magnetic sorbents shifted to 1,615 cm^{-1} after copper loading, indicating the amino groups reacted with copper ions. However, after detachment a new band at 1,711 cm^{-1} appeared, which is attributed to oxidization of amines, possibly imides which have little affinity to copper [132], thus reducing the reactivity of magnetic sorbents with copper in the following reloading test.

Considering that amino groups are susceptible to oxidation [133], using EDTA to extract loaded copper from magnetic sorbents may be beneficial. The minimal breakage of siloxane bonds, and hence the detachment of APTES films from the magnetic sorbents are anticipated. Therefore, using EDTA or similar complexing reagent to detach metal ions from loaded magnetic sorbents is worth exploring.

6.5.3 Poly(1-vinylimidazole)-Grafting on Magnetic Nanoparticles

Grafting of silane-terminated polymers on silica via chemical siloxane bonds has been reported in a number of studies [134, 135, 136]. In this study [137], a newly synthesized poly(1-vinylimidazole) with trimethoxysilyl terminal groups is chemically anchored (grafted) on nanosize maghemite particles. Poly(1-vinylimidazole) is chosen to graft on nanosize magnetic particles, as the resultant organic–inorganic hybrid magnetic materials are anticipated to expand the sorbent-based separation technology to a multiphase complex system, ranging from biological cell sorting to industrial effluent detoxification and recovery of valuables. Poly(1-vinylimidazole) can form complexes with such metal ions as Cu-(II) [138], Zn(II) [139], Cd(II) [140], Ag(I) [141], and Hg(II) [142].

Figure 6.17 shows schematically the preparation procedure and the resulting configuration of grafted polymers (thick lines) with bond metals (M). Compared with the polymer-coating method, the polymer-grafting (direct silanation) method offers a number of distinct advantages. First, particle size shows little effect on polymer immobilization. Polymer chains immobilized on magnetic particles would remain flexible. Polymer-grafted magnetic particles

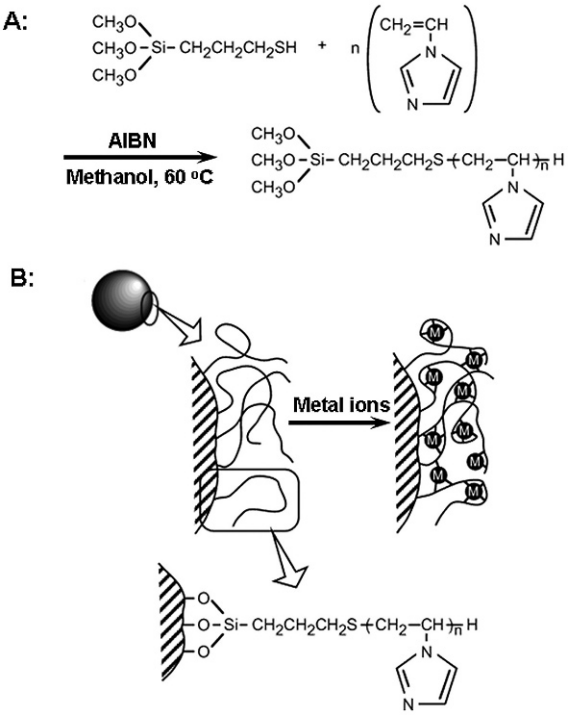

Fig. 6.17 Synthesis of poly(1-vinylimidazole) (**A**) and schematic illustration of polymer-grafted magnetic particles (**B**)

can be used in good solvents of the polymer. Finally, the method is applicable to many kinds of polymers.

Poly(1-vinylimidazole) with a terminal trimethoxysilyl group (Im_n) was prepared by telomerization of 1-vinylimidazole with 3-mercaptopropyltrimethoxysilane. The average degree of polymerization, *n*, is 18, as determined by 1H NMR. The DRIFTS measurement combined with elemental and TGA showed that immobilization of the synthesized polymer onto magnetic nanoparticles through siloxane bonds (Mag-Im_{18}) was successful. The Mag-Im_{18} was well-dispersed in water and in organic solvents such as methanol, ethanol, and chloroform. TEM micrograph confirms that the original size and shape of the particles were retained after Im_{18}-grafting. The grafted polymer is stable over a wide solution pH range from 3.5 to 10.0, so Mag-Im_{18} can be used in a wide range of aqueous environments.

The removal of various metal ions from aqueous solutions is possible by using the Mag-Im_{18} as a collector. Figure 6.18 shows the removal efficiency of Cu^{2+}, Ni^{2+}, and Co^{2+} from their bulk solutions. The order of removal efficiency of the metal ions by Mag-Im_{18} was found to be $Cu^{2+} > Ni^{2+} > Co^{2+}$. A loading capacity of 0.11 mmol/g at pH 5.3 was determined for copper. This capacity corresponds to a one-quarter amount of imidazolyl groups on the particles (0.44 mmol/g). This observation suggests a preferred coordination number of 4

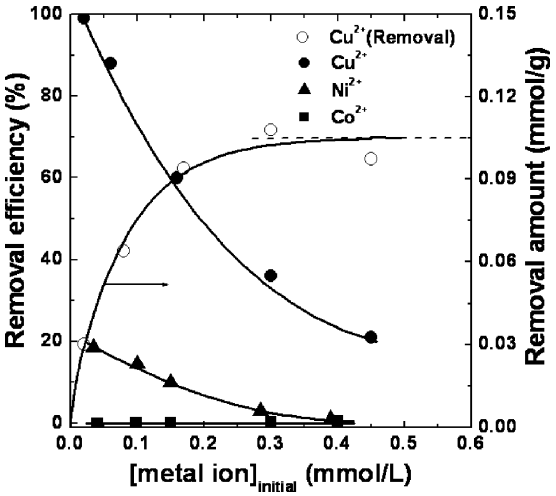

Fig. 6.18 Removal efficiency of Cu^{2+}, Ni^{2+} and Co^{2+} by, and loading capacity of Cu^{2+} on Mag-Im_{18}. Metal ion solution/Mag-Im_{18} = 10 mL/10 mg at initial solution pH 5.3

for Cu^{2+} to complex with imidazolyl groups and confirms that the imidazolyl groups on the flexible polymer chain are effective at capturing copper ions.

Selective removal of metal ions from aqueous solutions was evaluated by loading tests from a mixture of Cu^{2+}/Co^{2+} solutions. In this set of experiments, the initial concentration of Cu^{2+} and Co^{2+} was fixed at 0.157 mmol/L (10 ppm) and 0.170 mmol/L (10 ppm), respectively. As shown in Fig. 6.19, the removal

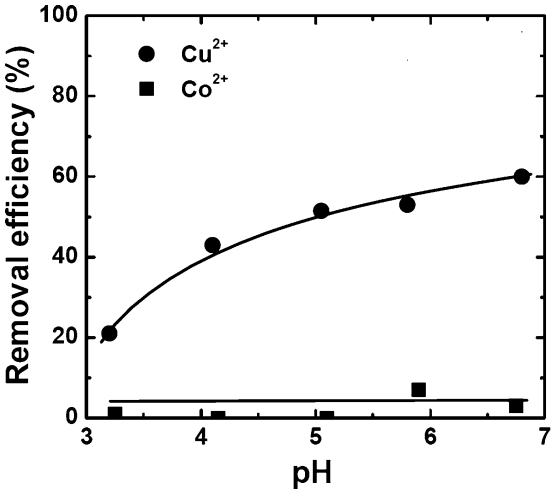

Fig. 6.19 Removal efficiencies of Cu^{2+} and Co^{2+} by $MagIm_{18}$ from a mixture of Cu^{2+}/Co^{2+} solution. Metal ion solution/Mag-Im_{18} = 10 mL/10 mg at initial [Cu^{2+}] and [Co^{2+}] concentration of 0.157 and 0.170 mmol/L, respectively

efficiency for Cu^{2+} increased with increasing solution pH. The adsorption of copper ions on Mag-Im_{18} is not significant below pH 3. The competitive adsorption of hydrogen ions with metal ions for imidazolyl groups at low pH values accounts for the observed low removal efficiency. Since the imidazolyl groups are most likely protonated at a low pH, the magnetic particles are positively charged, resulting in a strong electrostatic repulsive force between the poly(1-vinylimidazole) on the magnetic particles and positively charged metal ions. This long-range repulsive force also contributes to the observed low copper removal efficiency at solution pH below 3. On the other hand, Co^{2+} cannot be removed by Mag-Im_{18} over the entire pH range studied. The Mag-Im_{18} showed an effective and selective separation of Cu^{2+} from a mixture of Cu^{2+} and Co^{2+} solution. Given the wide selection of polymer functionality, polymer-grafted magnetic particles can provide vast potential applications.

6.5.4 Functionalized Mesoporous Silica-Coated Magnetic Particles

6.5.4.1 Separation of Transition Metals

Cupric ion adsorption tests were performed on magnetic composite particles with varying surface treatments. To illustrate the role of molecular templating in synthesis of the silica coating and subsequent capture of target species, the results obtained with the micrometer-sized magnetite coated with silica under the identical conditions but without templating are included for comparison.

From the results shown in Fig. 6.20, the following general conclusions can be made: (1) The capability of the particles to capture copper ions increased when mesoporous films were formed on the magnetite particles to produce a higher specific surface area (curves (b) and (d) are higher than curves (a) and (c), respectively). (2) Surface functionalization with amine groups by silanation increased the capability of the particles to capture metal ions, arisen from a stronger chemical affinity of the immobilized amine groups for copper ions (curves (c) and (d) are higher than curves (a) and (b), respectively). (3) The functionalized mesoporous surfaces showed the highest loading capacity for copper ions (curve (d)), suitable for detoxification or recovery of copper ions from industrial effluents.

Mesoporous magnetic particles functionalized with APTES were tested to determine the loadings of other soluble heavy metals. The extractability of soluble metals was examined by adding 50 mg of particles to 25-mL samples of aqueous solutions, each containing 0.5 mmol/L Cu^{2+}, Zn^{2+}, and/or Ni^{2+} ions. In this set of tests, the solution pH varied from 2 to 6. The upper pH limit was set at 6 to avoid precipitation of metal hydroxides, which would complicate the interpretation of results.

Figure 6.21A shows the loading distribution coefficients, K_d, of different metal ions from the corresponding single element solutions as a function of the equilibrium

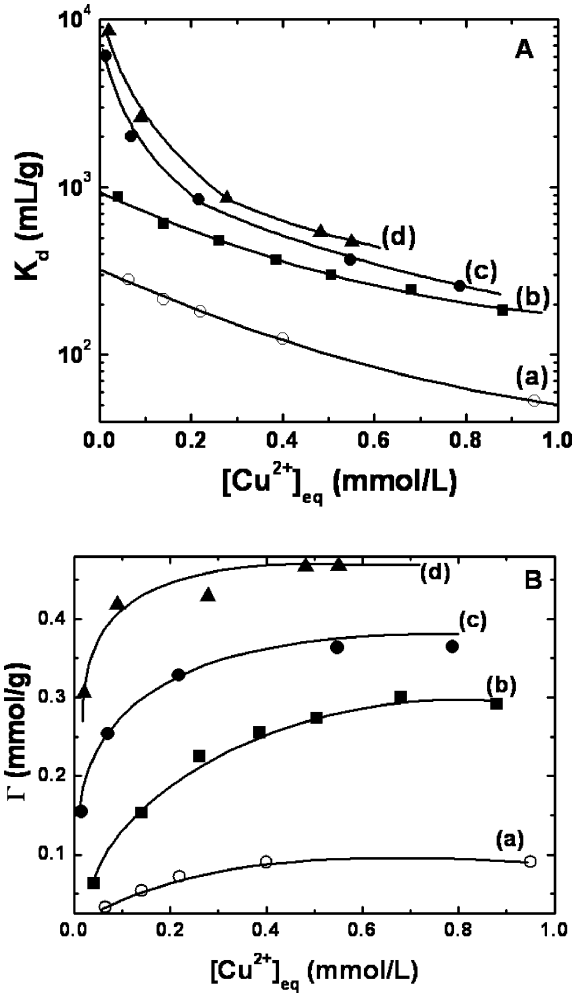

Fig. 6.20 (**A**) Distribution and (**B**) adsorption isotherms of copper ions on different magnetic particles as a function of copper concentration: (a) Fe_3O_4 coated with silica without templating, (b) mesoporous-Fe_3O_4, (c) Fe_3O_4 coated with silica without templating but silanized by 3-APTES, and (d) mesoporous-Fe_3O_4 silanized with 3-APTES

solution pH. The extractability obtained at pH < 6 was found to be in the order $Cu^{2+} > Ni^{2+} > Zn^{2+}$. The distribution coefficient for each metal is relatively low for pH < 2. At such a low pH, excess H^+ ions compete with metal ions for binding with surface amino groups, resulting in a low metal ion loading capacity [48]. From the results in this figure, a selective loading of copper ions over nickel and zinc is anticipated. The selective loading was confirmed with loading tests in a solution containing all three of these types of heavy metal ions. The distribution coefficient (K_d) obtained as a function of pH in Fig. 6.21B shows that the extractability of the

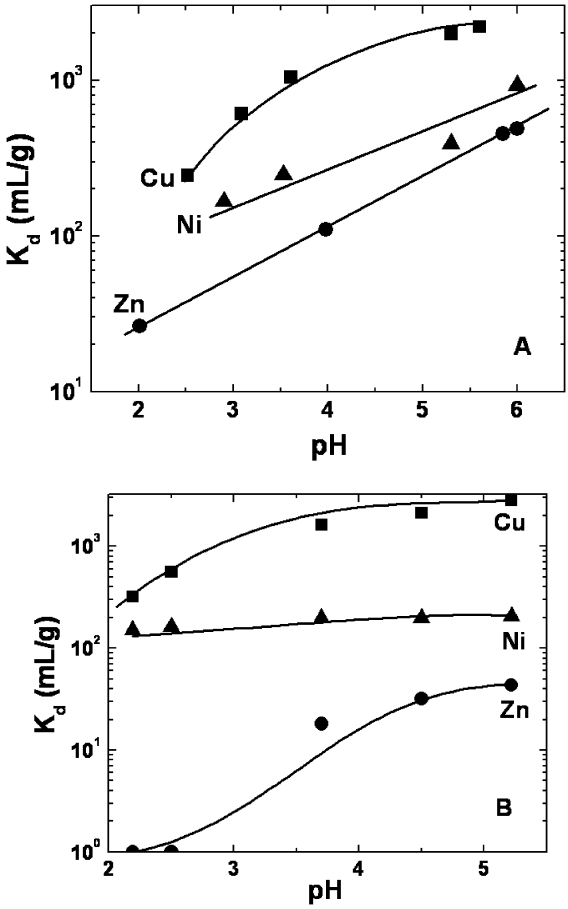

Fig. 6.21 Loadings of transition metal ions on the amine-terminated mesoporous magnetic particles as a function of solution pH from (**A**) single-element solutions; and (**B**) a solution containing copper, nickel, and zinc, each at 0.5 mmol/L concentration

metal ions from a mixture follows the same order as seen in the single-metal systems, i.e., $Cu^{2+} > Ni^{2+} > Zn^{2+}$. Metal ion loading increases with increasing pH above 2 up to the limiting pH of 5.2 for copper and zinc, but not for nickel.

6.5.4.2 Stripping and Recycling

The adsorbed metals were successfully desorbed with 1 M aqueous HCl solutions. The mechanism of copper detachment from silanized mesoporous-Fe_3O_4 particles by acid washing is similar to that explained before [48]. In the reloading test there is a decrease in the loading capacity of the recycled sorbents by 17%. The reasons for the observed decrease in the loading capacity of the APTES-silanized mesoporous-Fe_3O_4 particles after acid stripping of the loaded

copper remain to be investigated. A similar observation was reported by Liu for the loading of copper using amine-terminated nano Fe_2O_3 particles [48]. His work led to the conclusion that both the protonation/oxidation of amino groups and some degree of detachment of the silanized APTES films during acid stripping contributed to the reduced copper reloading efficiency. We believe that these effects also account for the observations made in the current study. Since long chain alkyl coupling agent will block the pore, it is not good to be used in the functionalization of mesoporous surface. We are continuing to explore other applications of the functionalized mesoporous magnetic particles and are studying the relevant mechanisms.

The above fundamental study demonstrates the feasibility of using APTES-silanized mesoporous-Fe_3O_4 particles in metal recovery and/or removal. The metal ions loaded on the functionalized mesoporous-Fe_3O_4 particles can be detached completely by acid washing. Although the loading capacity of copper on the recycled mesoporous-Fe_3O_4 particles is reduced, improving the stability of the silanized film is anticipated to make the recycling of silanized mesoporous-Fe_3O_4 particles feasible in practice. The concept of using mesoporous-Fe_3O_4 particles functionalized with reactive amine terminal groups for the effective recovery or selective removal of metal ions has thus been demonstrated.

6.5.4.3 Other Examples of Heavy Metal Removal

It should be noted that other functional groups can be attached onto mesoporous-Fe_3O_4 particles by a similar scheme. For example, carboxylic acid-terminated mesoporous magnetic sorbents can be readily synthesized following the same procedures as used for silanation of APTES [143]. Organic functional groups other than amines are suited to different applications. The surface tailoring method reported here is foreseen to enable diverse design of surface properties of mesoporous-Fe_3O_4 mesoporous materials and could lead to the synthesis of more advanced nanocomposite particles for industrial and environmental applications.

Taking functionalization with mercapto-propyl-trimethoxy-silane (MPTS) through silanation reaction, as an example, the mesoporous magnetic sorbents showed a strong affinity for mercury in aqueous solutions [144]. The Langmuir type of isotherm in Fig. 6.22A confirms monolayer adsorption, indicating a chemisorption mechanism of mercury on functionalized mesoporous magnetite surfaces. The maximum loading of mercury at pH 2 is 14 mg/g. The distribution coefficient as a measure of the affinity of an ion exchanger for a particular ion is a sensitive indicator of the selectivity of the ion exchanger to the particular ion in the presence of a complex matrix of interfering ions. For a successful separation, K_d must have a value > 100 mL/g. The result in Fig. 6.22B shows that the distribution coefficient at pH 2 is well above 100, which confirms the applicability of this kind of mesoporous magnetic particles for mercury removal from industrial effluents.

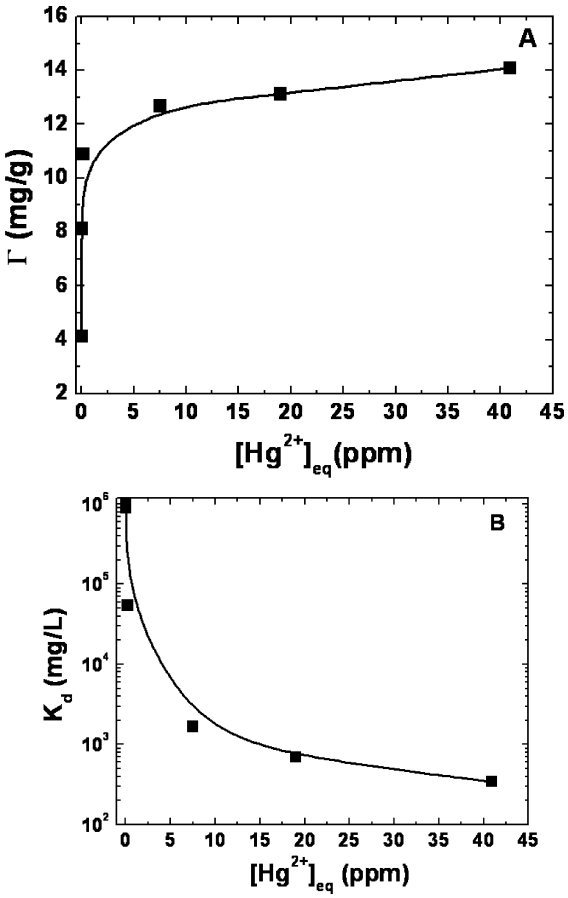

Fig. 6.22 Mercury adsorption by functionalized magnetic sorbents at pH 2: (**A**) isotherm; and (**B**) distribution

6.6 Further Directions

In our group, research and development of novel sorbents are taking directions for mercury removal from flue gases of coal-fired power plant. Large mercury adsorption capacity, effective capture, regenerability, and recyclability are a few features to be considered to reduce mercury emission, control cost, and recover mercury from coal-burning processes. The preliminary results showed promising research direction of zeolite-based magnetic sorbents. The research results will be published separately.

The mesoporous silica coating on magnetic particles has a well-characterized surface morphology and can be modified to a wide range of functionality owing to the presence of active hydroxyl groups. For example, the surface can be tuned

to strongly acidic or alkaline by grafting different functional groups. Thus it can promise for a wide range of surface catalytic systems with various types of chemical reactions for industrial, biological, and pharmacological processes. The industrial processes like flotation, flocculation, and ceramic processing, etc., which chiefly depend on the nature of the interface, can be controlled by manipulating surface characteristics. The surface charge and wettability of the silica-coated magnetite surfaces can also be tuned by the adsorption of surfactants, which can be beneficial for controlling dispersion and flocculation in various industrial processes. Silica surface can act as a template for the synthesis of high molecular weight polymers and bio-molecules of medical importance. Using this template, drug-delivery technique can be developed whereby specific drugs can be applied directly to localized area thus resulting in an enhanced remedy without affecting other parts of the body. Photosensitive compounds adsorbed on silica surface can be subjected to external irradiations and their reaction mechanisms can be studied in great detail with better profoundness. Such study can be utilized in developing photo-sensitized chemical machines which can replace electronic chips and can produce pollution-free micro machineries [145]. With magnetic property, the difficulties in recovery and recycling for some applications can be overcome.

In addition, co-condensation reactions, introduction of organic moieties within the silicate framework may increase the flexibility of mesoporous silica coating. The flexibility in choosing organic, inorganic, or hybrid building blocks, and combinations of templates allows one to control the materials' properties and to optimize them for each desired application. Periodic mesoporous organosilicas (PMOS) were independently initiated by three groups (Inagaki group [146], Ozin group [147], and Stein group [148]) in 1999. This category of materials is synthesized using organic molecules having multiple alkoxysilane groups such as bis(triethoxysilyl)ethane and bis(triethoxysilyl)-benzene [149]. Unlike in organic functionalized mesoporous silica phases obtained via grafting or co-condensation procedures the organic groups in PMOS are direct parts of the 3D framework structure, thus giving raise to enormous possibilities to turn their chemical and physical properties in designated ways by varying the structure of the precursors [150]. It is worth to integrate PMOS with magnetic nanoparticles.

6.7 Conclusion

Magnetic nanocomposites were successfully synthesized by SA. By controlling the reactivity of functional groups with surface, MHA was anchored onto γ-Fe_2O_3 surface through chemical bonding between the carboxylic head group of surfactant and iron on the surface, leaving the thiol or disulfide groups reactive. The molecular orientation of MHA self-assembled on γ-Fe_2O_3 was inferred from XPS, DRIFTS and film flotation. This SA film is resistant to acid and base attack.

APTES can be directly silanized onto magnetic particles from water or toluene solutions and the process is characterized by XPS, IR, and zeta-potential measurements. APTES films formed on bare magnetic particles from toluene are relatively stable in acid solution compared to the films formed from water. Both films are unstable in alkaline solution.

Silica coatings on magnetic particles were achieved by both sol–gel and DLS process. A uniform but porous silica layer was coated on magnetic particles by sol–gel process. At low supersaturation level, non-uniform silica coatings were formed by DLS process. A dense thin silica layer was coated on magnetic particles by a novel two-step process, i.e., sol–gel followed by DLS coating. The chemical stability of the two-step silica-coated magnetic particles was increased.

Mesoporous silica coating by a combination of DLS coating and the sol–gel process with molecular templating on magnetic particles can dramatically increase the surface area of the final composites. The templating mechanism and the mesoporous silica-coated magnetic particles were studied by AFM, DRIFTS, TEM, zeta-potential measurement, and leaching tests. The resultant particles show paramagnetic property with strong saturation magnetization, and the silica surface is amenable for various functionalizations.

The magnetic nanocomposite particles functionalized by silanation with different reactive functional groups, such as –SH, $–NH_2$, and –COOH, have been proven to be effective for removal or recovery of heavy metal ions such as Cu^{2+}, Zn^{2+}, Ni^{2+}, Ag^{+}, and Hg^{2+} from aqueous solutions. Selective separation of different metal ions can be achieved by controlling the solution pH. Loaded metal ions on the magnetic particles can be stripped off by acid washing. Magnetic nanocomposites particles with tailored functional groups have potential applications in many scientific and technological applications of different disciplines.

References

1. Alloway, B.J. (Ed.) (1995) Heavy Metals in Soils. Chapman and Hall, Glasgow, UK. Chapters 6, 8, 9 and 11.
2. McDonald, D. G., Grandt, A. F. (1981) Limestone – Lime Treatment of Acid Mine Drainage-Full Scale. *EPA Project Summary*. EPA-600/S7-81-033.
3. Yamamura, S. (2000) Drinking Water Guidelines and Standards, World Health Organization, Geneva, Switzerland, http://www.who.int/water_sanitation_health/dwq/arsenicun5.pdf
4. Maximum Contaminant Level Goals and National Primary Drinking Water Regulation for Lead and Copper; Proposed Rule (1996) http://www.epa.gov/EPA-WATER/1996/April/Day-12/pr-20958DIR/pr-20958.txt.html
5. Nuñez, L., Kaminski, M. D. (1998) *Chem. Technol*. 9, 41.
6. Xu, Z., Liu, Q., Finch, J. A. (1997) *Appl. Surf. Sci*. 120, 269.
7. Shiraishi, Y., Nishimura, G., Hirai, T., Komasawa, I. (2002) *Ind. Eng. Chem. Res*. 41, 5065.
8. Lee, B., Kim, Y., Lee, H., Yi, J. (2001) *Micropor. Mesopor. Mater* 50, 77.
9. Stumm, W., Morgan, J. J. (1995) Aquatic Chemistry, Jon Wiley & Sons, Inc., New York, 804.

10. Lee, J. S., Gomes-Salazar, S., Tavlarides, L. L. (2001) *React. Funct. Polym.* 49, 159.
11. Yu, M., Tian, W., Sun, D., Shen, W., Wang, G., Xu, N. (2001) *Anal. Chim. Acta.* 428, 209.
12. Nam, K. H., Tavlarides, L. L. (2003) *Solvent Extr. Ion Exc.*, 21, 899.
13. Pinfold, T. A. (1972) Ion Flotation, in Robert Lemlich (Ed.), Adsorptive Bubble Separation Techniques, Academic Press, New York.
14. Nicol, S. K., Galvin, K. P. and Engel, M. D. (1992) *Miner. Eng.* 5, 1259.
15. Berg, E. W., Downey, D. M. (1980) *Anal. Chim. Acta* 120, 273.
16. Willians, R. A. (Ed.). (1992) Colloid and Surface Engineering: Application.c in the Process Industries, Butterworth Heinemann, Oxford, UK. Chapter 8.
17. Booker, N. A., Keir, D., Priestley, A., Rithchie, C. D., Sudarmana, D. L., Woods, M. A. (1991) *Water Sci. Technol.* 123, 1703.
18. Sing, K. S. (1994) *Technol. Profile* 21, 60.
19. Safarik, I., Safarikova, M., Buricova, V. (1995) *Collect. Czech. Chem. Commun.* 60, 1448.
20. Wu, R., Qu, J., Chen, Y. (2005) *Water Res.* 39, 630.
21. Orbell, J. D., Godhino, L., Bigger, S. W., Nguyen, T. M., Ngeh, L. N. (1997) *J. Chem. Edu.* 74, 1446.
22. Borai, E. H., El-Sofany, E. A., Morocos, T. N. (2007) *Adsorption* 13, 95.
23. Feng, D., Aldrich, C., Tan, H. (2000) *Hydrometallurgy* 56, 359.
24. Denizli, A., Özkan, G., Arica, M. Y. (2000) *J. Appl. Polym. Sci.* 78, 81.
25. Duguet, E., Vasseur, S., Mornet, S., Devoisselle, J. M. (2006) *Nanomedicine* 1, 257.
26. Gupta, A. K., Naregalkar, R. R., Vaidya, V. D., Gupta, M. (2007) *Nanomedicin* 2, 23.
27. Gao, X., Yu, K. M. K., Tam, K. Y., Tsang, S. C. (2003) *Chem. Commun.* 24, 2998.
28. Rudge, S. R., Kurtz, T. L., Vessely, C. R., Catterall, L. G., Williamson, D. L. (2000) *Biomaterials* 21, 1411.
29. Wu, P., Xu, Z. (2005) *Ind. Eng. Chem. Res.* 44, 816.
30. Skold, C. N. (2007) U.S. Patent 7,169,618.
31. Giaever, I. (1976) U.S. Patent 3,970,518.
32. Whitehead, R. A., Chagnon, M. S., Groman, E. V., Josephson, L. (1985) U.S. Patent 4,554,088.
33. Phanapavudhikul, P., Waters, J. A., Perez de Oritiz, E. S. (2003) *J. Environ. Sci. Heal A* 38, 2277.
34. Liberti, P. A., Piccoli, S. P. (1996) U.S. Patent 5,512,332.
35. Liberti, P. A., Pino, M. A. (1997) U.S. Patent 5,597,531
36. Yen, S.-P. S., Rembaum, A., Molday, R. S. (1979) U.S. Patent 4,157,323.
37. Daniel, J.-C., Schuppiser, J.-L., Tricot, M. (1982) U.S. Patent 4,358,388.
38. Liu, X., Guan, Y., Ma, Z., Liu, H. (2004) *Langmuir* 20, 10278–10282.
39. Pich, A., Bhattacharya, S., Ghosh, A., Adler, H.-J. P. (2005) *Polymer* 46, 4596.
40. Senyei, A. E., Widder, K. J. (1980) U.S. Patent 4,230,685.
41. Molday, R. S. (1984) U.S. Patent 4,452,773.
42. Owen, C. S., Silvia, J. C., D'Angelo, L., Liberti, P. A. (1989) U.S. Patent 4,795,698.
43. Palmacci, S., Josephson, L. (1993) U.S. Patent 5,262,176.
44. Ugelstad, J., Ellingsen, T., Berge, A., Helgee, O. B. (1987) U.S. Patent 4,654,267.
45. Groman, E. V., Josephson, L., Lewis, J. M. (1989) U.S. Patent 4,827,945.
46. Li, L., Fan, M., Brown, R. C., Leeuwen, J. V., Wang, J., Wang, W., Song, Y., Zhang, P. (2006) *Crit. Rev. Env. Sci. Technol.* 36, 405.
47. Lu, A. H., Salabas, E. L., Schuth, F. (2007) *Angew. Chem. Int. Edit.* 46, 1222.
48. Liu, Q. (1996) An innovative approach in magnetic carrier technology, PhD. Thesis, McGill University, Montreal.
49. Ulman, A. (1991) An Introduction to Ultrathin Organic Films and Langmuir-Blodgett to Self-Assembly, Academic, San Diego.
50. Pomerantz, M., Segmuller, A., Netzer, L., Sagiv, J. (1986) *Thin Solid Films* 132, 153.
51. Netzer, L., Iscovici, R., Sagiv, J. (1983) *Thin Solid Films* 99, 235.
52. Allara, D. L., Nuzzo, R. G. (1985) *Langmuir* 1, 52.

53. Schlotter, N. E., Porter, M. D., Bright, T. B., Allara, D. L. (1986) *Chem. Phys. Lett*. 132, 93.
54. Laibinis, P. E., Hickman, J. J., Wrighton, M. S., Whitesides, G. M. (1989) *Science* 245, 845.
55. Bain, C. D., Troughton, E. B., Tao, Yu-Tai, Evall, J., Whitesides, G. M., Nuzzo, R. G. (1989) *J. Am. Chem. Soc*. 111, 321.
56. Walczak, M. M., Chung, C., Stole, S. M., Widrig, C. A., Porter, M.D. (1991) *J. Am. Chem. Soc*. 113, 2370.
57. Parikh, A. N., Allara, D. L., Azouz, I. B., Rondelez, F. (1994) *J. Phys.Chem*. 98, 7577.
58. Yoon, R.-H., Flinn, D. H., Guzonas, D. A. (1994) *Colloids Surf*. 87, 163.
59. Folkers, J. P., Gorman, L. B., Laibinis, P. E., Buchholz, S., Whitesides, G. M., Nuzzo, R. G. (1996) *Langmuir* 11, 813.
60. Allara, D. L., Hebard, A. F., Padden, F. J., Nuzzo, R. G., Falcone, D. R. (1983) *J. Vac. Sci. Technol*. AI(2), 376.
61. Ihs, A., Liedberg, B. (1991) *J. Colloid Interface Sci*. 144, 283.
62. Uvdal, K., Bodo, P., Liedberg, B. (1992) *J. Colloid Interface Sci*. 149, 163.
63. Goss, C. A., Charych, D. H., Majda, M. (1991) *Anal. Chem*. 63, 85.
64. Smith, E. L., Alves, L. A., Andergg, J. W., Porter, M. D., Siperko, L. M. (1992) *Langmuir* 8, 2707.
65. Rozenfeld, O., Koltypin,Y., Bamnoker, H., Margel, S., Gedanken, A. (1994) *Langmuir* 10, 3919.
66. Liu, Q., Friedlaender, F. (1994) *J. Min. Eng*. 7(4), 449.
67. Molday, R. S., Mackenzie, D. (1982) *J. Immunol. Meth*. 52, 353.
68. Saito, S. (Ed.). (1988) Fine Ceramics, Elsevier, Amsterdam.
69. Goldman, P. (1988) In: Electronic Ceramics: Properties, Deuices, and Applications, Levinson, L. M., (Ed.), Dekker, New York.
70. Sonti, S. V., Bose, A. (1995) *J. Colloid Interface Sci*. 170, 575.
71. Liu, Q., Xu, Z. (1995) *Langmuir* 11, 4617–4622.
72. Moulder, J. F., Stickle, W. F., Sobol, P. E., Bomben, K. D. (1992) Handbook of X-ray Photoelectron Spectroscopy, Perkin-Elmer Corp., Eden Prairie, MN.
73. Wood, R., Kim, D. S., Basilid, C. I., Yoon, R.-H. (1995) *Colloids Surf*. 94, 67.
74. Zhong, C. H., Poter, M. D. (1994) *J. Am. Chem. Soc*.116, 11616.
75. Plueddemann, E. P. (1985) In: Silane, Surfaces, and Interface, Leyden, D. E., (Ed.), Gordon and Breach Science Publisher, New York, 1–23.
76. Marquez, M., Grady, B. P., Robb, I. (2005) *Colloid Surf. A*, 266, 18.
77. Nalaskowski, J., Drelich, J., Hupka, J., Miller, J. D. (2003) *Langmuir* 19, 5311.
78. Ding, W. P., Meitzner, G. D., Iglesia, E. (2002) *J. Catal*. 206, 14.
79. Evans, J., Zaki, A. B., El-Sheikh, M. Y., El-Safty, S. A. (2000) *J. Phys. Chem. B* 104, 10271.
80. Brunel, D. (1999) *Micropor. Mesopor. Mater* 27, 329.
81. Lee, S. Y., Harris, M. T. (2006) *J. Colloid Interface Sci*. 293, 401.
82. Chagnon, M. S., Groman, E. V., Josephson, L., Whitehead, R. A. (1987) U.S. Patent 4,695,393.
83. Iler, R. K. (1973) *Surf. Colloid Sci*. 6, 1–100.
84. Maure, R. E. (1986) *J. Vac. Sci. Technol. A* 4, 3002.
85. Niwa, M., Katada, N., Murakami, Y. (1990) *J. Phys. Chem*. 94, 6441.
86. Atik, M., Zarzycki, J. (1994) *J. Mater. Sci. Lett*. 13, 1301.
87. Adamson, A. W. (1990) Physical Chemistry of Surfaces, 5th Ed., John Wiley, New York, 297.
88. Stokes, R. J., Evans, D. F. (1996) Fundamentals of Interfacial Engineering, John Wiley, New York, 65.
89. Liu, Q., Xu, Z., Finch, J. A., Egerton, R. (1998) *Chem. Mater*. 10, 3936–3940.
90. Kresge, C. T., Leonowicz, M. E., Roth, W. J., Vartuli, J. C., Beck, J. S. (1992). *Nature* 359, 710.

91. Beck, J. S., Vartuli, J. C., Roth, W. J., Leonowicz, M. E., Kresge, C. T., Schmitt, K. D., Chu, C. T.-W., Olson, D. H., Sheppard, E. W., McCullen, S. B., Higgins, J. B., Schlenker, J. L. (1992) *J. Am. Chem. Soc*. 114, 10834.
92. Kresge, C. T., Leonowicz, M. E., Roth, W. J., Vartuli, J. C. (1992) U.S. Patent 5,098,684.
93. Yanagisawa, T., Shimizu, T., Kuroda, K., Kato, C. (1990) *Bull. Chem. Soc. Jpn*. 63, 988.
94. Inagaki, S., Fukushima, Y., Kuroda, K. J. (1993) *Chem. Soc. Chem. Commun*. 8, 680.
95. Stein, A., Melde, B. J., Schroden, R. C. (2000) *Adv. Mater*. 12, 1403.
96. Berggren, A., Palmqvist, A. E. C., Holmberg, K. (2005) *Soft Matter* 1, 219.
97. Hoffmann, F., Cornelius, M., Morell, J., Froba, M. (2006) *J. Nanosci. Nanotechnol*. 6, 265.
98. Ford, D. M., Simanek, E. E., Shantz, D. F. (2005) *Nanotechnology* 16, S458.
99. Hartmann, M. (2005) *Chem. Mater*. 17, 4577.
100. Tsang, S. C., Yu, C. H., Gao, X., Tam, K. (2006) *J. Phys. Chem. B* 110, 16914.
101. Ariga, K. (2004) *J. Nanosci. Nanotechnol*. 4, 23.
102. Shi, J. L.,. Hua, Z. L, Zhang, L. X. (2004) *J. Mater. Chem*. 14, 795
103. Stein, A. (2003) *Adv. Mate*. 15, 763
104. Sanchez, C., Lebeau, B., Chaput, F., Boilot, J. P. (2003) *Adv. Mater*. 15, 1969.
105. Davis, M. E. (2002) *Nature* 417, 813
106. de Vos, D. E., Dams, M., Sels, B. E., Jacobs, P. A. (2002) *Chem. Rev*. 102, 3615
107. Schüth, F., Schmidt, W. (2002) *Adv. Mater*. 14, 629.
108. Cardin, D. J. (2002) *Adv. Mater*. 14, 553.
109. Beck, J. S., Vartali, J. C. (1996) *Curr. Opin. Solid State Mater. Sci*. 1, 76.
110. Huo, Q., Margolese, D., Ciesla, U., Feng, P. Y., Gier, T. E., Sieger, P., Leao, R., Petroff, P. M., Schuth, F., Stucky, G. D. (1994) *Nature* 368, 321.
111. Jones, C. M., Tsuji, K., Davis, M. (1998) *Nature* 393, 52.
112. Feng, X., Fryxell, G. E., Wang, L.-Q., Kim, A.Y., Liu, J., Kemner, K. M. (1997) *Science* 276, 923.
113. Israelachvili, J. N., Mitchell, D. J., Ninham, B. W. (1976) *J. Chem. Soc. Faraday Trans* 72, 525.
114. Israelachvili, J. N. (1992) Intermolecular and Surface Forces, (2nd Ed.), Academic Press, London.
115. Huo, Q., Margolese, D. I., Stucky, G. D. (1996) *Chem. Mater*. 8, 1147.
116. Øye, G., Sjöblom, J., Stöcker, M. (1999) *Micropor. Mesopor. Mater* 27, 171.
117. Kleitz, F., Blanchard, J., Zibrowius, B., Schueth, F., Aagren, P., Linden, M. (2002) *Langmuir* 18, 4963.
118. Aagren, P., Linden, M., Rosenholm, J. B., Blanchard, J., Schueth, F., Amenitsch, H. (2000) *Langmuir* 16, 8809.
119. Di Renzo, F., Testa, F., Chen, J. D., Cambon, H., Galarneau, A., Plee, D., Fajula, F. (1999) *Micropor. Mesopor. Mater* 28, 437.
120. Yang, H., Coombs, N., Sokolov, I., Ozin, G. A. (1996) *Nature* 381, 589.
121. Wang, L. Z., Yu, J., Shi, J. L., Yan, D. S. (1999) *J. Mater. Sci. Lett*. 18, 1171.
122. Wu, P., Zhu, J., Xu, Z. (2004) *Adv. Func. Mater*. 14, 345.
123. Dong, J., Xu, Z. (2006) In: Functional Fillers and Nanoscale Minerals, SME, Inc., Littleton, CO, 241–252.
124. Mercier, L., Pinnavaia, T. J. (1998) *Micropor. Mesopor. Mater* 20, 101.
125. Mercier, L., Pinnavaia, T. J. (1998) *Environ. Sci. Technol*. 32, 2749.
126. Lim, M. H., Blanford, C.F., Stein, A. (1998) *Chem. Mater*. 10, 467.
127. Brown, J., Mercier, L., Pinnavaia, T. J. (1999) *Chem. Commun*. 1, 69–70.
128. Brown, J., Richer, R., Mercier, L. (2000) *Micropor. Mesopor. Mater* 37, 41.
129. Antochshuk, V., Jaroniec, M. (2002) *Chem. Commun*. 3, 258.
130. Leyden, D. E., Luttrell, G. H. (1975) *Anal. Chem*. 47, 1612.
131. Arkels, B. (1992) Silane coupling agent chemistry, in silicon compounds, register and review, petrarch system catalogue, 59.

132. Goelzhauser, A., Panov, S., Mast, M., Schertel, A., Grunze, M., Woell, Ch. (1995) *Surf. Sci.* 334, 235.
133. Lund, H., Baizer, M. M. (1991) Organic Electrochemistry, Marcel Dekker, Inc. New York, 581.
134. Ihara, H., Okazaki, S., Ohmori, K., Uemura, S., Hirayama, C., Nagaoka, S. (1998) *Anal. Sci.* 14, 349.
135. Kanazawa, H., Kashiwase, Y., Yamamoto, K., Matsushima, Y. (1997) *Anal. Chem.* 69, 823.
136. Takafuji, M., Dong, W., Goto, Y., Sakurai, T., Nagaoka, S., Ihara, H. (2002) *Polym. J.* 34, 437.
137. Takafuji, M., Ide, S., Ihara, H., Xu, Z. (2004) *Chem. Mater* 16, 1977.
138. Gold, D. H., Gregor, H. P. (1960) *J. Phys. Chem.* 64, 1464
139. Liu, K. J., Gregor, H. P. (1965) *J. Phys. Chem.* 69, 1252
140. Tanford, C., Wagner, M. L. (1953) *J. Am. Chem. Soc.* 75, 434.
141. Gold, D. H., Gregor, H. P. (1960) *J. Phys. Chem.* 64, 1461.
142. Molina, M. J., Gomez-Anton, M. R., Rivas, B. L., Maturana, H. A., Pierola, I. F. (2001) *J. Appl. Polym. Sci.* 79, 1467
143. Shiraishi, Y., Nishimura, G., Hirai, T., Komasawa, I. (2002) *Ind. Eng. Chem. Res.* 41, 5065.
144. Dong, J., Xu, Z., Wang, F. (2008) *Appl. Surf. Sci.* 254, 3522.
145. Parida, S. K., Dash, S., Patel, S., Mishra, B. K. (2006) *Adv. Colloid Interface Sci.* 121, 77.
146. Inagaki, S., Guan, S., Fukushima, Y., Ohsuna, T., Terasaki, O. (1999) *J. Am. Chem. Soc.* 121, 9611.
147. Asefa, T., MacLachlan, M. J., Coombs, N., Ozin, G. A. (1999) *Nature* 402, 867.
148. Melde, B. J., Holland, B. T., Blanford, C. F., Stein, A. (1999) *Chem. Mater* 11, 3302.
149. Vinu, A., Hossain, K. Z., Ariga, K. (2005) *J. Nanosci. Nanotechnol.* 5/3, 347.
150. Hoffmann, F., Cornelius, M., Morell, J., Froba, M. (2006) *J. Nanosci. Nanotechnol.* 6, 265.

Chapter 7
Application of Bacterial Swimming and Chemotaxis for Enhanced Bioremediation

Rajveer Singh and Mira S. Olson

Abstract Contaminated soil and ground water persistently threatens drinking-water supplies, and is difficult and expensive to remediate. In situ bioremediation is an effective remediation strategy, but is often limited by inadequate distribution of bacteria throughout a contaminated region. Bacterial chemotaxis describes the ability of bacteria to sense chemical concentration gradients in their environment, and preferentially swim toward optimal concentrations of chemicals that are beneficial to their survival. This mechanism may greatly increase the efficiency of ground-water remediation technologies by enhancing bacterial mixing within contaminated zones. Many of the native soil-inhabiting bacteria that degrade common environmental pollutants also exhibit chemotaxis toward these compounds. In this paper, we present a review of bacterial chemotaxis to recalcitrant ground-water contaminants, including relevant techniques for mathematically quantifying chemotaxis, and propose improvements to field-scale bioremediation methods using chemotactic bacteria. By exploiting the degradative and chemotactic properties of bacteria, we can potentially improve both the economics and the efficiency of in situ bioremediation.

Keywords Chemotaxis · bioremediation · ground water

7.1 Background

Ground water is an invaluable national resource. Over half of the U.S. population relies on ground water as a source of drinking water [1]. Release of recalcitrant pollutants in industrial effluents and their continued contamination of ground water is therefore a major threat to our drinking-water supplies. Contaminated ground water is difficult to characterize and remediate, often requiring decades of treatment and monitoring [2]. Recognizing the prohibitively high cost

M.S. Olson
Department of Civil Architectural and Environmental Engineering, Drexel University, Philadelphia, PA 19104, USA
e-mail: mso28@drexel.edu

V. Shah (ed.), *Emerging Environmental Technologies*,

and impracticality of fully removing all trapped contaminant sources [3], researches have explored in situ bioremediation and biological stabilization as safe and efficient alternatives to physicochemical remediation strategies [4, 5]. Bioremediation refers to mineralization and/or transformation of pollutants into less harmful compounds via microbial degradation [6]. Quantification of advective and dispersive transport of bacteria and contaminants in the subsurface, and characterization of biochemical reactions involved in pollutant biodegradation, have been major areas of research in the past few decades. The roles of enzymes and genes in biodegradation are now relatively well understood. Current research efforts are focused on identifying additional features of bacterial behavior that may help enhance the rate of biodegradation [7]. Bacterial chemotaxis, a directed movement toward or away from chemicals (energy sources), is one such behavioral response that has the potential to enhance in situ bioremediation [7].

Chemotaxis may be applied to current technologies in bioaugmentation, monitored natural attenuation (MNA) and contaminant containment to improve overall remediation efficiency. Bioremediation is often limited by inadequate distribution of bacteria in regions favorable for pollutant degradation. For example, contaminants trapped in low-permeability pockets within the subsurface are persistent sources of long-term contamination in the environment; chemotaxis enables bacteria to locate, penetrate, and remediate these pollutant sources. While high concentrations of many environmental pollutants can be toxic, bacteria are able to degrade them at lower concentrations. Directed migration away from toxic hot spots toward lower peripheral chemical concentrations maximizes biodegradation efficiency by removing bacteria from high contaminant concentrations that inhibit growth and degradation and allowing them to accumulate in niches optimal for growth and metabolism. Chemotaxis has the potential to significantly improve in situ bioremediation processes; however, in order to apply this emerging technology to site remediation plans it is important that we optimize the unique transport processes that facilitate bacterial chemotaxis. This chapter presents a review of current literature on bacterial chemotaxis toward environmental pollutants, describes the specific assays available to quantify chemotactic transport parameters, and provides recommendations on how chemotaxis may be exploited to improve field-scale applications of in situ ground-water bioremediation.

7.2 Bacterial Chemotaxis

The ability of bacteria to sense and respond to chemical gradients in their surroundings and to direct their migration either toward or away from increasing concentrations of chemicals is known as chemotaxis [5, 8]. Bacterial migration toward and away from chemicals helps bacteria navigate to niches that are optimal for their growth and survival [5] and is termed positive and negative chemotaxis, respectively. Generally, chemicals that attract bacteria as sources

of carbon and/or energy are termed chemoattractants for those specific bacteria. Similarly, chemorepellents repel certain bacteria and are often toxic [5]. Recently, it has been reported that chemical contaminants that are readily degraded at low concentrations are toxic to bacteria above certain concentration thresholds [9, 10]. In such cases, a chemical can act both as a chemoattractant (at low concentrations) and a chemorepellent (at high concentrations) for the same bacterial strain.

7.2.1 Why Microorganisms Pose Chemotaxis

Responding to changes in the environment is a fundamental property of living cells and is of prime importance to single-cell microorganisms as they interact with their changing environment [5]. Through evolution, microorganisms have developed mechanisms that help them regulate their cellular mechanisms to changing environments [11]. Chemotaxis is an advantageous behavior selected by bacteria that has probably evolved as a result of bacterial pursuit of energy sources. It has been observed that numerous bacteria develop the ability to respond chemotactically to certain chemicals when they are grown under specific carbon and energy source conditions. Childers et al. [12] report that growth of flagella and pili, appendages responsible for chemotactic movement of bacteria, takes place on the surface of *Geobacter metallireducens* cells only when cells are grown under insoluble electron acceptor conditions. In contrast, cells grown in the presence of soluble substrates are neither chemotactic nor do they develop flagella and pili. They concluded that chemotaxis enables bacteria to establish contact with insoluble electron acceptors. Pandey and Jain [5] suggest that bacteria developed taxis, including chemotaxis, aerotaxis and phototaxis, over time as naturally available energy sources became limited. Introduction of anthropogenic pollutants into the environment, along with increased competition for natural resources, may have given bacteria the ability to respond to and degrade these chemical pollutants as sources of carbon and energy.

7.2.2 Molecular Mechanisms of Chemotaxis

In a uniform environment, bacteria swim in a random migration, which consists of relatively straight swimming, interrupted by tumbling events that change the swimming direction. This alternating series of runs and tumbles is governed by the direction of flagellar rotation. The overall bacterial motion results in a 3D random walk which is somewhat analogous to diffusion of gas molecules [8]. In the presence of chemical gradients in the surrounding medium, bacteria lengthen/shorten their run length between two consecutive tumbling movements; in other

words, they change their tumbling frequency depending on the presence of chemical stimuli.

Cell communication with their environment consists of complex extracellular signal reception and intracellular signal transduction mechanisms. A simple mechanism for *Escherichia coli* chemotaxis toward amino acids and sugars is described by Parales and Harwood [7]. *E. coli* are able to sense and respond to changes in their environment through surface receptor molecules called methyl-accepting chemotaxis proteins (MCPs) [8]. These MCPs embedded in the plasma membrane usually bind the attractant molecules. Upon binding, this activates intracellular signaling proteins which in turn alter the function of the effector [13]. This signal transudation mechanism results in a change in the direction of the flagellar rotation and is manifested as chemotaxis [7]. The chemotactic machinery of *E. coli* consists of five MCPs and six chemotactic proteins [7]. Complex signaling systems are found in many other chemotactic species with multiple sets of chemotactic genes. For example, 25 or more MCPs are found in *Pseudomonas putida* [7]. It is argued that despite these complexities, the fundamental mechanism of signal reception and transduction is similar in all species [14].

7.3 Random Motility and Chemotaxis Assays

A number of assays have been developed to evaluate the role of random motility and chemotaxis in bacterial transport. These assays can be divided into two general groups: single-cell and population-scale studies. A comparative study of bacterial random motility and chemotaxis quantification assays is presented by Lewus and Ford [15]. In this section, we describe experimental techniques for measuring and quantifying bacterial random motility and chemotaxis to specific chemoattractants.

7.3.1 Capillary Assay

This method was first introduced by Adler [16, 17] and has since been repeatedly modified to enable quantitative evaluation of chemotaxis. A typical capillary assay consists of a microcapillary tube filled with attractant and placed in a pool of motile bacteria at one end and sealed at the other (Fig. 7.1A). Motile bacteria respond to the chemical gradient formed as a result of diffusion into the pool and swim upgradient into the tube. The tube is removed after a pre-specified time interval and cells accumulated inside the tube are enumerated to quantify chemotaxis. A cloud of bacterial accumulation can also be observed microscopically around the mouth of the capillary for qualitative observation. Random motility can be quantified using similar experiments without a chemical attractant. Mathematical expressions for deriving quantitative expressions

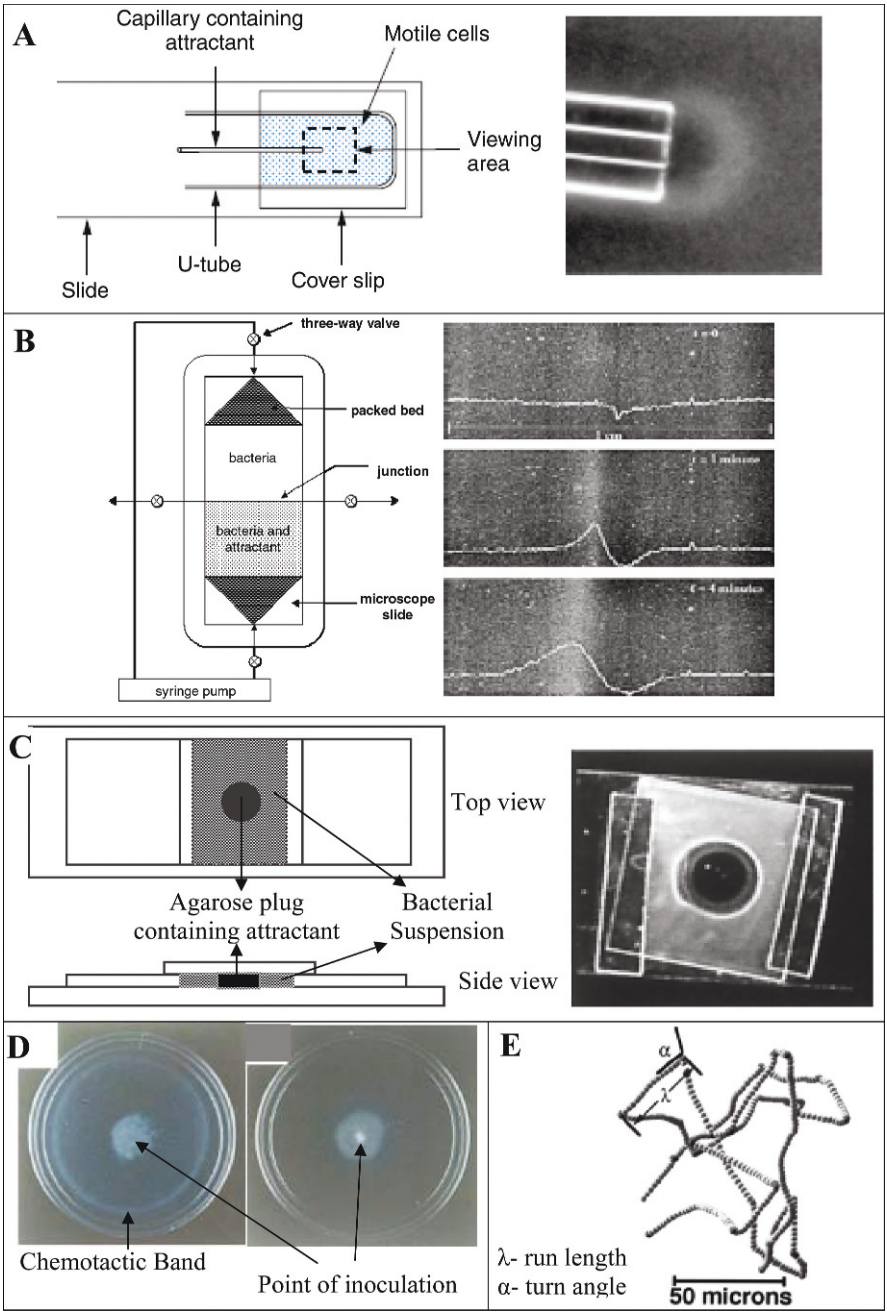

Fig. 7.1 Bacterial random motility and chemotaxis assays. Capillary assay (*Panel A*): Attractant, placed in capillary tube diffuses out into pool of motile bacteria and results into formation of chemical gradient. Bacteria sense and respond to this gradient and swim upgradient into the

of random motility and chemotaxis from capillary assay data will be described in Section 7.4.

Capillary assays are relatively easy to perform and have been widely used for quantitative evaluation of chemotaxis. However, data obtained from this method is not useful for relating population behavior to intrinsic cell parameters [18]. Mathematical models account for variability in setup geometry, but since flow patterns at the mouth of the capillary are complex, such models are based on simplified boundary conditions. This method is particularly suitable for testing chemotaxis of sparingly soluble compounds, such as naphthalene [7].

7.3.2 Stopped-Flow Diffusion Chamber (SFDC) Assay

Figure 7.1B represents an experimental design for the SFDC introduced by Ford et al. [18] for quantification of bacterial random motility and chemotaxis. This assay is based on the principle that two liquid streams, with different chemoattractant or chemorepellent concentrations, intersect via impinging flow to form a step change in chemical concentration. Chemotactic bacteria respond either positively or negatively to the chemical gradient. This assay overcomes limitations of the capillary assay by providing a well-characterized chemical concentration gradient.

Briefly, bacteria that are uniformly distributed in the SFDC respond to a chemical gradient induced by an initial step change in attractant concentration and migrate toward optimal concentrations, resulting in a moving bacterial band as time progresses (Fig. 7.1B). Light scattering microscopy is used to

Fig. 7.1 (continued) capillary tube that can be counted to quantify bacterial chemotaxis. Bacterial accumulation at the mouth of capillary can also be observed under microscope. SFDC assay (*Panel B*): Impinging flow is achieved by introducing two bacterial suspensions, which differ in attractant concentration, into a channel formed between two microscopic slides. After flow is stopped, temporal bacterial moving bands are imaged with light scattering microscope and are converted into bacterial density *vs* spatial plots to quantify bacterial chemotaxis. Agarose plug assay (*Panel C*): attractant is mixed with melted agarose plug and is placed in the middle of a chamber formed by using cover slip and plastic strips at the top of a microscopic slide. Bacterial suspension is flooded into chamber. Chemotactic band can be visualized under microscope. Swarm plate assay (*Panel D*): Attractant mixed with growth medium is poured into a Petri dish. Motile bacteria are stabbed in the middle. A sharp chemotactic band moving outward from inoculation point can be observed (*plate on left side*) in comparison to blank (*plate on right side*) which did not have any attractant with growth medium. Tracking microscope assay (*Panel E*): Individual bacterium random walk is tracked with tracking microscope to determine average run length and turn angle which in turn are used to calculate the random motility and chemotactic sensitivity coefficients. [Note: Pictures in Panels A, B, C (partially) D and E are adopted from Parales and Harwood (2002), Ford et al. (1991) and Lewus and Ford (2001), Parales et al. (2000), Samanta et al. (2000) and Ford and Harvey (2007), respectively.] Pictures in Panel B reprinted with permission of Wiley-Liss, Inc., a subsidiary of John Wiley & Sons, Inc.

detect moving bacterial bands. For random motility quantification, similar experiments can be performed with no chemoattractant.

Temporal bacterial concentration profiles can be obtained from digitized images and transformed into dimensionless bacterial concentration versus position plots (Fig. 7.1B). The area under the crest or above the trough represents bacterial concentration and is proportional to the number of migrated bacteria. Ford et al. [18] show that the area above the trough is linearly proportional to the square root of time. The following expression can be used to determine the random motility coefficient [15]:

$$\frac{b_0}{2}\sqrt{\frac{4\mu_0 t}{\pi}} = A_{\exp} \tag{7.1}$$

where b_0 is initial bacterial concentration in the injected solution, μ_0 is the random motility coefficient, t is elapsed time, and $A_{\exp}$ is the experimentally determined area under the bacterial concentration versus position curve. The random motility coefficient can be calculated using slope of the $A_{\exp}/b_0$ versus t curve and Eq. (7.1). A detailed procedure for determining chemotaxis parameters is provided by Lewus and Ford [15]. One of the main advantages of using this method is that it provides well-defined boundary conditions for attractant and bacterial concentrations in both spatial and temporal coordinates, and ease in mathematical analysis of experimentally obtained data. In addition, the initial chemical concentration is easily adjusted, enabling controlled studies of the chemotactic response at varying contaminant concentrations. The SFDC has been used to confirm that *P. putida* F1 exhibits both positive and negative chemotaxis toward benzene at low and high chemical concentrations, respectively.

7.3.3 Agarose Plug Assay

The agarose-in-plug bridge method was first developed by Yu and Alam [19] for studying chemotaxis. In this method, an attractant or repellent is mixed with low-melting temperature agarose and a drop of mixture is placed on the top of a microscope slide. A cover slip supported by plastic strips at both ends is placed on top to form a chamber around the agarose plug (Fig. 7.1C). A bacterial suspension is flooded into the chamber around the plug. A characteristic chemotactic band of bacterial accumulation is visualized surrounding the plug—a small distance from its edge—using light scattering microscopy. The limitation of this method is its poorly defined boundary conditions due to variability in the shape of the plug, making it difficult to model mathematically. This method has been used for toluene [20] and TCE [20, 21], and is particularly useful for volatile compounds, as the system is partially closed and therefore minimizes volatilization losses of the chemical [7].

7.3.4 Swarm Plate Assay

This qualitative method is based on metabolism of an attractant. A carbon source (attractant) is mixed with low percentage agar media (generally 0.3% [7]) and poured in a petri dish. Bacteria are stabbed in the middle of the petri dish and incubated. A sharp chemotactic band of bacteria growing outward is visualized in the petri dish as a result of attractant metabolization and the resultant concentration gradient (Fig. 7.1D). This method is well suited for identification of chemotactic bacteria and is widely used for enrichment of chemotactic mutants [7, 22, 23, 24, 25]. However, as metabolism is a primary requirement, this method is limited to testing chemotaxis of metabolizable chemoattractants [7].

7.3.5 Drop Assay

Similar to the swarm plate assay, this method is also based on population-scale imaging and may be used to study bacterial responses to both chemoattractants and chemorepellents. Chemotactic bacteria are suspended in a drop assay agar consisting of bacto-agar (0.3%) and a carbon source (1 mM glucose, for example) [25], and poured into a petri dish. The chemotactic response is determined by placing an attractant/repellent in the center of the petri dish, incubating, and observing the characteristic chemotactic band formed surrounding the drop.

7.3.6 Three-Dimensional Tracking Microscopy

In addition to the population-based assays described above, individual cell tracking assays for evaluating random motility and chemotaxis are also described in the literature [15, 18, 26], and are based on a three-dimensional tracking microscope developed by Berg [27]. This method consists of characterizing the 3D random walk, described earlier in Section 2.2, of individual bacteria (Fig. 7.1E). The parameters of interest are average run length (λ), average run time (τ), and average turn angle (α) of the bacteria. The following mathematical relationship, derived by Lovely and Dahlquist [26] and based on statistical analysis of individual cell-based parameters, can be used to calculate a population-based random motility coefficient.

$$\mu_0 = \frac{\lambda v}{3} \frac{1}{1 - \cos\alpha} \tag{7.2}$$

where v is the average chemotactic velocity and can be calculated from the average run length and average run time.

7.3.7 Chemotactic Index (C.I.)

A chemotaxis index parameter has been reported [25] to compare the chemotactic response of different species to the same attractant. In a capillary assay experiment, C.I. is defined as the ratio of the number of cells accumulated in the capillary with attractant to that in the control.

7.4 Chemotaxis Transport Parameters

To evaluate the potential applicability of chemotaxis to in situ bioremediation of environmental pollutants in soil and ground water, it is important to quantify this process in terms of quantifiable chemotactic transport parameters that can be directly incorporated into comprehensive bacterial fate and transport models. Ford and Harvey [8] have recently presented a systematic approach for quantification of these response parameters for laboratory-scale studies. This section presents a review of the transport parameters commonly reported in the literature.

7.4.1 Chemotaxis Sensitivity Coefficient (χ_0)

The chemotactic sensitivity coefficient, χ_0 is an intrinsic cell population-based parameter that theoretically relates the individual swimming behavior of a bacterium to the resulting migration of the bacterial population [28]. This parameter accounts for the mechanism by which bacteria respond to chemical gradients. Ford and Lauffenburger [28] derived the following analytical expression for determining the chemotactic sensitivity coefficient for commonly used capillary assay experiments:

$$\chi_0 = \sqrt{D\mu_0}\,\frac{(1+C_0)^2}{(C_\infty - C_0)}\left(\frac{N}{N_{RM}} - 1\right) \tag{7.3}$$

where D is attractant diffusivity; C_0 and C_∞ are normalized attractant concentrations at the mouth and far end of the capillary, respectively. Concentrations are normalized by the chemotaxis receptor constant, K_d (defined later); N and N_RM are numbers of cells accumulated in the capillary in the presence and absence of chemoattractant, respectively; and μ_0 is the cell random motility coefficient derived by Segel et al. [29]:

$$\mu_0 = \frac{\pi}{4t}\left(\frac{N_{RM}}{\pi r^2 b_\mathrm{c}}\right)^2 \tag{7.4}$$

where N_RM is the number of cells accumulated in a capillary of radius r at time t and b_c is the initial bacterial cell concentration in the chamber.

Table 7.1 Reported random motility and chemotactic sensitivity coefficients for bacteria under various experimental conditions

Bacterial strain	Chemoattractant	Random motility coefficient ($\times 10^{-6}$ cm^2/s)	Chemotactic sensitivity coefficient ($\times 10^{-4}$ cm^2/s)	Experimental condition	Reference
P. putida F1	TCE	0.15	0.08	Glass-coated polystyrene (250 μm diameter)	[21]
P. putida G7	Naphthalene	0.32	0.72 ± 0.14	Bulk liquid	[44]
			1.3	Saturated beads (50 μm)	[31]
P. putida PR2000	3-Chloro benzene	35 ± 2	1.9 ± 0.7	Bulk liquid quartz sand of diameter:	[48]
		0.7		81 μm	
		1.6		194 μm	
		3.1		326 μm	

Generally, the chemotactic sensitivity parameter is less directly quantified compared with other model parameters in bacterial transport models, and is therefore often determined as a fitted parameter. A higher value of χ_0 represents greater chemotactic response and thus results in more cell accumulation for similar concentrations of chemoattractants. Chemotactic sensitivity has units of distance^2/time (e.g., cm^2/s). A comparative list of bacterial random motility and chemotactic sensitivity coefficients for different bacterial species–chemoattractant combinations under various experimental condition is given in Table 7.1.

7.4.2 Chemotaxis Receptor Constant (K_d)

Chemoreceptor half-saturation constant and chemoreceptor binding constant are terms that are used interchangeably in the literature for the chemotaxis receptor constant, K_d. This parameter represents the propensity of bacteria to bind the attractant and characterizes the binding between attractant molecule and cell surface receptors, which are responsible for sensing concentration gradients in the surroundings. The value of this parameter corresponds to an optimal chemoattractant concentration, where bacteria elicit the strongest chemotactic response, and hence has units of concentrations (e.g. mM). This parameter is generally determined from dose–response curves, but can also be determined as a best fitted model parameter [21].

7.4.3 Chemotactic Velocity (v_c)

The chemotactic velocity, v_c is defined as an advective transport property and is a function of bacterial species, chemoattractant concentration, and chemoattractant concentration gradient. The following mathematical expression is commonly used for describing chemotactic velocity in shallow gradients [30]

$$v_c = \frac{\chi_0}{3} \frac{K_d}{(K_d + C)^2} \frac{dC}{dx} \tag{7.5}$$

for a one-dimensional system, where C is chemoattractant concentration and x is the spatial coordinate. There may exist a critical chemoattractant concentration, C_t below which no chemotactic response is elicited. Considering this fact, we suggest the following mathematical expression could be useful in calculating chemotactic velocity at low attractant concentrations:

$$v_c = \Theta(C - C_t) \frac{\chi_0}{3} \frac{K_d}{(K_d + C)^2} \frac{dC}{dx} \tag{7.6}$$

where $\Theta(C)$ is a Heaviside step function, the value of which is given by,

$$\Theta(C - C_t) = \begin{cases} 0; C < C_t \\ 1; C \geq C_t \end{cases} \tag{7.7}$$

The chemotactic velocity parameter is directly incorporated into bacterial transport models as an advective velocity term to account for bacterial transport due to chemotaxis.

7.4.4 Chemotactic Bacterial Transport Models

Mathematical models describing bacterial transport are modified to account for chemotaxis in porous media. One such model given by Pedit et al. [31] and Olson et al. [32] is based on a material balance for bacteria and chemoattractant in one dimension and can be represented as:

$$R \frac{\partial b}{\partial t} = -\frac{\partial (b v_x)}{\partial x} + D_b \frac{\partial^2 b}{\partial x^2} - \frac{\partial (b v_c)}{\partial x} + Y \frac{q_m C}{C + k_s} b - k_d b \tag{7.8}$$

and,

$$R \frac{\partial C}{\partial t} = -\frac{\partial (C v_x)}{\partial x} + D_c \frac{\partial^2 C}{\partial x^2} - \frac{q_m C}{C + k_s} b \tag{7.9}$$

where b is bacterial concentration, C is chemoattractant concentration, R is the retardation factor, v_x is the advective ground-water velocity, v_c is the chemotactic velocity, Y is the yield coefficient, q_m is the maximum chemoattractant utilization rate, k_s is the half-saturation constant, k_d is the bacterial decay rate, t is time, and x is the spatial coordinate in the direction of ground-water flow. D_b and D_c represent the longitudinal bacterial and chemical dispersion coefficients, respectively, and are given by:

$$D_{\mathrm{b}} = \alpha v_x + \frac{\mu_{eff}}{\varepsilon} \tag{7.10}$$

and

$$D_{\mathrm{c}} = \alpha v_x + \frac{D_{eff}}{\varepsilon} \tag{7.11}$$

where α is the longitudinal dispersivity, ε is porosity, μ_{eff} is the effective bacterial motility coefficient in porous media, and D_{eff} is the effective diffusion coefficient of the chemoattractant.

7.5 Review of Bacterial Chemotaxis Toward Environmental Pollutants

Various natural and anthropogenic activities have led to the expulsion of simple and polycyclic aromatic hydrocarbons (PAHs), nitroaromatic compounds (NACs) and chlorinated compounds into the environment [24]. Although the biodegradability of many of these compounds has been studied, bacterial chemotaxis toward environmental pollutants, which may be used to enhance remediation rates, has received relatively little attention [5]. Recently, a number of soil inhibiting bacteria were found to be chemotactic toward a variety of environmental pollutants and have been extensively reviewed by Pandey and Jain [5] and Parales and Harwood [7]. In several studies [5, 7, 20, 23, 25, 33], a direct or indirect correlation between chemotaxis and biodegradation has been reported and it is speculated that chemotaxis may potentially enhance bioremediation of contaminated soil and ground water. A comprehensive list of environmental pollutants and the identified bacterial strains that exhibit chemotaxis toward them is presented in Table 7.2.

7.5.1 Chemotaxis Toward Simple Aromatic Compounds

A large number of simple aromatic compounds are environmental pollutants, including benzene and toluene. Petroleum products, asphalt, coal tar, creosote, and incomplete combustion of fossil fuel are the major sources of these

Table 7.2 List of bacterial strains that are chemotactic toward various environmental pollutants

Pollutant group	Bacterial strain	Chemoattractants	Comments	Reference
Simple or single ring aromatic hydrocarbon	*P. putida* PRS2000	Benzoate; *m*-toluate; *p*-toluate; *o*-toluate; salicylate; *p*-hydroxybenzoate; benzoylformate; β-phenylpyruvate; salicylate; DL-p-hydroxymandelate; phenoxyacetate		[57]
	P. putida F1	Toluene; benzene, ethylbenzene; succinate isopropylbenzene; triflorotoluene (TFT)	Metabolism	[20]
	Ralstonia pickettii PKO1	Toluene		[20]
	Burkholderia cepacia G4	Toluene		[20]
	Azospinillum strains	Benzoate; catechol (1,2-dihydroxybenzene); 4-hydroxybenzoate; 3,4-dihydroxybenzoic acid; malate		[58]
	Rhizobium meliloti	4',7-Dihydroxyflavone; 4',7-dihydroxyflavanone; 4,4'-dihydroxy-2-methoxychalcone		[59, 60]
Polycyclic aromatic hydrocarbons (PAHs)	*P. putida* G7	Naphthalene; Salicylate, Biphenyl	Metabolism	[35, 44]
	Pseudomonas sp. strain NCIB 9816-4	Naphthalene; Salicylate		[35]
	P. putida RK J1	Naphthalene, Salicylate		[36]
Nitroaromatic compounds (NACs)	*Ralstonia* sp. SJ98	*p*-Nitrophenol (PNP); 4-nitrocatechol (NC); *o*-nitrobenzoate (ONB); *p*-nitrobenzoate (PNB); 3-methyl-4-nitrophenol (MNP)	Metabolism	[22, 25]
		2,4-Dinitrophenol; 2,5-dinitrophenol; 2,6-dinitrophenol; o-dinitrobenzene; m-dinitrobenzene; m-nitrophenol	Co-metabolism	[33]
Chlorinated hydrocarbon	*P. putida* PRS2000	3-Chlorobenzoate; 4-chlorobenzoate		[38, 39]
	P. putida F1	Trichloroethylene (TCE); Perchloroethylene (PCE) Dichloroethylene (DCE)	Co-metabolism	[20, 21]
	R. eutropha JMP123 (pJP4)	2,4-Dichlorophenoxyacetate (2,4-D)	Induced by growing on 2,4-D	[61]
Other compounds	*P. stutzeri* KC	Nitrate, acetate	Electron acceptor	[52, 62]
	G. metallireducens	Fe (III); Mn (IV)	Electron acceptor	[12]

compounds [6]. As a result of human activities in the extraction, transportation, refinement, and use of petroleum, these compounds have become serious environmental threats [7]. Due to their simple structure, mineralization of these compounds is relatively easy and thereby favorable for biodegradation. A number of soil bacteria, *Pseudomonas* sp., *Ralstonia* sp., *Burkholderia* sp. and *Rhizobium* sp., for example, exhibit chemotaxis toward aromatic hydrocarbons (Table 7.2). Chemotaxis can play an important role in biodegradation of these compounds by bringing degrading bacteria closer to sites that are contaminated with these pollutants.

7.5.2 Chemotaxis Toward Polycyclic Aromatic Hydrocarbons (PAHs)

PAHs are compounds that consist of two or more aromatic rings. Naphthalene, one of the most prevalent groundwater contaminants at sites contaminated with PAHs [34], is relatively easily degraded and is often used as a model compound in degradation studies of PAHs. A number of bacterial strains are chemotactic toward naphthalene, including *P. putida* G7, *Pseudomonas* sp. strain NCIB 9816-4 and *P. putida* RK J1 (Table 7.2). The chemotactic responses in G7 and NCIB 9816-4 species were induced when grown with naphthalene itself [35], whereas in RK J1 species, the response was induced by growing on salicylate [36]. The naphthalene chemoreceptor, NahY (an MCP), is encoded downstream of the naphthalene catabolic genes on the NAH7 plasmid [7]. Pandey and Jain [5] suggest that chemotaxis toward naphthalene and/or salicylate might be due to a change in cellular energy levels due to metabolism of these compounds and/or because of intracellular receptors that recognize such contaminants or their degradation intermediates.

7.5.3 Chemotaxis Toward Nitroaromatic Compounds (NACs)

NACs are man-made pollutants and are difficult to degrade. They are generally used as pesticides, herbicidal dyes, and explosives. Once released into the environment, NACs undergo complex physical, chemical, and biological changes resulting in harmful and toxic byproducts [25, 37]. Samanta et al. [25] isolated *Ralstonia* sp. SJ98 from pesticide-contaminated soil using the drop assay technique. Strain SJ98 is chemotactic toward a large number of NACs and subsequently degrades them by metabolism [22, 25] and co-metabolism [24] (Table 7.2). Bhushan et al. [33] reported chemotaxis-mediated biodegradation of cyclic nitramine explosives by an obligate anaerobic bacterium *Clostridium* sp. strain EDB2 (Table 7.2), which they isolated from marine sediments.

On the contrary, a number of other compounds such as *p*-nitroaniline, 2,3-dinitrotoluene, naphthalene, phenanthrene, and salicylic acid, were neither biodegradable nor chemoattractants for strain SJ98 [25]. These results further

reinforce the hypothesis that a correlation between chemotaxis and biodegradation exists.

7.5.4 Chemotaxis Toward Chlorinated Compounds

Both aliphatic and aromatic chlorinated hydrocarbons are of growing concern in the environment due to their abundant use as herbicides, pesticides, and solvents in various industries [38]. Dichloroethylene (DCE), trichloroethylene (TCE) and perchloroethylene (PCE) are common pollutants in the environment and most of them are recalcitrant to biodegradation [38].

Some bacterial strains that are chemotactic toward chlorinated compounds have been isolated for the biodegradation of chlorinated compounds (Table 7.2). A chemotactic response toward 2,4-dichlorophenoxyacetate (2,4-D) is induced in *R. eutropha* JMP123(pJP4) when grown on 2,4-D, which encodes the pJP4 plasmid containing genes for 2,4-D degradation [5]. *P. putida* PRS2000 exhibits chemotaxis to 3- and 4-chlorobenzoate, when induced with 4-hydroxybenzoate [38, 39]. *P. putida* F1, grown on toluene, is chemotactic toward TCE, DCE, PCE, and other chlorinated compounds [20].

A review of the molecular basis of chemotaxis toward different pollutants indicates that chemoreceptor genes are located within biodegradation gene clusters and are coordinately regulated with these genes [5, 7]. In cases, where the chemoreceptor has not yet been identified, chemotaxis toward different pollutants is induced by growing on the pollutant itself or one of its metabolites, which likely encodes the necessary chemoreceptors. Thus, it has been speculated that chemotaxis may be an integral feature of the biodegradation process [5, 7].

Genetic improvement of microorganisms has been suggested as an option for environmental restoration [40]. Identification, isolation, and characterization of chemotactic bacteria coupled with genetically improved degradation ability may have great potential in optimization of in situ bioremediation.

7.6 Quantification of Chemotaxis for Bioremediation

Both experimental and modeling approaches for quantification of chemotaxis with respect to bioremediation enhancement are described in the literature [21, 31, 41, 42, 43, 44, 45, 46, 47] and will be presented in this section.

7.6.1 Quantification of Chemotaxis in Bulk Liquids

Marx and Aitken [44] evaluated naphthalene degradation by *P. putida* G7 in a typical capillary assay experiment. Experimental data were fitted to a model in

order to predict the chemotactic sensitivity coefficient. The value obtained was found to be approximately three times lower than previously reported values from a relatively simpler model [48] that did not account for the bacterial transport in the chamber. Another model that also incorporated substrate consumption was able to predict chemotactic band formation, and replicated capillary assay data well [45]. Hilpert [41] presents a numerical modeling approach based on Lattice–Boltzmann methods for modeling bacterial chemotaxis and the fate and transport of a chemoattractant in bulk liquid. Chemotactic traveling bacterial bands in a uniformly distributed substrate region were simulated as a result of self-generated concentration gradients due to substrate consumption. Based on simulation results, they suggest that only a fraction of a bacterial slug injected into a chemoattractant domain forms a traveling band as the slug length exceeds a critical value. These findings are consistent with the capillary assay results from Adler [16].

7.6.2 Quantification of Chemotaxis in Saturated Porous Media

Pedit et al. [31] measured the chemotactic response of *P. putida* G7 toward naphthalene in saturated porous media. To simulate saturated porous media, a conventional capillary assay method was modified by packing glass beads in the capillary tube and surrounding reservoir. A model was developed to estimate transport parameters including naphthalene diffusion, random motility, and chemotactic sensitivity. Simulations indicate that an order of magnitude higher cell concentration of the non-chemotactic strain would be required to achieve the same amount of naphthalene degradation as from a chemotactic strain. Chemotaxis in porous media systems can be approximated by free-liquid systems by accounting for soil parameters including tortuosity and porosity [48]. Recently, an analytical solution for bacterial chemotaxis in homogeneous porous media was presented by Long and Hilpert [47]. They derived analytical solutions for chemotactic band velocities under different substrate input conditions. This approach could be important in comparing the chemotactic band velocity with groundwater velocity in order to assess the impact of chemotaxis on an overall remediation scheme.

Olson et al. [21] have used immunomagnetic labeling and magnetic resonance imaging (MRI) for non-invasive measurement of bacterial distributions in a packed column. Simulation of experimental data required addition of a non-zero chemotactic sensitivity term to account for the chemotactic response of *P. putida* F1 toward TCE. In addition, Olson et al. [49] mathematically demonstrated that bacteria traveling in a high-permeability region with advective flow can successfully migrate toward and accumulate around contaminant diffusing from low-permeability regions. The effect of pore size on transport parameters is also reported; a 50% reduction in both motility and chemotaxis is reported for a similar reduction in pore size. These studies demonstrate that

chemotaxis can potentially be exploited to enhance in situ bioremediation in the subsurface, particularly in heterogeneous and low-permeability regions, where low solubility contaminants such as NAPLs remain trapped.

7.6.3 Impact of Chemotaxis on Contaminant Degradation

A quantitative evaluation of enhanced chemoeffector degradation due to chemotaxis is presented by Law and Aitken [42]. Naphthalene desorption and degradation from a model NAPL was faster for a chemotactic wild-type *P. putida* G7 strain compared with non-chemotactic strains, which is attributed to the steep concentration gradient created by chemotactic bacteria near the NAPL surface. Thus, chemotaxis can be useful in increasing the rate of mass transfer and biodegradation of NAPL-associated hydrophobic pollutants.

The role of chemotaxis in naphthalene degradation by *P. putida* G7 in a heterogeneous aqueous system was evaluated experimentally by Marx and Aitken [46]. They demonstrated that mass transfer was a rate-limiting step in naphthalene biodegradation by non-chemotactic strains. In contrast, the removal rate clearly exceeded the mass transfer rate in the case of the chemotactic wild-type strain of *P. putida* G7 and was approximately five times faster than the non-chemotactic strains. These results clearly indicate the possibility of enhancing bioremediation in aqueous systems by chemotaxis.

7.7 Field-Scale Application of Chemotaxis to Ground-Water Bioremediation

Bacterial movement in soil as a result of chemotaxis and random motility is well documented by soil microbiologists [50, 51]. However, studies demonstrating direct evidence of enhanced bioremediation at the field scale due to chemotaxis are very rare. Witt et al. [52] demonstrated faster migration of *Pseudomonas stutzeri* KC, a denitrifying strain chemotactic toward nitrate, in comparison to groundwater flow velocities in a bench scale study of carbon tetrachloride (CT) degradation. CT and nitrate were injected with groundwater into a model aquifer column containing CT-saturated sediments. Bacteria and tracers were inoculated at the top of a column and it was observed that bacteria migrated through the column faster than the traces, removing both adsorbed and aqueous CT. This enhanced migration of strain KC was attributed to the chemotactic response as a result of nitrate depletion in the vicinity. Olson et al. [21] also reported chemotaxis of *P. putida* F1 toward TCE in small-scale laboratory columns packed with glass-coated polystyrene. Two field-scale bacterial transport studies recently reported faster transport and greater recovery of motile *Pseudomonas* compared with non-motile bacterial strains [12, 43]. However, no distinction between chemotaxis and motility was made in these two field

studies. Paul et al. [37] evaluated chemotaxis of *Ralstonia* sp. SJ98 toward *p*-nitrophenol in soil microcosms using qualitative and quantitative plate and tray assays. However, no effort was made to evaluate the effect of chemotaxis on biodegradation.

One concern for in situ bioremediation is the bioavailability of contaminants, or the proximity of target pollutants to degrading microorganisms. Many subsurface pollutants are hydrophobic, sparingly soluble in groundwater, and form a non-aqueous-phase liquid (NAPL) [6]. These NAPLs remain trapped in low-permeability regions in heterogeneous subsurface environments, making them difficult to remove by conventional pump-and-treat treatment methods. Chemotaxis is a mechanism for bringing cells in close proximity to contaminants [7, 8, 25] thereby reducing limitations in bioavailability due to mass transfer limitations or low contaminant solubility [7]. It also enables bacteria to adjust their proximity to toxic repellents, thereby increasing their odds for survival and optimizing their distribution in conditions favorable for bioremediation. A vigorous chemotactic response can enhance the availability of carbon and/or energy resources significantly and hence chemotactic bacteria can grow faster than their non-chemotactic counterparts. Faster chemoattractant consumption causes localized depletion of the contaminant which creates even steeper chemical gradients that trigger higher driving forces for dissolution of the contaminant. In light of this, groundwater treatment technologies can take advantage of bacterial chemotaxis for enhancement of contaminant removal. Scenarios of groundwater remediation in which chemotaxis can potentially be exploited to enhance biodegradation are described below.

7.7.1 Enhanced Remediation Due to Chemotaxis in Heterogeneous Porous Media

Contaminants often remain trapped in pockets of low permeability within the subsurface. Figure 7.2 depicts a contaminated aquifer scenario where contaminant is trapped in a low-permeability clay lens. In Fig. 7.2a, non-chemotactic degradative bacteria flow with advective ground water through the surrounding high-permeability region, limiting remediation to the slow diffusion of contaminants into the high-permeability region. Lanning et al. [53] recently reported that chemotactic bacteria can swim transverse to the flow direction at fluid velocities greater than typical ground-water flow velocities. Thus chemotactic bacteria flowing with ground water in the high-permeability regions can sense chemical gradients induced by diffusing contaminants and migrate toward the source (Fig. 7.2b). Chemotactic bacteria are able to swim upgradient in typical ground-water velocities [47] to penetrate low-permeability regions from the bulk flow in high-permeability areas [49]. Accumulation of bacterial bands surrounding contaminated low-permeability regions can significantly enhance contaminant removal.

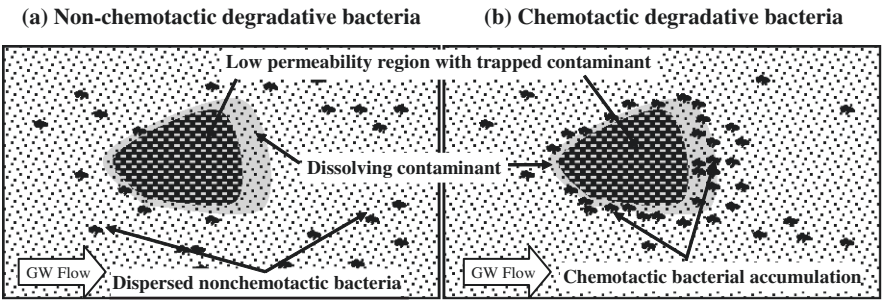

Fig. 7.2 Removal of contaminant trapped in low-permeability lenses. Non-chemotactic strains (**a**) remain dispersed and wash away with ground-water flow. Chemotactic bacteria (**b**) sense and respond to the chemical gradient formed due to contaminant diffusion and accumulate around the contaminated site

7.7.2 Application of Chemotaxis to Bioaugmentation

Introduction of beneficial microorganisms into contaminated aquifers for the purpose of enhancing biodegradation is referred to as bioaugmentation. Bioaugmentation is highly site-specific and dependent on the microbial ecology and physiology of the site [54], however, it is feasible for combined chemotaxis and genetically improved degradation capabilities to significantly improve the remediation rate of an aquifer.

Figure 7.3 shows a schematic of a bioaugmentation strategy that takes advantage of chemotaxis for improved contaminant removal from an aquifer contaminated due to leakage from an underground storage tank. Ground-water flow past the contaminated region will slowly dissolve the contaminant and a contaminant plume will form that may contaminate the entire aquifer system. Figure 7.3a represents the initial step of a bioaugmentation scheme. Injected non-chemotactic bacterial strains would consume the contaminant plume in the vicinity of an injection point or would rely on contaminant advection away from the injection point for further consumption (Fig. 7.3b). Formation and movement of chemotactic bacterial bands in a uniformly distributed contaminated region (such as a contaminant plume) has been demonstrated [47]. A moving bacterial band can migrate upgradient and/or downgradient against contaminant gradients that are moving with ground water to overcome mass transfer limitations (Fig. 7.3c). Moving bacterial bands capitalize on naturally available nutrient resources (such as electron acceptors) within the aquifer while non-chemotactic strains depend solely on the addition of external nutrients to stimulate the biodegradation process. Since chemotactic bacteria have the ability to swim against typical ground-water flow velocities [47, 53], a given bacterial washout rate may be slower for chemotactic strains compared with non-chemotactic strains, which would ultimately result in less frequent bacterial and nutrient injections. Bioaugmentation using

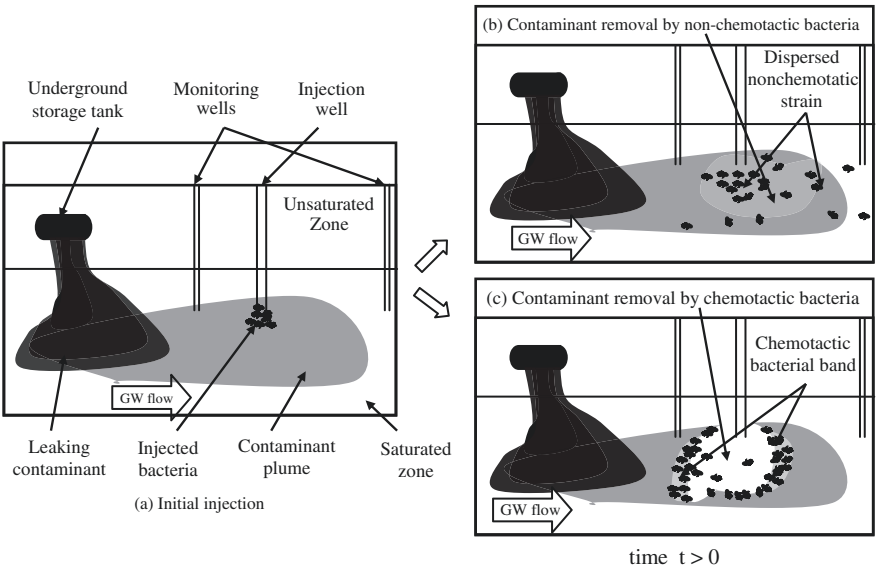

Fig. 7.3 Chemotaxis assisted bioaugmentation. Panel (**a**) represents the initial state of bioaugmentation, where bacterial strains are injected for remediation of a contaminant plume. Non-chemotactic strains (**b**) remain dispersed and are washed away with ground-water flow, resulting in a slow removal rate. Chemotactic strains (**c**) create a chemical gradient as a result of contaminant consumption and move upgradient and downgradient in the form of concentrated bands, resulting in an accelerated contaminant removal rate

chemotactic bacteria may significantly accelerate the degradation rate in contaminated aquifers and reduce overall remediation costs. Appropriate bacterial transport models, including chemotaxis transport parameters, will be helpful in selecting appropriate injection locations and rates to fully exploit the benefits of chemotaxis.

7.7.3 Chemotaxis in Monitored Natural Attenuation (MNA)

Natural attenuation of contaminants relies on various naturally occurring in situ physicochemical and biological processes. A careful evaluation of these processes to achieve site-specific remediation objectives within a reasonable timeframe is termed MNA. These in situ processes, under favorable conditions and without human intervention, may cause stabilization, transformation or complete destruction of contaminants [55]. Chemotaxis may enhance these natural processes. Incorporating moving bacterial bands in MNA predictions for a specific site may significantly reduce the remediation time by overcoming mass transfer and nutrient limitations.

7.7.4 Application of Chemotaxis for Contaminant Containment – A Variable Length Biocurtain

Preventing off-site migration of contaminants with ground-water flow thereby containing the source for biodegradation is known as contaminant containment. In practice, barriers such as slurry walls and reactive barriers in conjunction with continuous or intermittent pumping are used for containment of contaminated sites. A biocurtain is a biologically active zone around a contaminated region designed to contain and remediate the site. A biocurtain containing chemotactic bacteria can be advantageous by increasing the length of the reactive zone. Changes in ground-water flow conditions may occur due to pumping failures or extreme precipitation events. Chemotaxis enables bacteria to adjust their position with respect to changes in the physical and chemical characteristics of the contaminant plume, thereby reducing the risk of off-site migration. In addition, since chemotactic bacteria can sustain higher flow velocities [47, 53] pumping costs associated with contaminant containment can be reduced by decreasing pumping rates and frequency.

7.8 Conclusion

Chemotaxis is traditionally studied in medicine and other areas of microbiological research. It has recently attracted interest in the environmental research community due to its potential for improving in situ bioremediation. Research to understand the impact of chemotaxis on bacterial transport in the subsurface and its role in enhancing bioremediation is ongoing. However, there are several key areas, described below, which would lead to a better understanding of the role chemotaxis may play in improving remediation of contaminated aquifers.

- Only a portion of bacteria in a uniformly distributed contaminant plume forms a chemotactic band [41]. Identification of the critical bacterial concentration that maximizes chemotaxis would help engineers minimize bioclogging and optimize bacterial and nutrient injection requirements.
- High contaminant concentrations can be toxic to degrading bacteria [10, 56]. Negative chemotaxis enables bacteria to swim toward lower concentrations of contaminants, however, this process and the ultimate distribution of bacteria surrounding high contaminant loads are not well understood.
- Chemotaxis studies related to bioremediation have all been reported under aerobic conditions. However, anaerobic conditions prevail in many subsurface environments. Chemotaxis in anaerobic conditions should be considered for groundwater remediation processes.
- Evidence from recent laboratory column studies and numerical simulations suggests that chemotaxis can potentially improve in situ bioremediation of contaminated sites [5, 7, 8, 21, 41, 42, 43, 46, 47, 49, 53]. However, to the best

of our knowledge, there are neither studies explicitly measuring enhanced bioremediation at the field scale due to chemotaxis nor predictive models for expected enhanced degradation rates based on chemotactic parameters.

Adequate distribution of degradative bacteria in contaminated regions is paramount for effective in situ bioremediation. Bacterial chemotaxis is an important transport mechanism that can help achieve this goal. Experimental studies have shown that chemotaxis has the potential to enhance bioremediation, but applications at the field scale have yet to be demonstrated. Laboratory studies combined with additional field-scale experiments are needed to verify that chemotaxis does indeed stimulate in situ biodegradation.

References

1. U.S. EPA, *Safe Drinking Water Act*, in *Section 1429, Ground Water Report to Congress*. 1999.
2. U.S. EPA, *Recommendations from the EPA Ground Water Task Force*. 2007, United States Environmental Protection Agency.
3. U.S. EPA, *Guidance for evaluating the technical impracticality of groundwater restoration*, in *Office of Solid Waste and Emergency Response*. 1993, EPA: Washington, DC. p. Directive 9234.2-25.
4. Herbes, S.E. and L.R. Schwall, *Microbial transformation of polycyclic aromatic hydrocarbons in pristine and petroleum-contaminated sediments*. Appl. Environ. Microbiol., 1978. **35**(2): pp. 306–316.
5. Pandey, G. and R.K. Jain, *Bacterial chemotaxis toward environmental pollutants: role in bioremediation*. Appl. Environ. Microbiol., 2002. **68**(12): pp. 5789–5795.
6. Bedient, P.B., H.S. Rifai, and C.J. Newell, *Ground water Contamination: Transport and Remediaton*. Second edition, 1997, New Jersey: Prentice Hall PTR.
7. Parales, R.E. and C.S. Harwood, *Bacterial chemotaxis to pollutants and plant-derived aromatic molecules*. Curr. Opin. Microbiol., 2002. **5**(3): pp. 266–273.
8. Ford, R.M. and R.W. Harvey, *Role of chemotaxis in the transport of bacteria through saturated porous media*. Adv. Water Resour., 2007. **30**(6–7): pp. 1608–1617.
9. Collins, L.D. and A.J. Daugulis, *Benzene/toluene/p-xylene degradation. Part I. Solvent selection and toluene degradation in a two-phase partitioning bioreactor*. Appl. Microbiol. Biotechnol. 1999. **52**(3): pp. 354–359.
10. Kim, D.J., et al., *Modeling of growth kinetics for Pseudomonas spp. during benzene degradation*. Appl. Microbiol. Biotechnol., 2005. **69**(4): pp. 456–462.
11. Hoch, J.A., *Two-component and phosphorelay signal transduction*. Curr. Opin. Microbiol., 2000. **3**(2): pp. 165–170.
12. Childers, S.E., S. Ciufo, and D.R. Lovley, *Geobacter metallireducens accesses insoluble Fe(III) oxide by chemotaxis*. Nature, 2002. **416**(6882): pp. 767–769.
13. Alberts, B., A. Johnson, J. Lewis, M. Raff, K. Roberts, P. Walter, *Molecular Biology of the Cell*. Fourth edition, 2002, New York: Garland Science Publishing. 15:1-15:87.
14. Armitage, J.P. and R. Schmitt, *Bacterial chemotaxis: Rhodobacter sphaeroides and Sinorhizobium meliloti–variations on a theme?* Microbiology, 1997. **143**(12): pp. 3671–3682.
15. Lewus, P. and R.M. Ford, *Quantification of random motility and chemotaxis bacterial transport coefficients using individual-cell and population-scale assays*. Biotechnol. Bioeng., 2001. **75**(3): pp. 292–304.
16. Adler, J., *Chemotaxis in bacteria*. Science, 1966. **153**(737): pp. 708–716.

17. Adler, J., *A method for measuring chemotaxis and use of the method to determine optimum conditions for chemotaxis by Escherichia coli*. J. Gen. Microbiol., 1973. **74**(1): pp. 77–91.
18. Ford, R.M., B.R. Phillips, J.A. Quinn, and D.A. Lauffenburger, *Measurement of bacterial random motility and chemotaxis coefficients: I. Stopped-flow diffusion chamber assay*. Biotechnol. Bioeng., 1991. **37**(7): pp. 647–660.
19. Yu, H.S. and M. Alam, *An agarose-in-plug bridge method to study chemotaxis in the Archaeon Halobacterium salinarum*. FEMS Microbiol. Lett., 1997. **156**(2): pp. 265–269.
20. Parales, R.E., J.L. Ditty, and C.S. Harwood, *Toluene-degrading bacteria are chemotactic towards the environmental pollutants benzene, toluene, and trichloroethylene*. Appl. Environ. Microbiol., 2000. **66**(9): pp. 4098–4104.
21. Olson, M.S., et al., *Quantification of bacterial chemotaxis in porous media using magnetic resonance imaging*. Environ. Sci. Technol., 2004. **38**(14): pp. 3864–3870.
22. Bhushan, B., et al., *Chemotaxis and biodegradation of 3-methyl- 4-nitrophenol by Ralstonia sp. SJ98*. Biochem. Biophys. Res. Commun., 2000. **275**(1): pp. 129–133.
23. Harwood, C.S., et al., *Identification of the pcaRKF gene cluster from Pseudomonas putida: involvement in chemotaxis, biodegradation, and transport of 4-hydroxybenzoate*. J. Bacteriol., 1994. **176**(21): pp. 6479–6488.
24. Pandey, G., et al., *Chemotaxis of a Ralstonia sp. SJ98 toward co-metabolizable nitroaromatic compounds*. Biochem. Biophys. Res. Commun., 2002. **299**(3): pp. 404–409.
25. Samanta, S.K., et al., *Chemotaxis of a Ralstonia sp. SJ98 toward different nitroaromatic compounds and their degradation*. Biochem. Biophys. Res. Commun., 2000. **269**(1): pp. 117–123.
26. Lovely, P.S. and F.W. Dahlquist, *Statistical measures of bacterial motility and chemotaxis*. J. Theor. Biol., 1975. **50**: pp. 476–496.
27. Berg, H.C., *How to track bacteria*. Rev. Sci. Instrum., 1971. **42**(6): pp. 868–871.
28. Ford, R.M. and D.A. Lauffenburger, *A simple expression for quantifying bacterial chemotaxis using capillary assay data: application to the analysis of enhanced chemotactic responses from growth-limited cultures*. Math. Biosci., 1992. **109**(2): pp. 127–149.
29. Segel, L.A., I. Chet, and Y. Henis, *A simple quantitative assay for bacterial motility*. J. Gen. Microbiol., 1977. **98**(2): pp. 329–337.
30. Chen, K.C., R.M. Ford, and P.T. Cummings, *Mathematical models for motile bacterial transport in cylindrical tubes*. J. Theor. Biol., 1998. **195**(4): pp. 481–504.
31. Pedit, J.A., et al., *Quantitative analysis of experiments on bacterial chemotaxis to naphthalene*. Biotechnol. Bioeng., 2002. **78**(6): pp. 626–634.
32. Olson, M.S., et al., *Mathematical modeling of chemotactic bacterial transport through a two-dimensional heterogeneous porous medium*. Bioremediation J., 2006. **10**(1–2): pp. 1–11.
33. Bhushan, B., et al., *Chemotaxis-mediated biodegradation of cyclic nitramine explosives RDX, HMX, and CL-20 by Clostridium sp. EDB2*. Biochem. Biophys. Res. Commun., 2004. **316**(3): pp. 816–821.
34. Durant, N.D., L.P. Wilson, and E.J. Bouwer, *Microcosm studies of subsurface PAH-degrading bacteria from a former manufactured gas plant*. J. Contam. Hydrol., 1995. **17**: pp. 213–237.
35. Grimm, A.C. and C.S. Harwood, *Chemotaxis of Pseudomonas spp. to the polyaromatic hydrocarbon naphthalene*. Appl. Environ. Microbiol., 1997. **63**(10): pp. 4111–4115.
36. Samanta, S.K. and R.K. Jain, *Evidence for plasmid-mediated chemotaxis of Pseudomonas putida towards naphthalene and salicylate*. Can. J. Microbiol., 2000. **46**(1): pp. 1–6.
37. Paul, D., R. Singh, and R.K. Jain, *Chemotaxis of Ralstonia sp. SJ98 towards p-nitrophenol in soil*. Environ. Microbiol., 2006. **8**(10): pp. 1797–1804.
38. Harwood, C.S., R.E. Parales, and M. Dispensa, *Chemotaxis of Pseudomonas putida toward chlorinated benzoates*. Appl. Environ. Microbiol., 1990. **56**(5): pp. 1501–1503.
39. Harwood, C.S., *A methyl-accepting protein is involved in benzoate taxis in Pseudomonas putida*. J. Bacteriol., 1989. **171**(9): pp. 4603–4608.

40. Samanta, S.K., O.V. Singh, and R.K. Jain, *Polycyclic aromatic hydrocarbons: environmental pollution and bioremediation*. Trends in Biotechnol., 2002. **20**(6): pp. 243–248.
41. Hilpert, M., *Lattice-Boltzmann model for bacterial chemotaxis*. J. Math. Biol., 2005. **51**(3): pp. 302–332.
42. Law, A.M. and M.D. Aitken, *Bacterial chemotaxis to naphthalene desorbing from a nonaqueous liquid*. Appl. Environ. Microbiol., 2003. **69**(10): pp. 5968–5973.
43. Law, A.M. and M.D. Aitken, *Continuous-flow capillary assay for measuring bacterial chemotaxis*. Appl. Environ. Microbiol., 2005. **71**(6): pp. 3137–3143.
44. Marx, R.B. and M.D. Aitken, *Quantification of chemotaxis to naphthalene by Pseudomonas putida G7*. Appl. Environ. Microbiol., 1999. **65**(7): pp. 2847–2852.
45. Marx, R.B. and M.D. Aitken, *A material-balance approach for modeling bacterial chemotaxis to a consumable substrate in the capillary assay*. Biotechnol. Bioeng., 2000. **68**(3): pp. 308–315.
46. Marx, R.B. and M.D. Aitken, *Bacterial chemotaxis enhances naphthalene degradation in a heterogeneous aqueous system*. Environ. Sci. Technol., 2000. **34**(16): pp. 3379–3383.
47. Long, W. and M. Hilpert, *Analytical solutions for bacterial energy taxis (chemotaxis): Traveling bacterial bands*. Adv. Water Resour., 2007. **30**(11): pp. 2262–2270.
48. Barton, J.W. and R.M. Ford, *Determination of effective transport coefficients for bacterial migration in sand columns*. Appl. Environ. Microbiol., 1995. **61**(9): pp. 3329–3335.
49. Olson, M.S., et al., *Mathematical modeling of chemotactic bacterial transport through a two-dimensional heterogeneous porous medium*. Bioremediation J., 2006. **10**(1): pp. 13–23.
50. Bashan, Y. and G. Holguin, *Root-to-root travel of the beneficial bacterium azospirillum brasilense*. Appl. Environ. Microbiol., 1994. **60**(6): pp. 2120–2131.
51. Soby, S. and K. Bergman, *Motility and chemotaxis of rhizobium meliloti in soil*. Appl. Environ. Microbiol., 1983. **46**(5): pp. 995–998.
52. Witt, M.E., et al., *Motility-enhanced bioremediation of carbon tetrachloride-contaminated aquifer sediments*. Environ. Sci. Technol., 1999. **33**(17): pp. 2958–2964.
53. Lanning, L.M., R.M. Ford, and T. Long, *Bacterial chemotaxis transverse to axial flow in a microfluidic channel*. Biotechnol. Bioeng., 2008. 100(4): pp. 653–663.
54. U.S. EPA, *Technical Protocol for Evaluating Natural Attenuation of Chlorinated Solvents in Ground Water*. EPA/600/R-98/128, 1998.
55. U.S. EPA, *Engineered Approaches to In Situ Bioremediation of Chlorinated Solvents: Fundamentals and Field Applications*. EPA 542-R-00-008, 2000.
56. Kim, H.-S. and P.R. Jaffe, *Spatial distribution and physiological state of bacteria in a sand column experiment during the biodegradation of toluene*. Water Res., 2007. **41**(10): pp. 2089–2100.
57. Harwood, C.S., M. Rivelli, and L.N. Ornston, *Aromatic acids are chemoattractants for Pseudomonas putida*. J. Bacteriol., 1984. **160**(2): pp. 622–628.
58. Lopez-de-Victoria, G. and C.R. Lovell, *Chemotaxis of azospirillum species to aromatic compounds*. Appl. Environ. Microbiol., 1993. **59**(9): pp. 2951–2955.
59. Dharmatilake, A.J. and W.D. Bauer, *Chemotaxis of rhizobium meliloti towards nodulation gene-inducing compounds from alfalfa roots*. Appl. Environ. Microbiol., 1992. **58**(4): pp. 1153–1158.
60. Parke, D., M. Rivelli, and L.N. Ornston, *Chemotaxis to aromatic and hydroaromatic acids: comparison of bradyrhizobium japonicum and rhizobium trifolii*. J. Bacteriol., 1985. **163**(2): pp. 417–422.
61. Hawkins, A.C. and C.S. Harwood, *Chemotaxis of ralstonia eutropha JMP134(pJP4) to the herbicide 2,4-dichlorophenoxyacetate*. Appl. Environ. Microbiol., 2002. **68**(2): pp. 968–972.
62. Roush, C.J., C.M. Lastoskie, and R.M. Worden, *Denitrification and chemotaxis of pseudomonas stutzeri KC in porous media*. J. Environ. Sci. Health, Part A, 2006. **41**(6): pp. 967–983.

Index